

Exclusive ϕ meson production in HERMES

DISSERTATION

zur Erlangung des Doktorgrades
des Fachbereichs Physik
der Universität Hamburg

vorgelegt von

Mayya Golembiovskaya

aus Saratov, Russland

Hamburg

2014

Gutachter der Dissertation:	Prof. Dr. P. Schleper Prof. Dr. G. Schnell
Gutachter der Disputation:	Dr. M. Diehl Prof. Dr. G. Schnell
Datum der Disputation:	23 Januar 2014
Vorsitzender des Prüfungsausschusses:	Dr. G. Steinbrück
Vorsitzender des Promotionsausschusses:	Prof. Dr. P. Hauschildt
Leiterin des Fachbereichs Physik:	Prof. Dr. D. Pfannkuche
Dekan der Fakultät für Mathematik, Informatik und Naturwissenschaften:	Prof. Dr. H. Graener

Abstract

In the present work exclusive ϕ meson leptonproduction at HERMES experiment in DESY was studied using the data collected at HERA accelerator in the period from 1998 till 2000 and from 2006 till 2007 years. In the analysis unpolarized and longitudinally polarized hydrogen and deuteron targets were used, the beam consisted of longitudinally polarized leptons. Via measurement of the angular and momentum distribution of the ϕ meson decay products 23 spin density matrix elements (SDMEs) for the ϕ meson were obtained. The number of SDMEs was defined by the experiment conditions, e.g. by the beam and target polarization directions. For the mentioned time period ϕ meson SDMEs were defined at HERMES for the first time. The quantities U_1 , U_2 and U_3 which can be used to check presence of unnatural parity exchange (UPE) mechanism in ϕ meson production were calculated from SDMEs. All the results were obtained in 3 kinematic bins of Q^2 , 4 kinematic bins of t' and for the integrated kinematics. No statistically significant difference between the results for hydrogen and deuteron targets was observed. The UPE quantities were found to be zero within 2σ for the integrated kinematics, indicating negligible contribution of UPE for the ϕ meson production which is in agreement with theory predictions. The test of s-channel helicity conservation hypothesis via comparison of corresponding SDME values showed helicity conservation for the ϕ meson production.

Zusammenfassung

In der vorliegenden Dissertation wurde exklusive ϕ -Meson Leptoproduktion am HERMES Experiment am DESY studiert. Dafür wurden die Daten, die im Laufe des Betriebs des Elektronenbeschleuniger von 1998 bis 2000 und von 2006 bis 2007 gesammelt worden waren, verwendet. Als Targetmaterial waren unpolarisierter und longitudinal polarisierter Wasserstoff und Deuterium im Einsatz, der Strahl bestand entweder aus longitudinal polarisierten Elektronen oder Positronen. Durch die Messung der Winkelverteilung der ϕ -Meson-Zerfallsprodukte wurden dreiundzwanzig Spindichtematrixelemente bestimmt. Die Anzahl der Elemente wurde von den experimentellen Bedingungen, nämlich der Polarization des Targetmaterials und des Strahls, bestimmt. Für die entsprechenden Daten wurden die Elemente zum ersten Mal bei HERMES gemessen. Aus den Elementen der Spindichtematrix wurden die Werte U_1 , U_2 and U_3 ermittelt, mit denen die Mitwirkung von unnatürlichem Paritätsaustausch getestet werden kann. Alle Ergebnisse wurden für 3 kinematische Bereiche in Q^2 und 4 kinematischen Bereichen in t' , sowie für den kinematischen Gesamtbereich bestimmt. Die Ergebnisse für die Spindichtematrixelemente für Wasserstoff und Deuterium haben keinen statistisch aussagekräftigen Unterschied aufgezeigt. Die Werte U_1 , U_2 and U_3 sind für alle kinematischen Bereiche innerhalb zwei Sigma mit Null verträglich. Dies bedeutet, dass der Beitrag vom UPE-Mechanismus zur Formation des ϕ -Mesons nebensächlich ist. Das ist im Einklang mit den theoretischen Prognosen. Der Test der s-Kanal-Helizitätsbewahrung, der durch die Gleichstellungen bestimmter Elemente durchgeführt wurde, zeigte, dass die Helizität im Prozess erhalten bleibt.

Contents

1	Introduction	1
2	Exclusive ϕ meson production	3
2.1	Kinematics	3
2.2	Deep-inelastic scattering	5
2.3	Parton distribution function	7
2.4	Form factors	8
2.5	Generalized parton distributions	8
2.6	Vector meson dominance model	12
2.7	Regge theory	14
2.8	The vector meson spin density matrix in Wolf-Schilling notation	15
2.9	Definition of the scattering angles in vector meson production	17
2.10	The decay angular distribution of vector meson production in Wolf-Schilling formalism	19
2.11	The spin density matrix elements of the vector meson production in Markus-Diehl formalism	21
2.12	The decay angular distribution of the vector meson production in Markus-Diehl formalism	21
2.13	s-channel helicity conservation	22
2.14	Natural and unnatural parity exchange	23
2.15	Radiative corrections	24
3	The HERMES experiment	26
3.1	The HERA ring	26
3.2	Beam	27
3.3	Target	28
3.4	Spectrometer	29
3.4.1	The tracking system	31
3.4.2	Particle identification	32
3.4.3	Trigger system	34
3.5	Data structure	34

4	Analysis	36
4.1	The data and Monte Carlo event selection	36
4.1.1	Data quality	36
4.1.2	Geometrical restrictions	37
4.1.3	Selection of exclusive events	39
4.1.4	Separation of coherent and incoherent parts for deuteron data	43
4.1.5	ϕ meson invariant mass distribution	45
4.1.6	Final data sample used in the analysis	46
4.1.7	Monte Carlo event selection	47
4.1.8	Data to Monte Carlo comparison	49
4.2	SDME extraction	49
4.2.1	Maximum-likelihood method	50
4.2.2	Monte Carlo studies of the MLH fit stability	54
4.2.3	Cross-checks of the results	57
4.2.4	Extracted SDMEs and U_1, U_2, U_3 values.	58
4.2.5	Compatibility of hydrogen and deuteron results.	58
4.3	Systematics	62
4.3.1	All-in-one procedure	63
4.3.2	Different Monte Carlo models	70
4.3.3	Background subtraction	70
4.3.4	Contribution of each source of the uncertainty to the total systematic uncertainty.	73
4.3.5	Total systematic uncertainty	77
5	Results	82
5.1	Kinematic dependencies of Wolf-Schilling SDMEs	82
5.2	Test of SCHC hypotheses	88
5.3	Kinematic dependencies of Markus-Diehl SDMEs	88
5.4	UPE quantities	99
5.5	Cross section ratio	100
6	Conclusions	103
A	The relations between the SDME notation of Wolf-Schilling and that of Markus Diehl	104
B	The relations between the SDMEs in the Wolf-Schilling notation and amplitudes	105
C	Comparison of data to Monte Carlo (PYTHIA and RhoMC generators)	107

D	SDMEs extracted with and without semi-inclusive background subtraction	116
E	SDMEs extracted using for the p. d. f. normalization PYTHIA and RhoMC generated sets.	121
F	Tables of results	126
	Bibliography	146

Chapter 1

Introduction

Studying the structure of matter during the last two centuries brought physicist to the conclusion, that the matter is composed from the small invisible discrete parts. The present understanding of the matter composition is expressed in the Standard Model. According to it, the three types of interaction exist: strong, electromagnetic and weak (gravitation is not included in the Standard Model). The interactions are described via exchange of bosons which are particle with an integer spin.¹ The strong interaction is mediated by the gluons and described in Quantum Chromodynamic (QCD), electromagnetic interactions are carried by photons, weak interactions are distributed by W and Z bosons. In terms of the Standard Model, the matter is build from the three generations of fermions which are, in contrast to bosons, particles with a half-integer spin. Each generation includes a lepton, 2 quarks and one neutrino. Each of the 12 particles mentioned above has a corresponding antiparticle. Hadrons are composite particles built from different combinations of quarks. It was confirmed for the first time in 1955 [1] via the reaction of elastic ep scattering. The scattering pattern was different from the theoretically predicted model of a point-like nucleon. The possible explanation was provided by the model, describing a nucleon as a conglomeration of a few scattering centers. Apart from these centers, identified later as valence quarks, the nucleon contains gluons (so called “sea”) which can produce quark-antiquark pairs, e.g. sea quarks.

The experiments of a type $ep \rightarrow eX$, e.g. deep-inelastic scattering (DIS) experiments, e.g. where the proton breaks up, have become the main tool to investigate the inner nucleon structure. The latter becomes visible only when the de Brogile wave-length $\lambda = h/p$ of the photon, mediating electromagnetic interactions, is comparable to the nucleon size, in other words when the lepton momenta p is large enough. Therefore the more is the energy - the less is the wave length, that is why it is important to achieve high energies of the beam particles (electrons), colliding with target particles (nucleons). If no final product of the reaction, except from the scattered lepton, e.g. no X is detected – then the process is called inclusive DIS. If one of the products and the lepton are registered, than the process is referred to as semi-inclusive

¹Spin is in units of \hbar . In this work $\hbar = 1$ and the light speed $c = 1$.

DIS. In case when the whole signature of the reaction is known, the reaction is an exclusive one.

In early DIS experiments the quark spin was found to be $1/2$. Since nucleon contains three quarks, its spin can then be naturally represented as a sum of the two quarks aligned in one direction and the third quark spin anti-aligned to it. Later the EMC experiment ([2]) discovered that the quark contribution to the nucleon spin does not exceed 30%. This situation is called the spin crisis. The way out of the situation was to assume that not only the quark spin is responsible for the nucleon spin, but also orbital angular momenta of quarks and gluons and gluon spin contribute to the nucleon spin:

$$S = \frac{1}{2} = \frac{1}{2}\Delta\Sigma + \Delta G + L_q + L_g, \quad (1.1)$$

where $\Delta\Sigma$ is the contribution of the quark spins, ΔG is that of gluon spin, L_q and L_g are the orbital angular momenta of quarks and gluons correspondingly. The recently developed generalized parton distributions (GPDs) formalism provides 3-dimensional nucleon structure by unification of the two previously developed concepts of probability density functions, describing deep-inelastic scattering, and the form factors, describing the elastic scattering processes. GPDs can not be measured directly, but are accessible in exclusive reactions, where all the reaction products are detected. One of such reactions is a reaction of an exclusive ϕ meson leptonproduction which is a subject of this work.

In chapter 2 the theoretical framework and the physical motivation of the analysis are given. Then the relevant details of the experiment HERMES are presented in chapter 3. The analysis is described in chapter 4, where the chain of event selection (Section 4.1), SDME extraction (Section 4.2) and systematic studies (Section 4.3) are discussed. The results and conclusions are subject of chapters 5 and 6.

Chapter 2

Exclusive ϕ meson production

Exclusive leptonproduction of vector mesons from deep-inelastic scattering gives a possibility to study the structure of both vector meson (V) and the nucleon (N) via measurements of angular and momentum distributions of the vector meson decay products. The corresponding kinematic variables of the exclusive vector meson production are presented in Section 2.1. The deep-inelastic scattering (DIS) reaction phenomenology and the concise introduction to the functions, describing the inner nucleon structure, is given in Section 2.2. Exclusive ϕ meson production can be explained in terms of the Vector Meson Dominance (VMD) model, described in Section 2.6. In this model, the virtual photon fluctuates into a vector meson whose interaction with the nucleon can be represented using Regge phenomenology, given in Section 2.7. On the other hand, exclusive meson production at large values of Q^2 and W can be described in terms of perturbative QCD, which involves non-perturbative QCD objects, namely generalized parton distributions (GPDs), whose definition and properties are presented in Section 2.5.

The ϕ meson is a vector meson formed from a strange quark and a strange antiquark. It has a mass of $1019.445 \pm 0.020 MeV$, total angular momentum $J = 1$, odd parity $J^{PC} = 1^{--}$, G-parity $I^G = 0^-$, strange flavour (strangeness) $S = 0$, charm flavour $C = 0$, bottom flavour $B = 0$. It is short living particle, after the formation reaction it decays into two oppositely charged kaons in $49.1 \pm 0.8\%$ ([54]) of the case.

2.1 Kinematics

The exclusive vector meson production from deep-inelastic lepton scattering is described by the equation

$$e(k) + P(p) \rightarrow e'(k') + P'(p') + V(v) \quad (2.1)$$

where $e(k)$, $e'(k')$ are initial and scattered leptons with four-momenta k and k' ; $P(p)$, $P'(p')$ are initial and scattered nucleons with their four-momenta p and p' ; $V(v)$ is the vector meson produced with the four-momentum v . The schematic view of the process is shown in Figure 2.1,

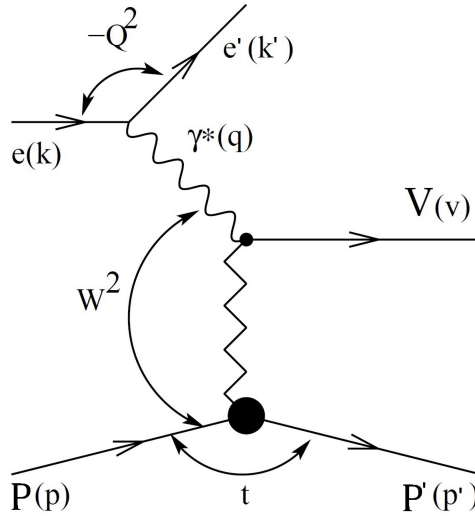


Figure 2.1: The reaction of exclusive ϕ meson production.

the particle's four-momenta are given in parentheses. The electromagnetic interaction prevails at HERMES level of energies over the weak one, therefore Z and W boson exchanges are neglected and only photon is considered as an interaction mediator. Multi-photon exchange is suppressed by the factor of electromagnetic fine structure constant $\alpha_{em} = 1/137$.

An exchanged photon lives for a time $\Delta t \geq \hbar/2\Delta E$ and is therefore termed a virtual photon with a virtuality given by the formula

$$Q^2 = -q^2 = -(k - k')^2 \stackrel{lab}{=} 4EE' \sin^2 \frac{\theta}{2}, \quad (2.2)$$

where q is the four-momentum of the virtual photon γ^* , E and E' are energies of the incoming and outgoing leptons correspondingly, θ is the scattering angle of the lepton in the laboratory frame. The Bjorken scaling variable is defined as

$$x_B = \frac{Q^2}{2p \cdot q} \stackrel{lab}{=} \frac{Q^2}{2M\nu}, \quad (2.3)$$

where M is the nucleon mass, ν is the energy transferred from the initial lepton to the virtual photon in the laboratory frame:

$$\nu = \frac{p \cdot q}{M} \stackrel{lab}{=} E - E'. \quad (2.4)$$

The lepton-nucleon system center-of-mass energy s is given by $s = (k + p)^2$, the photon-nucleon system center-of-mass energy squared W^2 is specified by

$$W^2 = (q + p)^2 \stackrel{lab}{=} M^2 + 2M\nu - Q^2 = M^2 + Q^2 \frac{1 - x_B}{x_B}. \quad (2.5)$$

If $x_B = 1$, then $W = M$, which corresponds to the case of elastic scattering. The squared four-momentum transfer from the initial to the final nucleon, or in other words from the virtual photon to the ϕ meson produced is

$$t = (q - v)^2 = (p - p')^2. \quad (2.6)$$

The smallest kinematically allowed value of $-t$ at the fixed ν and Q is denoted as t_0 . The variable $t' = t - t_0$ is equal to zero if in the photon-nucleon center-of-mass system the momentum of the produced ϕ meson is collinear to that of the γ^* . The variable ϵ , representing the ratio of fluxes of longitudinal and transverse virtual photons, reads as

$$\epsilon = \frac{1 - y - y^2 \frac{Q^2}{4\nu^2}}{1 - y + \frac{1}{4}y^2 \left(\frac{Q^2}{\nu^2} + 2 \right)}, \quad (2.7)$$

where $y = \frac{p \cdot q}{p \cdot k} \stackrel{lab}{=} \frac{\nu}{E}$ - the energy transfer from the initial lepton to the nucleon, $0 < y < 1$.

2.2 Deep-inelastic scattering

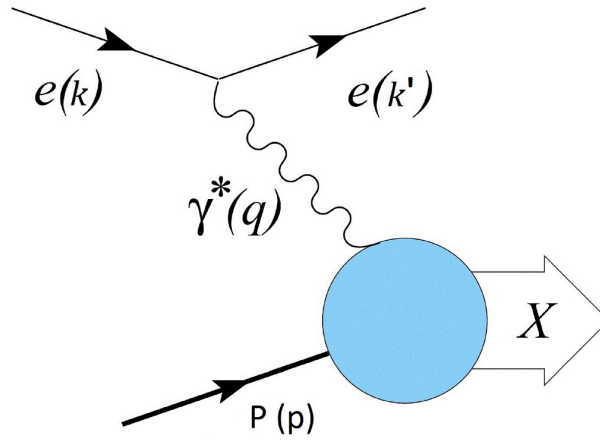


Figure 2.2: The deep-inelastic scattering process.

The leading-order Feynman diagram of the deep-inelastic scattering (DIS) process of a lepton on a nucleon is depicted in Figure 2.2. DIS may be represented as a consequence of two processes - emission of a virtual photon by a lepton and absorption of the photon by a nucleon. The corresponding cross section can be expressed as the contraction of a leptonic tensor $L^{\mu\nu}$ with a hadronic tensor $W_{\mu\nu}^{DIS}$ ([3], [4]):

$$d\sigma \propto L^{\mu\nu} W_{\mu\nu}^{DIS}, \quad (2.8)$$

The leptonic tensor describes the lepton transition from the initial to the final state via emission of the virtual photon and is calculable in quantum electrodynamic (QED):

$$L^{\mu\nu} = 2[k'^{\mu}k^{\nu} + k^{\mu}k'^{\nu} + (m_e^2 - k \cdot k')g^{\mu\nu}] - 2im_e\epsilon^{\mu\nu\alpha\beta}q_{\alpha}s_{\beta}, \quad (2.9)$$

where m_e is the electron mass and s_{β} is the lepton-spin four-vector, $g^{\mu\nu}$ is the metric tensor, $\epsilon^{\mu\nu\alpha\beta}$ is the totally anti-symmetric Levi-Civita tensor and $\epsilon^{0123} = 1$. The first part is symmetric with the respect to the indexes μ , and ν , while the second term is anti-symmetric and describes the initial lepton spin s_{β} . The hadronic tensor describes the absorption of the exchanged virtual photon by the nucleon and the transition of the nucleon to the final hadronic state X:

$$W_{\mu\nu}^{DIS}(q, p, S) = \frac{1}{4\pi M} \sum_n \int \frac{d^3 P'_n}{(2\pi)^3 2P'_n} \times (2\pi)^4 \delta^4 \left(p + q - \sum_n P'_n \right) H_{\mu\nu}(p, S, P'_X), \quad (2.10)$$

where $H_{\mu\nu}(p, S, P_X) = \langle p, S | J_{\mu}(0) | X \rangle \langle X | J_{\nu}(0) | P, S \rangle$, J_{μ} represents the electromagnetic proton transition-current four-vector, S , p and M the proton spin, momentum and mass correspondingly. The sum in Equation 2.10 is over all particles X in the final state, having four momenta $p_X = (E_X, P_X)$. The δ^4 guarantees 4-momentum conservation. The hadronic tensor cannot be calculated from first principles and has to be parametrized. As a result of the symmetry properties parity, time reversal and transition invariance, current conservation, the number of terms in the parametrization is restricted. The resulting parametrization is:

$$W_{\mu\nu}^{DIS} = W_{\mu\nu}^S(q, p) + W_{\mu\nu}^A(q, p, S), \quad (2.11)$$

where the first term parametrizes the symmetric spin-independent hadronic tensor part ([4]):

$$W_{\mu\nu}^{(S)}(q, p) = \left(-g_{\mu\nu} - \frac{q_{\mu}q_{\nu}}{Q^2} \right) W_1(p \cdot q, q^2) + \frac{W_2(p \cdot q, q^2)}{M^2} \left(p_{\mu} - \frac{p \cdot q}{q^2} q_{\mu} \right) \left(p_{\nu} - \frac{p \cdot q}{q^2} q_{\nu} \right) \quad (2.12)$$

and the second part parametrizes the antisymmetric spin-associated part ([4]):

$$W_{\mu\nu}^A(q, p, S) = i\epsilon_{\mu\nu\alpha\beta}q^{\alpha} \left(MS^{\beta}G_1 + [(p \cdot q)S^{\beta} - (S \cdot q)p^{\beta}] \frac{G_2}{M} \right). \quad (2.13)$$

Each of the terms is either a function of the two spin-averaged structure functions W_1 , W_2 , or the two spin-dependent structure functions G_1 , G_2 . In the Bjorken limit, or DIS regime, when large Q^2 implies large ν : $-q^2 \rightarrow \infty$, $\nu = E - E' \rightarrow \infty$, the structure functions depend on $x = \frac{Q^2}{2p \cdot q} = \frac{Q^2}{2M\nu}$.

In the Bjorken limit the structure functions scale approximately:

$$\lim_{\substack{Q^2 \rightarrow \infty \\ x \text{ fixed}}} MW_1(Q^2, x) \equiv F_1(x), \quad \lim_{\substack{Q^2 \rightarrow \infty \\ x \text{ fixed}}} \nu W_2(Q^2, x) \equiv F_2(x), \quad (2.14)$$

$$\lim_{\substack{Q^2 \rightarrow \infty \\ x \text{ fixed}}} \nu M^2 G_1(Q^2, x) \equiv g_1(x), \quad \lim_{\substack{Q^2 \rightarrow \infty \\ x \text{ fixed}}} \nu^2 M G_2(Q^2, x) \equiv g_2(x). \quad (2.15)$$

Independence of F_i on Q^2 was explained by Feynman in the parton model. The main idea was that scattering occurs from a point-like object (parton) in a proton. However, for relatively low values of x scaling violations are observed, which can be explained by partonic interactions, leading to the logarithmic dependence of the structure functions on Q^2 . The structure functions describe the internal structure of the target nucleon. Taking into account Equations 2.14 - 2.15 and 2.8, an expression for the unpolarized DIS cross section can be written:

$$\frac{d^2\sigma}{dx dQ^2} = \frac{4\pi\alpha^2}{Q^4} \left[F_1(x, Q^2) y^2 + \frac{F_2(x, Q^2)}{x} \left(1 - y - \frac{Mxy}{2E} \right) \right] \quad (2.16)$$

in terms of the structure functions F_1 and F_2 , which need to be determined experimentally.

2.3 Parton distribution function

In terms of the parton model the nucleon consists of partons (quarks and gluons) of flavour f and electric charge e_f , each having a spin s which can be parallel to that of the nucleon ($s = S$) or antiparallel to it ($s = -S$). The DIS structure functions can be expressed via quark distribution functions q_f and quark helicity distribution functions Δq_f [4]:

$$F_1(x) = \frac{1}{2} \sum_f e_f^2 q_f(x), \quad F_2(x) = \sum_f e_f^2 x q_f(x), \quad (2.17)$$

$$g_1(x) = \frac{1}{2} \sum_f e_f^2 \Delta q_f(x), \quad g_2(x) = 0, \quad (2.18)$$

The unpolarized quark distribution function $q_f = q_f^+ + q_f^-$ and the polarized quark distribution function $\Delta q_f = q_f^+ - q_f^-$ represent the probability to find a quark in the nucleon with momentum fraction x and spin parallel (q_f^+) or anti-parallel (q_f^-) to the longitudinal nucleon spin. In the infinite momentum frame, where the nucleon moves fast in the z -direction, the unpolarized (polarized) structure function $F_1(g_1)$ is proportional to the sum of the unpolarized (polarized) quark density functions weighted by the squared quark charge. Under an assumption that the partons inside the protons are quarks (gluons are therefore neglected), e.g. spin-1/2 particles, the following relation between Equations 2.17 is fulfilled: $2xF_1(x) = F_2(x)$ and is called Gallan-Gross relation. The unpolarized distribution $q(x)$ of quarks in the proton is accessible experimentally via measurements of the structure functions F_1 and F_2 . The polarized structure

function g_1 gives information about the distribution of quarks with certain helicities.

2.4 Form factors

Nucleon form factors $F^f(Q^2)$ are measured in the elastic process $lN \rightarrow l'N'$ and contain the information on the nucleon structure at a given four-momentum transfer Q^2 . Helicity conserving process corresponds to Dirac form factor $F_{1p(n)}^f$, while the spin-flip process is described by the Pauli, $F_{2p(n)}^f$, form factor for proton (neutron), correspondingly. They have following values in the limit $Q^2 \rightarrow 0$:

$$F_{1p}^f(0) = 1, \quad F_{2p}^f(0) = \kappa_p, \quad F_{1n}^f(0) = 0, \quad F_{2n}^f(0) = \kappa_n, \quad (2.19)$$

where $\kappa_p = \mu_p - 1$ (μ_p - magnetic moment of the proton) and $\kappa_n = \mu_n - 1$ (μ_n - magnetic moment of the neutron) are the anomalous magnetic moment of the proton and neutron, respectively. The measured quantities, constructed from the form factors, are electric $G_E \equiv F_{1p(n)}^f \frac{Q^2}{4M^2}$ and magnetic $G_M \equiv F_{1p(n)}^f + F_{2p(n)}^f$, form factors. For very low momentum transfer, G_E and G_M may be represented as Fourier transforms of the transverse charge and magnetization current densities inside the nucleon [14].

2.5 Generalized parton distributions

Both the form factors and PDFs, mentioned above, provide only one dimensional images of the nucleon structure, describing the transverse distance from the center of a fast moving nucleon and - the probability to find a quark with the certain momentum fraction and spin direction, respectively. The “unification” of these quantities leads to the generalized parton distribution (GPD) formalism, which was developed in the last decades. The GPDs include form factors and PDFs, being their boundary conditions, and therefore providing a 3-dimensional image of partons inside hadrons. Figure 2.3 shows the comparison of information about inner parton structure provided by the form factors, GPDs and parton density functions, respectively.

Various contributions to the DIS process in the infinite momentum frame can be scaled according to the order of $1/Q$ in the hadronic tensor expansion ([18]). This order is called twist. The terms of the expansion has a form $(1/Q)^{\tau-2}$. The leading twist, e.g. the lowest order of suppression is then twist-two.

At leading twist for parton helicity non-flip configurations the nucleon structure information can be parametrized in terms of four GPDs for each type of partons, named H , \tilde{H} , E , \tilde{E} . Parton helicity flip processes provide four more GPDs, but the amplitudes of the corresponding processes show ([16]) suppression factor for the gluonic suppress to be $-t/Q^2$ and for quark one $\sqrt{-t}/Q$. From the four helicity-conserving GPDs for unpolarized targets the most important one is the GPD H ; the three other either contribute less (\tilde{H} , \tilde{E}) or can be neglected (E).

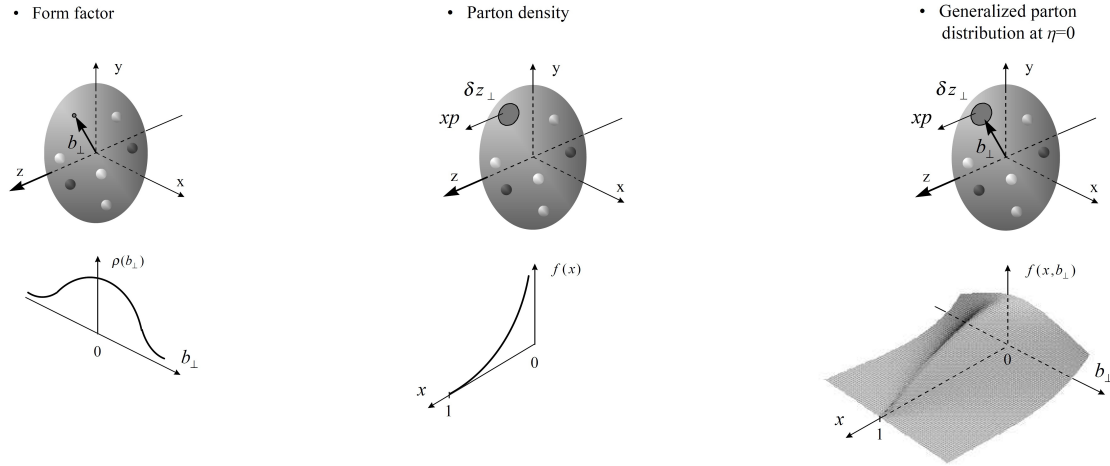


Figure 2.3: Probabilistic interpretation of form factors, GPDs and parton densities in the infinite momentum frame [14]

For transversely polarized targets also GPD E provides not a negligible contribution. Apart from parton helicity information, GPDs also provide information on helicity transitions of the hadron. The GPDs H , \tilde{H} are devoted to hadron helicity non-flip process, while E , \tilde{E} are referred to hadron helicity flip one. The GPDs depend on three variables: the average longitudinal momentum fraction \bar{x} of the parton in the initial and final states, a skewness parameter ξ representing the difference between these two momenta, and on the four-momentum transfer t to the nucleon. The average longitudinal momentum fraction \bar{x} is given by $\bar{k}^+ = \bar{x}\bar{P}^+$, where \bar{k}^+ and \bar{P}^+ are the longitudinal light-cone components¹ of \bar{k} and \bar{P} correspondingly. The average nucleon momentum is $\bar{P} = (P + P')/2$. The skewness parameter ξ is defined via $\Delta^+ = -2\xi P^+$, where Δ^+ is the longitudinal light-cone component of $\Delta^2 = t$. In a kinematic situation in which the invariant mass of the photon-nucleon system W and the photon virtuality are large, Bjorken's variable $x_{Bj} = \frac{Q^2}{W^2 + Q^2 - M^2}$ is therefore small [12]. Under such kinematic conditions the skewness parameter is given by

$$\xi \approx \frac{x_{Bj}}{2 - x_{Bj}}(1 + M_V^2/Q^2). \quad (2.20)$$

The GPDs can describe various exclusive processes of the shape $ep \rightarrow eNY$, with Y being a detected, e.g. observed state, in particular hard exclusive vector meson production. It was shown in [12], [13] that the amplitude of the process $\gamma^*p \rightarrow Vp$ can in the Bjorken limit (which in practice means large, but limit Q^2 value) be factorized in the framework of QCD into hard parton-level subprocesses and a non-perturbative proton matrix element representing the GPD. Factorization was proved for the longitudinal transition only, other transitions can be calculated

¹In the light cone coordinates the momentum p can be written as $P = (P^+, P^-, P^T)$, where $\bar{P}^+ = \frac{1}{\sqrt{2}}(\bar{P}^0 + \bar{P}^Z)$.

in a model-dependent way. The hard part was shown [12] to be represented for the vector meson production as an interaction of $q\bar{q}$ pair, originating from dissociation of the exchange photon, with a nucleon and is calculable in terms of pQCD or Regge phenomenology (Section 2.7). After the interaction $q\bar{q}$ pair forms the observed vector meson. The interaction with a nucleon can either be mediated via two-gluon (Figure 2.4, a)) or quark exchange (Figure 2.4, b)).

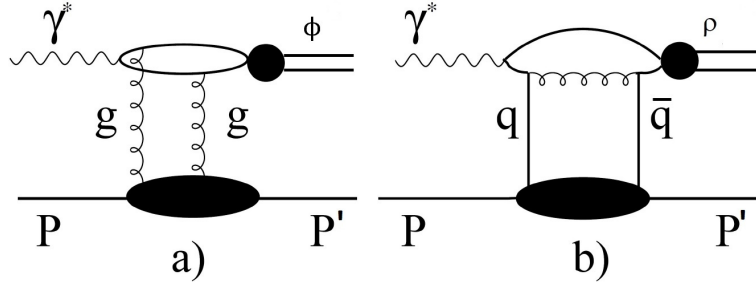


Figure 2.4: The mechanism of an exclusive ϕ meson production: a) two-gluon b) quark-antiquark exchanges.

The production of vector mesons at small $x_{Bj} < 10^{-2}$ is controlled by gluonic GPDs, while the quark GPDs play only a minor role. However, at intermediate energies, for ρ meson production both two-gluon exchange and quark-exchange are important. For ϕ even at intermediate beam energy gluon exchange is dominating, since the ϕ meson, aside from the valence $s\bar{s}$ pair, contains only a small admixture of quark-antiquark pairs with other flavours. The admixture of $s\bar{s}$ pair in the nucleon is also small at the x_{Bj} range studied at HERMES experiment. Exchanges with the u and d quarks demand additional gluon emission and are suppressed according to OZI rule that forbids energetically uneconomical exchanges. Therefore for ϕ meson the two- (or more) gluon exchange is dominating the quark one.

According to [17] the process $\gamma^*p \rightarrow Vp$ is dominated by transitions from longitudinally polarized photons to longitudinally polarized vector mesons ($\gamma_L^*p \rightarrow V_Lp$) at large Q^2 ; the amplitudes for other photon-meson transitions are suppressed at the leading twist by inverse powers of Q . Besides the longitudinal amplitude, dominating the process, mainly a transverse one ($\gamma_T^*p \rightarrow V_Tp$) is to be considered, since it is the most important one of the suppressed amplitudes at small $-t$.

The contribution from GPD H to the exclusive vector meson production amplitude reads ($i = g, q, x_g = 0, x_q = -1$) ([17])

$$\mathfrak{M}_{\mu_+, \mu_+}^{N_i}(V) = \frac{e}{2} \sum_a e_a C_V^a \int_{\bar{x}_i}^1 d\bar{x} \sum_\lambda \mathfrak{H}_{\mu\lambda, \mu\lambda}^{V_i}(\bar{x}, \xi, Q^2, t = 0) H^i(\bar{x}, \xi, t), \quad (2.21)$$

The sum runs over the quark flavours a , and e_a denote the quark charges in units of the positron charge e . C_V^a is a numerical flavour weight factor, μ and λ are helicities of γ and vector meson correspondingly, $\mathfrak{H}_{\mu\lambda, \mu\lambda}^{V_i}(\bar{x}, \xi, Q^2, t = 0)$ is the subprocess amplitude. Index i denotes quark or

and for gluon GPDs in the region of $\bar{x} > 0$:

$$H^g(\bar{x}, 0, 0) = \bar{x}g(\bar{x}), \quad \tilde{H}^g(\bar{x}, 0, 0) = \bar{x}\Delta g(\bar{x}) \quad (2.28)$$

The nucleon-helicity non-conserving GPDs E and \tilde{E} have a multiplicative factor Δ ($\Delta^2 = t$) and therefore vanish in the forward limit.

It was shown in [13] that the total angular momentum of quarks (gluons) $J^{q(g)}$ is related to the second \bar{x} moment of the GPDs $H^{q(g)}$, $E^{q(g)}$:

$$J^q = \frac{1}{2} \lim_{t \rightarrow 0} \int_{-1}^1 \bar{x} (H^q(\bar{x}, \xi, t) + E^q(\bar{x}, \xi, t)) d\bar{x}, \quad (2.29)$$

$$J^g = \frac{1}{2} \lim_{t \rightarrow 0} \int_0^1 (H^g(\bar{x}, \xi, t) + E^g(\bar{x}, \xi, t)) d\bar{x} \quad (2.30)$$

This relation is known as Ji's sum rule and gives nowadays the only known way to access experimentally the total angular momentum carried by quarks and gluons in the nucleon.

2.6 Vector meson dominance model

Vector meson dominance model (VMD) was developed in the 1960s by J. J. Sakurai in order to describe interactions between photons and hadrons. In QCD the photon is a massless, neutral gauge boson, which couples to charged particles and mediates the electromagnetic interaction. At first photon was introduced as a structureless particle, but later it was found out that photon can fluctuate into an electron-positron pair: $\gamma \rightarrow e^+e^-$, which was one of the first indications that photon can have a more complicated internal structure. Photon interactions show some similarities to hadron interactions, such as same shapes of the momentum transfer t distributions, resembling behavior of the total cross sections, nearly identical photon and hadron cross sections on neutrons and protons. This can be explained by the fact that the photon is a superposition of a bare photon, responsible for electromagnetic interactions, and hadronic component, which takes part in hadronic interactions

$$|\gamma\rangle = \sqrt{Z_3}|\gamma_B\rangle + \sqrt{\alpha}|\gamma_h\rangle, \quad (2.31)$$

where Z_3 is the normalization factor of $|\gamma_B\rangle$, $\alpha = 1/137$ [6]. At high energies bare photon $|\gamma_B\rangle$ is several orders of magnitude smaller than hadronic part and therefore can be neglected. Conservation laws dictate that $|\gamma_h\rangle$ has the same quantum numbers as the photon, i.e. $J^{PC} = 1^{--}$, $Q = B = S = 0$. Moreover the relatively large cross section for production of the light spin-1 vector mesons ρ^0 , ω , and ϕ from photon-hadron interactions suggests that they provide the dominant contribution to the hadronic photon component γ_h . VMD is based on the assumption

that these three vector mesons are the only hadronic constituents of the photon.

In the approach given above the internal photon structure is worked out independently from the target, and then the various components are permitted to interact with the target. For this picture to be valid, the virtual hadrons must be presented for a time long enough for the interaction to occur with an ordinary "real" hadron. The physical photon is always making transitions back and forth between a bare photon and hadronic states. For these interactions to satisfy the separability conditions it is necessary that the fluctuations lasts a typical time, called the formation time, which is relatively long compared to the interaction time with the target. The fluctuation or formation time of a photon into a $q\bar{q}$ or virtual vector meson state in the laboratory system is given by [6]

$$t_f \approx \frac{2\nu}{Q^2 + M_v^2}, \quad (2.32)$$

where M_v is a virtual vector meson mass. For fixed Q^2 and M_v , t_f is directly proportional to the photon's energy. The formation time is to be long enough for the virtual meson to travel over a distance much larger than the nucleon radius of about 1 fm, because photon-to-virtual-meson fluctuations occurs long before the last one hits the target. According to [6], the hadron-related part of the equation 2.31 can be defined as

$$\sqrt{\alpha}|\gamma_h\rangle = \sum_V \frac{e}{f_V} \frac{M_V^2}{M_V^2 + Q^2} |V\rangle, \quad (2.33)$$

where $|V\rangle$ is a vector meson state, $\frac{e}{f_V}$ is a normalization constant, M_V is a vector meson mass. The factor $e = \sqrt{4\pi\alpha_{em}}$, f_V is $\gamma \leftrightarrow V$ coupling constant. Equation 2.33 gives the Q^2 dependence of the vector meson production cross section as a propagator of single vector meson states. Then an expression for the transverse and longitudinal cross section in ep inelastic scattering in terms of VMD can be written:

$$\sigma_T^{\gamma^*p}(Q^2, W) = \sum_V \frac{e^2}{f_V^2} \left(\frac{M_V^2}{M_V^2 + Q^2} \right)^2 \sigma_T^{Vp}(W), \quad (2.34)$$

$$\sigma_L^{\gamma^*p}(Q^2, W) = \sum_V \frac{e^2}{f_V^2} \left(\frac{M_V^2}{M_V^2 + Q^2} \right)^2 \xi_V^2 \frac{Q^2}{M_V^2} \sigma_T^{Vp}(W), \quad (2.35)$$

where σ_T^{Vp} is the total Vp cross section for the transversely polarized vector meson, the parameter ξ is defined by

$$\xi_V^2 = \sigma_L^{Vp} / \sigma_T^{Vp}. \quad (2.36)$$

VMD model predicts the factor ξ_V^2 to be of the order of unity, but the experimental results on

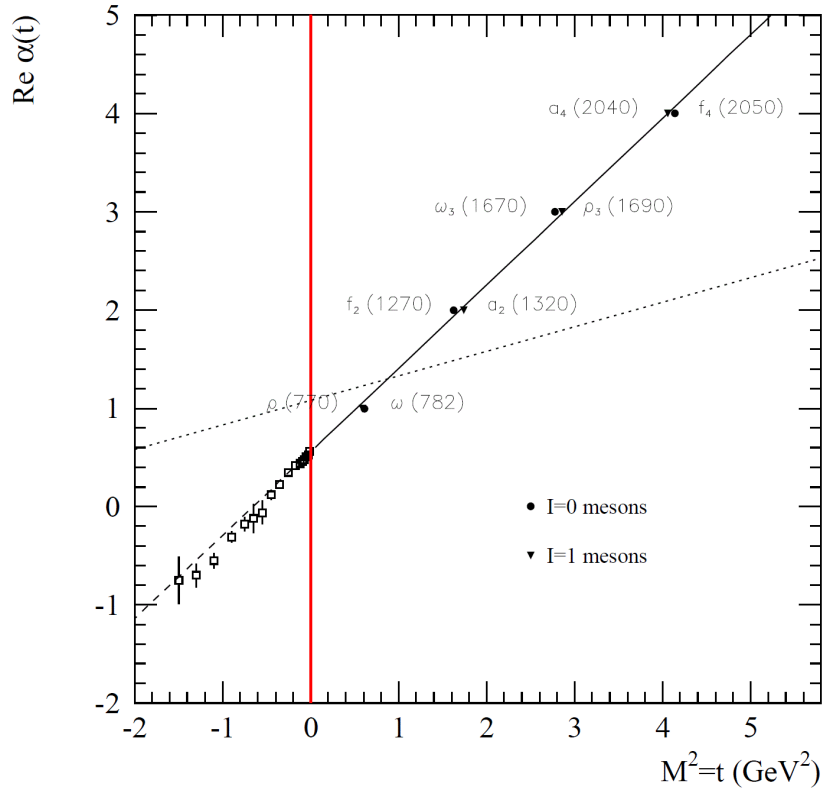


Figure 2.5: Chew-Frautschi plot for Regge trajectories [11]. The full line shows a fit of mesons with Equation 2.38. The dashed line is an approximation of the fit for $t < 0$. The dotted line is a Pomeron trajectory.

ρ^0 indicate lower value ([9],[10]). The longitudinal-to-transverse cross section ratio reads

$$R = \frac{\sigma_L^{\gamma^*p}(Q^2, W)}{\sigma_T^{\gamma^*p}(Q^2, Wu)} = \xi_V^2 \frac{Q^2}{M_V^2} \quad (2.37)$$

The ratio is predicted ([7]) to vary as q^2 at fixed ν/q^2 (as long as ξ is slowly varying).

2.7 Regge theory

As described above, the virtual photon, emitted by the beam lepton, can in terms of VMD be represented as a vector meson. The further interaction of a target nucleon with a vector meson can be explained by Regge theory, which describes hadron-hadron interaction. The basic idea of Regge is that the angular momenta can be represented as a complex value and the scattering amplitude can be extrapolated on the complex angular momentum plane. For a given spin l at an energy t the singularities of a scattering amplitude appear as poles, called Regge poles. The poles can be either bound states or resonances and are located at values defined by a relation $l = \text{Re}(\alpha(t))$ is called Regge trajectory. In Figure 2.5 the angular momentum is plotted versus the particle mass squared $t = M^2$. In such a coordinate system Regge trajectories become

straight lines with slope α' and intercept $\alpha(0)$:

$$\alpha(t) = \alpha(0) + \alpha'(t) \quad (2.38)$$

The experimental results of diffractive scattering processes with negative momentum transfer t align along straight lines for all the known trajectories. The scattering reactions are mediated by exchange of resonances in the t -channel whose interpolation is given by a Regge trajectory.

The scattering amplitude is given by the equation

$$A(s, t) \propto s^{\alpha(t)} \quad (2.39)$$

The total cross-section is connected with the imaginary part of the scattering amplitude as

$$\sigma_{tot} = \frac{1}{s} \text{Im}(A_{t=0}) \quad (2.40)$$

Equations 2.39 and 2.40 give the energy dependence of the cross-section

$$\sigma_{tot} = s^{\alpha(t=0)-1} \quad (2.41)$$

This means that the intercept of the trajectory determines the cross section dependence on the energy s . All trajectories associated with mesonic resonances have intercepts around 0.5. The cross section is than to behave as $\sigma_{tot}s^{-1/2}$. This is true up to a few GeV center of mass energy, after that the cross section dependence has a plato. Such a behavior can be explained in terms of Regge theory via introduction of a trajectory with an interception at 1 and quantum numbers of the vacuum. Such a trajectory was called Pomeron trajectory.

2.8 The vector meson spin density matrix in Wolf-Schilling notation

The differential cross section for vector meson production reads:

$$\frac{d\sigma_{ep \rightarrow epV}}{dE' d\Omega d\Phi dt} = \frac{1}{(2\pi)^5} \frac{E'}{E} \frac{M^2}{4\sqrt{(\nu^2 + Q^2)}} \frac{1}{4} \sum_{spins} |M|^2, \quad (2.42)$$

where E , E' are energies of initial and final lepton, $d\Omega$ is the volume element of the scattered lepton, Φ is the angle between the normals to the lepton scattering plane and the hadron production plane (see Figure 2.6) and M is the matrix element describing the scattering process. It was shown in [19] that $\frac{1}{4} \sum_{spins} |M|^2 = \frac{1}{4} \sum_{spins} L_{\mu\nu} T^{\mu\nu}$, so that the cross section form is

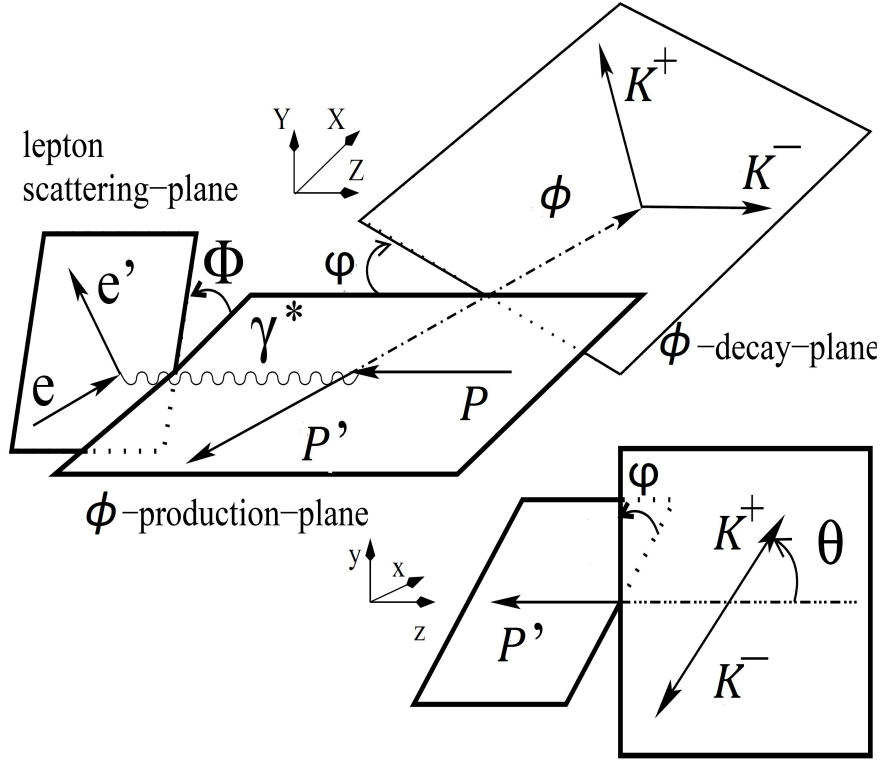


Figure 2.6: Definition of production and decay angles for vector meson production.

similar to that of DIS (see 2.8). The leptonic tensor $L_{\mu\nu}$ is given by

$$L_{\mu\nu} = \sum_{spins} m^2 \langle e' | j_\mu | e \rangle \cdot \langle e' | j_\nu | e \rangle, \quad (2.43)$$

where j is electromagnetic current operator, e and e' are the spinors of the initial and final leptons. Therefore, the leptonic tensor, describing the emission of the virtual photon, represents photon spin density matrix $L_{\mu\nu} \propto \varrho(\gamma)_{\lambda\lambda'}$. The latter can be decomposed into an orthogonal set of nine independent hermitian matrices Σ^α :

$$\varrho(\gamma) = \frac{1}{2} \sum_{\alpha=0}^8 \tilde{\Pi}_\alpha \Sigma^\alpha, \quad (2.44)$$

where $\tilde{\Pi}_\alpha$ is a known normalization vector. The four matrices $\varrho(\gamma)$ for $\alpha = 0, 1, 2, 3$ describe vector meson production by transverse virtual photons: unpolarized, linearly polarized in two orthogonal directions, and circularly polarized vector meson, respectively. Vector meson production by longitudinal virtual photons corresponds to $\alpha = 4$ and $\alpha = 5, 6, 7, 8$ provide transverse-longitudinal interference terms. Unlike DIS, the hadronic tensor for vector meson leptonproduction can not be parametrized by structure functions. Instead, the vector meson

production is described in terms of a vector meson spin density matrix:

$$\frac{d\sigma_{\gamma p \rightarrow V p}}{dt d\Phi} = \frac{1}{32\pi^2 \sqrt{(\nu^2 + Q^2)}} \text{Tr}(F\rho(\gamma)F^+). \quad (2.45)$$

The vector meson density matrix is then given by

$$\rho(V) = \frac{1}{2} T \rho(\gamma) T^+ \left/ \int \frac{d\Phi}{2\pi} \text{Tr} \left(\frac{1}{2} F \rho(\gamma) F^+ \right) \right., \quad (2.46)$$

where an averaging over Φ and a summation over nucleon helicities is being done and T is a production amplitude. The same as the photon one, the vector meson spin density matrix can be decomposed into a set of hermitian matrices:

$$\rho(V) = \sum_{\alpha=0}^8 \prod_{\alpha} \rho^{\alpha}, \quad (2.47)$$

where \prod_{α} is a known normalization vector, and the matrix element of the matrix $\rho(V)$ can be written as

$$\rho_{\lambda_V \lambda_V'}^{\alpha} = \frac{1}{2N_{\alpha}} \sum_{\lambda_{N'}, \lambda_N, \lambda_{\gamma}, \lambda_{\gamma'}} F_{\lambda_V, \lambda_{N'}, \lambda_{\gamma}, \lambda_N} \Sigma_{\lambda_{\gamma} \lambda_{\gamma'}}^{\alpha} F_{\lambda_V', \lambda_{N'}, \lambda_{\gamma}', \lambda_N}^*. \quad (2.48)$$

Here N_{α} are normalization constants and $F_{\lambda_V, \lambda_{N'}, \lambda_{\gamma}, \lambda_N}$ are helicity amplitudes

$$F_{\lambda_V, \lambda_{N'}, \lambda_{\gamma}, \lambda_N} = \langle \lambda_V \lambda_{N'} | j_{\lambda_{\gamma}} | \lambda_N \rangle, \quad (2.49)$$

defined in the center-of-mass system of virtual photon and target nucleon and describing a transition from the initial nucleon state $|\lambda_N\rangle$ to the final ϕ meson and scattered nucleon state $\langle \lambda_V \lambda_{N'} |$. The spin states of the virtual photon, ϕ meson, initial (outcoming) nucleon are denoted by λ_{γ} , λ_V , $\lambda_{N(N')}$ correspondingly.

2.9 Definition of the scattering angles in vector meson production

Both the two vector mesons, presented in this thesis, namely ρ and ϕ , decay after the formation into two oppositely charged particles: kaons in case of ϕ meson ($\phi \rightarrow K^+ K^-$), pions in case of ρ meson ($\rho \rightarrow \pi^+ \pi^-$). In Figure 2.6 angles are denoted, that are used for the description of vector meson production. In the center-of-mass system of virtual photon and target nucleon Z-axis is directed along the virtual-photon three-momentum, and the Y-axis is parallel to the

vector product of virtual-photon and vector meson three-vectors:

$$Z = \frac{\mathbf{q}}{|\mathbf{q}|}, \quad Y = \frac{\mathbf{q} \times \mathbf{v}}{|\mathbf{q} \times \mathbf{v}|}, \quad X = Y \times Z \quad (2.50)$$

In the ‘‘hadronic’’ center of mass system of virtual photon and target nucleon the angle between the vector meson production plane and the lepton-scattering plane is specified by

$$\cos \Phi = \frac{(\mathbf{q} \times \mathbf{v}) \cdot (\mathbf{k} \times \mathbf{k}')}{|\mathbf{q} \times \mathbf{v}| \cdot |\mathbf{k} \times \mathbf{k}'|}, \quad \sin \Phi = \frac{[(\mathbf{q} \times \mathbf{v}) \times (\mathbf{k} \times \mathbf{k}')] \cdot \mathbf{q}}{|\mathbf{q} \times \mathbf{v}| \cdot |\mathbf{k} \times \mathbf{k}'| \cdot |\mathbf{q}|}. \quad (2.51)$$

The polar and azimuthal angles φ and Θ of the positively charged decay particle are defined in the vector meson rest frame where the z -axis is aligned opposite to the outgoing nucleon momentum \mathbf{P}' and the y -axis parallel to Y and directed along $\mathbf{P}' \times \mathbf{q}$:

$$z = \frac{-\mathbf{P}'}{|\mathbf{P}'|}, \quad y = Y, \quad x = y \times z. \quad (2.52)$$

The angle φ between vector meson production plane and ϕ meson decay plane is defined by

$$\cos \varphi = \frac{(\mathbf{q} \times \mathbf{v}) \cdot (\mathbf{v} \times \mathbf{p}_{\mathbf{K}^+})}{|\mathbf{q} \times \mathbf{v}| \cdot |\mathbf{v} \times \mathbf{p}_{\mathbf{K}^+}|}, \quad \sin \varphi = \frac{[(\mathbf{q} \times \mathbf{v}) \times \mathbf{v}] \cdot (\mathbf{p}_{\mathbf{K}^+} \times \mathbf{v})}{|(\mathbf{q} \times \mathbf{v}) \times \mathbf{v}| |\mathbf{p}_{\mathbf{K}^+} \times \mathbf{v}|}, \quad (2.53)$$

where $\mathbf{p}_{\mathbf{K}^+}$ is the three-momentum of the positive decay particle, kaon in case of ϕ meson, pion in case of ρ meson.

The angle Θ is given by

$$\cos \Theta = \frac{-\mathbf{P}' \times \mathbf{p}_{\mathbf{K}^+}}{|\mathbf{P}'| \cdot |\mathbf{p}_{\mathbf{K}^+}|}. \quad (2.54)$$

The angle definition given above are according to [20] and are used in the Wolf-Schilling formalism. The relations of these definitions to ‘‘Trento convention’’ [22] and Ref. [21] read:

$$\Phi = -\phi_{h,Trento}, \quad \phi = \varphi_{[21]}, \quad \Theta = \theta_{[21]} \quad (2.55)$$

2.10 The decay angular distribution of vector meson production in Wolf-Schilling formalism

Taking into account Expressions 2.45 and 2.48 the differential cross section in terms of helicity amplitudes can be written as ([19])

$$\frac{d\sigma_{full}(\mathcal{W}, Q^2)}{d\Omega d\Phi dt} = \frac{1}{(64\pi^2)} \sum_{\lambda_\gamma \lambda'_\gamma \lambda_V \lambda'_V \lambda_N \lambda'_N} F_{\lambda_V \lambda'_N; \lambda_\gamma \lambda_N} \times \varrho_{\lambda_\gamma \lambda'_\gamma}(\epsilon, \Phi) F_{\lambda_V \lambda'_N; \lambda_\gamma \lambda_N}^* Y_{1\lambda_V}(\varphi, \cos \Theta) \times Y_{1\lambda_V}(\varphi, \cos \Theta)^*, \quad (2.56)$$

where $\varrho_{\lambda_\gamma \lambda'_\gamma}$ is the virtual photon spin density matrix, the helicity amplitudes $F_{\lambda_V \lambda'_N; \lambda_\gamma \lambda_N}$ are describing the transition of the virtual photon with helicity λ_γ to the vector meson with helicity λ_V , and $Y_{1\lambda_V}(\varphi, \cos \Theta) \times Y_{1\lambda_V}(\varphi, \cos \Theta)$ - the angular distribution of the vector meson decay products. The total cross section can be obtained after integration over the angles $\Phi, \varphi, \cos \Theta$:

$$\frac{d\sigma_{full}}{dt} = \frac{d\sigma_T}{dt} + \epsilon \frac{d\sigma_L}{dt}, \quad (2.57)$$

and can be accessed experimentally via the measured quantity, as will be shown below. The decay angular distribution \mathcal{W} of the vector meson decay products can be decomposed for different beam and target polarization cases

$$\mathcal{W} = \mathcal{W}_{UU} + P_L \mathcal{W}_{LU} \quad (2.58)$$

where L denotes longitudinal polarization of the beam, U means unpolarized beam or target. The unpolarized-beam part of the angular distribution is a function of matrix elements with $\alpha = 0, 1, 2, 4, 5, 6$. The polarized-beam part of the angular distribution contains matrix elements with $\alpha = 3, 7, 8$ for longitudinal beam polarization. Measurements with a transversely polarized beam gives elements with $\alpha = 7, 8$ and therefore provide no new information compared to the case of longitudinal beam polarization. In case of longitudinally polarized beam and an unpolarized target the total number of independent matrix elements in the equation above is 26. At a fixed beam energy no separation between σ_L and σ_T is possible; the number of independent unpolarized matrix elements is reduced from 18 to 15 because the elements with $\alpha = 4$ and $\alpha = 0$ can not be disentangled and are combined by the following relation, which merely can be measured:

$$r_{\lambda\lambda'}^{04} = \frac{\rho_{\lambda\lambda'}^0 + \epsilon R \rho_{\lambda\lambda'}^4}{1 + \epsilon R}. \quad (2.59)$$

The measurable matrix elements for the other α values can also be expressed in terms of $\rho_{\lambda\lambda'}^\alpha$:

$$r_{\lambda\lambda'}^\alpha = \begin{cases} \frac{\rho_{\lambda\lambda'}^\alpha}{1+\epsilon R} & \alpha = 1, 2, 3 \\ \frac{\rho_{\lambda\lambda'}^\alpha \sqrt{R}}{1+\epsilon R} & \alpha = 5, 6, 7, 8. \end{cases} \quad (2.60)$$

The decay angular distribution of the vector meson can now be expressed via the angles described above ($\Phi, \varphi, \cos\Theta$) and quantities $r_{\lambda\lambda'}^\alpha$, called spin density matrix elements (SDMEs). The beam-polarization independent part is given by the equation:

$$\begin{aligned} \mathcal{W}^{UU}(\Phi, \varphi, \cos\theta) = & \frac{3}{4\pi} \left[\frac{1}{2}(1 - r_{00}^{04}) + \frac{1}{2}(3r_{00}^{04} - 1) \cos^2 \theta - \sqrt{2} \Re \{r_{10}^{04}\} \sin 2\theta \cos \varphi \right. \\ & - r_{1-1}^{04} \sin^2 \theta \cos 2\varphi - \epsilon \cos 2\Phi \left(r_{11}^1 \sin^2 \theta + r_{00}^1 \cos^2 \theta \right. \\ & \left. \left. - \sqrt{2} \Re \{r_{10}^1\} \sin 2\theta \cos \varphi - r_{1-1}^1 \sin^2 \theta \cos 2\varphi \right) \right. \\ & \left. - \epsilon \sin 2\Phi \left(\sqrt{2} \Im \{r_{10}^2\} \sin 2\theta \sin \varphi + \Im \{r_{1-1}^2\} \sin^2 \theta \sin 2\varphi \right) \right. \\ & + \sqrt{2\epsilon(1+\epsilon)} \cos \Phi \left(r_{11}^5 \sin^2 \theta + r_{00}^5 \cos^2 \theta - \sqrt{2} \Re \{r_{10}^5\} \sin 2\theta \cos \varphi \right. \\ & \left. - r_{1-1}^5 \sin^2 \theta \cos 2\varphi \right) + \sqrt{2\epsilon(1+\epsilon)} \sin \Phi \left(\sqrt{2} \Im \{r_{10}^6\} \sin 2\theta \sin \varphi \right. \\ & \left. \left. + \Im \{r_{1-1}^6\} \sin^2 \theta \sin 2\varphi \right) \right]. \quad (2.61) \end{aligned}$$

It is parametrized by 15 independent unpolarized SDMEs. The part involving longitudinally polarized beam contains 8 polarized SDMEs:

$$\begin{aligned} \mathcal{W}^{LL}(\Phi, \varphi, \cos\theta) = & \frac{3}{4\pi} P \left[\sqrt{1-\epsilon^2} \left(\sqrt{2} \Im \{r_{10}^3\} \sin 2\theta \sin \varphi + \Im \{r_{1-1}^3\} \sin^2 \theta \sin 2\varphi \right) \right. \\ & + \sqrt{2\epsilon(1-\epsilon)} \cos \Phi \left(\sqrt{2} \Im \{r_{10}^7\} \sin 2\theta \sin \varphi + \Im \{r_{1-1}^7\} \sin^2 \theta \sin 2\varphi \right) \\ & + \sqrt{2\epsilon(1-\epsilon)} \sin \Phi \left(r_{11}^8 \sin^2 \theta + r_{00}^8 \cos^2 \theta - \sqrt{2} \Re \{r_{10}^8\} \sin 2\theta \cos \varphi \right. \\ & \left. \left. - r_{1-1}^8 \sin^2 \theta \cos 2\varphi \right) \right]. \quad (2.62) \end{aligned}$$

These 15+8 quantities for vector meson production at HERMES are presented in this thesis.

The angular distribution is normalized (according to [21])

$$\int \frac{d\Phi}{2\pi} \int d\cos\theta d\varphi W(\theta, \varphi, \Phi) = 1. \quad (2.63)$$

2.11 The spin density matrix elements of the vector meson production in Markus-Diehl formalism

Helicity amplitudes $T_{\mu\lambda}^{\nu\sigma}$ for the process $\gamma^*(\mu) + p(\lambda) \rightarrow VM(\nu) + p(\sigma)$ were introduced by Markus Diehl with definite helicities $\mu, \lambda, \nu, \sigma$. The helicity amplitudes depend on Q^2, x_B, t . In terms of the amplitudes the spin density matrix can be written as

$$\rho_{\mu\mu',\lambda\lambda'}^{\nu\nu'} = (N_T + \epsilon N_L)^{-1} \sum_{\sigma} T_{\mu\lambda}^{\nu\sigma} (T_{\mu'\lambda'}^{\nu'\sigma})^*, \quad (2.64)$$

where N_T and N_L are the normalization factors and are proportional to the differential transverse and longitudinal cross sections correspondingly. The SDMEs for unpolarized target are denoted as $u_{\mu\mu'}^{\nu\nu'}$ and obtained as

$$u_{\mu\mu'}^{\nu\nu'} = \frac{1}{2} (\rho_{\mu\mu',++}^{\nu\nu'} + \rho_{\mu\mu',--}^{\nu\nu'}), \quad (2.65)$$

where the target polarization is designated as just + or - instead of +1/2, -1/2. Therefore from comparison of Equation 2.48 to 2.65 one can see that the lower indices of the matrix element ρ in Wolf-Schilling notation correspond to the upper indices of the matrix element u in Markus-Diehl notation.

2.12 The decay angular distribution of the vector meson production in Markus-Diehl formalism

For the beam polarization X and the target polarization Y the angular distribution can be written using the angles definition from Trento convention [22] and Ref. [21] as

$$\mathcal{W}_{XY}(\phi_h, \varphi, \theta) = \frac{3}{4\pi} \left[\cos^2\theta \mathcal{W}_{XY}^{LL}(\phi_h) + \sqrt{2} \cos\theta \sin\theta \mathcal{W}_{XY}^{LT}(\phi_h, \varphi) + \sin^2\theta \mathcal{W}_{XY}^{TT}(\phi_h, \varphi) \right]. \quad (2.66)$$

The upper indices denote longitudinal LL , transverse TT vector meson production and their interference LT . For the unpolarized target and beam the angular distribution is parametrized

by unpolarized SDMEs $u_{\nu\nu'}^{\mu\mu'}$:

$$\mathcal{W}_{UU}^{LL}(\phi_h) = (u_{++}^{00} + \epsilon u_{00}^{00}) - 2 \cos \phi_h \sqrt{\epsilon(1+\epsilon)} \Re \{u_{0+}^{00}\} - \cos(2\phi_h) \epsilon u_{-+}^{00}, \quad (2.67)$$

$$\begin{aligned} \mathcal{W}_{UU}^{LT}(\phi_h, \varphi) &= \cos(\phi_h + \varphi) \sqrt{\epsilon(1+\epsilon)} \Re \{u_{0+}^{0+} - u_{0+}^{-0}\} - \cos \varphi \Re \{u_{++}^{0+} - u_{++}^{-0} + 2\epsilon u_{00}^{0+}\} \\ &\quad + \cos(2\phi_h + \varphi) \epsilon \Re \{u_{-+}^{0+}\} - \cos(\phi_h - \varphi) \sqrt{\epsilon(1+\epsilon)} \Re \{u_{0+}^{0-} - u_{0+}^{+0}\} \\ &\quad + \cos(2\phi_h - \varphi) \epsilon \Re \{u_{-+}^{+0}\}, \end{aligned} \quad (2.68)$$

$$\begin{aligned} \mathcal{W}_{UU}^{TT}(\phi_h, \varphi) &= \frac{1}{2}(u_{++}^{++} + u_{++}^{--} + 2\epsilon u_{00}^{++}) + \frac{1}{2} \cos(2\phi_h + 2\varphi) - \cos(\phi_h) \sqrt{\epsilon(1+\epsilon)} \Re \{u_{0+}^{++} + u_{0+}^{--}\} \\ &\quad + \cos(\phi_h + 2\varphi) \sqrt{\epsilon(1+\epsilon)} \Re \{u_{0+}^{-+}\} - \cos(2\phi_h) \Re \{u_{0+}^{-+} + \epsilon u_{00}^{-+}\} \\ &\quad - \cos(2\phi_h) \epsilon \Re \{u_{-+}^{++}\} + \cos(\phi_h - 2\varphi) \sqrt{\epsilon(1+\epsilon)} \Re \{u_{0+}^{+-}\} + \frac{1}{2} \cos(2\phi_h - 2\varphi) \epsilon u_{-+}^{+-}. \end{aligned} \quad (2.69)$$

The terms independent of φ and ϕ_h in W_{UU}^{TT} and W_{UU}^{LL} are related as

$$u_{++}^{++} + u_{++}^{--} + 2\epsilon u_{00}^{++} = 1 - (u_{++}^{00} + \epsilon u_{00}^{00}). \quad (2.70)$$

The angular distribution for unpolarized target and polarized beam is given by the equation:

$$\mathcal{W}_{LL}^{LU}(\phi_h) = -2 \sin \phi_h \sqrt{\epsilon(1+\epsilon)} \Im \{u_{0++}^{00}\}, \quad (2.71)$$

$$\begin{aligned} \mathcal{W}_{LT}^{LU}(\phi_h, \varphi) &= \sin(\phi_h + \varphi) \sqrt{\epsilon(1-\epsilon)} \Im \{u_{++}^{0+} - u_{0+}^{-0}\} - \sin \varphi \sqrt{1-\epsilon^2} \Im \{u_{++}^{0+} - u_{++}^{-0}\} \\ &\quad - \sin(\phi_h - \varphi) \sqrt{\epsilon(1-\epsilon)} \Im \{u_{0+}^{0-} - u_{0+}^{+0}\}, \end{aligned} \quad (2.72)$$

$$\begin{aligned} \mathcal{W}_{TT}^{LU}(\phi_h, \varphi) &= -\sin \phi_h \sqrt{\epsilon(1-\epsilon)} \Im \{u_{0+}^{++} - u_{0+}^{--}\} + \sin(\phi_h + 2\varphi) \sqrt{1-\epsilon^2} \Im \{u_{0+}^{-+}\} \\ &\quad - \sin(2\varphi) \sqrt{1-\epsilon^2} \Im \{u_{++}^{-+}\} + \sin(\phi_h - 2\varphi) \sqrt{\epsilon(1-\epsilon)} \Im \{u_{0+}^{+-}\}. \end{aligned} \quad (2.73)$$

2.13 s-channel helicity conservation

From the measurement of SDMEs, s channel helicity conservation (SCHC) hypothesis can be tested. SCHC implies that the vector meson produced conserves the helicity of the virtual photon, e.g., $\lambda_\gamma = \lambda_V$ in the process $\gamma_{\lambda_\gamma}^* \rightarrow \phi_{\lambda_V}$. In terms of Wolf-Schilling helicity amplitudes it means that

$$F_{\lambda_V \lambda_{N'} \lambda_\gamma \lambda_N} = F_{\lambda_V \lambda_{N'} \lambda_\gamma \lambda_N} \delta_{\lambda_V \lambda_{N'} \lambda_\gamma \lambda_N} \quad (2.74)$$

Then all the helicity-flip transitions ($\lambda_\gamma \neq \lambda_V$) vanish and the corresponding amplitudes become zero:

$$F_{01} = F_{10} = F_{0-1} = F_{-10} = F_{1-1} = F_{-11} = 0 \quad (2.75)$$

Only three amplitudes remain non-zero – F_{00} , F_{11} , F_{-1-1} . Using relations between the amplitudes and SDMEs (see [19]), the non-vanishing SDMEs can be obtained: r_{00}^{04} , r_{1-1}^1 , $\Im m r_{1-1}^2$, $\Re e r_{10}^5$, $\Im m r_{10}^6$, $\Im m r_{10}^7$, $\Re e r_{10}^8$. If SCHC holds, also the following relations are to be fulfilled: $r_{1-1}^1 = -\Im m r_{1-1}^2$, $\Re e r_{10}^5 = \Im m r_{10}^6$, $\Re e r_{10}^8 = \Im m r_{10}^7$.

From the non-vanishing SDMEs the phase difference δ (see Equation 2.74) between F_{00} and F_{11} amplitudes is among the quantities, which can be accessed experimentally and then compared with theory (GPDs) calculations. The decay angular distribution in case of SCHC can be written as a function of $\cos \Theta$ and the angle $\Psi = \varphi - \Phi$ between the vector meson decay plane and the lepton scattering plane

$$W(\cos \Theta, \Psi) = \frac{3}{4\pi} \left[\frac{1}{2}(1 - r_{00}^{04}) + \frac{1}{2}(3r_{00}^{04} - 1) \cos^2 \Theta + \epsilon r_{1-1}^1 \sin^2 \Theta \cos 2\Psi \right. \\ \left. - 2\sqrt{\epsilon(1 + \epsilon)} \Re e r_{10}^5 \sin 2\Theta \cos \Psi + 2P\sqrt{\epsilon(1 + \epsilon)} \sin 2\Theta \sin \Psi \Im m r_{10}^7 \right] \quad (2.76)$$

The presently existing data show s -channel helicity violation for ρ : ZEUS in [23], H1 in [25], where the SDME r_{00}^5 was pronouncedly non-zero. The SDME is proportional to $\Re e F_{01} F_{00}^*$, which contains the largest amplitude at high energy F_{00} and the largest spin-flip amplitude F_{01} , therefore this matrix element provides the cleanest SCHC-violating (SCHCV) signal. At HERMES level of energy both amplitudes are comparable. This explains why HERMES measured stronger SCHCV signal [26] than ZEUS [23] and H1 [25]. No SCHCV was found for ϕ at ZEUS [27], H1 [28] and CLAS [29].

2.14 Natural and unnatural parity exchange

As was described in Section 2.7, the diffractive production of vector mesons can be represented as an exchange of a particle via t -channel. The exchanged particle can have either natural parity $P = (-1)^J$ or unnatural parity $P = -(-1)^J$. In the first case the reaction is called natural parity exchange (NPE), in the second - unnatural (NPE). A Wolf-Schilling helicity amplitude can be decomposed into NPE (N) and UPE (U) amplitudes:

$$F_{\alpha_V, \alpha_{N'}, \alpha_\gamma, \alpha_N} = N_{\alpha_V, \alpha_{N'}, \alpha_\gamma, \alpha_N} + U_{\alpha_V, \alpha_{N'}, \alpha_\gamma, \alpha_N}. \quad (2.77)$$

A measurement of the corresponding SDMEs, related to NPE and UPE amplitudes, allows to separate both contributions and to determine the natural and unnatural parity exchange

fractions of the transverse and longitudinal cross section. If NPE dominates, the quantities defined as:

$$U_1 = 1 - r_{00}^{04} + 2r_{1-1}^{04} - 2r_{1-1}^1 - 2r_{11}^1, \quad (2.78)$$

$$U_2 = r_{1-1}^5 + r_{11}^5, \quad (2.79)$$

$$U_3 = r_{1-1}^8 + r_{11}^8 \quad (2.80)$$

are equal to zero or small. The amplitude hierarchy can be both built experimentally and calculated theoretically. The SDMEs-to-amplitudes connection is presented in Appendix B.

For NPE amplitudes diagonal transitions in nucleon spin are dominant ($\lambda'_N = \lambda_N$), while for unnatural ones it is not proven. NPE prevails over UPE, since the latter is suppressed by a factor of $\propto (M/W)^2$, while a natural one by a factor of $\propto (M/W)$. If both SCHC and NPE are assumed, the decay angular distribution depends only on the longitudinal-to-transverse cross section ratio R and the phase difference δ between the only two non-zero amplitudes N_{00} and N_{11} :

$$W(\cos \Theta, \Psi) = \frac{1}{1 + \epsilon R} \frac{3}{8\pi} \left[\sin^2 \Theta (1 + \epsilon \cos 2\Psi) + 2\epsilon R \cos^2 \Theta - \sqrt{2\epsilon(1 + \epsilon)R} \cos \delta \sin 2\Theta \cos \Psi + \sqrt{2\epsilon(1 - \epsilon)R} P_l \sin \delta \sin 2\Theta \sin \Psi \right]. \quad (2.81)$$

In terms of Markus Diehl notation, SDME can be represented via NPE $N_{\mu\lambda}^{\nu\sigma}$ and UPE $U_{\mu\lambda}^{\nu\sigma}$ amplitudes:

$$u_{\mu\mu'}^{\nu\nu'} = (N_T + \epsilon N_L)^{-1} \sum_{\sigma} \left[N_{\mu+}^{\nu\sigma} (N_{\mu'+}^{\nu'\sigma})^* + U_{\mu+}^{\nu\sigma} (U_{\mu'+}^{\nu'\sigma})^* \right] \quad (2.82)$$

The matrix elements u involve a product of two NPE amplitudes plus a product of two UPE amplitudes.

For ρ meson statistically significant UPE contribution was observed in HERMES ([26]) and other experiments (H1 [25], ZEUS [23]), while for ϕ meson the contribution is negligible (H1 [28], ZEUS [27]).

2.15 Radiative corrections

Figure 2.1 describes DIS on the Born level, not including next to leading order contributions. However, emission of a real photon by the lepton changes the reaction kinematics significantly.

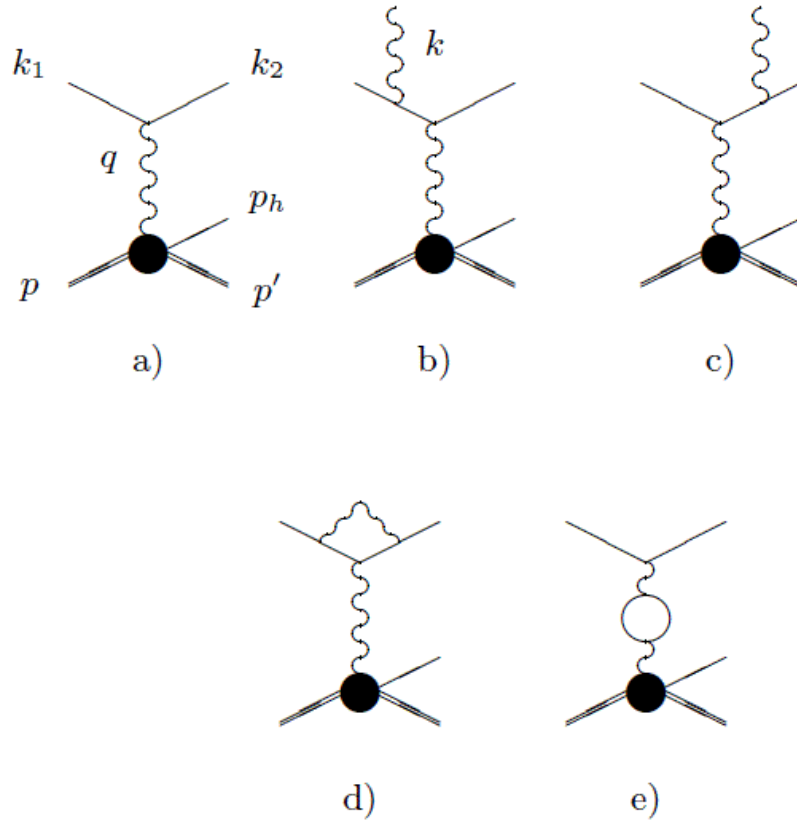


Figure 2.7: Feynman diagrams of processes contributing to the Born and the next order cross sections.

In Figure 2.7 Feynman diagrams for leptonic radiation are presented. The corresponding contributions to the vector meson production cross section are taken into account via radiative corrections and in the diffractive region ($-t < 0.3$) can reach 20% ([30]). For the majority of the matrix elements which are to be 0 if SCHC holds, relative radiative corrections estimated as $\delta r = \frac{r_{obs} - r_{Born}}{r_{obs}}$ do not exceed 1%, according to [31]. However, for two of them, namely $\Re r_{10}^{04}$ and r_{00}^5 , the correction may reach 20% ([31]). Therefore, non-zero values of these SDMEs might be explained not only by SCHC-violation, but also by large radiative corrections.

Chapter 3

The HERMES experiment

3.1 The HERA ring

HERMES (HERA MEasurement of Spin) is one of the four HERA experiments and operated from 1995 till 2007 at the DESY (Deutsche Elektronen Synchrotron) research center using HERA (Hadron Elektron Ring Anlage) storage ring in Hamburg, Germany. The DESY research center was established in 1959 with the goal of multiple studies in particle physics, among them are investigations of the fundamental properties of matter, development and construction of accelerator facilities, use of synchrotron radiation in material science, chemistry, molecular biology and biophysics. The HERA accelerator ring has a length of 6.3 Km with four straight parts and four bending ones between them. It operated with two beams of particles, moving in the opposite directions: protons mostly with an energy of 920 GeV and leptons mostly with an energy of 27.6 GeV. Both beams were pre-accelerated before injection into HERA in two linear accelerators and synchrotron accelerator (DORIS) and PETRA ring. The historical development, the objectives and the results achieved are described in [33] There are four underground experimental halls in the ring, two of them belonging to the collider experiments - H1 and ZEUS, and two belonging to fixed-target experiments - HERA-B and HERMES. H1 and ZEUS, located in the North and South halls, respectively, employed both the accelerated beams to obtain electron-proton collisions. HERA-B was located in the West hall, used the proton beam for colliding with atomic nuclei. The initial aim of HERMES was the study of the spin structure of the nucleons and of shedding light on the "spin crisis" situation (see Equation 1.1). Among the specialties of HERMES experiment the measurement possibility with various beam and target polarizations and reliable particle identification system should be mentioned. The schematic view of HERA and the four experiments is shown in Figure 3.1.

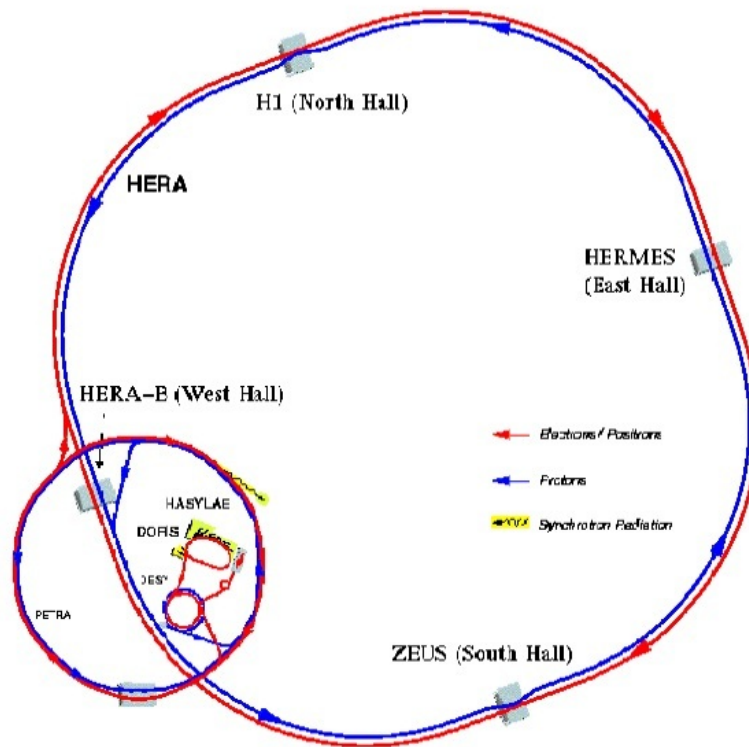


Figure 3.1: The schematic view of the HERA accelerator ring of 1995-2007 years.

3.2 Beam

HERMES used only the lepton beam, the proton one passed in the detector intact. The injected lepton beam had a current of 50mA and consisted of approximately 190 bunches, emitted with the time interval of 96ns. Both H1 and ZEUS needed effectively unpolarized beam, while HERMES needed the longitudinal one at the interaction point. After injection the lepton beam, which was a subject of interests of HERMES, was transversely self-polarized in the arcs because of the Sokolov-Ternov effect [32]: in a storage ring electrons can become polarized antiparallel to the guide field by the emission of synchrotron radiation. Therefore, two beam-spin rotators were installed downstream and upstream of the HERMES apparatus, which turned vertical spin into longitudinal direction without changing the degree of the beam polarization. It was achieved by using a certain combination of horizontal and vertical dipole magnets, which rotated the polarization by 90° within 60m. The depolarization effects due to magnet misalignment and orbit errors were taken into account by permanent measurement of the polarization by the transverse polarimeter (TPOL [36]) and the longitudinal one (LPOL [35]). Both of the polarization monitors were based on Compton scattering of circularly polarized photons from an intense pulsed laser beam. A fractional systematic uncertainty of the polarization measurement

was 1.6%. The polarization developed in time according to [35]

$$P(t) = P_{\infty}(1 - e^{-t/\tau}) \quad (3.1)$$

where the asymptotic polarization P_{∞} and the time constant τ are characteristics of the ring conditions. If the reasons for the depolarization processes, mentioned above, were not present, then the maximum theoretically achievable polarization was $P_{th} = 92\%$. The build-up time for the beam polarization, which depends on the bending radius of the storage ring and the beam energy, was $\tau = 37\text{min}$. The practically obtained value of the polarization was 50-60% in the years 1996-2000 and 40-50% in 2003-2007. The behaviour of the beam polarization is shown in Figure 3.2.

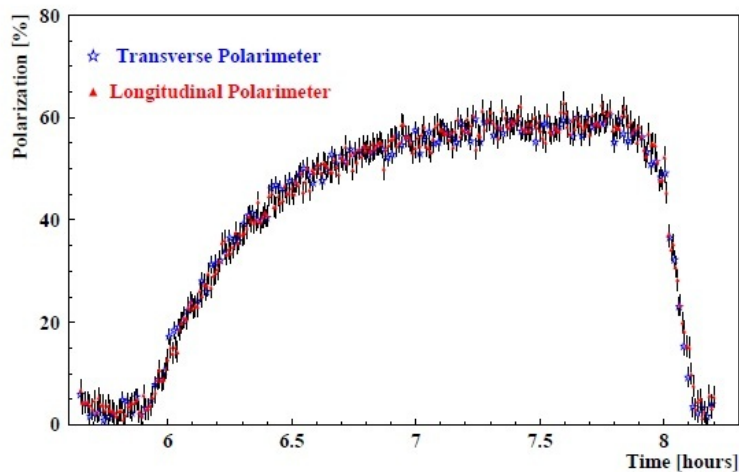


Figure 3.2: The beam polarization measured by transverse and longitudinal polarimeters.

3.3 Target

The HERMES target ([34]) had to keep the beam in a condition that allowed its further usage by the neighbors in the ring - ZEUS and H1. Due to this reason, the target material was chosen to be a gas, whose density is lower than liquid or solid and therefore does not affect the beam intensity too much. The advantage of such a target was that it was pure and high polarization values can be achieved. It was operated with longitudinally polarized ^3He , hydrogen and deuterium, transversely polarized hydrogen, unpolarized hydrogen and deuterium, unpolarized ^4He , N, Kr, Ne, Xe gases. The storage cell, e.g. the place of interactions of the gas with the beam, was internal to the beam pipe. A schematic view of the HERMES target is presented in Figure 3.3. There the main target elements are shown: the atomic beam source (ABS), the storage cell, the target gas analyzer (TGA), the Breit-Rabi polarimeter (BRP) and the target

magnet.

ABS pumping system injected a spin-polarized gas beam in the center part of storage cell, so that the gas density distribution had a triangle shape with the center coincident with the cell center. The injection speed was about 6.5×10^{16} atom/s with the polarization above 90% and a degree of molecules-to-atoms dissociation up to 80%. The dissociation was obtained by a radio-frequency electric discharge. The dissociated gas diffused into the vacuum chamber, where a sextupole magnet system focused atoms with electron spin $+1/2$ into the storage cell and deflected those with $-1/2$ spin. The storage cell was made of thin pure aluminum sheets. The thickness of the cell sides together with their low temperature (100 K) were essential for reducing recombination and the scattering of the particles on the sides. The length of the cell was 400 mm, after the recoil detector was installed the target cell was shifted and made shorter, it was open on both ends and had an elliptical cross section. Two collimators installed upstream protected the cell from synchrotron radiation of the beam. The gas densities of about $1\text{-}2 \times 10^{14}$ nucleons/cm² were achieved, which is a few orders of magnitude more than those obtained with a gas jet target. From the storage cell gas diffused from the middle of the cell into BRP, which measured the atomic polarization or into TGA, which measured the relative atomic and molecular content of the gas. Together they used approximately 5% of the gas. The molecular and atomic gas fractions had different polarizations, therefore the TGA measurement were essential. TGA was connected to the center part of the storage cell on the opposite site relative to the ABS injection tube. From the BRP measurements and the known target magnetic field strength the absolute atomic polarization could be calculated. The actual polarization value was different from that of the injected gas because of the recombination processes and spin relaxation mentioned above.

A superconducting solenoid magnet for longitudinal polarization (1996-2000 years) and a conventional dipole magnet for the transverse one (2002-2005 years) provided a field defining the polarization of the nucleons. Moreover, they prevented spin relaxation by nucleon interactions with the target cell and decoupling of electrons and nucleons. For the longitudinally polarized target the magnet field had a strength of about 350 mT and was directed parallel to the HERA beam direction. For the transversely polarized target the magnetic field had a strength of about 300 mT and was directed parallel to the negative y direction of the HERMES coordinate system. The spin state of the nucleons was flipped every 1-3 min in order to provide data in both spin states and to reduce systematics.

3.4 Spectrometer

The HERMES spectrometer was a forward-angle spectrometer, consisting of two identical halves, designed for measurements of inclusive and semi-inclusive scattering. The halves surrounded the beam pipe and were set behind the target cell to catch the outgoing particles.

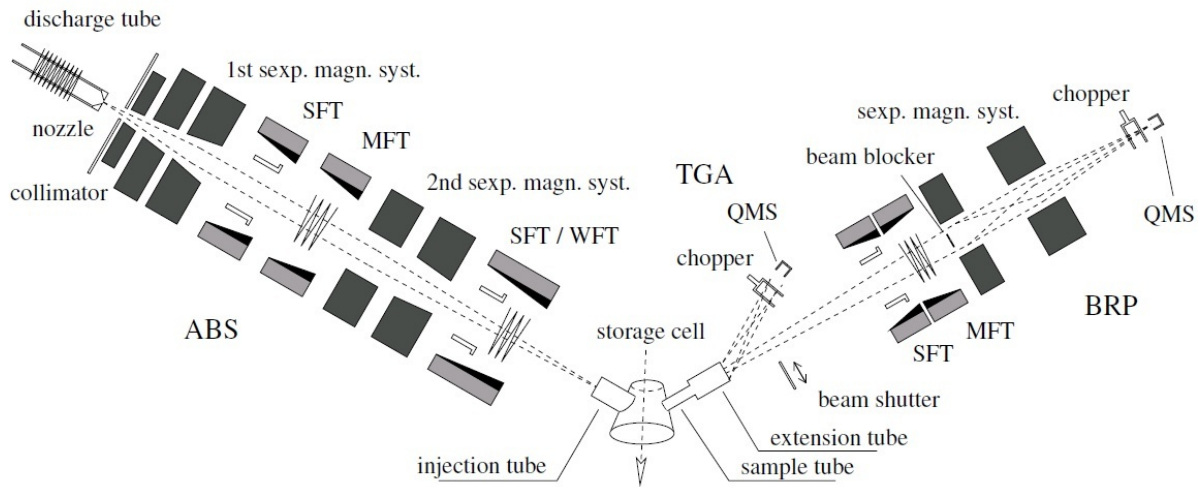


Figure 3.3: The HERMES target setup.

The detector was mounted on a movable platform, so that the detector could be moved out of the beam area. It was located 25 meter below the ground and covered with the concrete wall to protect the outside from the radiation. The schematic view of the detector is presented on Figure 3.4.

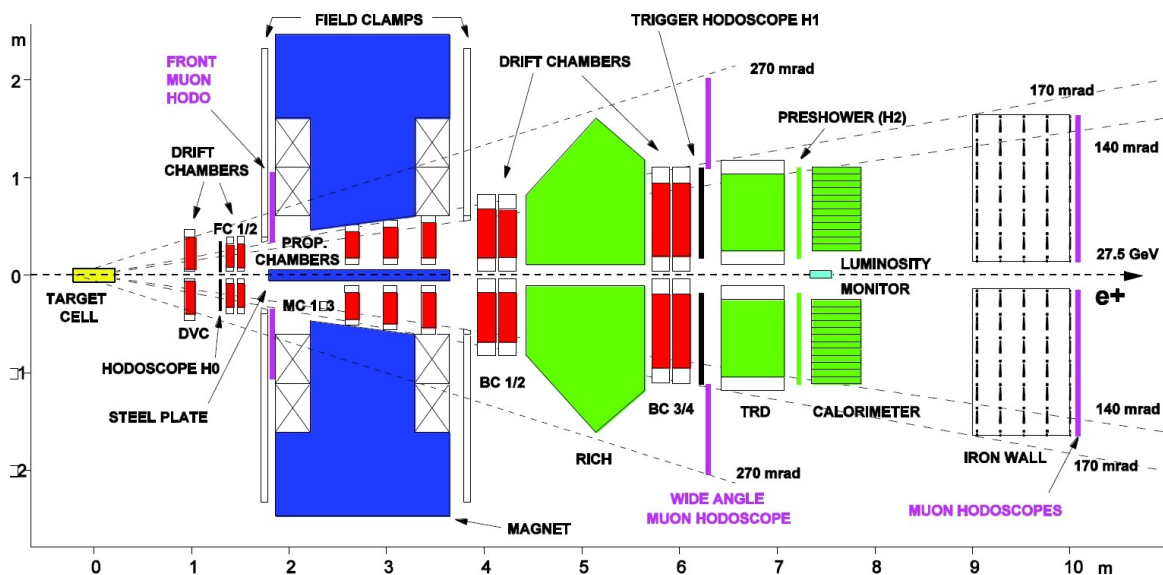


Figure 3.4: The sideview of the HERMES spectrometer in the years 1998-2000. The tracking detectors are in red, the particle identification detectors are in green. The later changes of the experimental setup (for example, recoil detector installed in 2006) do not affect the measurement of an exclusive ϕ meson production.

The coordinate system used by HERMES has the z-axis along the beam axis, y-axis vertical

upwards and the x-axis horizontal, pointing towards the HERA proton ring. The point (0,0) is situated in the center of the target cell. The HERMES coordinate system is shown on Figure 3.4. After interactions in the target cell the particles pass through pre-magnet tracking detectors, which were presented by the silicon detector, drift vertex chambers (DVC) and the front chambers (FC), where the scattering angles and the trajectories of the charged particles are recorded. Then the charged particles are bent horizontally according to their momenta by the magnetic field with a deflecting power of $\int Bdl = 1.3\text{Tm}$, created by the dipole magnet. To shield the lepton and proton beams from the magnetic field, an 11cm thick iron septum plate was installed between the two detector halves. The lower vertical acceptance of the HERMES detector, limited by the plate, is $\pm 40\text{mrad}$. The upper acceptance limit is defined by the magnet size and amounts horizontally: $\pm 170\text{mrad}$, and in the vertical direction $\pm 140\text{mrad}$. In the magnet area additional set of the magnet chambers (MC) was installed. After the magnet the particles passed through the set of back chambers (BC) and particle identification detectors (PID detectors), namely a ring-imaging Cherenkov (RICH) detector, a transition-radiation detector (TRD), a preshower detector and the electromagnetic calorimeter. Around the pipe close to the calorimeter luminosity monitors were situated, permanently measuring the current luminosity.

3.4.1 The tracking system

The main aim of the HERMES tracking system was the determination of the charged particles scattering angles, the vertex positions of the interactions, and particle momentum. The silicon detector (Lambda wheels, [38]) was installed in order to broaden geometrical acceptance for Λ -baryons, which has a long decay length. The next tracking detectors, DVC provided optionally used information. The majority of the information about the particle projections came from the FCs [39] and BC [40], which were drift chambers of a standard design with alternating anode-cathode wire geometry. The FC were filled with Ar/CF₄/CO₂ gas mixture. Each chamber consisted of six wire planes, the two middle were vertical, while first and last pairs were tilted $\pm 30^\circ$ from the vertical. The efficiency per plane was more than 97%. The BCs consist of two pairs of large planar 6-plane drift chambers, which were organized in the same way as the FCs, filled with the same gas mixture and having the similar efficiency.

The magnet chambers were conventional proportional wire chambers and were used to track low-momentum particles, strongly deflected in the magnetic field and not reaching the BC.

Through all the HERMES running years, the tracking algorithm based on matching of the hits in the FCs and BCs was used. After the transverse magnet installation in 2002, the HERMES reconstruction code (HRC) was supplemented with the two transverse magnet corrections algorithms (TMC1 and TMC2, see [43]). HRC does not track particles via magnetic field. To take into account track distortion, energy loss and the effects of residual magnetic fields outside the spectrometer, another tracking algorithm named HTC (HERMES Tracking Code) was

created relatively recently. HTC re-tracks the given number of tracks, found by HRC, based on material passed and possible magnetic field correction. The HTC algorithm determines a common vertex, taking into account the beam position and ascribing each track the probability to originate from the vertex found. The common vertex itself also has a probability to be the true vertex of the possible event. For the present thesis topic, ϕ meson production, no difference was found between the two tracking methods, HTC and HRC because of cleanliness of the reaction channel and primordial sharpness of ϕ meson invariant mass peak [44]. The momentum resolution of the HERMES tracking system was finer than 2%, the angular one 1.8 mrad.

3.4.2 Particle identification

The RICH detector [41] was installed in 1998, replacing a threshold Cherenkov detector that was used in 1995-1997. Its aim was unambiguous determination of pions, kaons, and protons in a wide range of energy. To achieve this, the phenomenon of Cherenkov radiation was employed, which reads that a particle traversing through a radiator material with a velocity larger than the light velocity in the material will emit electromagnetic radiation. The particles with the same momentum but different masses will emit radiation with different opening angles, therefore via measurement of the the angles one can distinguish the particles. The detector consisted of two radiators, one made of aerogel, second one with C_4F_{10} . The radiators refracts light differently, which provided additional information on the particle passed. The produced Cherenkov light was reflected by an array of mirrors, which directed the light onto photoelement array. The obtained picture was a slice of the cone, e.g. an ellipse. To associate the ellipse with the pattern of a certain particle, two reconstruction methods were used. The direct ray tracing (DRT) compared the obtained patterns to simulations of the several particle hypotheses, ascribing them probabilities. For few-track events the event level tracking (EVT) combined all expected DRT patterns for the tracks in onedetector half with overlapping Cherenkov rings.

The RICH provided a reliable separation of the hadrons with momenta from 2 to 15 GeV. The resulting efficiencies were: 95% for pions, 86% for protons, 63% for kaons ([41]). In Figure 3.5 the angles as a function of momenta are shown.

The TRD contributed to the lepton-hadron separation. It consisted of six modules above and below the beam, each of them contains a radiator and a proportional chamber. Its working principle is based on the fact that relativistic charged particles emit transition radiation in the forward direction while crossing a boundary between two materials with different dielectric constants. Under HERMES kinematic conditions, leptons have higher possibility to emit transition radiation while crossing multiple boundaries of fibers in the chambers. Both hadrons and leptons loose energy in the TRD due to ionization of the chamber gas, but the lepton energy deposit is much larger because of the additional emitted transition radiation. The maximum achieved lepton identification efficiency is about 95% [37].

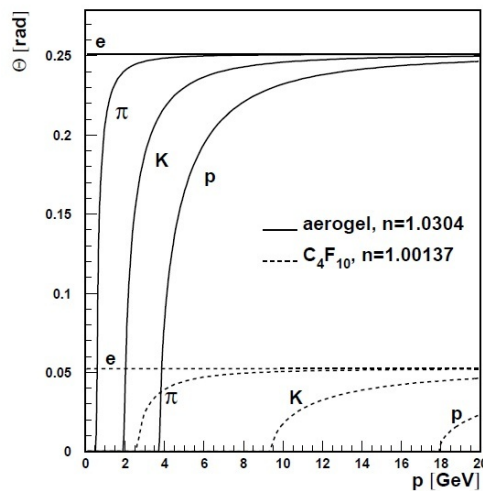


Figure 3.5: The Cherenkov angle θ versus hadron momentum [41].

Another part of information on the particle identification came from Pb-scintillator preshower counter (H2), which consists of 1.1cm thick lead sheet situated in front of the scintillator. Such a wall thickness corresponds to approximately two radiation lengths. While passing through it, leptons lose a few times more energy than hadrons by initialization of electromagnetic showers, producing a signal of a corresponding strength in the scintillator.

The working principle of the calorimeter ([42]) is the same as that of the preshower detector. The total length of the lead-glass blocks is 50cm (equal to about 18 radiation lengths), which ensures the loss of 99% of the initial energy by most of the leptons. Besides the energy deposit from leptons and hadrons, it also measure that of photons.

Information from each particle identification detector number i was summarized in PID_i number, which was calculated as a ratio of probabilities for the detected particle to be a positron to probability to be a hadron:

$$PID_i = \frac{P(S_e, p)}{P(S_h, p)}, \quad (3.2)$$

where p is a momentum, S is a detector response. The final PID value, used in the analysis for lepton-hadron separation, contain information from all the particle identification detectors:

$$\begin{aligned} PID_2 &= PID_{CALO} + PID_{Pre} \\ PID_3 &= PID_{CALO} + PID_{Pre} + PID_{RICH} \\ PID_5 &= PID_{TRD} \end{aligned}$$

Usually in the analysis either $PID_2 + PID_5$ or $PID_3 + PID_5$ were used for particle identification. According to Figure 3.6, the reliable identification of leptons started from PID values more than 2; for hadrons - less than -1.

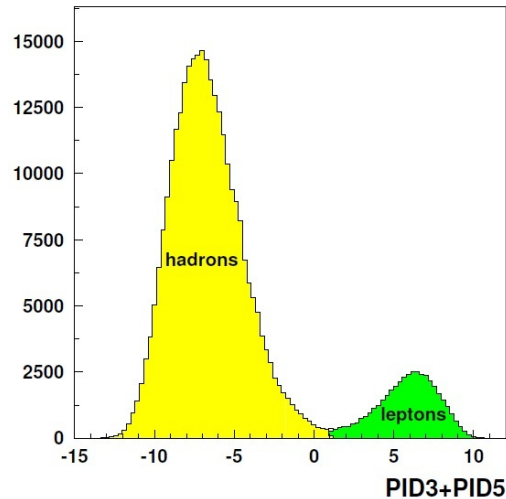


Figure 3.6: The PID distribution of measured particles. The shift of the distribution minimum from 0 is caused by a lower lepton flux.

3.4.3 Trigger system

The trigger system was employed to select useful events and reject background. The coincident signal from the triggers initiate readout of detector signals. The HERMES trigger system used signals from three hodoscopes H0, H1, H2, the calorimeter, BC and the HERA bunch-crossing clock. Charged particles deposit energy in all the mentioned detectors, while photons produced electromagnetic showers only in H2 and the calorimeter. A typical DIS event, the one most often used in analysis, is characterized by presence of a scattered lepton, which was to leave traces in the hodoscopes and energy deposition in the calorimeter. This step in DIS event selection involved the threshold of 3.5 GeV in the energy deposition in the calorimeter and the coincidence of signals from all the hodoscopes and the calorimeter. The threshold of 3.5 GeV separates leptons from hadrons, which leave lower energy deposition with the minimum value of 1.4 GeV.

3.5 Data structure

The data acquisition system (DAQ) recorded the detector information in case the triggers had accepted the event. Each event needed time to be considered by the triggers and to be recorded by the DAQ. This time loss is called the DAQ dead time and usually did not exceed 10% percent of the total working time. The DAQ digitalized the information obtained from the detectors and stored it in the experimental physics input output (EPIO) format. This raw data was stored in runs, defined as a data amount of 450MB. The runs were subdivided into bursts, which were characterized by the same experimental conditions automatically recorded every 10 seconds (like luminosity, beam and target polarizations, beam current, state of the detectors etc.). Then the raw data was converted into physical values in analysable format by

the HERMES decoder software (HDC) and stored in ADAMO (Aleph DATA MODEL) tables. The HERMES reconstruction code (HRC) built actual tracks from this decoded information. The recently created HTC code used the hit positions from HRC and provided the particle tracks, taking into account magnet fields and energy loss due to passage through material. This result of the data processing chain was synchronized with the detector conditions (so-called slow-control data) and written to μ DST (micro Data Summary Tape). The μ DST data productions for each year were updated in terms of up-to-date knowledges about the detector working abilities in different time periods and detector calibrations. The μ DST files contain three data levels: runs, bursts and events. The latter two are described above. The event level consists of the values used in the analysis: momenta, angles, PIDs, vertex positions in the HERMES coordinate system etc of all tracks associated with one interaction (physics event).

Chapter 4

Analysis

4.1 The data and Monte Carlo event selection

In this section the criteria that were applied to obtain the data set used in the analysis from the volume of information registered by the HERMES spectrometer are presented. The two data sets measured with slightly different experimental conditions (see Section 3) are included in this analysis. The first one is the 1998-2000 data from HERA-I, excluding the earlier data due to the absence of RICH detector (see Section 3), which was installed in 1998. The second one is the 2006-2007 data from HERA-II. The 2002-2005 years data set was excluded, since it was taken with a transversely polarized target which causes the distortion of the acceptance for charged particles due to the magnetic field of the transverse-target holding field.

4.1.1 Data quality

To obtain reliable results, the data used in any analysis has to be of a good quality, and should be affected by the measurement conditions as less as possible. The selection criteria are individual for each analysis, however, the basic requirements to the data are common for all studies. The data quality information should be available, all the detector components have to operate stable, the beam and target should be in a good state. After the offline study of all the data recorded, all the experiment condition information was encoded for each burst (see Section 3.5 for the definition) in a 32-bit number pattern. Each of the bits was responsible for a single selection criteria. These patterns were stored in so-called burstlists, which are unique for each data production. The description of each bit for each data production used can be found on the HERMES Data Quality webpage [53].

As already mentioned, if any part of the data quality information was missing or if the slow control data (see Section 3.5 for the definition) was not synchronized with the event data, then that part of the data was discarded. Also, detector calibration runs and data for detector and apparatus studies were not used. Only the bursts of reasonable length and with reasonable dead time of the DAQ system were accepted. The first burst of each run was rejected, since

it was written incorrectly in many cases. Good performance of the subdetectors used in the analysis was also required. Bursts during which one of the PID detectors did not operate or PID information is not available were discarded, the same as for bursts that had high voltage trips in the FCs, BCs, or TRD. If at least one calorimeter block was not responding or no calorimeter threshold was recorded then the burst was skipped.

The beam and target performance also affects the results and therefore was checked. Only the bursts that, according to the parameter information, had stable direction of target polarization with respect to the beam, were accepted. This implies that the runs during which the direction of target polarization was switched were discarded. Selection criteria on target polarization performance were applied mostly for historical reasons. The measured polarization direction was also compared with the expected one and the data which has disagreement between the two values were rejected. Not only qualitative but also quantitative constraints were implied to the target polarization: the upper limit removed the bursts with nonphysically high polarization, the lower one - the bursts where the polarization had not raised up to its maximum value.

For the beam polarization value only an upper limit was imposed to exclude data with beam polarization values that technically could not be achieved. The low-beam-polarization data could contribute to the unpolarized SDMEs and therefore was accepted. Only the data with true up-to-date beam polarization value was selected, e.g., with the polarization measured less than 5 minutes ago. Also the constrain on the beam current was implemented in order to exclude data which was referred either to the very beginning of the fill or to its end, since they were often unreliable. All the quantities, on which these requirements were applied, are listed in Table 4.1

4.1.2 Geometrical restrictions

All physical events used in the analysis should occur from beam interaction with the target cell gas and not with the detector material. To ensure that all the tracks originate from the target cell, certain geometrical restrictions were applied. Moreover, all the tracks were required to be registered by the pre-magnet and after-magnet detectors to exclude tracks that pass only through the septum plate or one of the field clamps of the detector. Therefore all the tracks composed of front and back parts were connected into full tracks in contrast to “short ones”, which consist only of front tracks. Also the HERMES acceptance implies additional constraints on the tracks passing through various detector components. These constraints, called “fiducial volume cuts”, ensure that only appropriate tracks are accepted by checking the hit coordinates in the front and rear field-clamp plates of the spectrometer magnet and at the septum plate enclosing the beam pipe. A box-like fiducial volume cut is defined for the calorimeter cell, removing tracks from the edges where the measurement efficiency decreases because of shower

Quantity	Constraint
Life time	$50\% < t < 100\%$
Burst length	$0 \text{ s} < L < 11 \text{ s}$
Beam current	$2 \text{ mA} < I < 50 \text{ mA}$
First burst in a run	discarded
Bad μ DST record	discarded
No PID available	discarded
Not analyzable according to logbook	discarded
No DQ information	discarded
Dead blocks in calo	discarded
Dead blocks in H2	discarded
TRD not operated	discarded
High voltage trips in FCs, BCs	discarded
RICH problems	discarded
Beam polarization measured more than 5 minutes ago	discarded

Table 4.1: Data quality criteria for the analysis

Position	Constrain
Front field clamp ($z_{lab}=172 \text{ cm}$)	$ x < 31 \text{ cm}$
Septum plate ($z_{lab}=181 \text{ cm}$)	$ y > 7 \text{ cm}$
Rear field clamp (front track) ($z_{lab}=383 \text{ cm}$)	$ y < 54 \text{ cm}$
Rear field clamp (long track) ($z_{lab}=383 \text{ cm}$)	$ x < 100 \text{ cm}, y < 54 \text{ cm}$
Calorimeter ($z_{lab}=783 \text{ cm}$)	$ x < 175 \text{ cm}, 30 < y < 108 \text{ cm}$
Vertex position 1998-2005	$-18 \text{ cm} < Z_{vertex} < 18 \text{ cm}$
Vertex position 2006-2007	$0 \text{ cm} < Z_{vertex} < 25 \text{ cm}$

Table 4.2: Geometrical constraints for the analysis

leakage. Leptons deposited almost all their energy in the calorimeter blocks, while hadrons lost the energy only partially. All the geometrical constraints are listed in Table 4.2. In 2006, to make space for the recoil detector in the HERMES apparatus, the target cell was shifted and made shorter, therefore the boundary value on the vertex-in-target position are different before and after 2006 year. In the present analysis no information from the recoil detector is used, the information on target nucleon after the interaction was obtained from the reconstructed tracks of the other particles via momentum and energy conservation principles.

4.1.3 Selection of exclusive events

As already mentioned in Chapter 2, both ϕ and ρ mesons are short-living particles, which decay into two oppositely charged hadrons – kaons in case of ϕ mesons (the branching ratio of such a decay is $49.1 \pm 0.8\%$ [54] and pions in case of ρ meson. The decay occurs inside the target cell. The two produced hadrons together with the scattered lepton provide a signature of an exclusive ϕ (ρ) meson production event candidate. The basic restriction to select exclusive vector meson events is consequently the presence of three charged-particle tracks in the forward direction. For each of the tracks the geometrical constraints described in Section 4.1.2 are applied. Moreover, tracking probability provided by HTC tracking method for each track, e.g. the probability for the track to satisfy the found vertex, was demanded to be more than 0. The probability of the found vertex to be the point of interaction was also required to be more than 0 (see Section 3.4.1 for the details of HTC tracking method, track and vertex probabilities). Then the scattered lepton is identified by PID type, a charge that is to be the same as the beam charge, and a minimum momentum (3.5 GeV). To select deeply inelastic scattered leptons, photon virtuality Q^2 was required to be larger than 1 GeV². Radiative effects discussed in Section 2.15 here were decreased to negligible level by imposing the maximum value on the relative lepton energy loss ($y < 0.85$). The squared invariant mass of the γ^*p system, W was demanded to be larger than 2 GeV to move away from the nucleon resonances region.

The kaons (pions) are first identified as oppositely charged hadrons with momenta from 2 to 15 GeV. Then a restriction on the kaon PID type is applied. Despite of the fact that the RICH efficiency for kaon identification is 80% only, such a requirement is obligatory to select the events of interest reliably. Figure 4.1 illustrates the effectiveness of the RICH kaon type cut, showing significant decrease of the background (from black to green histogram) in the exclusive region ($\Delta E < 0.6$ GeV), compared to the sample selected without RICH information. For pions, however, another strategy might be used: most of the detected hadrons are pions and can be accepted as such without a strict RICH-type constraint implementation.

Another possible algorithm is to use the constraint on ϕ meson momenta $P_\phi > 7.5$ GeV instead of RICH kaon type, since most of the low-energetic ϕ mesons, shown in Figure 4.1 as the blue histogram, correspond to three track combinations that are not related to exclusive production. As can be concluded from Figure 4.1, the requirement on ϕ meson momentum is efficient in case of absence of RICH kaon type constraint; if using the latter, then the momentum restriction is redundant (only small background decrease from green to magenta histogram in Figure 4.1). To discard the tails of the invariant mass distribution (See Figure 4.6), the mass window $1.012 \text{ GeV} < M_{K^+K^-} < 1.028 \text{ GeV}$ was used.

After implementation of all the requirements described above, one obtains the pronounced invariant mass $M_{K^+K^-}$ ($M_{\pi^+\pi^-}$) peak. However, the selected sample would still contain background contribution, namely the non-exclusive events, in which some other particle were produced in addition to 2 kaons (pions) but not detected due to the limited HERMES detector

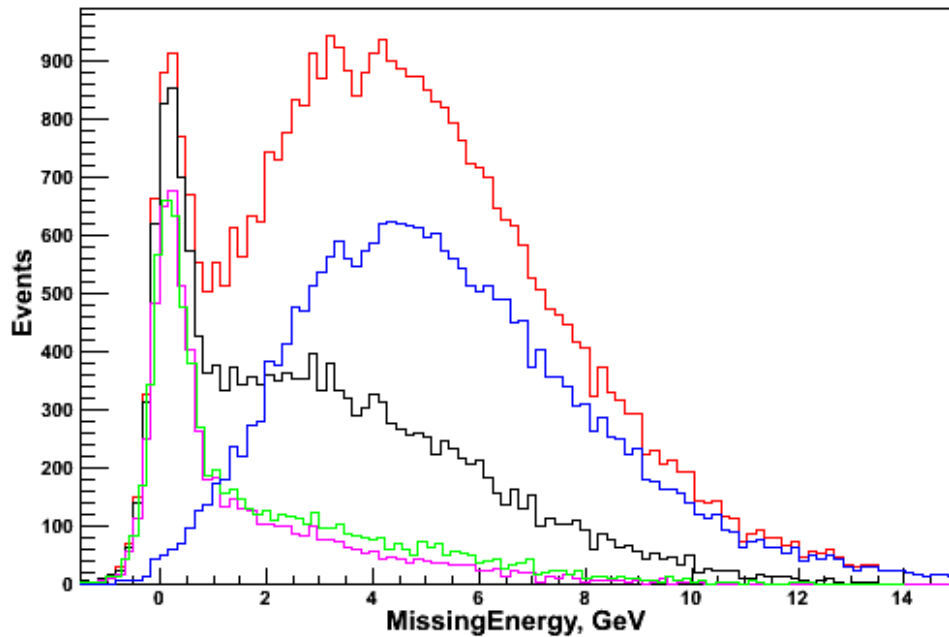


Figure 4.1: The missing energy distribution for ϕ meson production. Black histogram shows sample selected without constraint on RICH kaon type but with restriction on ϕ meson momentum. Green histogram was built with requirement on RICH kaon type and without constraint on ϕ meson momentum. Blue histogram represents events with $P_\phi < 7.5$ GeV, which are mostly background. Red histogram denotes events without constraint on RICH kaon type and without restriction on ϕ meson momentum. Magenta histogram represents the sample with constraint on RICH kaon type and with constraint on the ϕ meson momentum.

acceptance. To select only exclusive vector meson events, the requirements described below were applied.

The recoiling nucleon was reconstructed from the information of all the remaining tracks of the event:

$$p'_X = p + k - k' - p_{VM}, \quad (4.1)$$

where all the variables are 4-vectors of the corresponding particle kinematics (see Section 2.1 for the details). The mass of this unobserved state, M_X , is to be equal to the target nucleon mass in case of exclusive reaction and is called the missing mass. Therefore, the missing-energy of the reaction, calculated as

$$\Delta E = \frac{M_X^2 - M^2}{2M}, \quad (4.2)$$

is to be zero for the exclusive production (M is the known target nucleon mass). However,

due to the HERMES detector resolution the ΔE distribution is smeared and forms a Gaussian around zero. Non-exclusive events have $\Delta E > 0$ and the recoiling particle mass different from the target nucleon mass. To cut away this background, a restriction on ΔE has to be implemented. Too strict constraints would result in loss of exclusive event, while too wide ones would increase the statistics but leave too much of the background. The optimal constraint on the missing-energy was determined using Monte Carlo simulation, e.g., Monte Carlo simulated background was used to estimate the relation between the background and the signal from the real data. In Figure 4.2 a comparison of the missing-energy distribution for the real data to that of Monte Carlo together with the Monte Carlo generated background in all the kinematic bins is presented.

PYTHIA generator was not tuned for ϕ meson production, that is why the yield of the Monte Carlo signal (e.g only the exclusive process 91 is selected) is much less for PYTHIA than for data. The worst situation is for the large Q^2 and t' bins, where the disagreement between the data and PYTHIA in the signal region is up to two times. However, tuning this would require quite some time and is not obligatory, since this PYTHIA set was used only for semi-inclusive background estimation. SIDIS background simulation (magenta dashed lines in Figure 4.2) is in satisfactory agreement with the data and was used in the study described below. The noticeable disagreement of the background from the real data and from Monte Carlo was taken into account via assigning of systematic uncertainty due to the background subtraction.

As a first guess on the optimal constraint on the missing energy, the minimum total relative uncertainty of the resulting exclusive sample was calculated for the overall kinematics. The total uncertainty was obtained as the square root from the sum of systematic and statistical uncertainties squared, statistical and systematic uncertainties are:

$$(\text{Relative statistical uncertainty})_i = \frac{\sqrt{N_i^{Data} + N_i^{background}}}{\sqrt{N_i^{Data} - N_i^{background}}}, \quad (4.3)$$

$$(\text{Systematic uncertainty})_i = \epsilon * \frac{N_i^{background}}{N_i^{Data}}, \quad (4.4)$$

where N_i^{Data} and $N_i^{background}$ are data and Monte Carlo background yields for each iteration of ΔE cut from 0.1 to 2 GeV with the step 0.1 GeV, ϵ is a parameter indicating how well Monte Carlo generated background describes the data one. To estimate the goodness of the description, a ratio of the data N^{Data} (black histogram in Figure 4.1) and Monte Carlo generated background $N^{Background}$ (magenta histogram in Figure 4.2 in the region $2 \text{ GeV} < \Delta E < 6 \text{ GeV}$) was calculated and was found to be 0.92.

Resulting statistical, systematic and total uncertainty are plotted in Figure 4.3, left side.

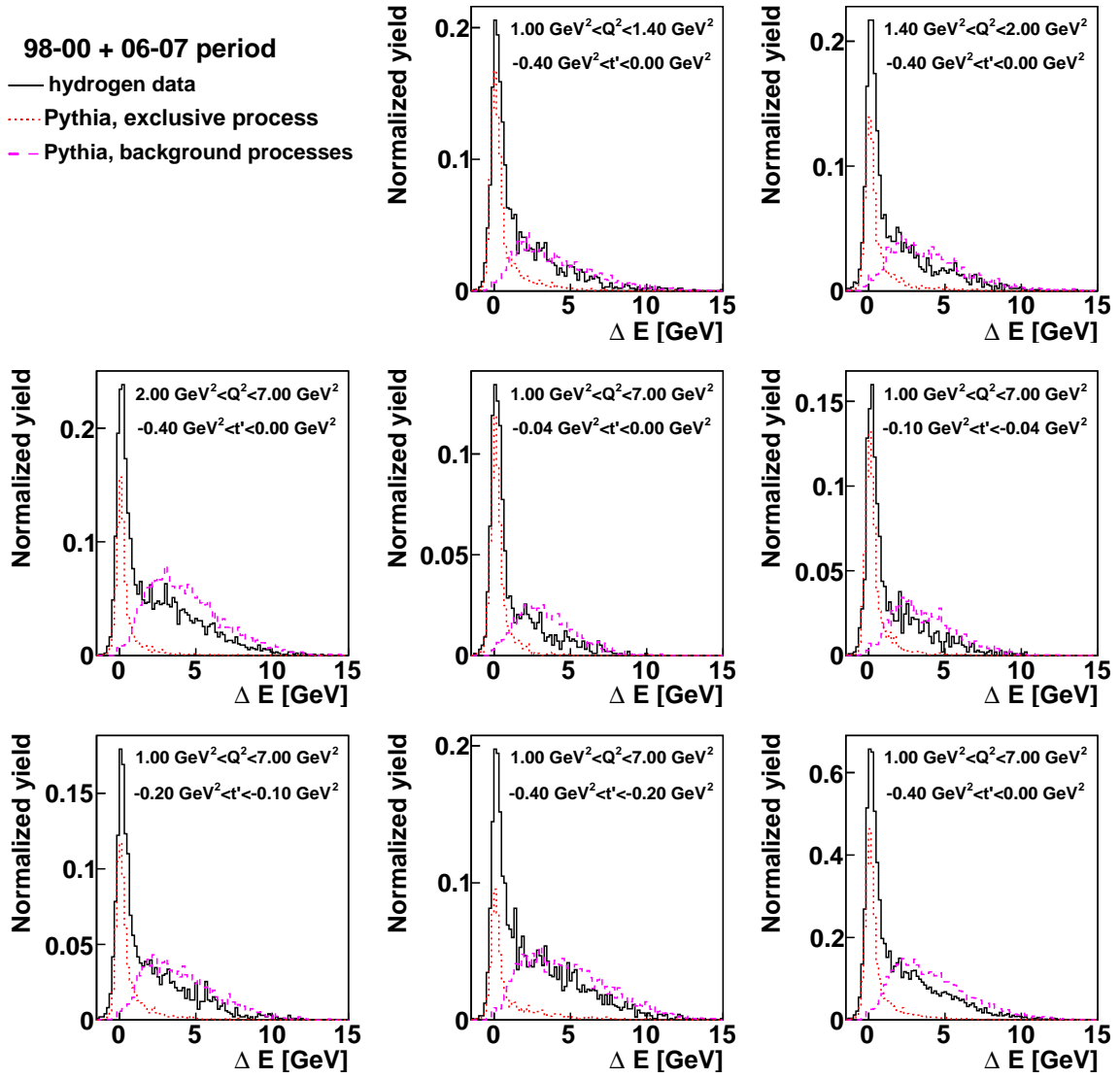


Figure 4.2: The missing energy of the reaction of exclusive ϕ meson production for the data (black line), PYTHIA Monte Carlo set with only the ϕ meson production process selected (red dotted line), PYTHIA Monte Carlo set with the background process selected (magenta dashed line). All the kinematic bins, used in the analysis, are presented. The overall kinematic case is shown in the bottom right box. The plots are done with absolute normalization.

From Figure 4.3 (right side) a minimum of the curve is around 1, but since the traditional value for the constrain was 0.6 GeV, it was chosen for the consistency with previous analysis. The background in the exclusive region is negligible: for hydrogen it is 2.5%, for deuteron 3.4%.

Another requirement on the reaction exclusivity is connected to the four-momentum transfer from the initial to the final nucleons $t = (p - p')^2$, where p' is obtained from Equation 4.1. The minimal kinematically allowed value of t , t_0 can be calculated in the center-of-mass system of

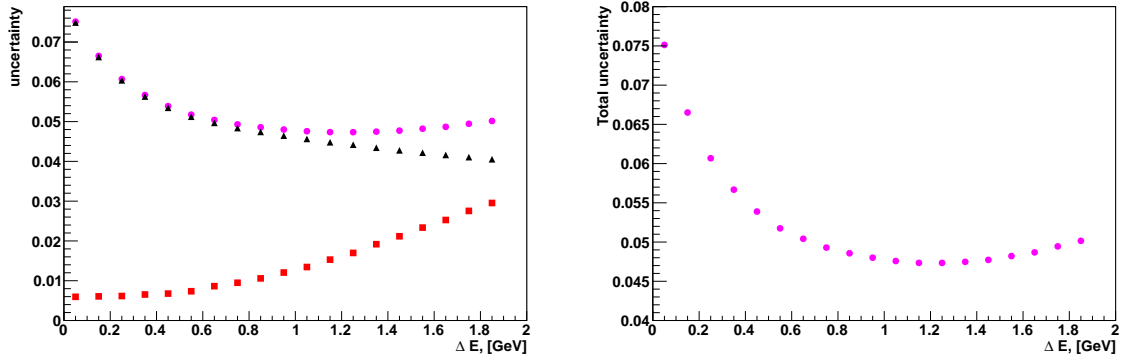


Figure 4.3: Left plot: Total relative uncertainty of the number of exclusive ϕ meson events are denoted by magenta circles; systematic uncertainty is shown by red squares; statistical uncertainty is represented by black triangles. Right plot: Total relative uncertainty zoomed.

the virtual photon and nucleon as

$$t_0 = (E_\gamma - E_{VM})^2 - (|q| - |v|)^2, \quad (4.5)$$

where

$$E_\gamma = \frac{W^2 - Q^2 - M^2}{2W}, \quad E_{VM} = \frac{W^2 + M_{VM}^2 - M_X^2}{2W} \quad (4.6)$$

$$|q| = \sqrt{E_\gamma^2 + Q^2}, \quad |v| = \sqrt{E_{VM}^2 - M_{VM}^2}. \quad (4.7)$$

In the photon-nucleon center-of-mass frame the condition $t = t_0$ corresponds to the case where the momentum of the produced vector meson is collinear with that of the photon.

Since the target nucleon remains intact, the difference t between the initial and the final nucleon momentum is small, as well as t_0 . Therefore the quantity $t' = t - t_0$ is to be small in the exclusive region. The restriction used in the present analysis was $t' > -0.4 \text{ GeV}^2$. In Figure 4.4 the correlation of the missing energy and the t' value is presented, showing the pronounced peak at low ΔE and low $-t'$, which corresponds to the reaction of exclusive ϕ meson production under HERMES kinematic conditions.

4.1.4 Separation of coherent and incoherent parts for deuteron data

A contribution of coherent scattering, when the incoming lepton interacts with the whole deuteron nucleus, e.g., when the interaction might occur either on proton or on neutron, is expected to affect the results for deuteron data. Indeed, the SDME formalism described in Sections 2.8 and 2.11 is valid for spin 1/2 targets only. For hydrogen only incoherent scattering

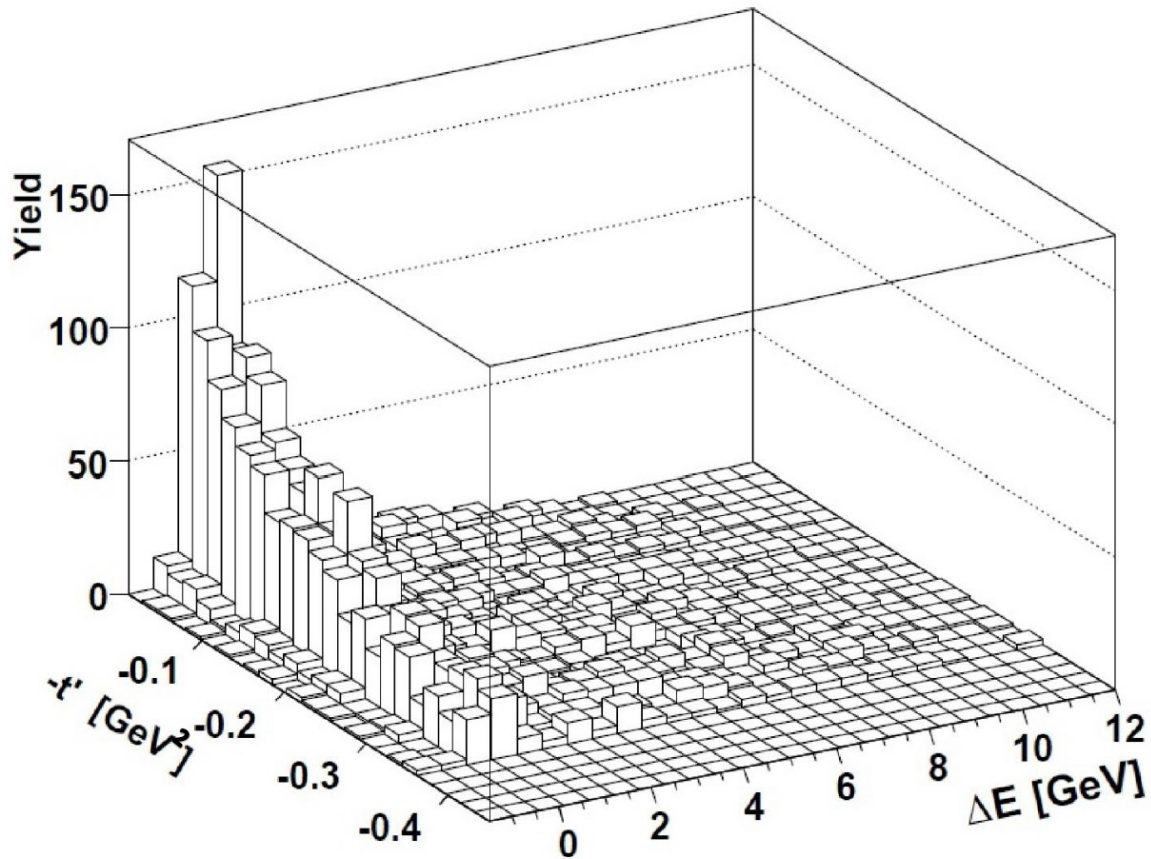


Figure 4.4: The $(t', \Delta E)$ distribution of ϕ meson production on hydrogen target of 1998-2000, 2006-2007 periods.

exists. To exclude the coherent contribution, an additional requirement on t' was implemented for the deuteron data. The cross section dependence on t' has an exponential form, e.g., $\frac{d\sigma}{d|t'|} \propto \exp^{-b|t'|}$ [11], with b being a slope parameter. For the sum of coherent and incoherent contributions one can write

$$\frac{d\sigma}{d|t'|} \propto p_1 \exp(-b_{incoh}|t'|) + p_2 \exp(-b_{coh}|t'|). \quad (4.8)$$

Each of coherent and incoherent part related parameters was fitted to the data, e.g. the distribution was fit by the sum of two exponents. Figure 4.5 shows the fit of the t' distributions in each of Q^2 bins and overall kinematics.

The cut position was defined as the crossing point of the two exponents and was found to be about -0.035. The fraction of the coherent events in the rest sample ($t' > -0.35 \text{ GeV}^2$) is 10%. Since the fitting parameter value is close to the first t' bin boundary (-0.04), this boundary was chosen to be the constraint position.

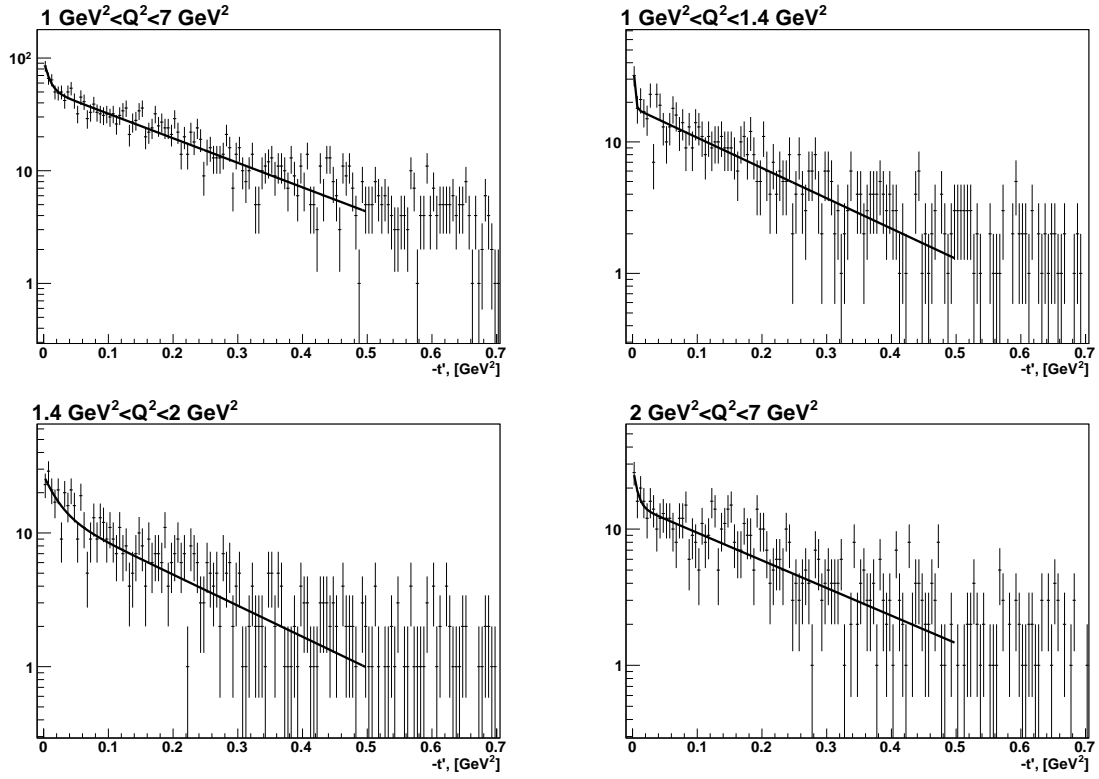


Figure 4.5: The fit of t' distribution for all the Q^2 bins in the logarithmic scale. The two areas of the exponential fit with different slopes represent coherent ($0 < -t' < 0.035 \text{ GeV}^2$) and incoherent ($0.035 \text{ GeV}^2 < -t' < 0.5 \text{ GeV}^2$) parts of the distribution.

4.1.5 ϕ meson invariant mass distribution

In Figure 4.6 the two-kaon invariant mass is depicted, with the constraints on t' and ΔE described above. The two-kaon invariant mass calculated via formula $M_{K^+K^-} = \sqrt{(p_{K^+} + p_{K^-})^2}$, with p_{K^+} , p_{K^-} being 4-vectors of positively and negatively charged kaons. The narrow clean peak at the expected mass can be seen, corresponding to exclusive ϕ meson production. The peak is fitted by the Breit-Wigner function. The relativistic Breit-Wigner distribution describing a spin-1 object decaying into two spin-0 objects, or, in other words, describing the mass of ϕ meson decaying into two kaons, is given by the formula

$$\frac{dN}{dM_{K^+K^-}} = BW(M_{K^+K^-}) = \frac{2}{\pi} \frac{M_{K^+K^-} M_\phi \Gamma(M_{K^+K^-})}{(M_\phi^2 - M_{K^+K^-}^2)^2 + M_\phi^2 \Gamma^2(M_{K^+K^-})}, \quad (4.9)$$

where $M_{K^+K^-}$ is two kaon mass, M_ϕ^2 and $\Gamma(M_{K^+K^-})$ are the mass and the width of the ϕ meson resonance. The χ^2 of the fit reflects the fact that a relativistic Breit-Wigner function does not describe the skewing of the ϕ peak to lower mass values.

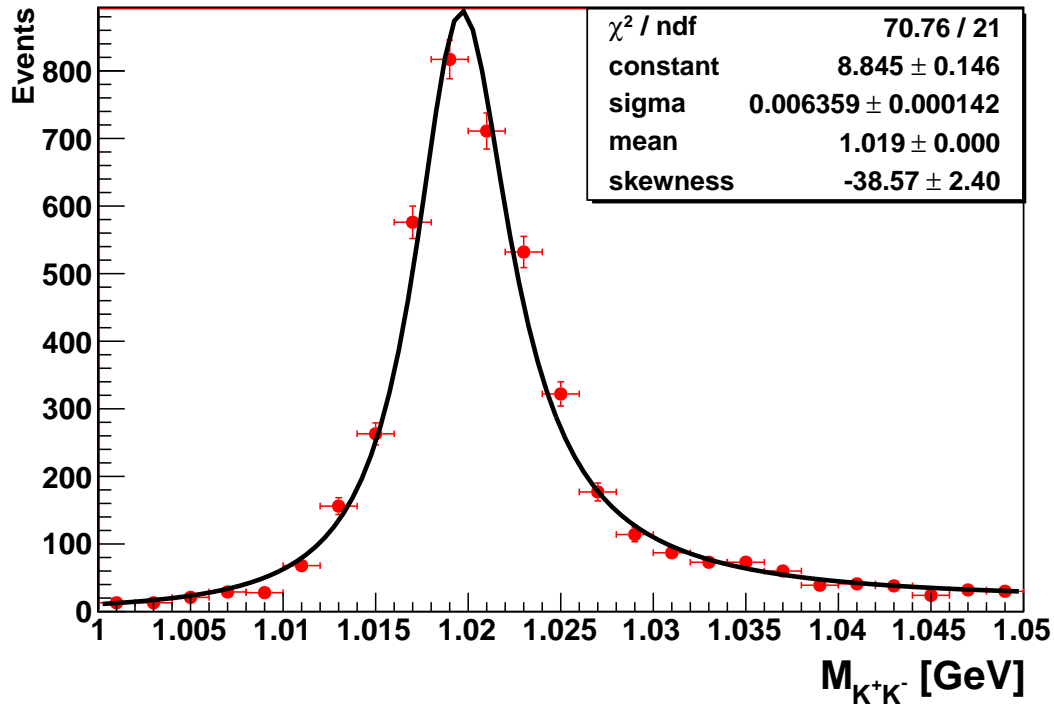


Figure 4.6: Two-kaons invariant mass distribution in the exclusive region for hydrogen data sample (red points). The line represents a fit of a Breit-Wigner function.

Year	Runs		N_{DIS}		N_{ϕ}	
	Hydrogen	Deuteron	Hydrogen	Deuteron	Hydrogen	Deuteron
1998	617	7647	482740	1924447	24	93
1999	0	11615	0	854994	0	78
2000	1511	19613	6022023	5352782	286	308
2006	34406	8254	28301671	5253267	1568	306
2007	29786	9382	20858417	4793406	1210	294

Table 4.3: Numbers of runs, DIS events and exclusive ϕ meson events for hydrogen and deuteron targets for 1998-2000 and 2006-2007 periods.

4.1.6 Final data sample used in the analysis

The collected statistics for each year of the united data taking period of 1998-2000 and 2006-2007 periods is presented in Table 4.3.

The constraints described above resulted in the numbers of events, presented in Table 4.4 for each of the kinematic Q^2 and t' bins for hydrogen and deuteron targets.

Target	Hydrogen	Deuteron
Kinematic bin	Number of events	
$1 \text{ GeV}^2 < Q^2 < 1.4 \text{ GeV}^2$	955	370
$1.4 \text{ GeV}^2 < Q^2 < 2 \text{ GeV}^2$	1021	338
$2 \text{ GeV}^2 < Q^2 < 7 \text{ GeV}^2$	1112	371
$0 \text{ GeV}^2 < -t' < 0.04 \text{ GeV}^2$	661	(332)
$0.04 \text{ GeV}^2 < -t' < 0.1 \text{ GeV}^2$	709	313
$0.1 \text{ GeV}^2 < -t' < 0.2 \text{ GeV}^2$	821	392
$0.2 \text{ GeV}^2 < -t' < 0.4 \text{ GeV}^2$	896	374
overall	3088	1079

Table 4.4: Numbers of events used in the analysis for hydrogen and deuteron targets for 1998-2000 and 2006-2007 periods. Q^2 and t' binings are independent from each other, e.g. 1D binning is done for each variable separately. For deuteron data in the Q^2 bins an additional constrain $t' > 0.04 \text{ GeV}^2$ is implemented, e.g. the first t' bin data is excluded from all the Q^2 bins and the overall data set.

4.1.7 Monte Carlo event selection

The two Monte Carlo event generators, PYTHIA ([45]) and RhoMC ([46]) are used in this analysis for systematic studies, background determination and for the SDME extraction. In this section a short description of the two generators is presented together with the analysis goals they were used for. The main features of the two generators, important for this analysis, are the following: PYTHIA is able to generate various types of processes, in particular hard interactions in e^+e^- , pp , and ep colliders, while RhoMC can produce only exclusive vector meson processes. PYTHIA is capable to generate sets with unpolarized beam and target only, in contrast to RhoMC, where beam polarization can be implemented. Another difference is that SDMEs can be implemented in RhoMC-produced decay angular distribution of a vector meson, which is not possible for PYTHIA (only the first SDME can be implemented, See Equation 4.18).

The event generation scheme for both PYTHIA and RhoMC generators is shown in Figure 4.7. After physical event generation and detector simulation the same tracking method as for the real data, HTC (see Section 3.4.1) was employed. Then reconstructed and generated tracks were stored in μ DSTs(see Section 3.5). Monte Carlo μ DSTs have the same structure as data ones, but contain additional information like generated tracks, born-level tracks etc.

PYTHIA generator

The PYTHIA generator can be used to produce high-energy-physics events, e.g sets of outgoing particles originating from the interaction between two incoming particles. The generation

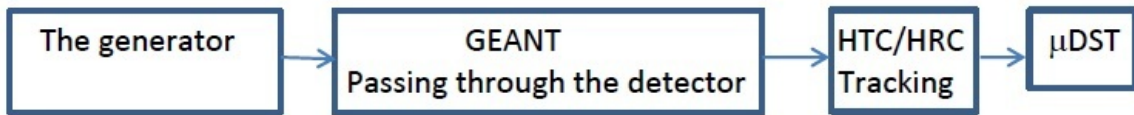


Figure 4.7: The scheme of event generation chain using PYTHIA.

is done according to the relative cross section, using the "accept-reject" method. For some processes cross sections were tuned to HERMES kinematics, for example exclusive ρ meson production, but not ϕ production.

The scattered lepton kinematics (Q^2, ν) are generated according to the relative cross sections of the corresponding processes (DIS, QCD-Compton and boson-gluon fusion processes). The momentum of the scattered lepton can be modified by initial- and final-state radiation, which is taken into account by an external program RADGEN ([47]). RADGEN recalculated the generated Born level kinematics to true ones. As was mentioned in Section 2, the ep collision can be represented as γ^*p process. The development of the last one in PYTHIA follows one of the next scenarios, depending on the value of transverse momentum k_{\perp} of the quarks with respect to the virtual-photon direction. If the process virtuality is large, e.g. if k_{\perp} is larger than cutoff parameter of the order of 0.5 GeV, then the process is described via pQCD involving formation of hadron from $q\bar{q}$ pair, e.g. fragmentation (hadronization), which is done by an additional code JETSET([48]). If the virtuality is low and k_{\perp} is small, pQCD is not applicable and VMD (see Section 2.6) model is used. HERMES detector effects, e.g. its geometrical acceptance, efficiency and smearing was simulated by GEANT package ([50]).

Two types of PYTHIA productions were used in this analysis: the one containing various diffractive processes was used for normalization in Maximum Likelihood Method (MLH)(see Section 4.2) and another one, containing also semi-inclusive processes, was used for background estimation. Each of the Monte Carlo sets used in the analysis consists of two subsets from the two detector-composition geometries, mixed in the same ratio as the corresponding geometries are presented in the real data. The subsets were generated for the two target types (proton and neutron) and two beam types (electron and positron). The proton and neutron subsets were mixed in final sets in such a proportion that their absolute luminosities are equal. The luminosity of a Monte Carlo set is calculated via the total cross-section of the generated processes – *extraweight*, the number of attempts to generate acceptable events – *ievgen*, and number of generated runs N . These numbers are stored in the files produced during generation of the Monte Carlo set. The total luminosity reads

$$L_{MC} = \frac{\sum_{i=1}^N ievgen_i}{\sum_{i=1}^N extraweight_i/N}. \quad (4.10)$$

RhoMC generator

RhoMC generator was designed especially for exclusive vector meson production generation and in contrast to PYTHIA, which generates the whole stochastic spectrum of the final states, produces these according to the VMD model. RhoMC generates flat distributions in a kinematic box for most of the kinematic variables and then weights each event with the corresponding cross section. While in PYTHIA event weights are equal to 1, RhoMC weights are hence different from 1. The RhoMC kinematic distributions are physical only after weighting each generated event with the corresponding event weight.

RhoMC generated sets were used for the systematic uncertainties estimation, e.g. so-called "all-in-one" procedure (Section 4.3.1) and uncertainty due to the different Monte Carlo models (Section 4.3.2). All-in-one procedure is used for estimation of the systematic uncertainties of SDME extraction method, limited statistics, detector smearing and misalignment. RhoMC sets were used as pseudo-data in the procedure, e.g. known implemented SDMEs were extracted from RhoMC set instead of the real data set.

RhoMC sets with vanishing SDME values, e.g. with uniform decay angular distributions, distorted by HERMES acceptance only, were used as normalization samples in Maximum Likelihood Method (MLH) for estimation of the systematic uncertainty due to the different Monte Carlo models.

4.1.8 Data to Monte Carlo comparison

In Figure 4.2 data-to-PYTHIA comparison for the missing energy distribution in different kinematic Q^2 and t' bins, used in the analysis, is presented. Event selection was done with the same constraints as for data, the Monte Carlo signal (red dotted histogram in Figure 4.2) consists of the events with a process type number, corresponding to the exclusive ϕ meson production. For the background sample (magenta dashed histogram in Figure 4.2) events which pass all the exclusive cuts (except from the missing energy cut) but are of background types, were selected.

In Appendix C kinematic distributions in different Q^2 and t' bins for data, PYTHIA and RhoMC without implemented SDMEs are presented.

4.2 SDME extraction

In this chapter the procedure of SDME extraction from the decay angular distribution in Wolf-Schilling and Markus Diehl notations using the unbinned maximum likelihood method is described. The decay angular distribution W (Equations 2.61 - 2.62 - in Wolf-Schilling form, Equation 2.66 - in Markus Diehl form) of the vector meson contains the measured decay angles and unknown SDMEs, which are the object of interest. The angular distribution is, therefore,

affected by the HERMES apparatus (acceptance, measured efficiency, tracking etc.) and by SDMEs. To extract the latter ones, the instrumental effects were to be excluded from the decay angular distribution. The acceptance description was provided by the Monte Carlo set, which was tuned for the HERMES geometrical and kinematic acceptance and whose angular distributions do not contain SDMEs, except from the first SDME r_{00}^{04} (see Equation 4.18). Unbinned MLH was chosen for SDME extraction due to its higher reliability compared to the binned MLH in case when the limited statistics.

4.2.1 Maximum-likelihood method

The first step in MLH method implementation is to build the probability density function p. d. f. The probability dp for a single event to be detected is given by the formula ([57])

$$dp = \frac{(\mathcal{L}\sigma EW)^{w_D}}{\mathfrak{N}^{w_{MC}}}, \quad (4.11)$$

where \mathcal{L} denoted the integrated luminosity determined by counting DIS events, $E \equiv E(\Phi, \varphi, \cos \theta)$ is the detector efficiency, $W \equiv W(\Phi, \varphi, \cos \theta, P_b, \bar{\lambda})$ is the theoretically predicted decay angular distribution of the vector meson in Wolf-Schilling or Marcus Diehl representation, P_b is the beam polarization, $\bar{\lambda}$ denotes a vector of 23 SDMEs, w_D is the event weight (if any) for real data, w_{MC} is that of Monte Carlo. The denominator of this function is the normalization of the p. d. f. and is responsible for the acceptance of the HERMES spectrometer. The normalization factor \mathfrak{N} is to be such, that the total probability to detect final particles for all angles $d\Omega = d\Phi d\varphi d\cos \theta$ is equal to unity:

$$\int dp = \int W(\Phi, \varphi, \cos \theta, P_b, \bar{\lambda}) d\Omega = 1. \quad (4.12)$$

For the total set of N events the likelihood function L is defined:

$$L(\lambda) = \prod_i \frac{W(\phi_i, \theta_i, \Phi_i, P_i, \bar{\lambda})^{w_i}}{\mathfrak{N}(\bar{\lambda})}, \quad (4.13)$$

where the detector efficiency is omitted since it does not depend on $\bar{\lambda}$ parameters. The product in the denominator is independent of λ parameters and can be ignored in the likelihood fit, if the whole data set has no net beam polarization (See [58]): $\int P dP = 0$. To achieve this, the data set has to be either unpolarized or beam-polarization balanced. The balanced sample, e.g. the sample consisting of the two sup-samples with opposite beam polarization signs and equal luminosities, can be obtained either by skipping of a part of the data with the prevailing polarization sign or by assigning a beam-balancing weight. The weight for the data with a certain beam polarization sign was calculated from the definition of the beam-balanced sample: $|\sum Lumi_+ P^+| = |\sum Lumi_- P^-|$, where $Lumi$ is the luminosity of the data set with the cor-

responding polarization sign, P is the beam polarization value. The luminosity was calculated via DIS sample: $w^{+/-} = \frac{\sum_i^{N^{-/+DIS}} P_i^{-/+DIS}}{\sum_j^{N^{+/-DIS}} P_j^{+/-DIS}}$. The weight was always implemented to the larger set, therefore it was always less than 1. The weight w_D used in formula 4.11 can represent beam balancing weight. The parameters are defined by maximization of the logarithm of the likelihood (LH) function, or alternatively by minimization of $-\ln L(\lambda)$:

$$\left. \frac{d \ln L(\lambda)}{d\lambda} \right|_{\bar{\lambda}=\bar{\lambda}_{true}} = 0, \quad (4.14)$$

The $\ln L(\bar{\lambda})$ is given by the formula

$$-\ln L(\bar{\lambda}) = - \left[\sum_i (w_i \ln(W^{U+L}(\Phi_i, \phi_i, \cos\theta_i, P, \bar{\lambda}))) - N_{ev} \ln \left\{ \sum_j (w_j(W^U(\Phi_j, \phi_j, \cos\theta_j))) \right\} \right], \quad (4.15)$$

where sum on index i implies sum of data events, sum on j - sum of Monte Carlo events, N_{ev} is number of events in data, $w_i(w_j)$ is weight of data or Monte Carlo event correspondingly. The second sum, referred to Monte Carlo events, does not depend on the beam polarization and therefore does not contain the part of angular distribution involving longitudinal beam polarization. The logarithm of the likelihood function is to be given to the minimization program. For this analysis MINUIT package was used. SDMEs were treated as free parameters during the fitting. The result of the minimization program are SDME values with fitting uncertainties. The uncertainties are root squares of the diagonal elements of the covariance matrix V with the dimensions $k \times n$, $k = n$, which can be determined from the matrix of the second derivative $\ln L$ via

$$(\hat{V}^{-1})_{kn} = \left. \frac{\partial \ln L}{\partial \lambda_k \partial \lambda_n} \right|_{\bar{\lambda}}. \quad (4.16)$$

In Figure 4.9 angular distributions are shown for hydrogen data sample for the real data, isotropic Monte Carlo sample used for MLH normalization, and Monte Carlo set reweighted with the obtained SDME values. The reweighted distributions are in agreement with the data.

Unbinned MLH: implementation without beam balancing weights

As an additional cross-check of the beam-balancing procedure and the whole MLH method implementation an alternative representation of the LH function without beam-balancing weights was used. In such a representation of a MLH function the normalization factor depends of the polarization even in the case of the polarization balance. In Formula 4.17 the sum over Monte Carlo events runs inside the sum over data ones. This means that instead of calculation of the normalization integral on each fit iteration as it was done in Formula 4.15, the intergal was

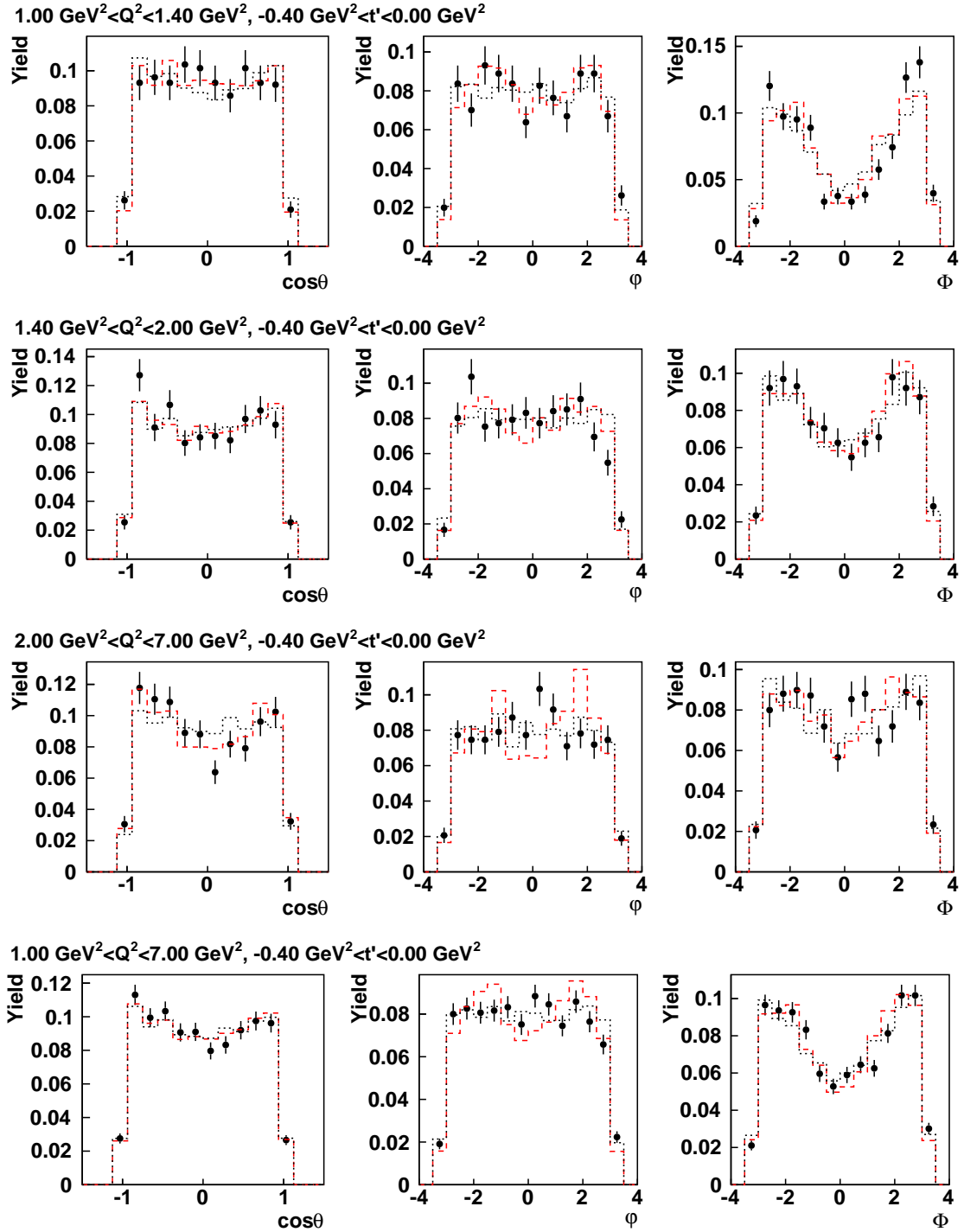


Figure 4.8: The angular distribution for hydrogen data of the periods 1998-2000, 2006-2007 (black points), the uniform Monte Carlo generated angular distribution used for p.d.f normalization in the fitting procedure (black dotted lines), Monte Carlo distributions reweighted with the corresponding SDME values (red dashed lines) for Q^2 bins and overall kinematics. All the distributions are normalized to unity.

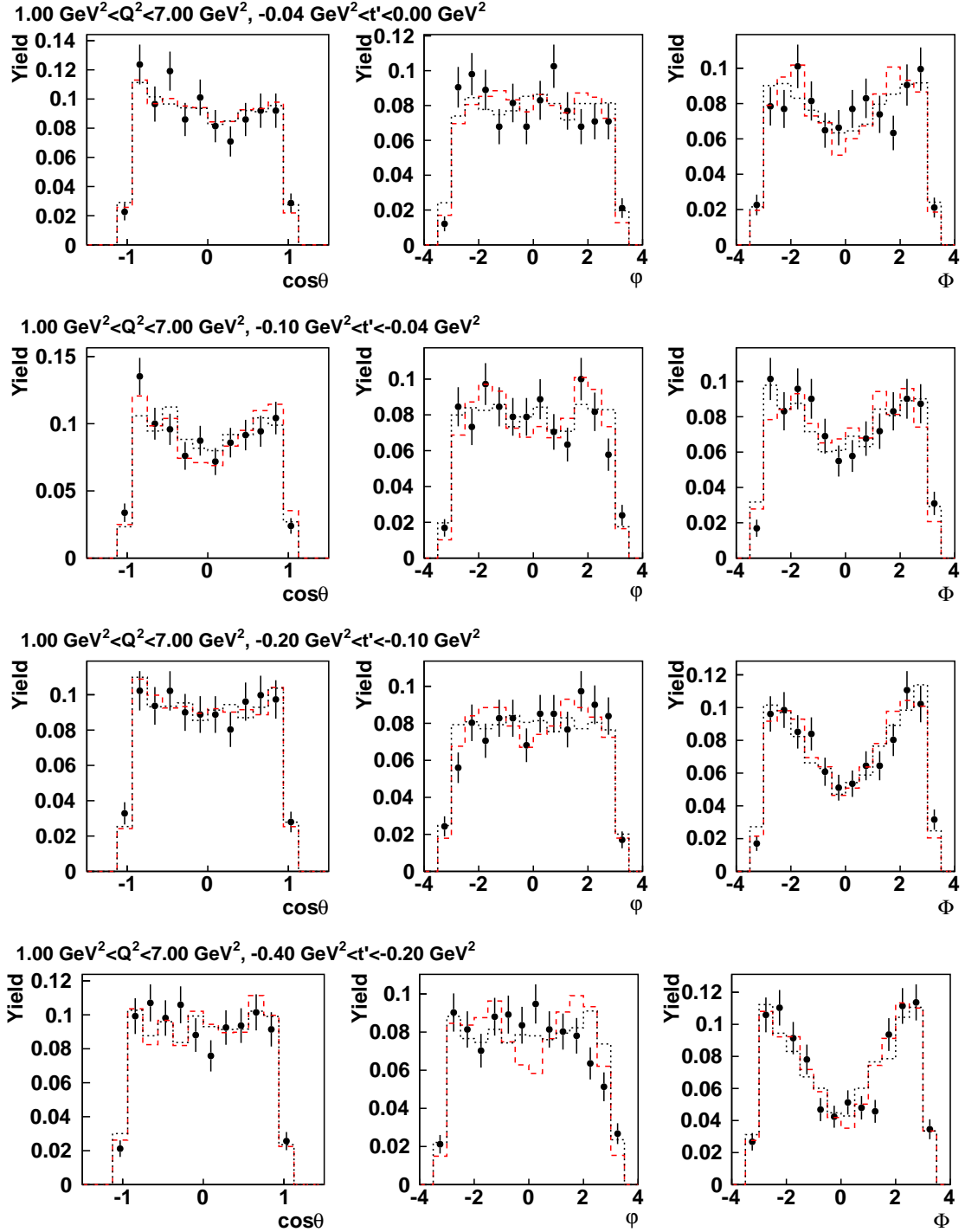


Figure 4.9: The angular distribution for hydrogen data of the periods 1998-2000, 2006-2007 (black points), the uniform Monte Carlo generated angular distribution used for p.d.f normalization in the fitting procedure (black dotted lines), Monte Carlo distributions reweighted with the corresponding SDME values (red dashed lines) for t' bins and overall kinematics. All the distributions are normalized to unity.

calculated for each particular data event individually using the beam polarization value for this event.

$$\ln L(\bar{\lambda}) = \sum_i \left[w_i \ln (W^{U+L}(\Phi_i, \phi_i, \cos\theta_i, P_i, \bar{\lambda})) - N_{ev} \ln \left(\sum_j (w_j (W^{U+L}(\Phi_j, \phi_j, \cos\theta_j, P_j))) \right) \right] \quad (4.17)$$

Figure 4.10 shows an agreement within half σ between the two methods for the hydrogen and deuteron data sets taken in the period 1998-2000, 2006-2007 years. In the present analysis the MLH with the beam-balancing weights was used.

4.2.2 Monte Carlo studies of the MLH fit stability

To check that the chosen method is correct and that the PYTHIA-generated Monte Carlo set used for p. d. f. normalization does not produce any bias in SDME measurement, the so called "zero-test" was performed. In this test instead of the data set, the parameters were extracted from a Monte Carlo set with uniform angular distribution, e.g. without angular dependences. To obtain such a distribution, all SDMEs have to be set on 0 except from the first one. According to Equation 4.18, if $r_{00}^{04} = \frac{1}{3}$, then all the dependences are excluded from the angular distribution and $\int W d\Omega = 1$, e.g. the distribution is normalized.

$$\begin{aligned} W_{UU}(\cos\theta, \varphi, \Phi) &= \frac{3}{4\pi} \left(\cos^2\theta r_{00}^{04} + \frac{1}{2} \sin^2\theta (1 - r_{00}^{04}) \right) = \frac{1}{4\pi} \\ \frac{1}{3} &= \cos^2\theta \frac{1}{3} + \frac{1}{2} \sin^2\theta \left(1 - \frac{1}{3} \right) \\ \frac{1}{3} &= \frac{1}{3} (\cos^2\theta + \sin^2\theta) \end{aligned} \quad (4.18)$$

On Figure 4.11 the extracted Wolf-Schilling SDMEs from pseudo-data corresponding to the data taking period 1998-2000, 2006-2007 years are presented. All SDMEs except from the first one are equal to zero within 1-2 σ , showing no bias in the method of extraction and no artificial effects produced by the Monte Carlo sets.

A more precise test using a RhoMC-generated Monte Carlo set with non-zero SDMEs implemented in it as a pseudo-data, was also performed. The statistics for both pseudo-data and normalization sets was also large enough to check the fit procedure reliability without limited statistics effects. On Figure 4.12 the extracted Wolf-Schilling SDMEs from pseudo-data for hydrogen and deuteron targets are presented. The extracted values agree with the implemented ones within 1-2 σ , except from the SDME value of r_{00}^5 , which is unstable in all the systematics checks, listed in Section 4.3. Such an instability can be explained via radiative effects, whose

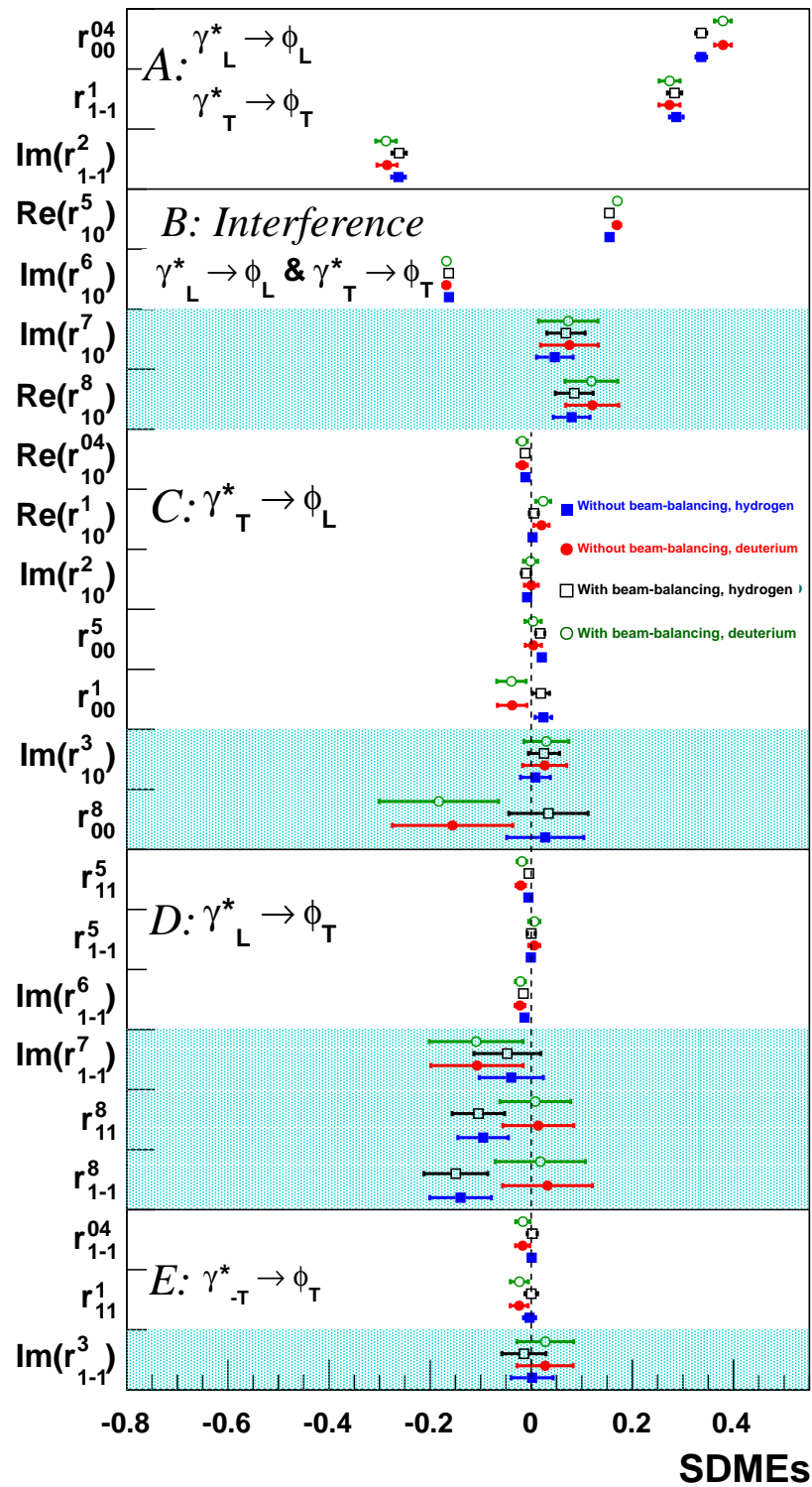


Figure 4.10: The comparison of the method with beam-balancing weights (open symbols) and without beam balancing weights (closed symbols) for hydrogen (squares) and deuteron (circles) for overall kinematics.

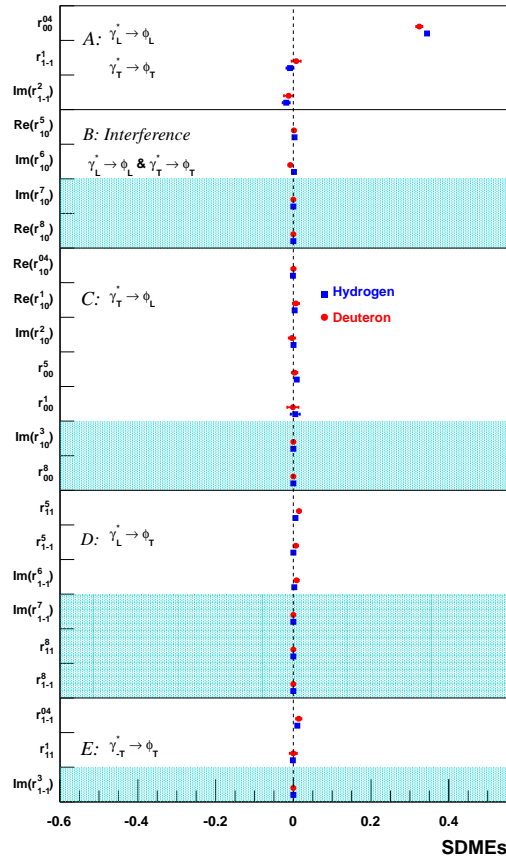


Figure 4.11: Parameters extracted from hydrogen and deuteron Monte Carlo sets corresponding to the data taking period 1998-2000, 2006-2007, for the overall kinematics. The angular distributions of the sets do not contain SDMEs, therefore the extracted parameters are to be zero except from the first one. The statistical uncertainties are not visible due to the large statistics used.

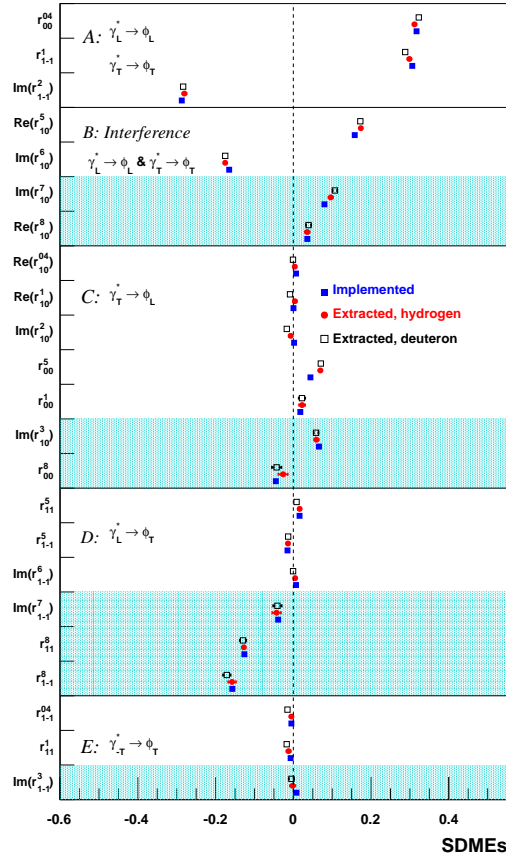


Figure 4.12: SDMEs extracted from hydrogen and deuteron Monte Carlo sets corresponding to the data taking period 1998-2000, 2006-2007, for the overall kinematics. Blue solid squares denote the implemented in pseudo-data SDME values, red circles designate the values extracted from hydrogen data set, black open squares are the values extracted from deuteron data set. The statistical uncertainties of the extracted values are almost invisible because of the large statistics used.

influence on SDME r_{00}^5 is stronger than on all the others (Section 2.15). The agreement between the other implemented and extracted SDME values shows the ability of the MLH fitting method to provide reliable SDMEs.

4.2.3 Cross-checks of the results

All the steps of the analysis, e.g. the event selection, SDME extraction, U_1, U_2, U_3 quantities calculation were cross checked, as required by the HERMES collaboration rules. For the cross check of the fitting procedure three independent programs were used. All of them provided almost identical results (differences are lower than 0.1%) in case of using the same input data, e.g. same event lists. For the cross check of the whole analysis, e.g. starting from the event selection, two independent implementations were used. The discrepancy of the event numbers was up to 2%, resulting in approximately 5% differences in the final SDME values. This can be explained by the low statistics for the ϕ meson, which makes the fit very sensible even to

the differences in the event lists of the order of a few percents. The U_1, U_2, U_3 quantities also showed differences up to 5%.

4.2.4 Extracted SDMEs and U_1, U_2, U_3 values.

The measured SDMEs in Wolf-Schilling notation for 1998 – 2000 and 2006 – 2007 unified data sets, for hydrogen and deuteron targets are presented in Figure 4.13. The extraction was done in 3 Q^2 and 4 t' bins described above (Table 4.4), the same as for the overall kinematic range. SDMEs are divided into 5 classes according to the helicity transition type. The vertical dashed line denotes SCHC. The same results in Markus Diehl notation are presented in Figure 4.14. They are divided into three main classes, which represent spin conserving transitions, spin-flip transitions and double flip transitions correspondingly.

Only statistical uncertainties are plotted. SDMEs involving the beam polarization are shown in shadowed areas. The statistical uncertainties of polarized SDMEs are larger, since they have an additional multiplication factor (see Formulas 2.62, 2.71, 2.72, 2.73) in the angular distribution, e.g. the beam polarization, which has an average value 0.35.

As was mentioned above (see Section 2), SDMEs from Wolf-Schilling and Markus Diehl notations are connected via relations listed in Appendix A. In Figure 4.15 Markus Diehl SDMEs for hydrogen and deuteron targets for overall kinematics extracted using MLH method are compared to SDMEs recalculated from Wolf-Schilling ones. The equality of SDMEs obtained via two different ways excludes the possibility that MLH fit got stuck to a local minimum in only one of the two cases.

4.2.5 Compatibility of hydrogen and deuteron results.

Vector meson SDMEs are expected to be similar for hydrogen and deuteron data, since after exclusion of coherent deuteron data both hydrogen and deuteron targets are 3-quark systems from the point of view of gluon, mediating the exchange between γ and nucleon. For both deuteron and hydrogen targets at HERMES level of energies the process is dominated by gluonic GPDs. To check if the results are compatible, a χ^2 test for the two independent sets of results (e.g. different targets) was fulfilled in each kinematic bin. The obtained χ^2 values are shown in Table 4.5; all of them (except from the first two Q^2 bins) are less than one, indicating an agreements between the SDMEs for the two targets.

As an additional statistical check, the deviations between proton and incoherent deuteron results were calculated as

$$d_i = \frac{SDME_1^i - SDME_2^i}{\sqrt{\sigma_{1,i}^2 + \sigma_{2,i}^2}} \quad (4.19)$$

for each SDME in each kinematic bin. From figures 4.21 - 4.25, where the deviations are plotted,

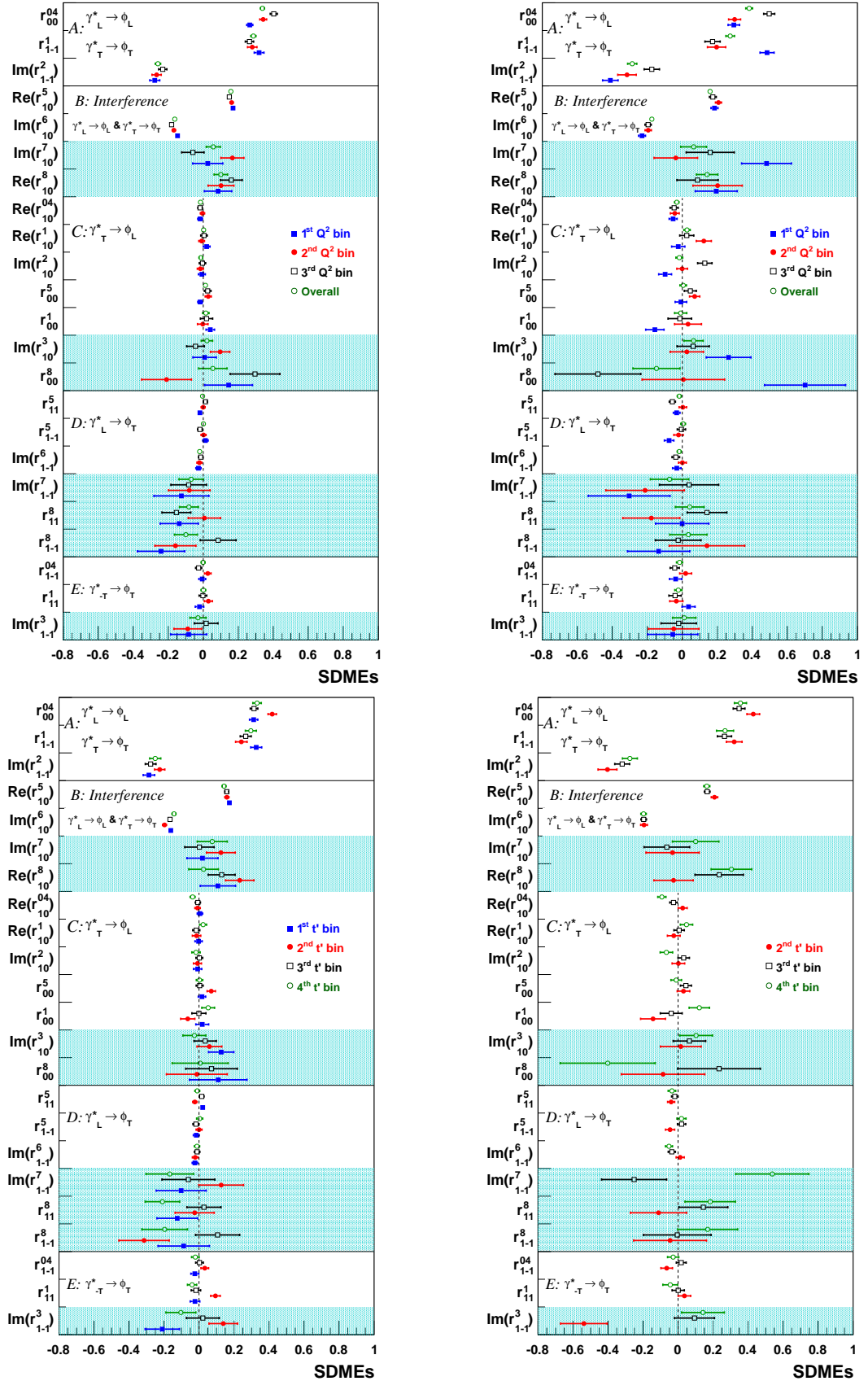


Figure 4.13: SDMEs in Wolf-Schilling representation extracted from hydrogen (left side figures) and deuterium (right side figures) data sets of 1998 – 2000, 2006 – 2007 years in Q^2 (top figures) and t' (bottom figures) kinematic bins.

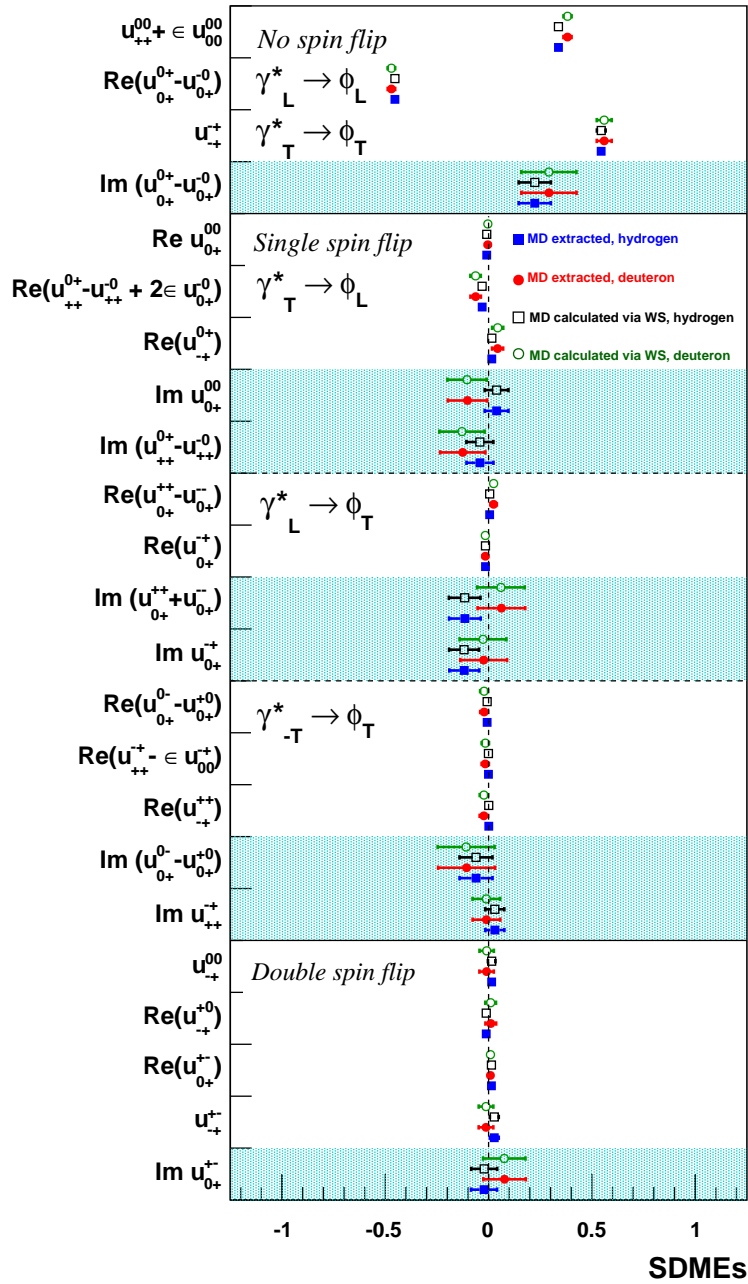


Figure 4.15: SDMEs in Markus Diehl representation extracted from hydrogen (squares) and deuteron (circles) data are shown as solid symbols. Those calculated (open symbols) from SDMEs in Wolf-Schilling representation are represented as open symbols. The results are obtained for the data set with overall kinematics.

one can conclude that 10 deviation values out of 161 (4 bins in t' * 23 SDMEs + 3 bins in Q^2 * 23 SDMEs=161 points) are larger than 2σ . The 10 points correspond to 6.2% from the total amount of 161 points and are statistically allowed percentage of the difference, proving compatibility of SDMEs for hydrogen and deuteron targets.

Kinematic bin	χ^2
$1 \text{ GeV}^2 < Q^2 < 1.4 \text{ GeV}^2$	2.39
$1.4 \text{ GeV}^2 < Q^2 < 2 \text{ GeV}^2$	2.1
$2 \text{ GeV}^2 < Q^2 < 7 \text{ GeV}^2$	0.58
$0 < \text{GeV}^2 - t' < 0.04 \text{ GeV}^2$	0.40
$0.04 \text{ GeV}^2 < -t' < 0.1 \text{ GeV}^2$	1.16
$0.1 \text{ GeV}^2 < -t' < 0.2 \text{ GeV}^2$	0.17
$0.2 \text{ GeV}^2 < -t' < 0.4 \text{ GeV}^2$	0.50
overall	0.05

Table 4.5: Values of χ^2 characterizing compatibility of the hydrogen and deuteron data sets in each kinematic bin. The first t' bin is added in the comparison for the completeness, although it is excluded from deuteron Q^2 bins.

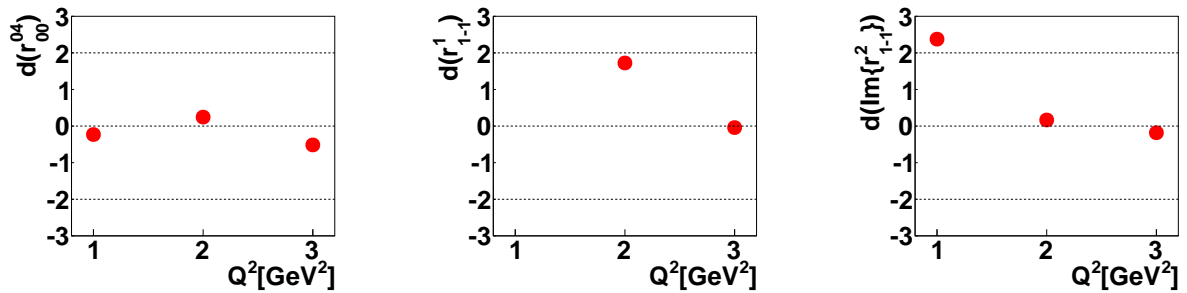


Figure 4.16: The proton to deuteron deviations of ϕ SDMEs from class A on Q^2 .

4.3 Systematics

Each of the sources of systematic uncertainty can create a bias in the measurement. The systematic uncertainty sources, relevant to this analysis, are imperfect calibration or operation of measurement instruments (in the context of this analysis these are uncertainties due to the beam misalignment and smearing of the detector measurements), changes in the environment which interfere with the measured process (in terms of this analysis - background contamination) and imperfect methods of calculation (in terms of this analysis - uncertainty of unbinned MLH and the model of Monte Carlo generator producing the p. d. f. normalization sample). The uncertainties due to the beam misalignment, detector smearing and uncertainty of the unbinned MLH method are estimated via so-called “all-in-one procedure”, described in Section 4.3.1. The SDME systematic error due to the imperfectness of the physical model used for event generation of the Monte Carlo set is described in Section 4.3.2 and was evaluated by using the two different generators described above (Section 4.1.7). The uncertainty due to the semi-

inclusive background subtraction is described in Section 4.3.3.

4.3.1 All-in-one procedure

As was mentioned above (Section 4.2.2), the method of SDME extraction can be checked by using so-called pseudo-data instead of the real data. Pseudo-data is a RhoMC generated Monte Carlo set, whose angular distributions contain known SDMEs, implemented via event weights. The pseudo-data set included the smearing effects of the detector and the misaligned beam position, therefore the extracted SDMEs allow one to check the effect of these systematic sources together with the uncertainty coming from the method of extraction.

As a first check, SDMEs were extracted from the set with the huge statistics to verify only the method itself without possible influence from statistical fluctuations (see Section 4.2.2). However, the limited statistics, being the case for the ϕ meson, can affect the results strongly. In order to check this, the pseudo-data set for each of the kinematic bins was divided into 50 sets with the statistics, comparable to that of the real data. The resulting uncertainty for each SDME in each kinematic bin was obtained as a maximum of two values: the first one is the squared average difference between extracted and implemented values, e.g.:

$$\Delta^2 = \frac{(s_1 - s)^2 + (s_2 - s)^2 + \dots + (s_N - s)^2}{N} \quad (4.20)$$

where s is an implemented SDME value, s_1 is the extracted value in a certain kinematic bin in one of 50 test sets, N is the number of test sets. The second one is the squared average statistical uncertainty, calculated as

$$\delta^2 = \frac{\delta_{s_1}^2 + \delta_{s_2}^2 + \dots + \delta_{s_{50}}^2}{N}. \quad (4.21)$$

For the most part of SDMEs in the kinematic bins the value calculated via the deviations from the true value turned out to be larger than the one calculated via systematic uncertainty, therefore the final SDME uncertainty was calculated according to the Equation 4.20. Differences between implemented and extracted values for each SDME in each kinematic bin for the first 20 test samples are plotted in [59] for Wolf-Schilling SDMEs and in [60] for Markus Diehl SDMEs.

For the uncertainty calculation of U_1 , U_2 , U_3 quantities was used the same way as for SDME ones. In Figures 4.26 - 4.28 the averaged squared deviations of U_1 , U_2 , U_3 quantities for the first 20 test sets in each kinematic bin are shown. They are typically larger than the systematic uncertainties of the corresponding values. The value of the resulting systematic uncertainty for SDMEs is of the order of 10^{-3} .

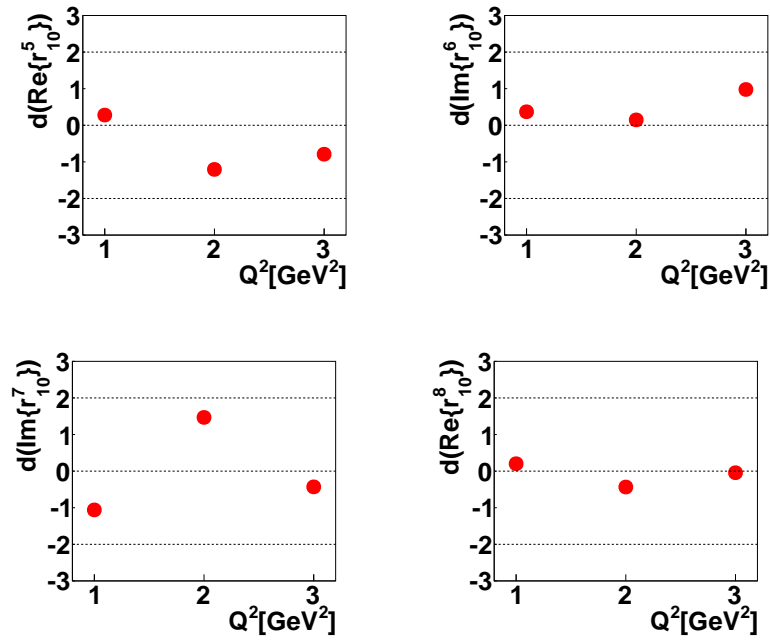


Figure 4.17: The proton to deuteron deviations of ϕ SDMEs from class B on Q^2 .

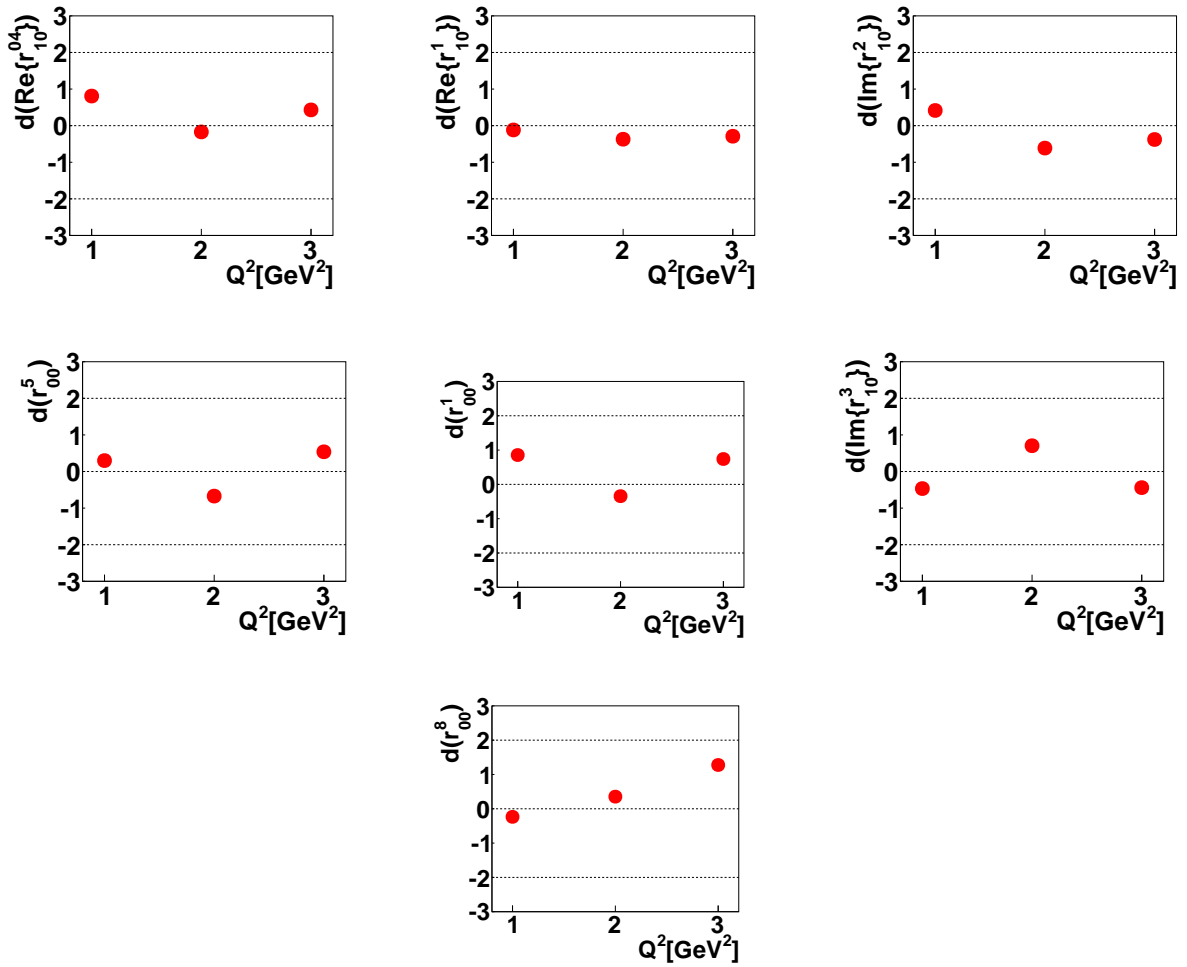


Figure 4.18: The proton to deuteron deviations of ϕ SDMEs from class C on Q^2 .

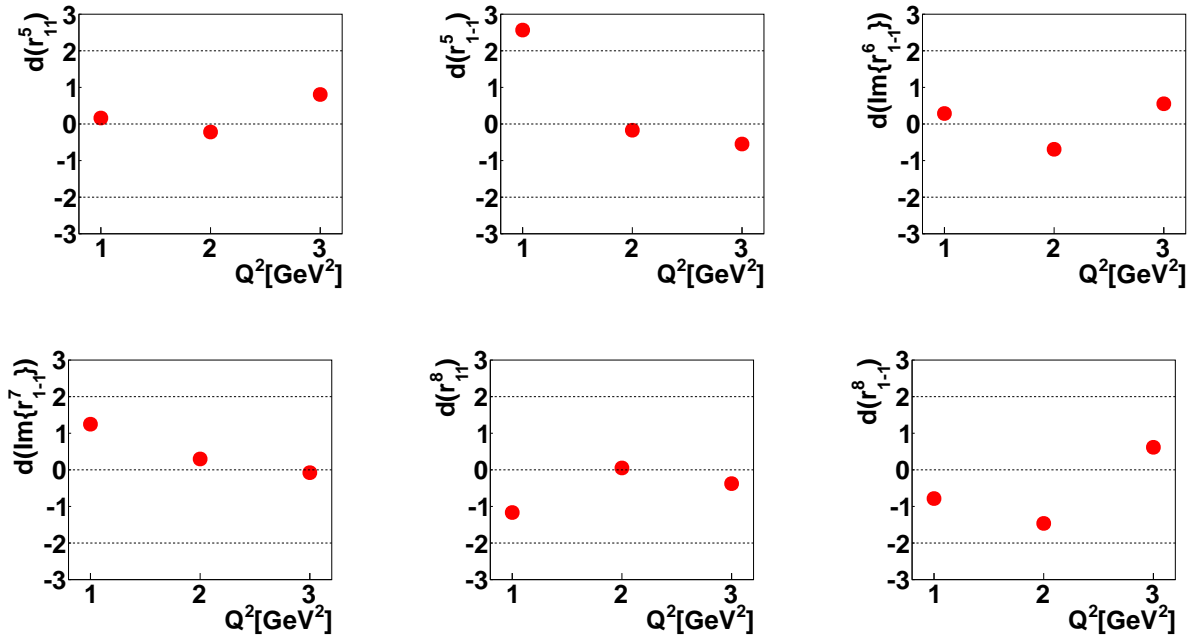


Figure 4.19: The proton to deuteron deviations of ϕ SDMEs from class D on Q^2 .

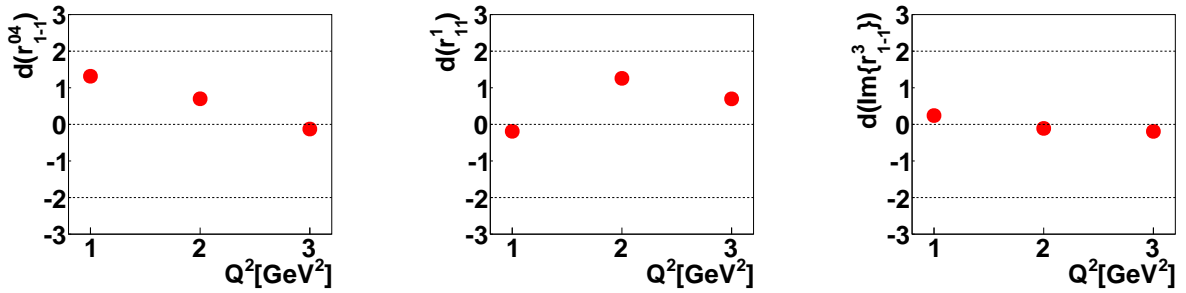


Figure 4.20: The proton to deuteron deviations of ϕ SDMEs from class E on Q^2 .

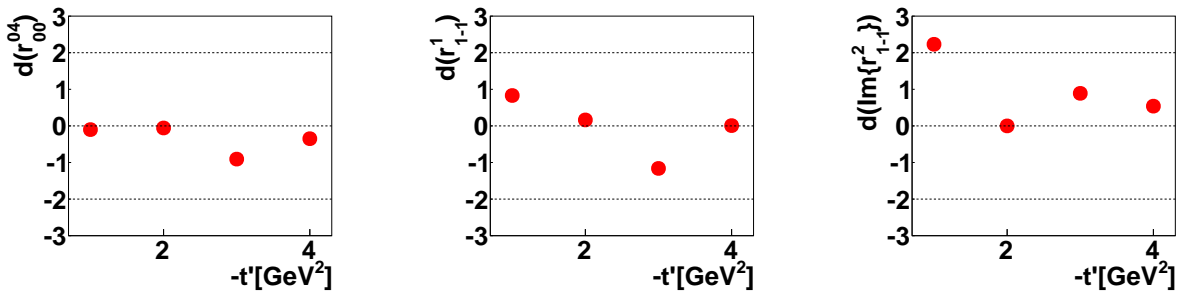


Figure 4.21: The proton to deuteron deviations of ϕ SDMEs from class A on $-t'$.

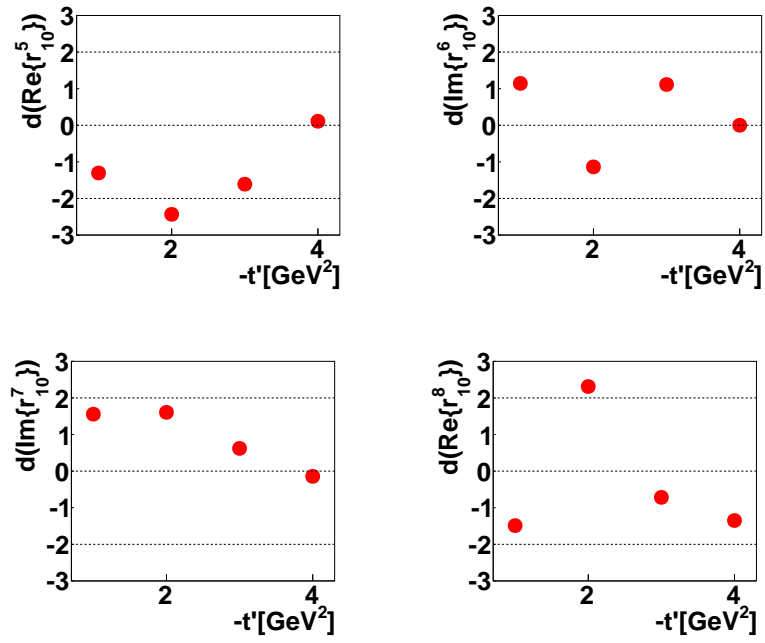


Figure 4.22: The proton to deuteron deviations of ϕ SDMEs from class B on $-t'$.

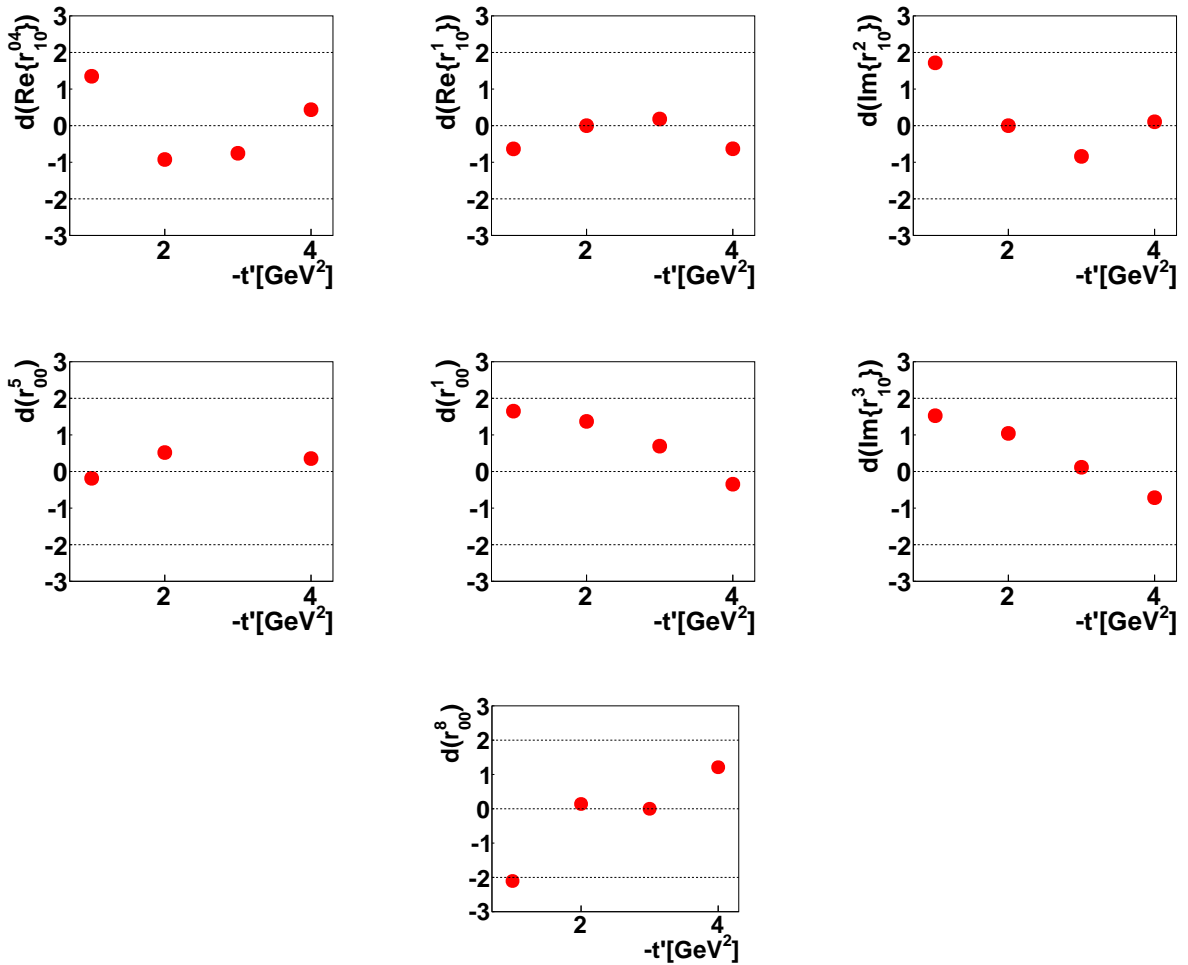


Figure 4.23: The proton to deuteron deviations of ϕ SDMEs from class C on $-t'$.

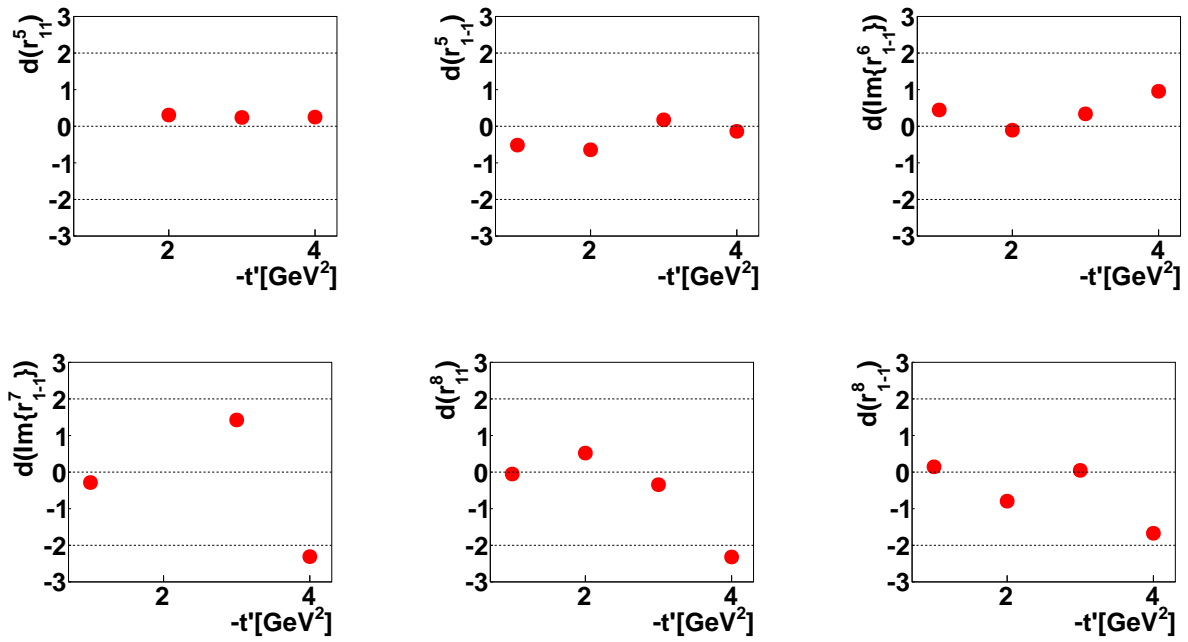


Figure 4.24: The proton to deuteron deviations of ϕ SDMEs from class D on $-t'$.

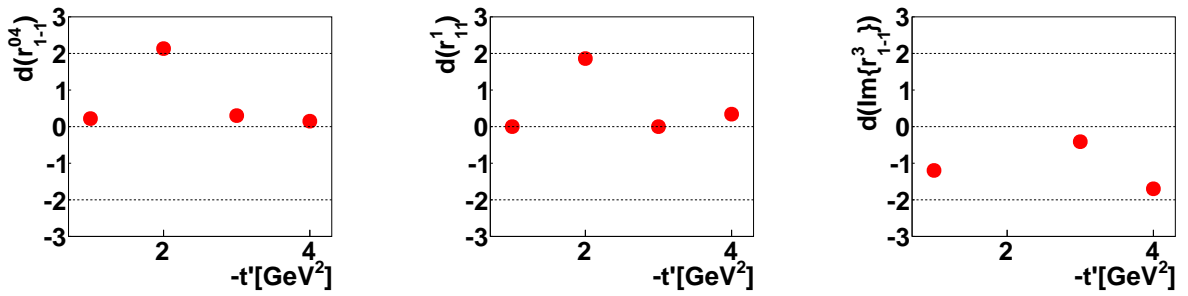


Figure 4.25: The proton to deuteron deviations of ϕ SDMEs from class E on $-t'$.

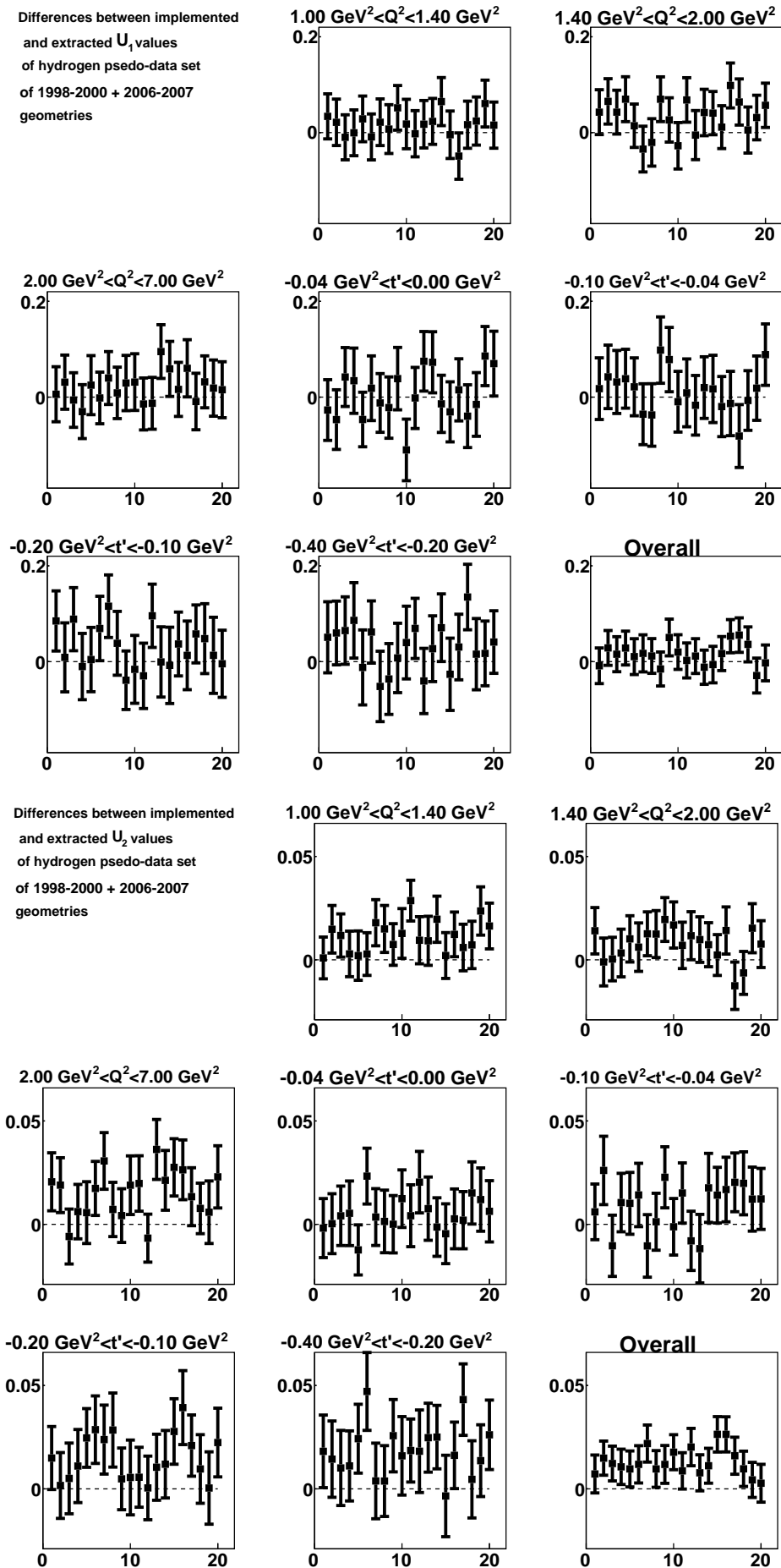


Figure 4.26: The differences between implemented and extracted U_1, U_2 , for hydrogen

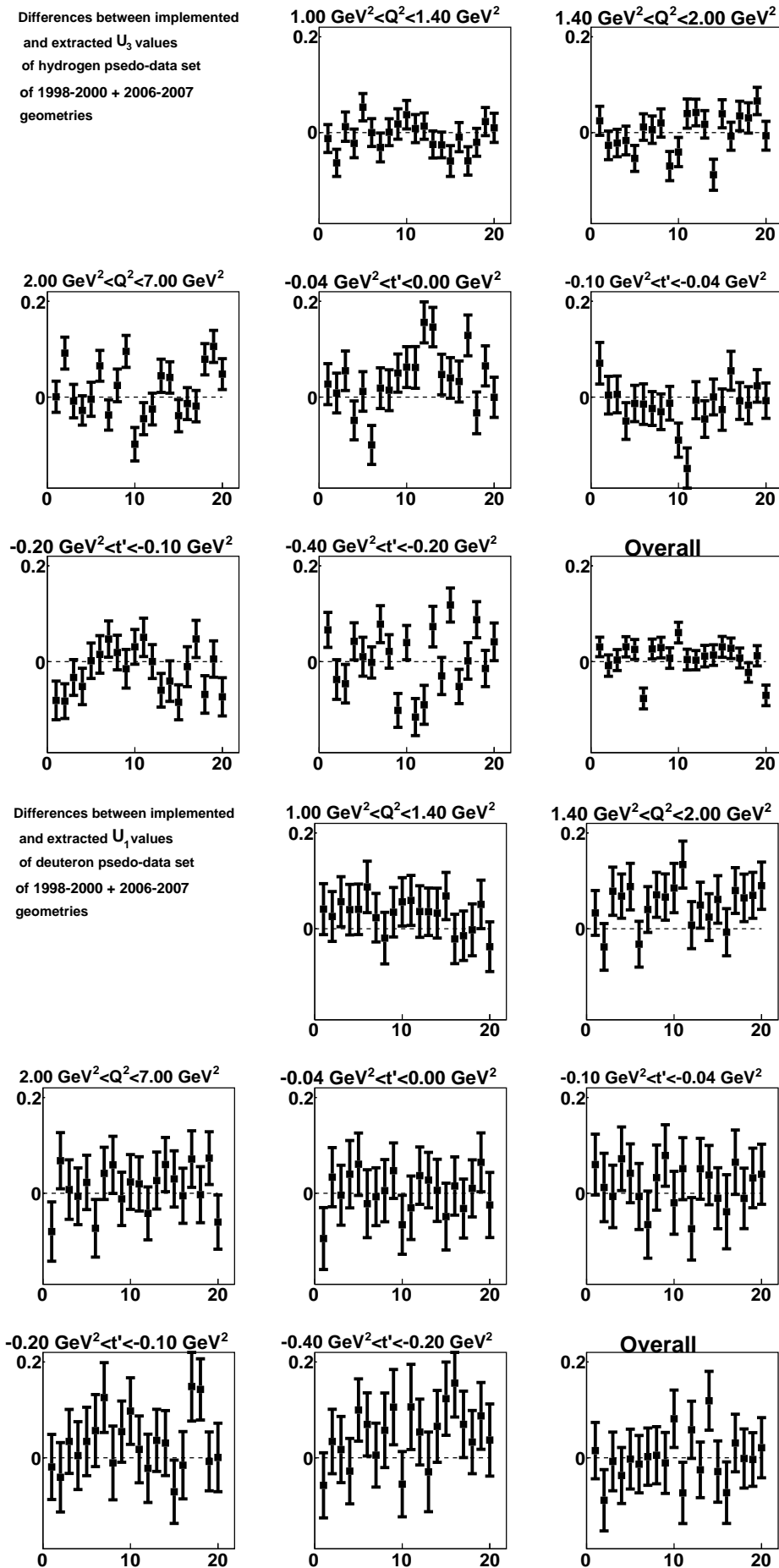


Figure 4.27: The differences between implemented and extracted U_3 for hydrogen and U_1 for deuteron

4.3.2 Different Monte Carlo models

Monte Carlo set used for p.d.f normalization might affect the results. As was mentioned in Section 4.1.7, the two generators suitable for ϕ meson production contain different cross section models, different ways of implementing the Q^2 and t' cross section dependencies. As the HERMES spectrometer acceptance depends on Q^2 , different cross section Q^2 -dependence models result in slightly different reconstructed angular distributions and consequently differences in SDME values. The uncertainty due to the Monte Carlo model was estimated as the difference between SDMEs obtained using PYTHIA generated set and RhoMC generated set for the p.d.f normalization, e.g. the difference between each two sets of the same symbols in Figure 4.29, where the results for overall kinematics are presented. For all the kinematic bins the results can be found in Appendix E. The uncertainty varies from 10^{-3} up to 10^{-1} , the largest uncertainties are observed for the 1st Q^2 bin of the deuteron data.

As was mentioned in Section 4.1.7, RhoMC does not include radiative corrections for the kinematics, therefore the difference between SDMEs extracted using Pythia and using RhoMC reflects also radiative effects, which are negligible for most SDMEs according to [61].

4.3.3 Background subtraction

A sample of semi-inclusive events generated by PYTHIA Monte Carlo was used to subtract the semi-inclusive background from the exclusive channel. The procedure of extraction implies that first the background sample is used as pseudo data, e.g. the parameters, which represent SDMEs for the background but have no physical meaning, are extracted from it. Then the MLH function is modified to extract the data SDMEs $\bar{\lambda}$ using the known values of the background parameters $\bar{\alpha}$ and the probability of each event to be an exclusive one $\frac{N_\phi}{N_{total}}$ or a background one $\frac{N_{BKG}}{N_{total}}$:

$$\ln(L(\bar{\lambda})) = \sum_{i=1}^N \ln \left[\frac{N_\phi}{N_{tot}} * \frac{W(\phi_i, \theta_i, \Phi_i, P_i, \bar{\lambda})}{N(\bar{\lambda})} + \frac{N_{BKG}}{N_{tot}} * \frac{W(\phi_i, \theta_i, \Phi_i, P_i, \bar{\alpha})}{N(\bar{\alpha})} \right] \quad (4.22)$$

For both normalization parts in the formula above the exclusive PYTHIA sample is used, the first fraction contains unknown background-subtracted data SDMEs, the second one contains known background parameters.

The Table 4.6 shows the background fractions in different kinematic bins. They were obtained as ratios of the missing energy distributions for the data to those of PYTHIA-simulated background in each Q^2 and t' kinematic bin, e.g. ratios of the yields of the magenta histograms to that of black histograms on Figure 4.2. The ratios were calculated in the exclusive region: $\Delta E < 0.6$ GeV.

The systematic uncertainty due to the subtraction procedure was estimated as the difference

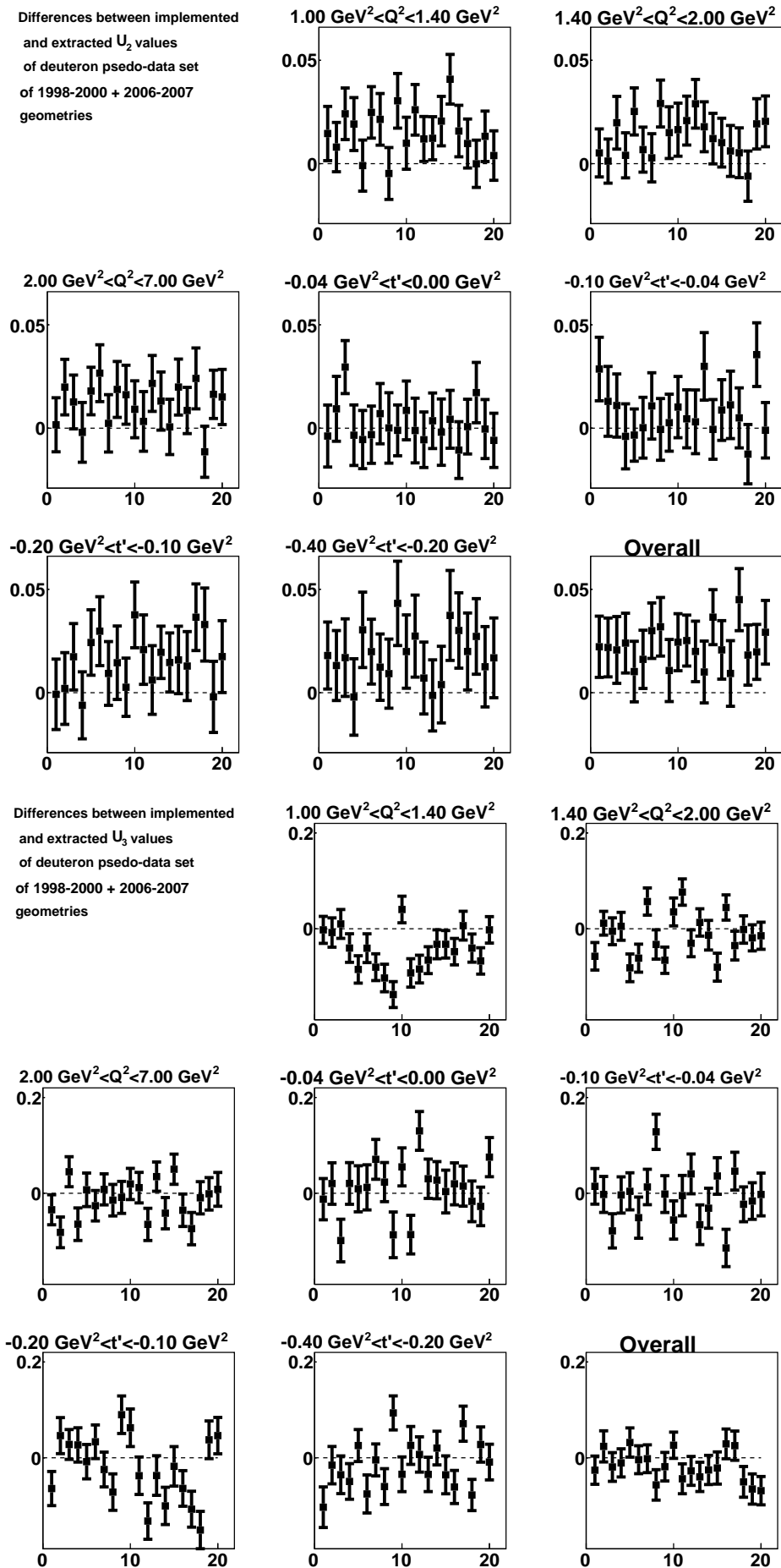


Figure 4.28: The differences between implemented and extracted U_2 and U_3 for deuteron

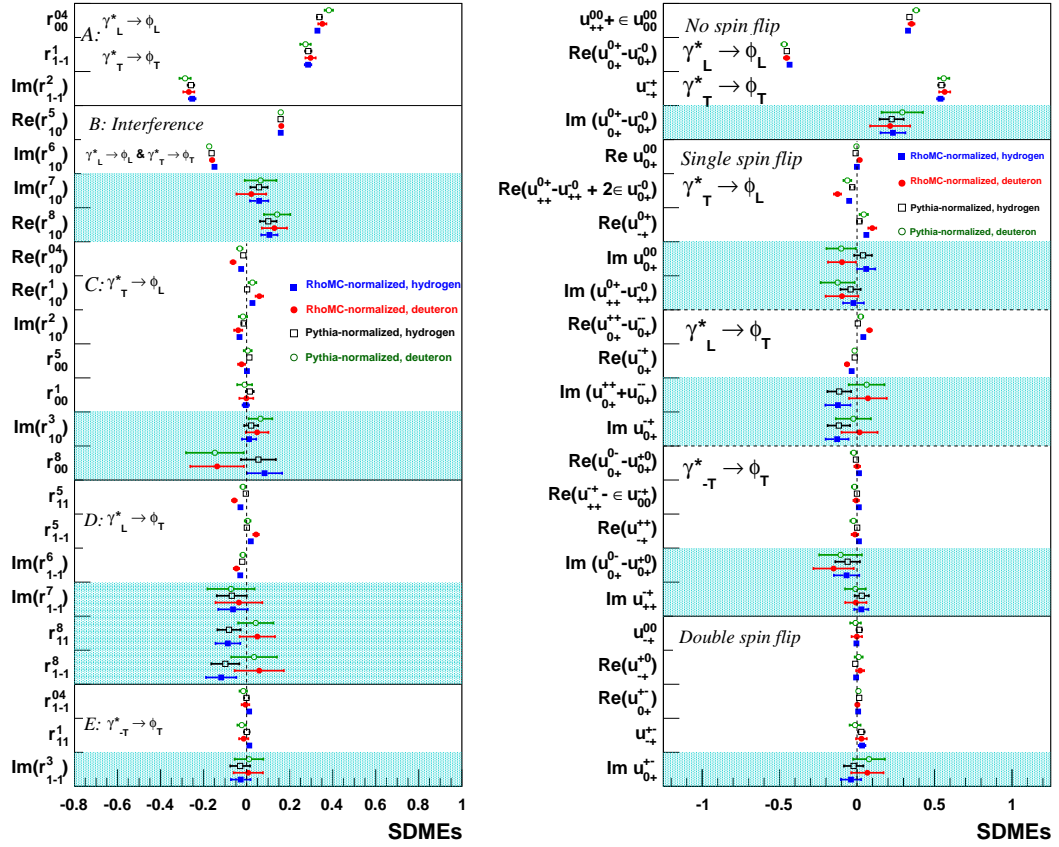


Figure 4.29: Wolf Schilling SDMEs (left figure) and Markus Diehl SDMEs (right figure) extracted using Pythia (open symbols), RhoMC (solid symbols) for the p.d.f. normalization for overall kinematics.

Kinematic bin	Background fraction
$1 \text{ GeV}^2 < Q^2 < 1.4 \text{ GeV}^2$	2.99%
$1.4 \text{ GeV}^2 < Q^2 < 2 \text{ GeV}^2$	2.78%
$2 \text{ GeV}^2 < Q^2 < 7 \text{ GeV}^2$	2.38%
$0 \text{ GeV}^2 < -t' < 0.04 \text{ GeV}^2$	0.38%
$0.04 \text{ GeV}^2 < -t' < 0.1 \text{ GeV}^2$	3.01%
$0.1 \text{ GeV}^2 < -t' < 0.2 \text{ GeV}^2$	2.54%
$0.2 \text{ GeV}^2 < -t' < 0.4 \text{ GeV}^2$	2.90%
$1 \text{ GeV}^2 < Q^2 < 1.4 \text{ GeV}^2, 0.04 \text{ GeV}^2 < -t' < 0.4 \text{ GeV}^2$	3.14%
$1.4 \text{ GeV}^2 < Q^2 < 2 \text{ GeV}^2, 0.04 \text{ GeV}^2 < -t' < 0.4 \text{ GeV}^2$	3.04%
$2 \text{ GeV}^2 < Q^2 < 7 \text{ GeV}^2, 0.04 \text{ GeV}^2 < -t' < 0.4 \text{ GeV}^2$	2.63%

Table 4.6: The background fraction in each bin

between SDMEs obtained with and without background subtraction, e.g. the difference between each two sets of the same shape symbols in Figure 4.30, where results for the overall kinematics

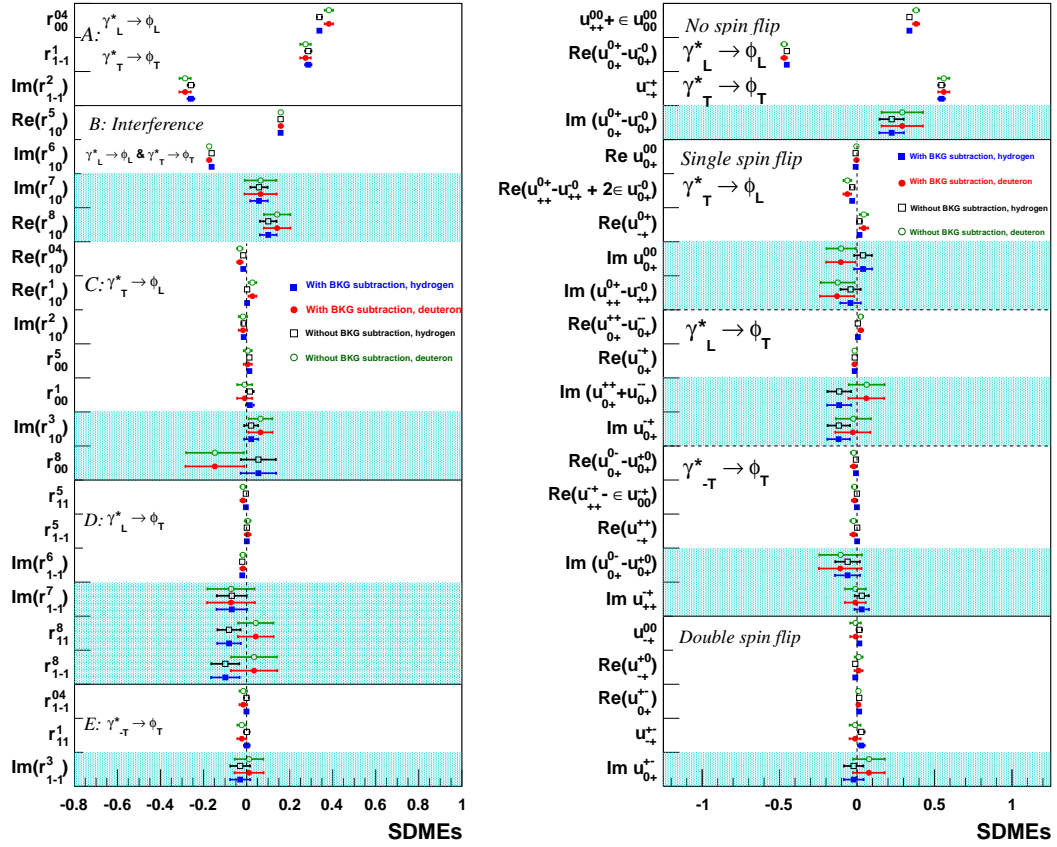


Figure 4.30: Background subtracted (solid symbols) and not-subtracted (open symbols) SDMEs in Wolf-Schilling notation (left figure) and Markus Diehl notation (right figure) for overall kinematics.

are shown. The results for each of the kinematic bins can be found in Appendix D. The resulting uncertainty due to the background subtraction is of the order of 10^{-3} .

4.3.4 Contribution of each source of the uncertainty to the total systematic uncertainty.

In Figures 4.31 - 4.40 the contribution of each systematic source is shown for each SDME in bars for overall kinematics. Uncertainties are shown as blocks, put on each other, e.g. they do not overlay. As can be concluded from the plots, the smallest contribution comes from the uncertainty due to the background subtraction procedure, since the SIDIS background in the exclusive region does not exceed 3.2%. For some SDMEs, namely $\Im m r_{1-1}^7$ in the bins of Q^2 for hydrogen data, SDMEs r_{00}^1 and $\Im m r_{10}^6$ in the 1st Q^2 bin for hydrogen and deuteron data, the uncertainty due to the all-in-one-procedure prevails over all the other sources. For most of SDMEs, however, the uncertainty due to the different Monte Carlo model of p. d. f. normalization set gives the largest contribution.

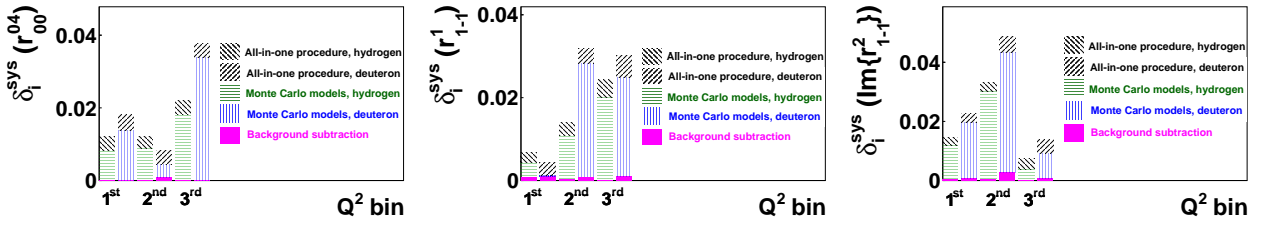


Figure 4.31: Contribution to the systematic uncertainties of the class A SDMEs in the various Q^2 bins for both hydrogen and deuteron.

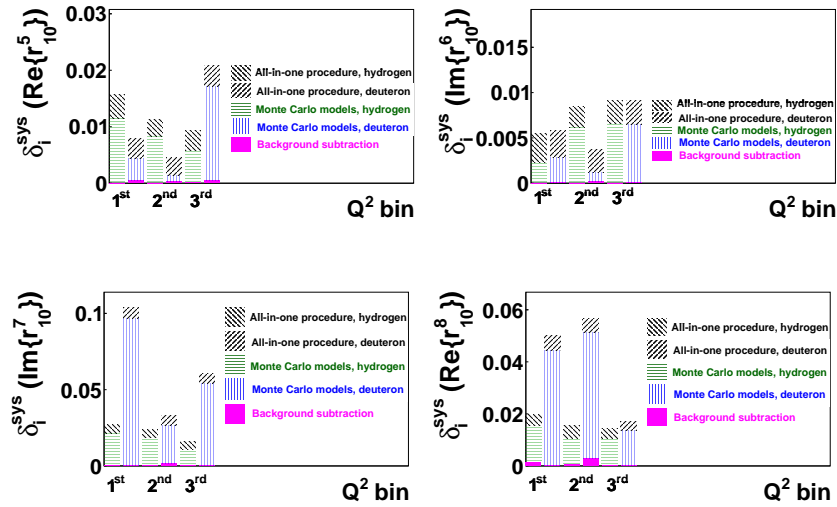


Figure 4.32: As in Figure 4.31, but for class B SDMEs.

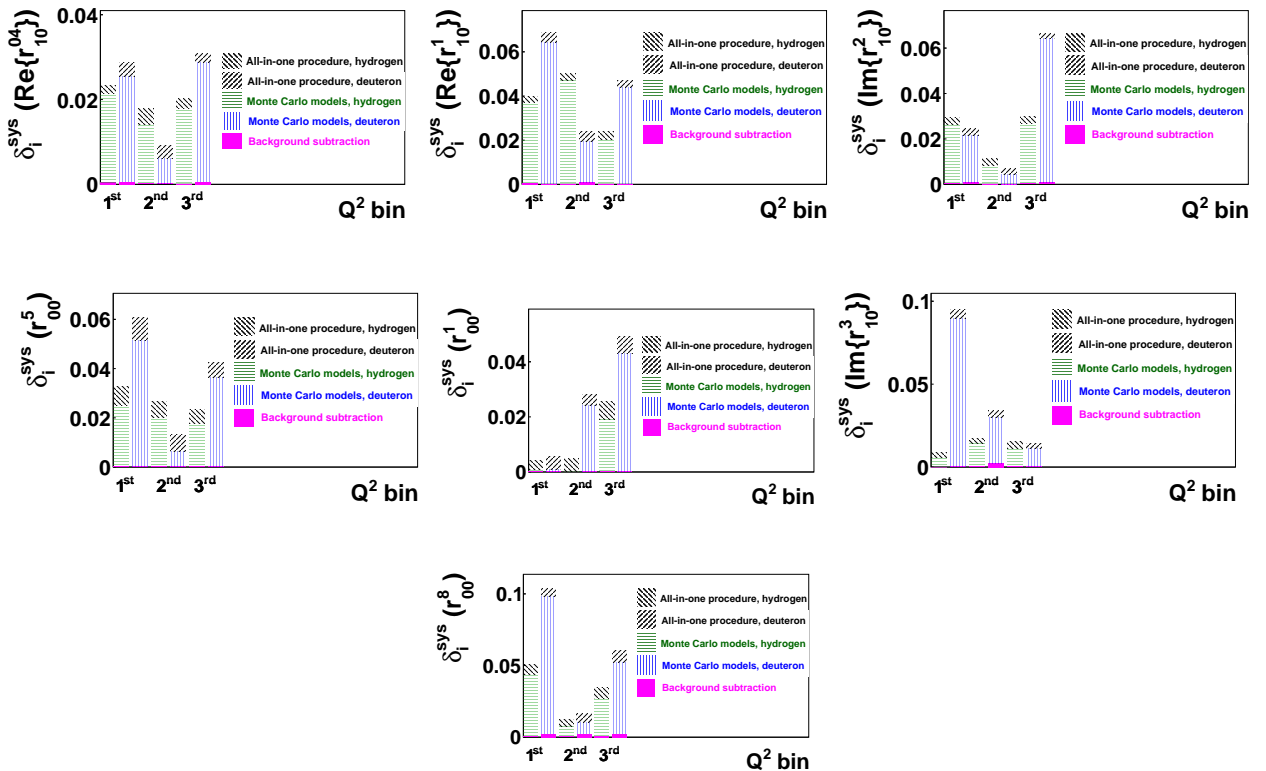


Figure 4.33: As in Figure 4.31, but for class C SDMEs.

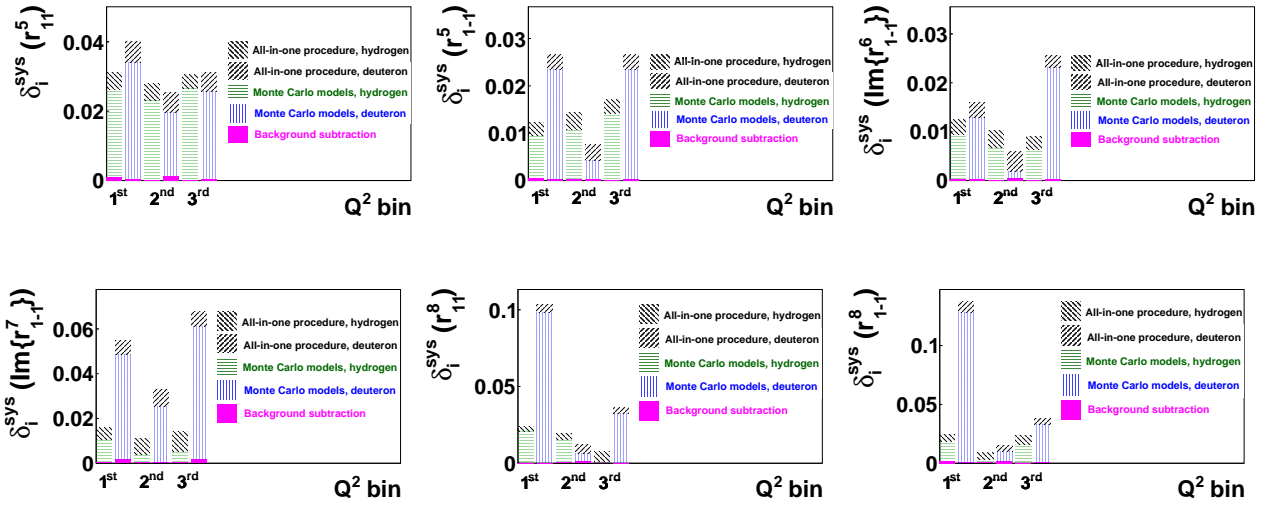


Figure 4.34: As in Figure 4.31, but for class D SDMEs.

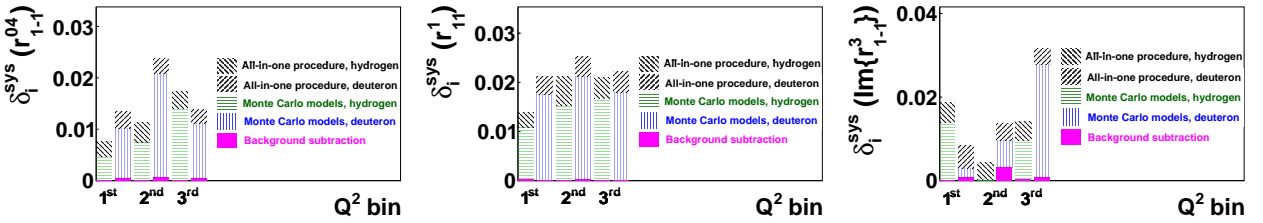


Figure 4.35: As in Figure 4.31, but for class E SDMEs.

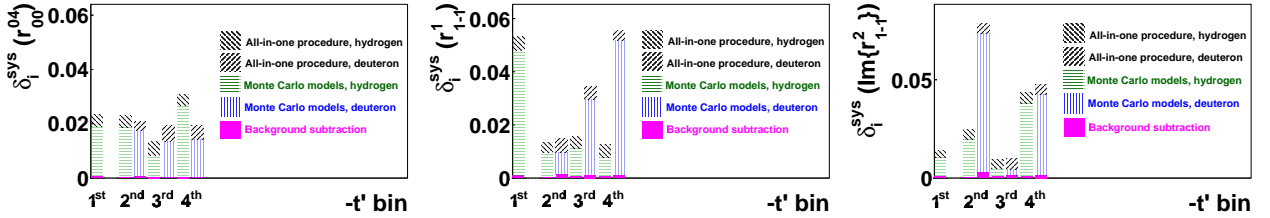


Figure 4.36:

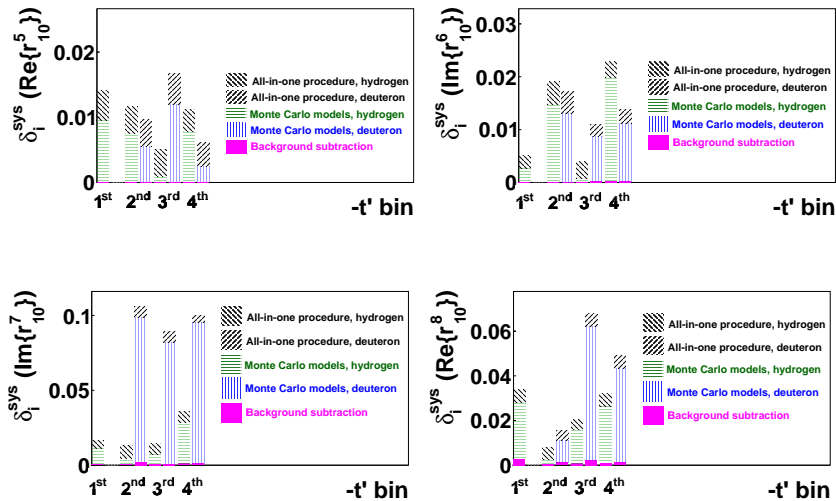


Figure 4.37: As in Figure 4.31, but in bins of t' .

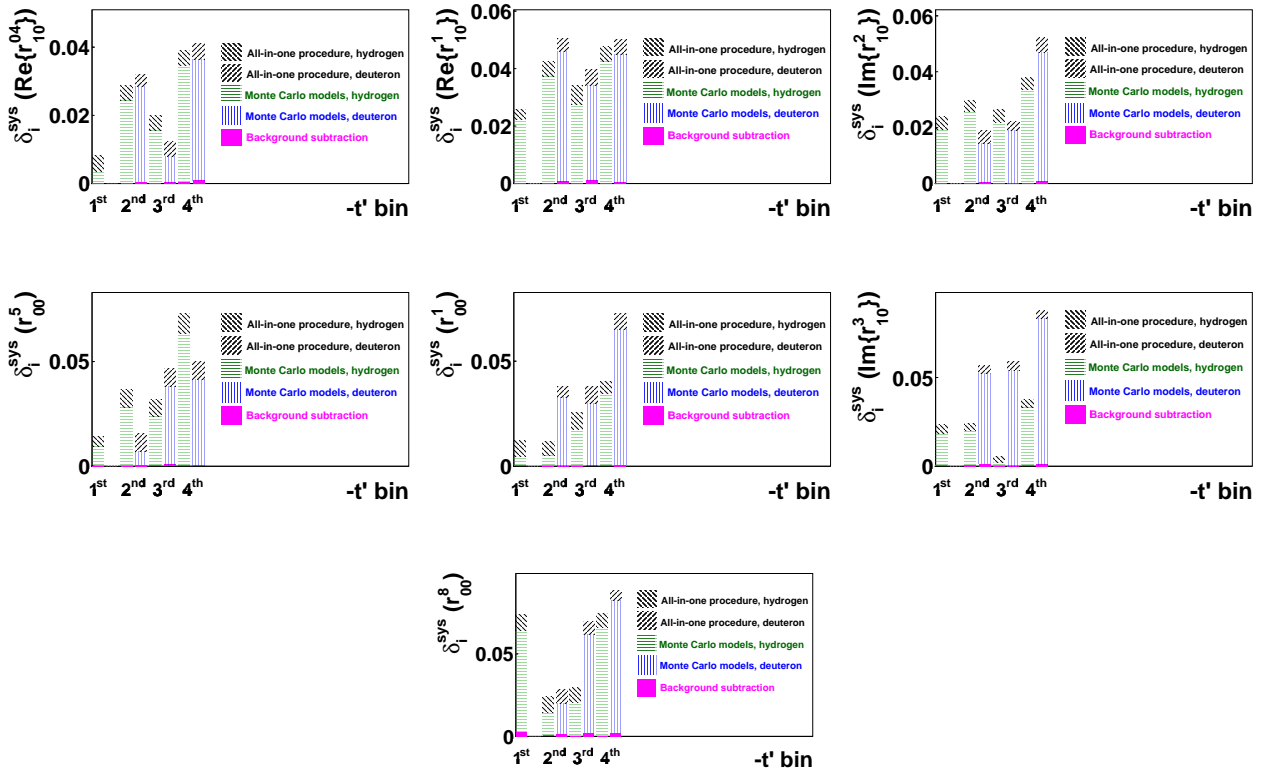


Figure 4.38: As in Figure 4.33, but in bins of t' .

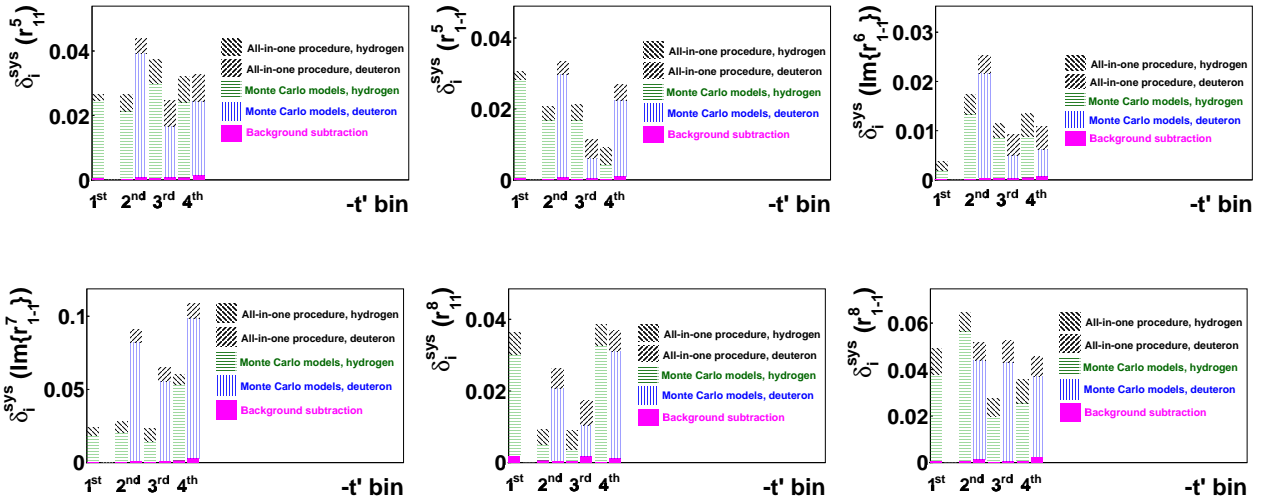


Figure 4.39: As in Figure 4.34, but in bins of t' .

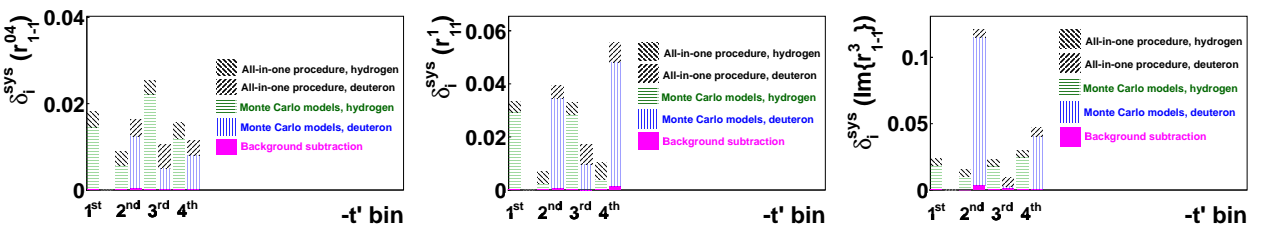


Figure 4.40: As in Figure 4.35, but in bins of t' .

4.3.5 Total systematic uncertainty

The total systematic uncertainty was obtained as the square root of the sum of individual squared systematic uncertainties. In Figures 4.41 - 4.50 the ratio of systematic to statistical uncertainty for Wolf-Schilling SDMEs is shown. Since polarized SDMEs have larger statistical uncertainties (the reason is given in Section 4.2.4), the ratio is around 0.1-0.3 for the most of them. For unpolarized SDMEs the ratio varies from 0.6-0.8 up to 1.2-1.5, e.g. statistical and systematic uncertainties have comparable values. The largest ratios (around 2) are observed for SDMEs r_{11}^5 , $\Re r_{10}^1$, r_{00}^5 , whose values varied strongly in all the systematic studies, listed above.

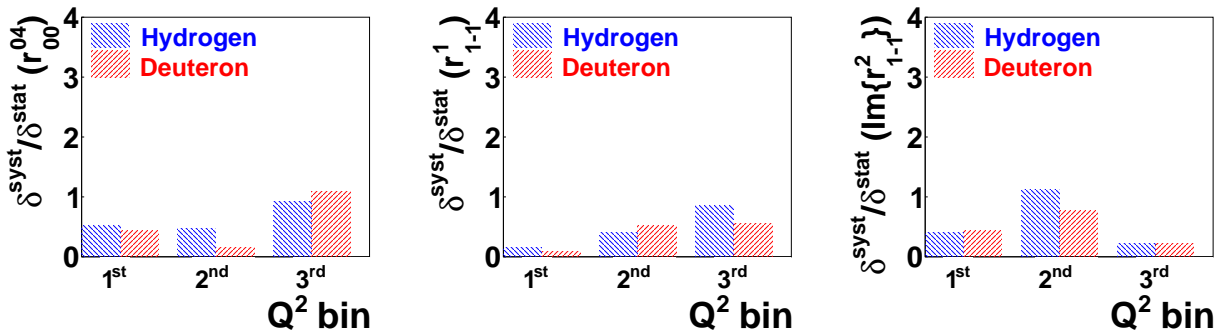


Figure 4.41: The ratios of systematic to statistical uncertainties for hydrogen (blue) and deuteron (red) of ϕ SDMEs from class A, Q^2 dependence.

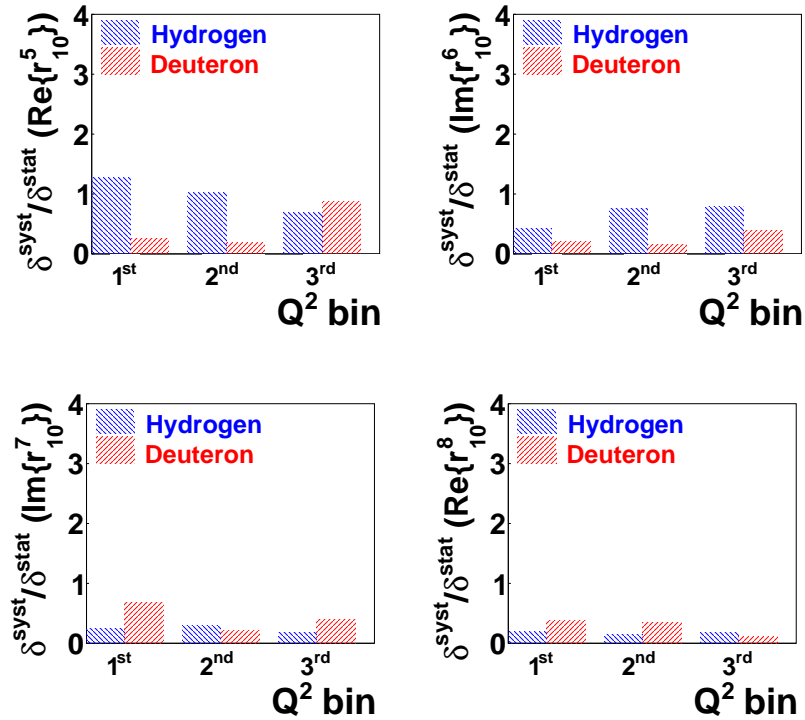


Figure 4.42: As in Figure 4.41 but for class B.

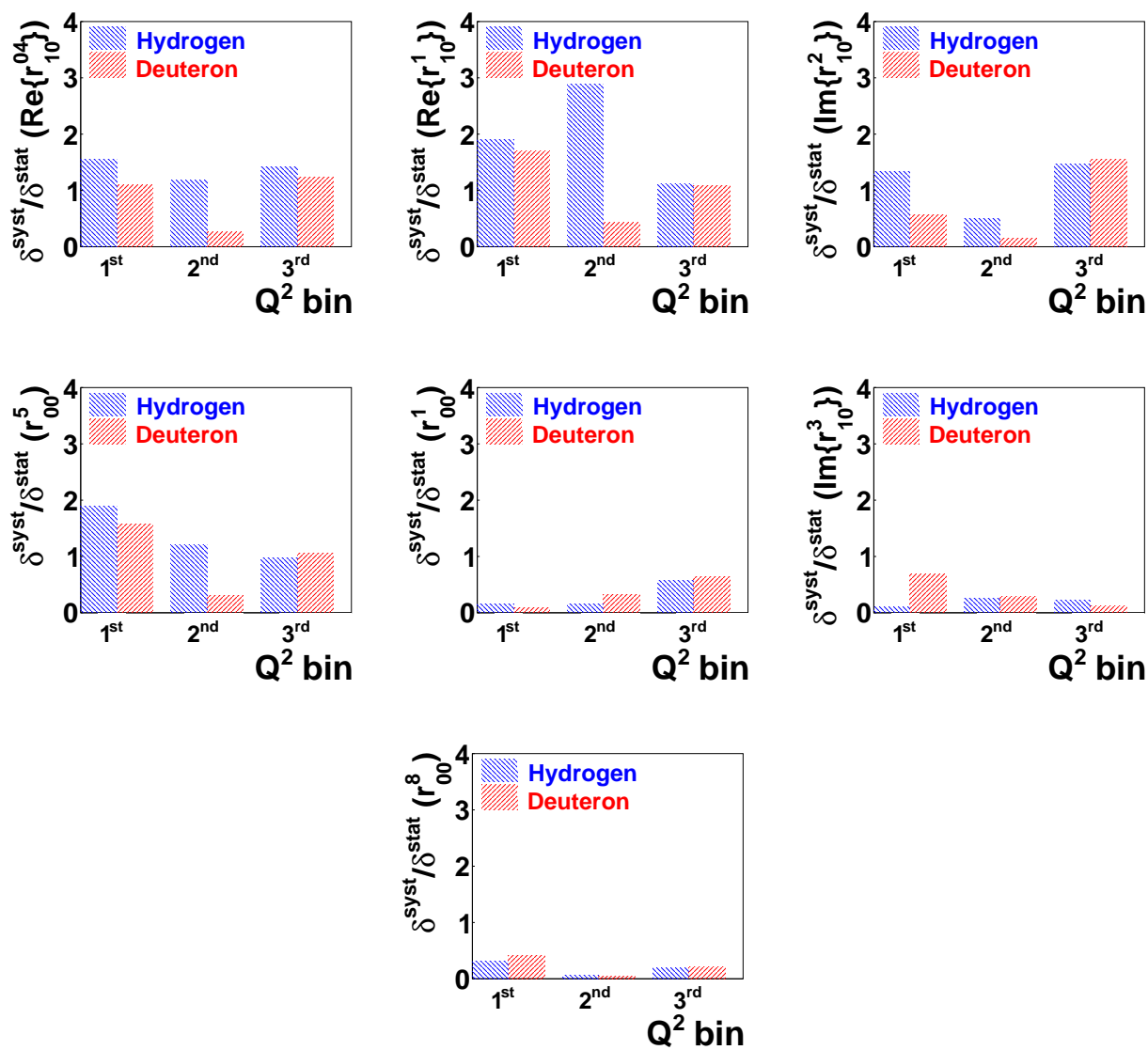


Figure 4.43: As in Figure 4.41 but for class C.

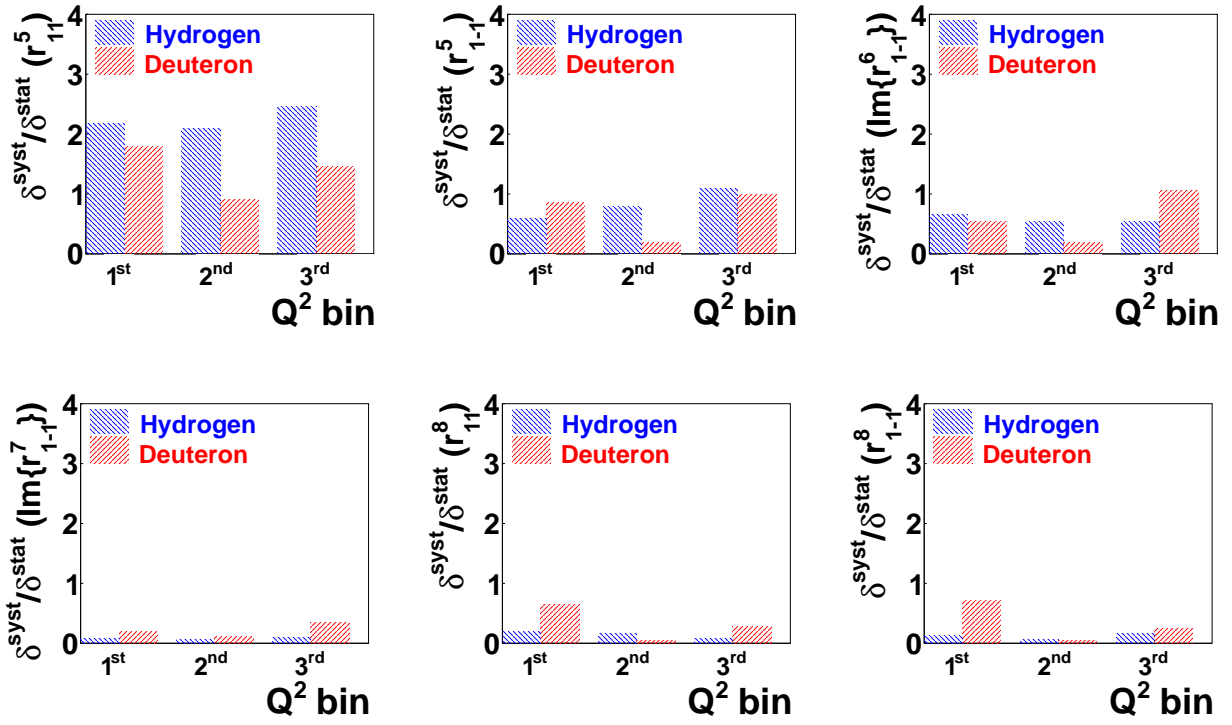


Figure 4.44: As in Figure 4.41 but for class D.

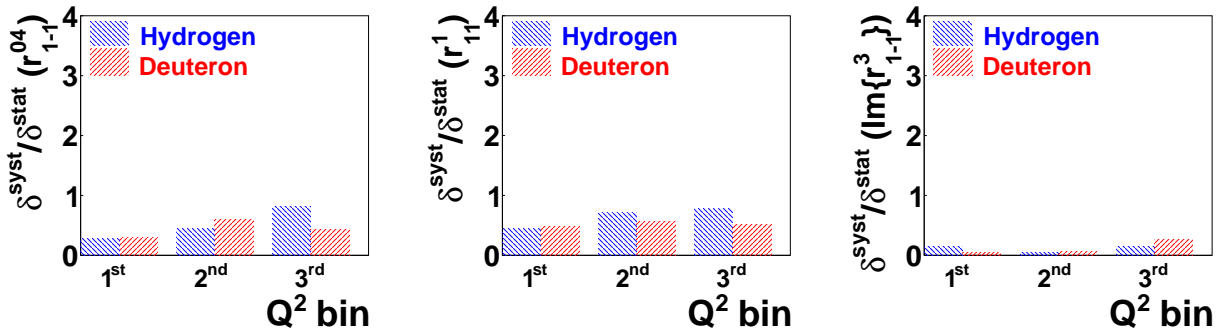


Figure 4.45: As in Figure 4.41 but for class E.

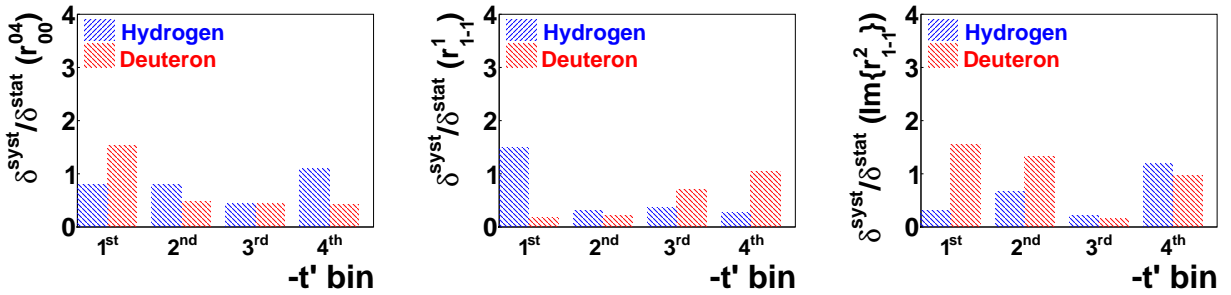


Figure 4.46: As in Figure 4.41 but for $-t'$ dependence.

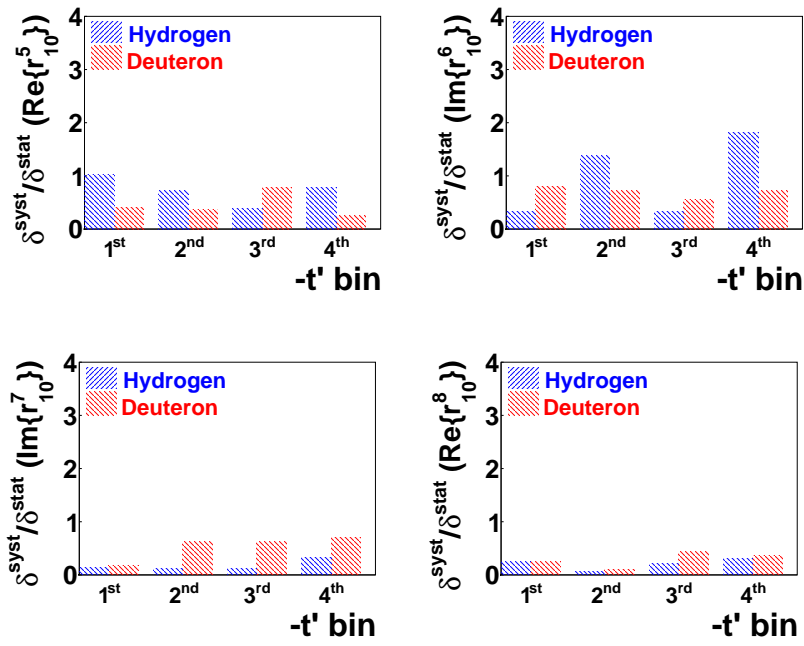


Figure 4.47: As in Figure 4.47 but for $-t'$ dependence.

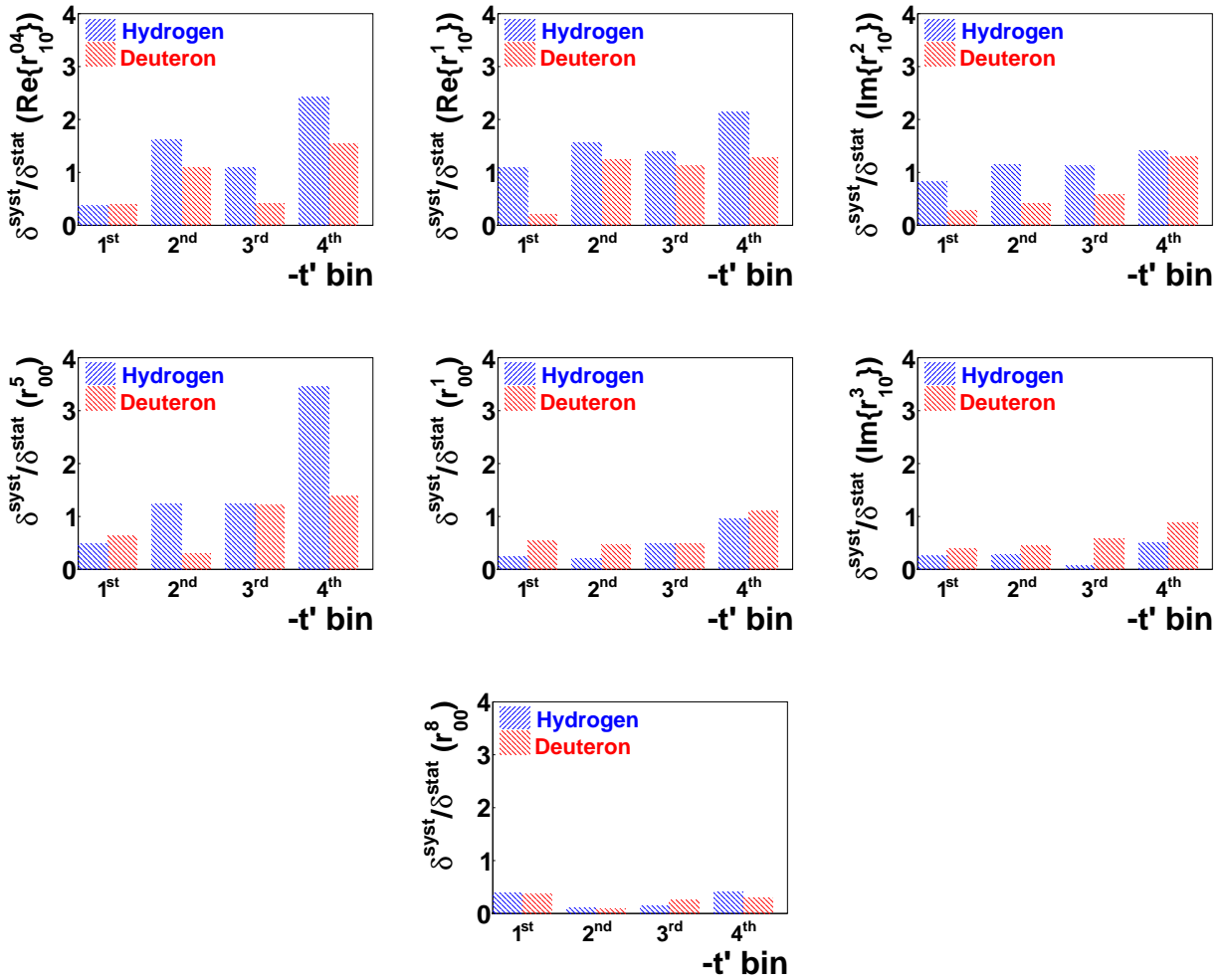


Figure 4.48: As in Figure 4.43 but for $-t'$ dependence.

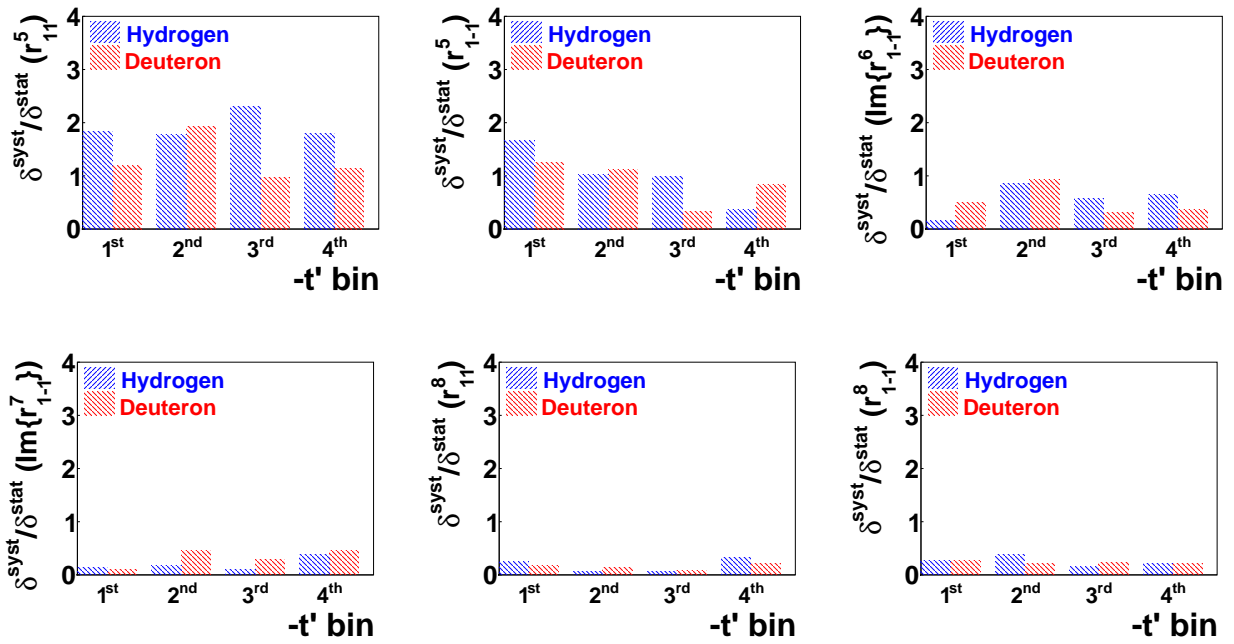


Figure 4.49: As in Figure 4.44 but for $-t'$ dependence.

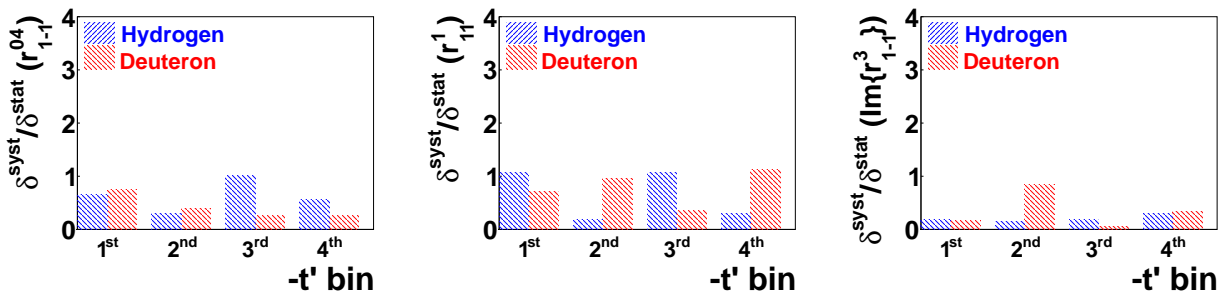


Figure 4.50: As in Figure 4.45 but for $-t'$ dependence.

Chapter 5

Results

In this section the SDMEs in Wolf-Schilling (Equations 2.61, 2.62) and Markus Diehl (Equations 2.66- 2.73) notations are presented. They were extracted from the unified data sets of 1998–2000 years and 2006-2007 years for hydrogen and deuteron targets separately. The data were obtained on unpolarized targets with the longitudinally polarized beam, therefore (see Section 2.10 for the explanation) 15 unpolarized SDMEs and 8 SDMEs which include the beam-polarization dependence were obtained. The extraction was performed using unbinned MLH (See Section 4.2.1) method for the data divided into three kinematic bins in Q^2 or four kinematic bins in t' value. Binning was independent, e.g. by each variable one-dimensional binning was done. The first t' bin, e.g. the data, referred to as coherent scattering (see Section 4.1.4) is excluded from each Q^2 bin of deuteron data. For the t' dependence it is still shown for completeness.

5.1 Kinematic dependencies of Wolf-Schilling SDMEs

In the Figures 5.1 – 5.10 the Q^2 and t' dependencies for SDMEs are presented, extracted from hydrogen and incoherent deuteron sets (see Table 4.4 for the bin boundary values). The SDMEs are divided into the classes A–E, related to certain transition types. Each plot presents either Q^2 – in Figures 5.1 – 5.5 or t' – Figures 5.6 – 5.10 dependence of certain SDME. For the comparison also the ρ meson SDMEs, obtained by HERMES ([26]) in the years 1996-2005, are shown in the figures. The invisible uncertainties for most of ρ meson SDMEs are explained by the large statistics (~ 10 times larger than for the ϕ meson). SDMEs for ρ meson for of hydrogen and deuteron target are in most cases very close to each other. ϕ meson SDMEs show larger spread, however it the deviations do not exceed 2σ in most of the cases (see Section 4.2.5).

The values of Wolf-Schilling ϕ meson SDMEs together with the statistical and systematic uncertainties in all the kinematic bins and for integrated kinematics are given in Appendix F.

Class A: dominant transitions $\gamma_L^* \rightarrow \phi_L$ and $\gamma_T^* \rightarrow \phi_T$. (Figures 5.1, 5.6).

Class A includes SDMEs, related to the dominant helicity-conserving transitions. The

amplitudes, responsible for such reaction types, are T_{11} and T_{00} (see Appendix B for SDMEs-to-amplitudes relations). All the kinematic dependencies were fitted by the linear function. The first SDME, namely r_{00}^{04} , exhibit Q^2 dependence for both hydrogen and deuteron target, e.g. the slope in the fit function is different from zero by more than 2σ . SDMEs r_{1-1}^1 and $\Im(r_{1-1}^2)$ of ϕ meson show Q^2 dependencies for deuteron target, which is stronger than that of ρ meson SDMEs. Neither for ϕ nor for ρ meson t' dependencies of A-Class SDMEs is observed.

Theory expectations are that only the first SDME, namely r_{00}^{04} must have Q^2 dependence, all the other SDMEs have to be Q^2 and t' independent.

Class B: interference of $\gamma_L^* \rightarrow \phi_L$ and $\gamma_T^* \rightarrow \phi_T$ transitions. (Figures 5.2, 5.7).

Class B consists of SDMEs describing the interference of the dominant transitions. The interference is reflected as a product of the corresponding amplitudes T_{11} and T_{00} . Polarized (unpolarized) SDMEs are related to the real (imaginary) part of the product. No pronounced Q^2 (Figure 5.2) or t' (Figure 5.7) dependence for SDMEs of B class was found, neither for ρ meson nor for ϕ .

Class C: helicity flip transition $\gamma_T^* \rightarrow \phi_L$. (Figures 5.3, 5.8).

Class C comprises SDMEs containing a product of the helicity non-conserving amplitude T_{01} and one of the amplitudes T_{00} , T_{11} , T_{01} . If SCHC is hold, all the SDMEs of classes C - E have to be zero. The SDME significantly violating the hypotheses for both ϕ and ρ mesons is r_{00}^5 . For ρ meson this is theoretically expected and experimentally observed at HERA by ZEUS ([24]) and H1 ([25]). For the ϕ meson the non-zero value is less pronounced, but theoretically unexpected. The r_{00}^5 value obtained by H1 ([28]) was zero within 2σ in all the kinematic bins. The possible explanation to the observation of HERMES a non zero value is the effect from the radiative corrections and was provided in Section 2.15. The remaining SDMEs of the C class are statistically consistent with zero.

No clear Q^2 dependence was found for the ρ meson SDMEs of class C. Several ϕ meson SDMEs of deuteron exhibit Q^2 ($\Im(r_{10}^2)$, r_{00}^8) or t' (r_{00}^8) dependencies.

Class D: helicity flip transition $\gamma_L^* \rightarrow \phi_T$. (Figure 5.4, 5.9).

Class D contains SDMEs that are a product of the small helicity-flip amplitude T_{10} with the complex conjugate of T_{11} . Unpolarized (polarized) SDMEs represent the real (imaginary) part of this product. The ρ meson SDMEs show i at all weak kinematic dependencies and are consistent with zero ([26]) apart from r_{11}^5 . For ϕ meson r_{1-1}^8 for hydrogen is weakly Q^2 dependent, $\Im(r_{1-1}^7)$ and r_{11}^8 for deuteron are t' dependent.

Class E: helicity flip transition $\gamma_{-T}^* \rightarrow \phi_T$. (Figure 5.5, 5.10).

Class E consists of SDMEs, which are a product of the double spin-flip amplitude T_{1-1} with the complex conjugate of the helicity-conserving amplitude T_{11} . Unpolarized (polarized) SDMEs represent the real (imaginary) part of this product. Neither ρ nor ϕ meson SDMEs show significant kinematic dependencies.

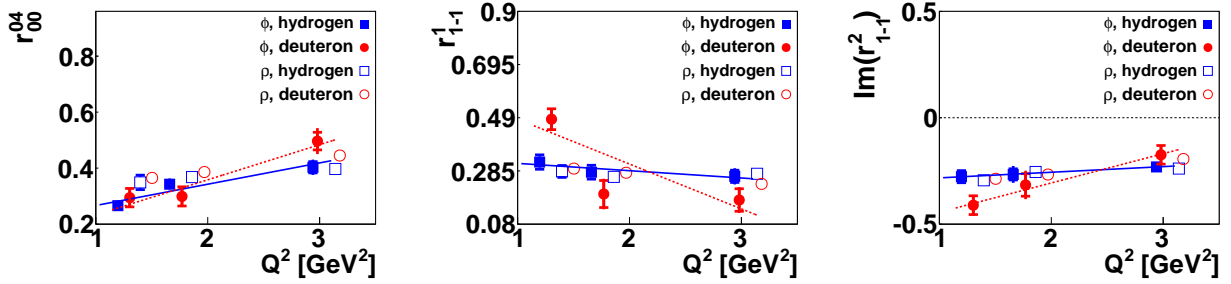


Figure 5.1: The Q^2 dependence of Wolf-Schilling SDMEs from class A for proton (blue squares) and deuteron (red circles) targets for ϕ meson (solid symbols) and ρ meson (open symbols). The inner error bars represent the statistical uncertainties, while the outer ones, if visible, indicate the statistical and systematic uncertainties added in quadrature.

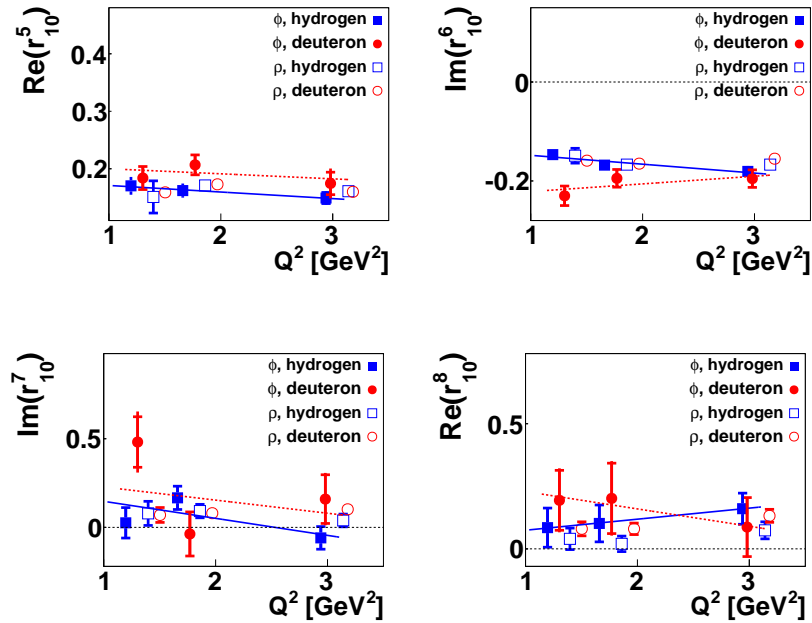


Figure 5.2: As Figure 5.1 but for class B SDMEs.

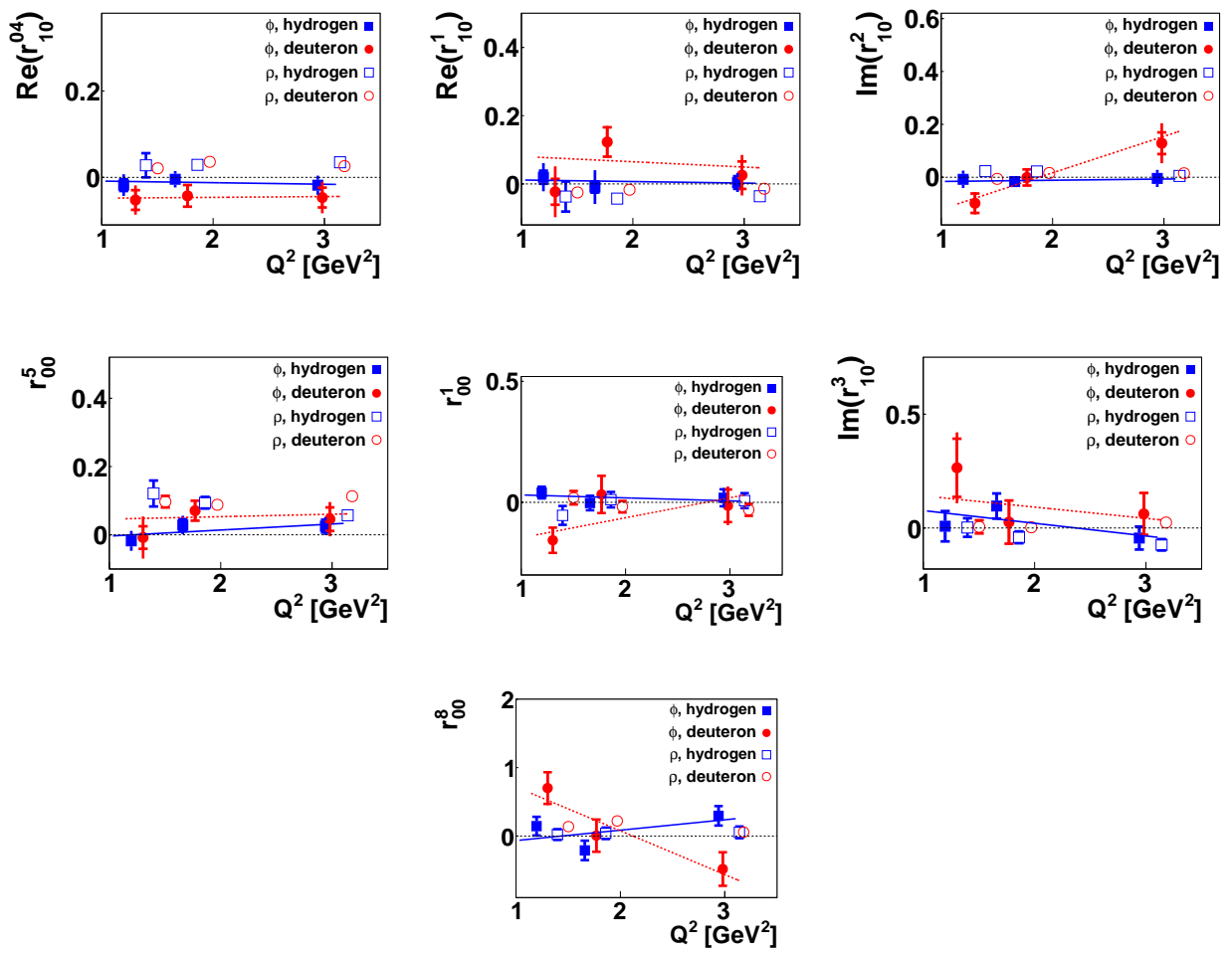


Figure 5.3: As Figure 5.1 but for class C SDMEs.

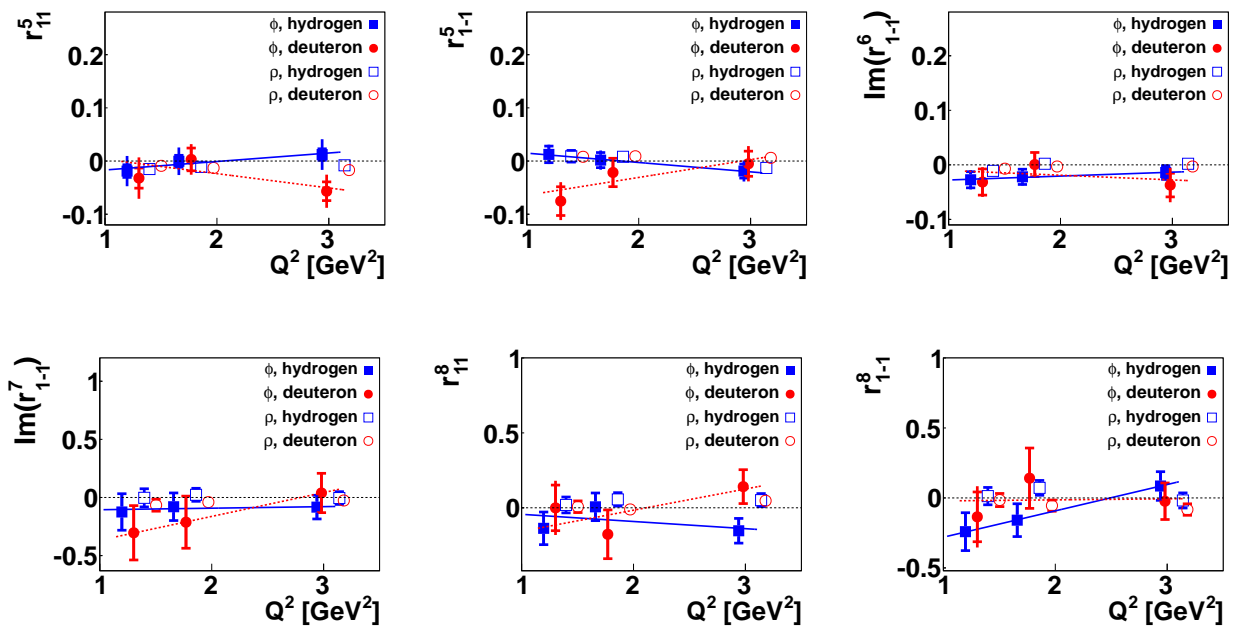


Figure 5.4: As Figure 5.1 but for class D SDMEs.

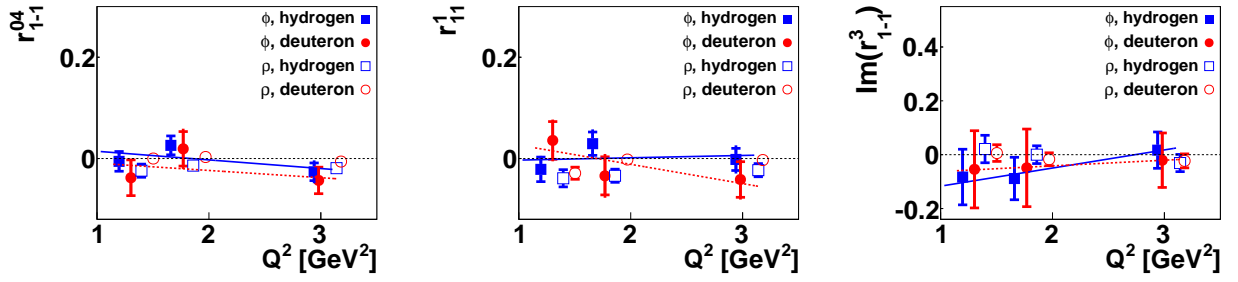
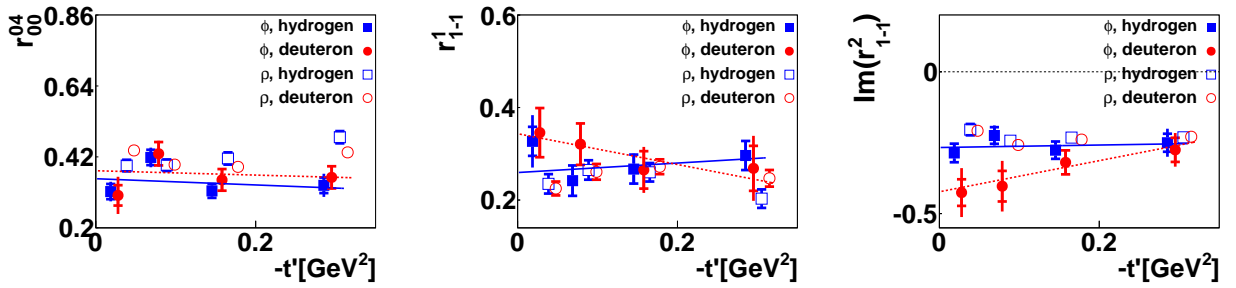
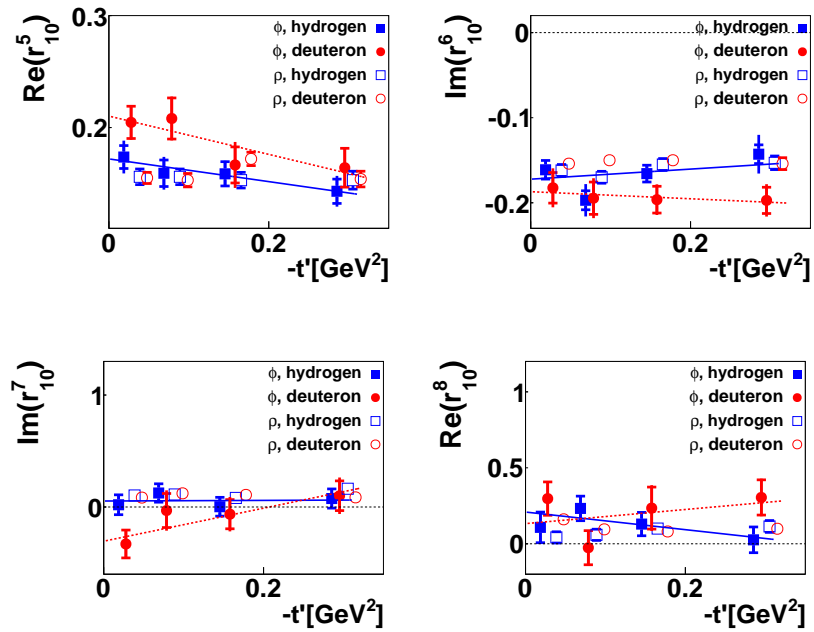


Figure 5.5: As Figure 5.1 but for class E SDMEs.

Figure 5.6: As Figure 5.1 but for t' dependence of SDMEs.Figure 5.7: As Figure 5.2 but for t' dependence of SDMEs.

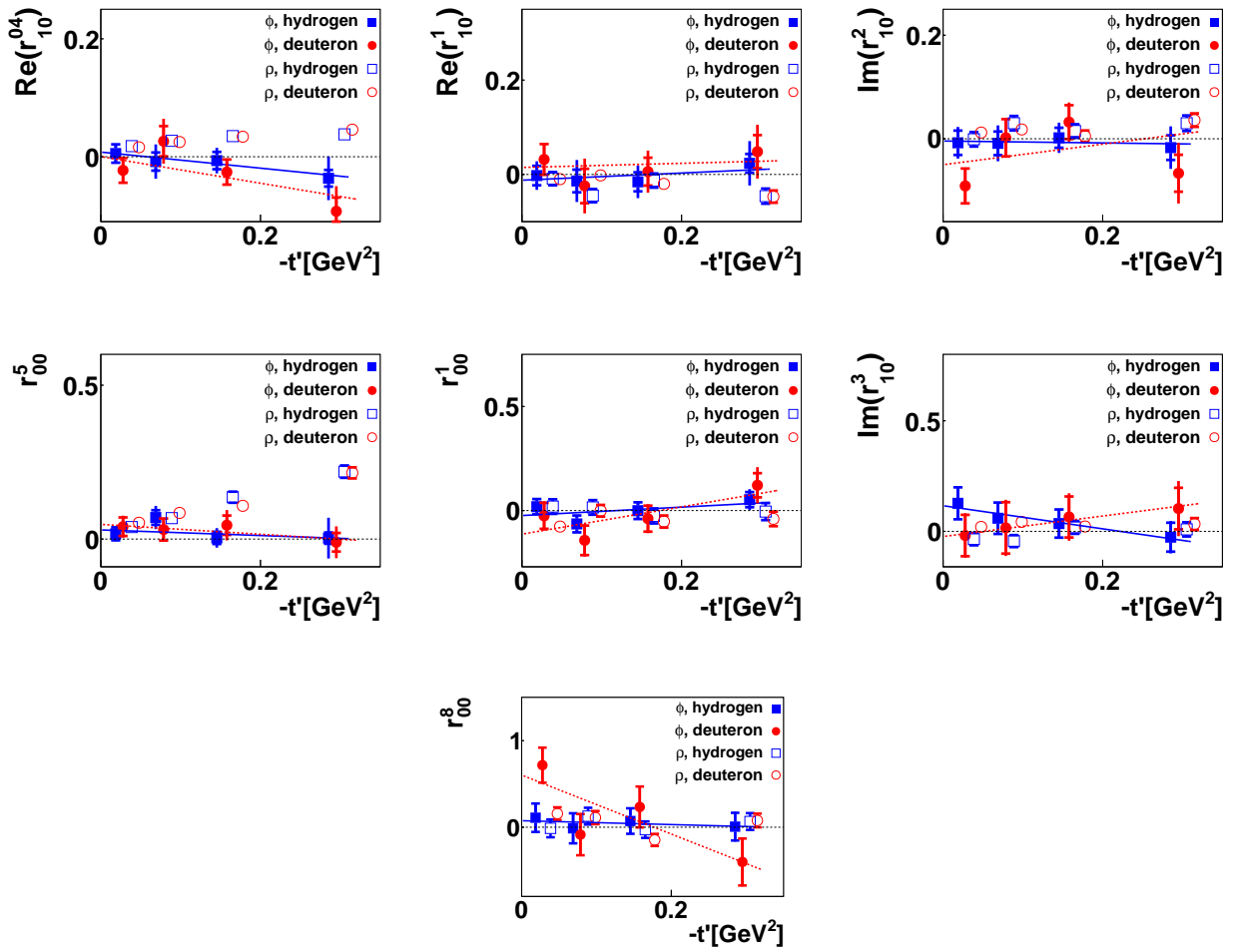


Figure 5.8: As Figure 5.3 but for t' dependence of SDMEs.

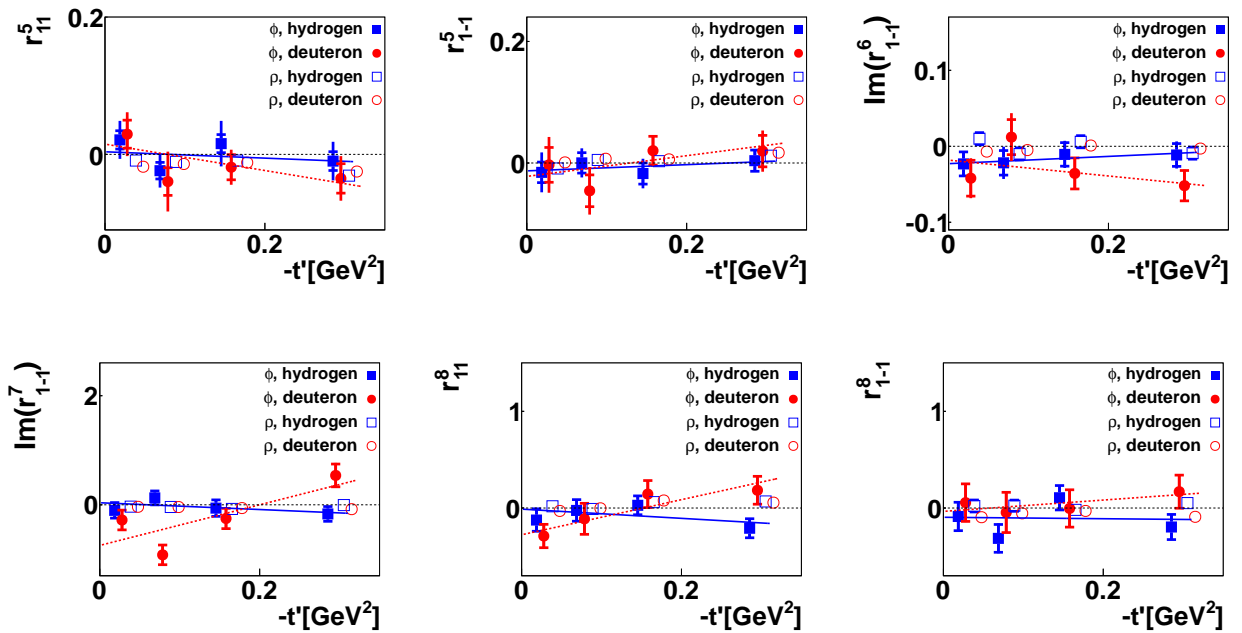


Figure 5.9: As Figure 5.4 but for t' dependence of SDMEs.

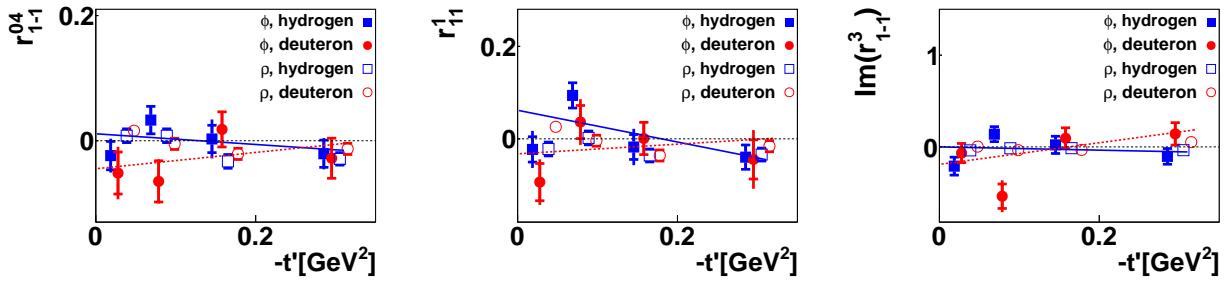


Figure 5.10: As Figure 5.5 but for t' dependence of SDMEs.

5.2 Test of SCHC hypotheses

SDMEs of class B together with the second and third SDMEs of the class A, provide a possibility to test SCHC hypotheses. In Figures 5.11 and 5.12 the pairs of SDMEs (see Equations 2.13) whose absolute values are to be equal in case of SCHC are plotted together. In Figure 5.13 the differences between SDMEs of each of the pairs are presented. There are two deviations of the differences from zero for more than 2σ , in other words in two pairs the absolute SDME values deviate from each other. These are $\Im m(r_{10}^7) - \Re e(r_{10}^8)$ in 1^{st} Q^2 bin of deuteron data and $\Im m(r_{10}^7) - \Re e(r_{10}^8)$ in 2^{nd} t' bin of hydrogen data. For SDMEs $\Im m(r_{10}^7)$ and $\Re e(r_{10}^8)$, formulas in Appendix B show that the largest SCHC amplitude T_{00} is multiplied by the smallest T_{1-1} amplitude in the terms that violate SCHC. The 2 deviations make 5.5% from the total number of SDME differences, most of the remaining values (77.8%) are lying within 1σ from zero. This indicates that SCHC holds for ϕ meson and is in agreement with theory expectations.

5.3 Kinematic dependencies of Markus-Diehl SDMEs

In Figures 5.14 - 5.18 Q^2 dependencies of Markus Diehl SDMEs are presented. In Figures 5.19 - 5.23 those for t' dependencies are shown. The same as for SDMEs in Wolf-Schilling notation, these in Markus notation are divided into 3 classes according to helicity transition type.

Note that the values of the first SDMEs in Wolf-Schilling and Markus Diehl notations are equal (formulas connecting the two notations can be found in Appendix A) which one can see in comparison of first plots in Figures 5.1 and 5.14, 5.6 and 5.19.

In Figures 5.14, 5.19 the kinematic dependencies of SDMEs related to s-channel helicity conserving transition are shown. These SDMEs are significantly different from 0. In Figures 5.15, 5.20, 5.16, 5.21, 5.17, 5.22 the SDMEs describing the helicity-flip transitions $\gamma_T^* \rightarrow \phi_L$, $\gamma_L^* \rightarrow \phi_T$ and $\gamma_{-T}^* \rightarrow \phi_T$ are presented. They are mostly compatible with zero for hydrogen and larger in some kinematic bins for deuterium. Some of them, e.g. $\Re e\{u_{++}^{0+} - u_{++}^{-0} + 2\epsilon u_{0+}^{-0}\}$ and u_{-+}^{00} , exhibit clear t' dependence. Figures 5.18, 5.23 show SDMEs which represent double

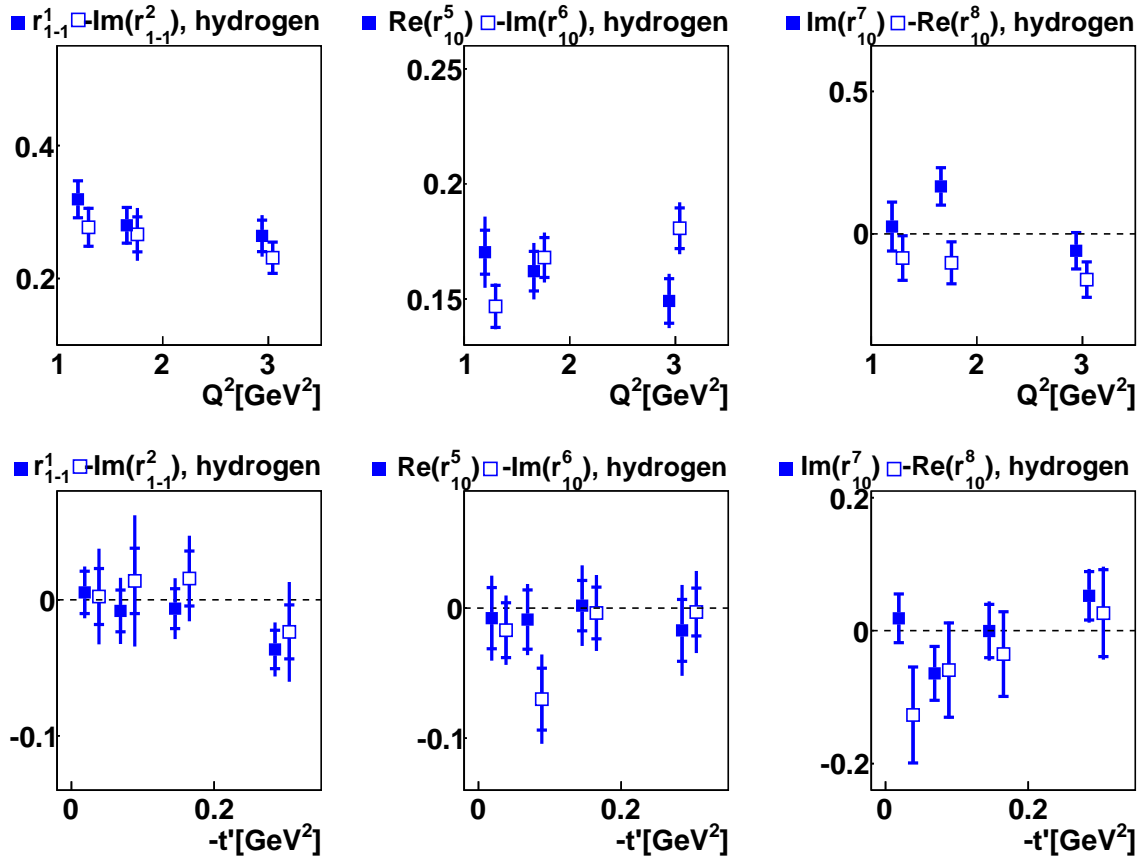


Figure 5.11: Each of the plots is related to the couple of hydrogen SDMEs whose absolute values are to be equal in case of SCHC.

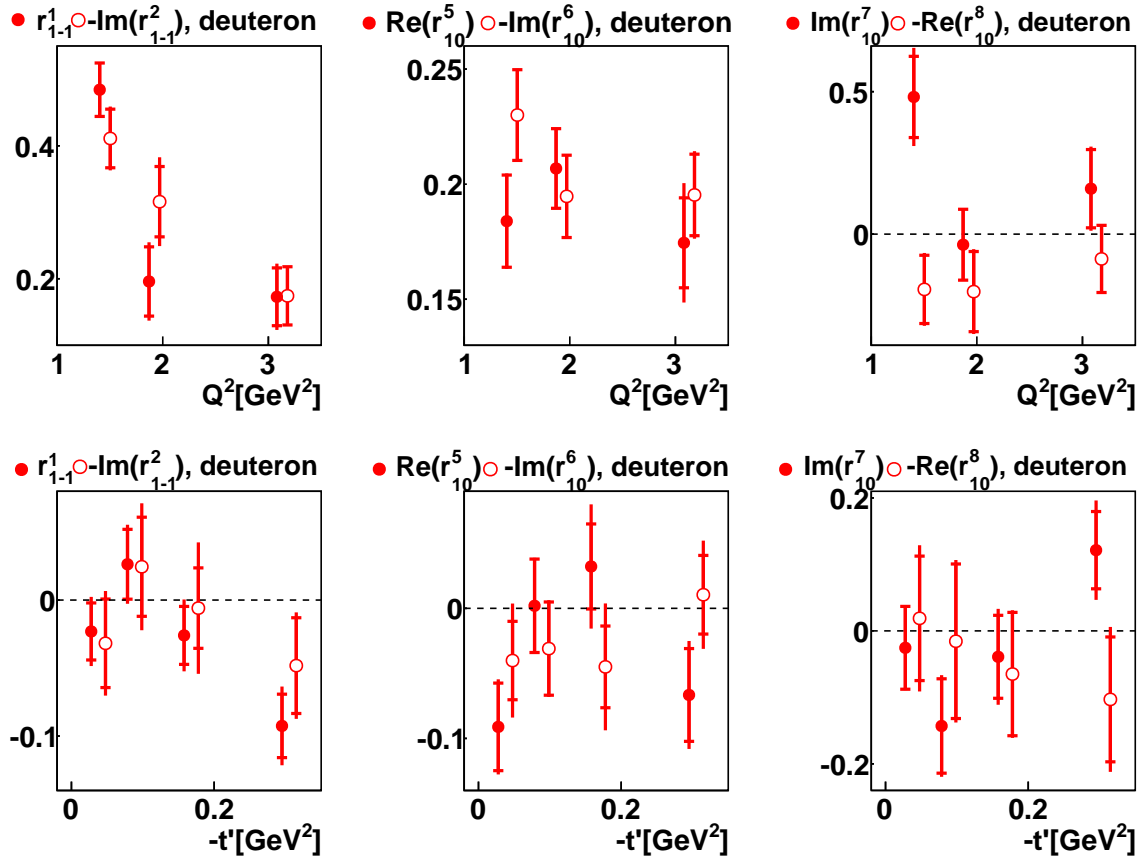


Figure 5.12: As in Figure 5.11 but for deuteron.

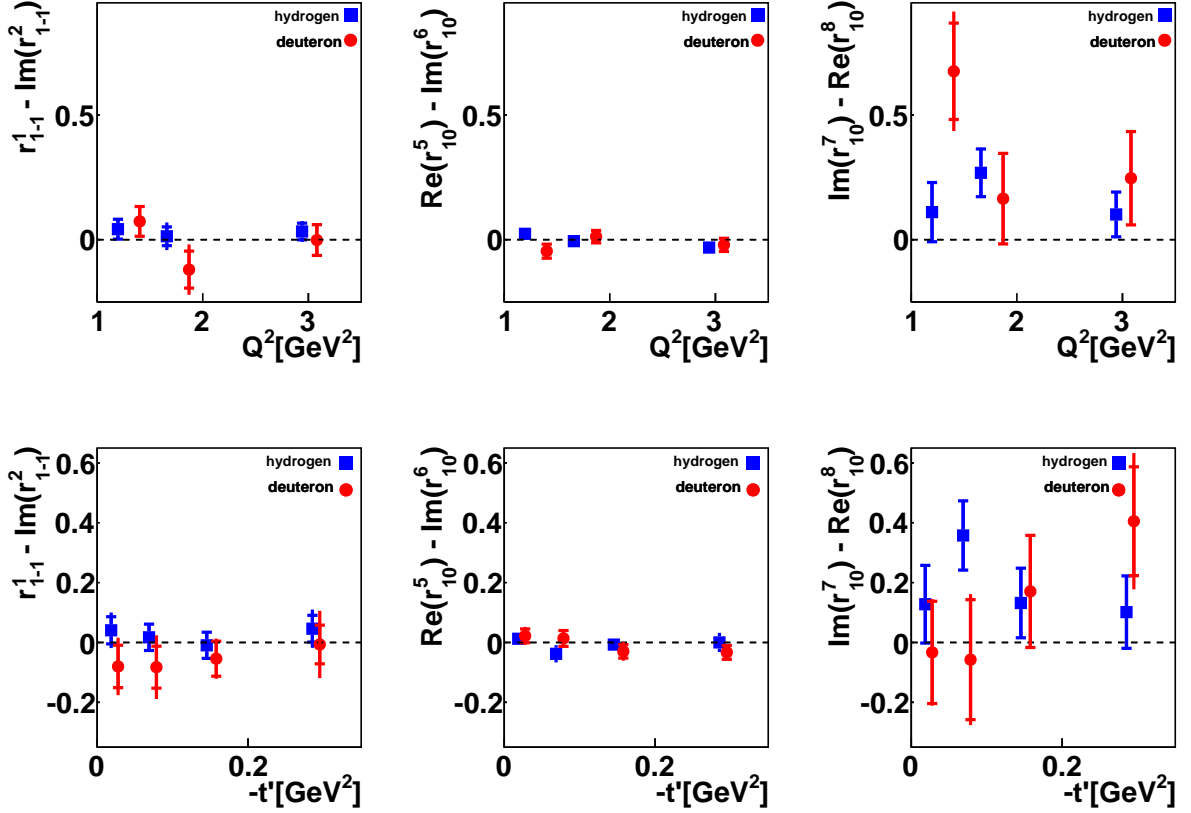


Figure 5.13: The differences of the SDME pairs, which are to be zero in case of SCHC, are presented. Results for hydrogen target are presented as blue squares, for deuterium as red circles. Both statistical (inner) and systematic (outer, if visible) uncertainties were calculated with consideration of the statistical correlations between SDMEs, e.g. using the covariance matrix.

spin flip transitions. For hydrogen SDMEs of that class are close to zero while for deuterium significant deviations from zero in some kinematic bins are observed. The form of t' dependence of unpolarized SDMEs was predicted theoretically in Diehl notation ([21]) as $u_{\mu\mu'}^{\nu\nu'} \sim a * (t')^{p_{min}/2}$. The dependence form holds for $t' \rightarrow 0$ and in the forward scattering limit, e.g. when the scattering angle of the vector meson is small. In Figures 5.19- 5.23 the t' dependencies are fitted using theory-predicted ([21]) p_{min} values and then treating p as a free parameter. The notation defines only the minimum values of the parameter p , its actual value can be larger. The p values together with corresponding $\frac{\chi^2}{n.d.f}$ are given in Table 5.3. Taking into account the fit uncertainty, p values obtained as free fit parameters are larger than the theory-provided values.

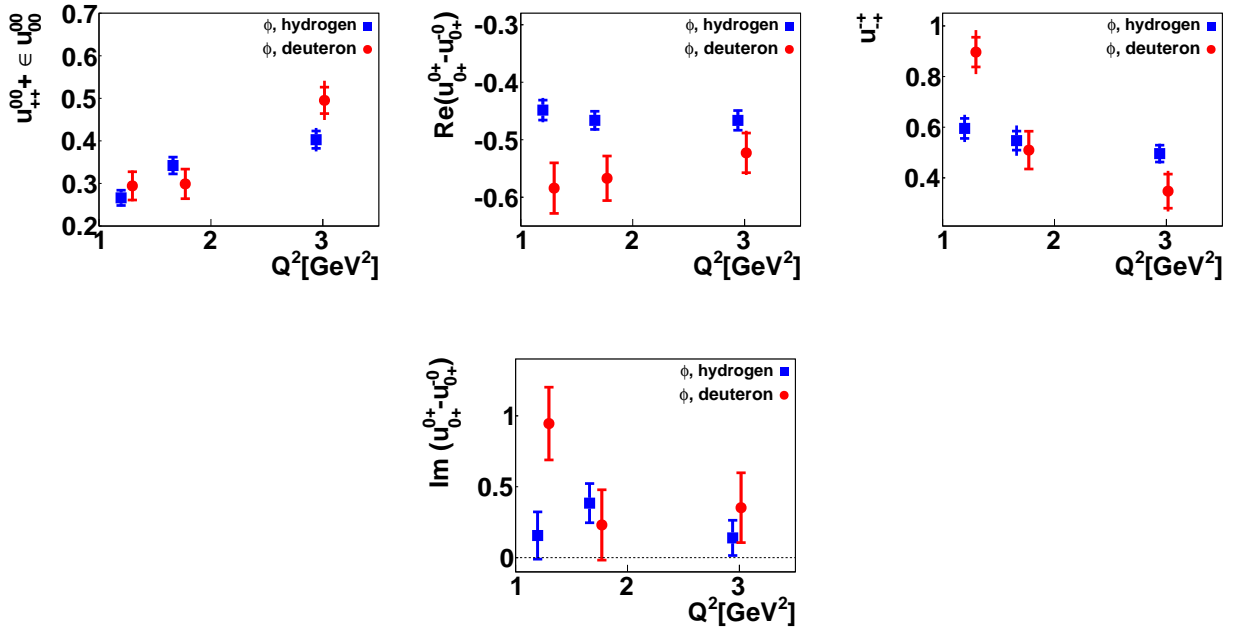


Figure 5.14: The Q^2 dependence of Markus Diehl SDMEs related to helicity-conserving transition $\gamma_L^* \rightarrow \phi_L$ and $\gamma_T^* \rightarrow \phi_T$ for ϕ meson. Proton (deuteron) SDMEs are shown as blue squares (red circles). The inner error bars represent the statistical uncertainties, while the outer ones, if visible, indicate the statistical and systematic uncertainties added in quadrature.

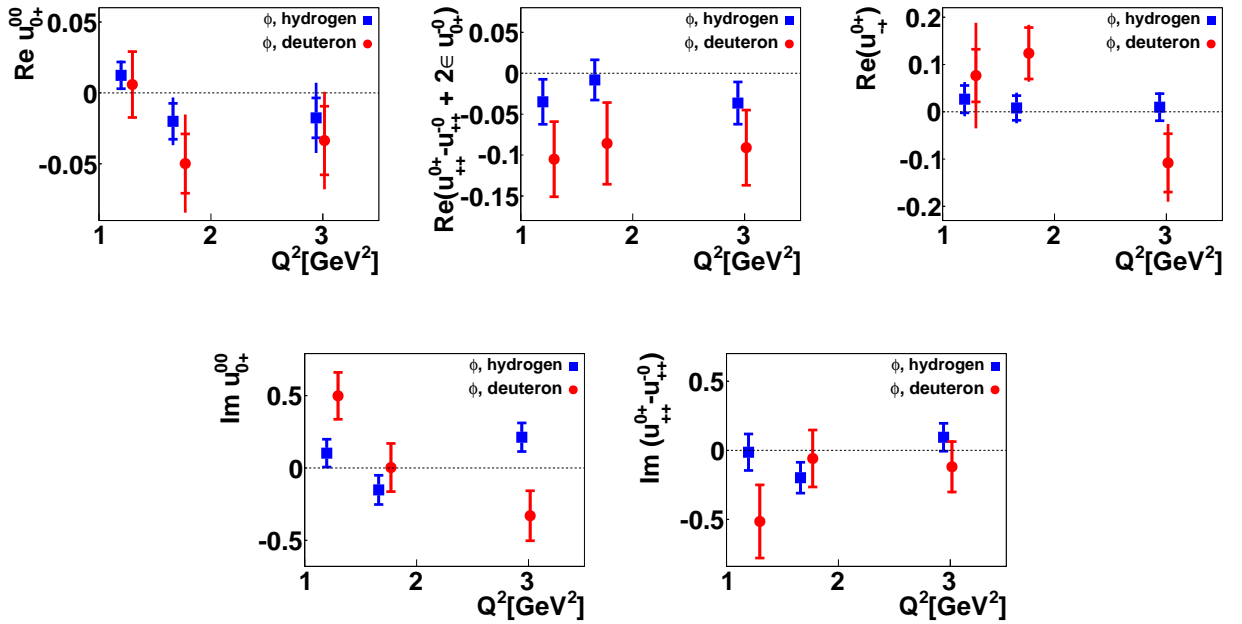


Figure 5.15: As in Figure 5.14, but for SDMEs related to the helicity flip transition $\gamma_T^* \rightarrow \phi_L$.

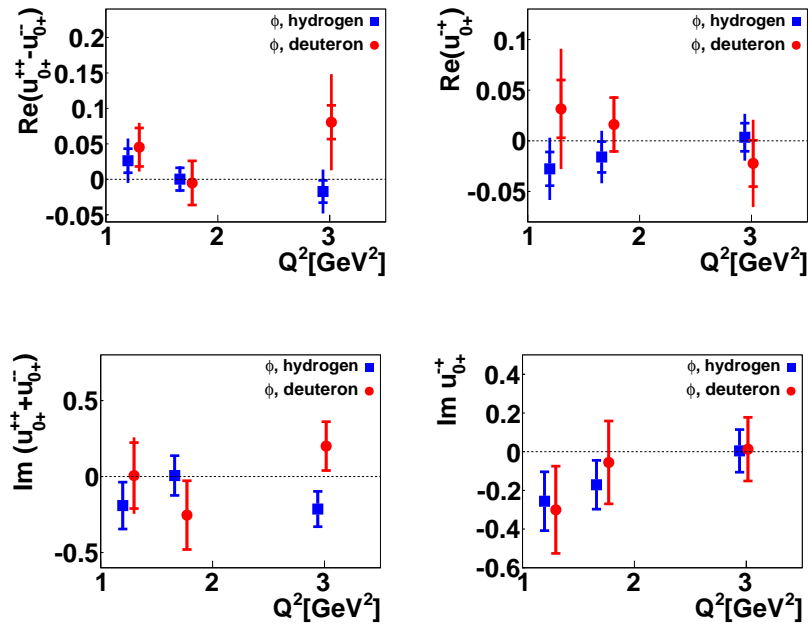


Figure 5.16: As in Figure 5.14, but for SDMEs related to the helicity flip transition $\gamma_L^* \rightarrow \phi_T$.

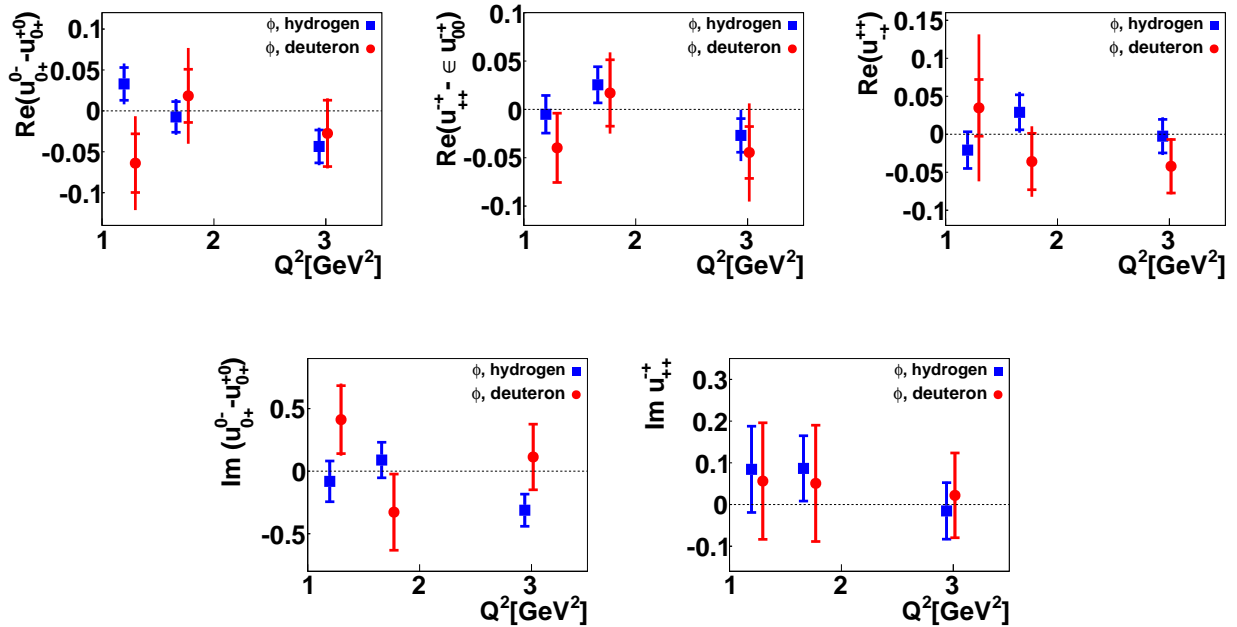


Figure 5.17: As in Figure 5.14, but for SDMEs related to the helicity flip transition $\gamma_{-T}^* \rightarrow \phi_T$.

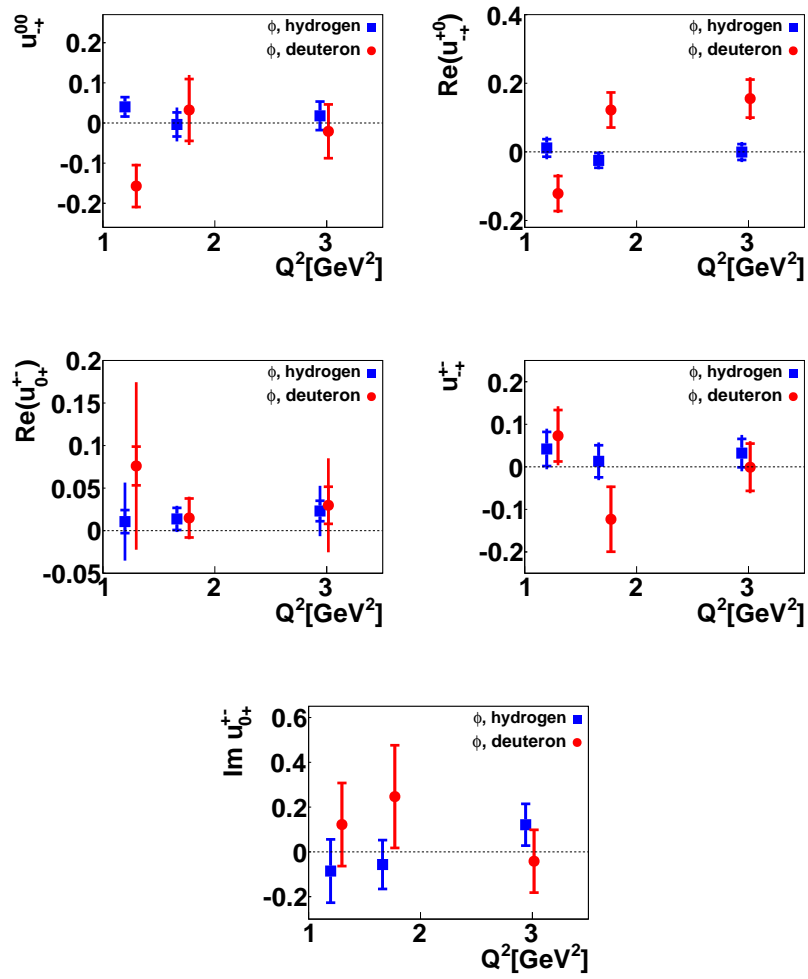


Figure 5.18: As in Figure 5.14, but for SDMEs related to the helicity double-flip transitions.

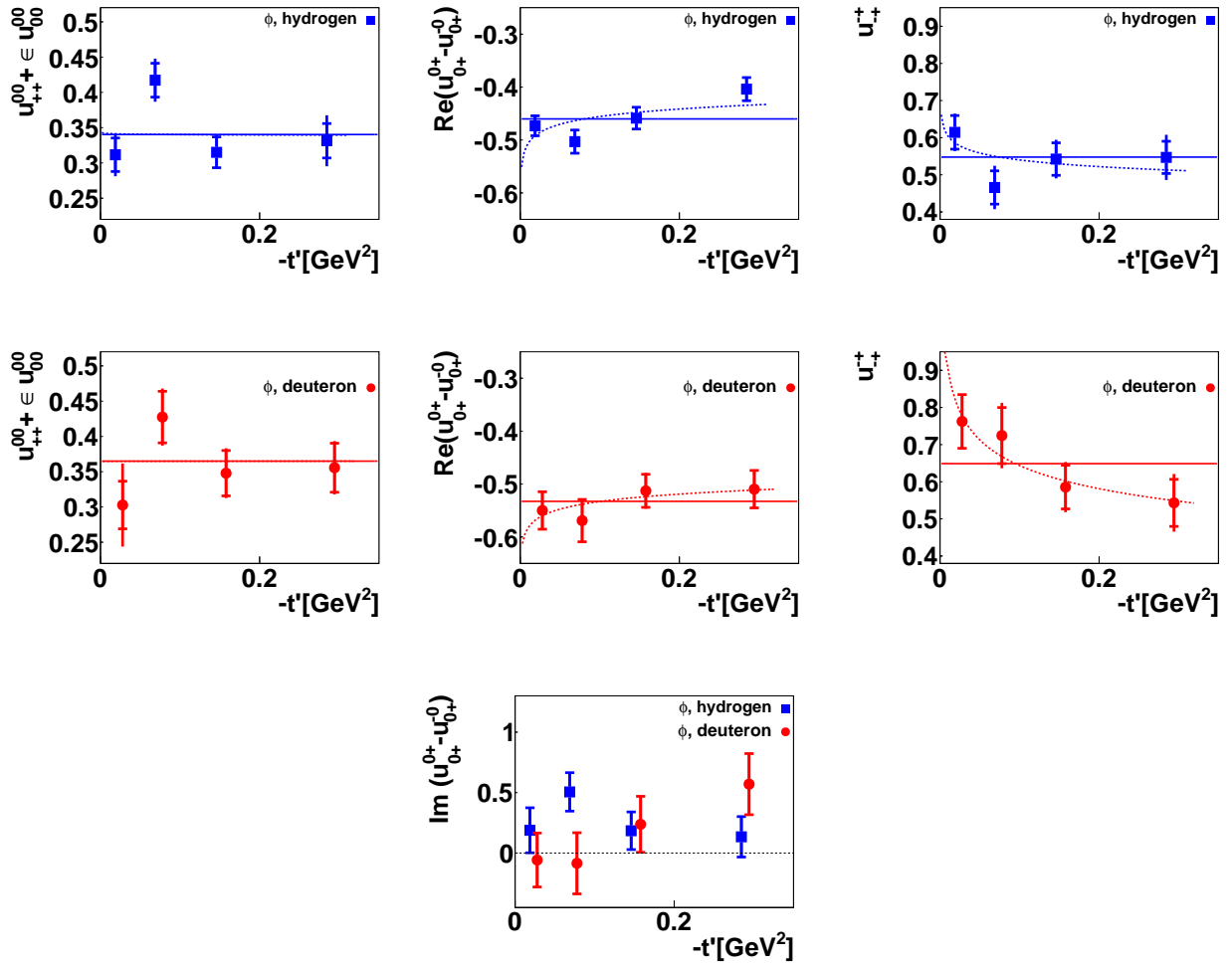


Figure 5.19: As in Figure 5.14, but for t' dependence. In the upper (middle) raw hydrogen (deuteron) SDMEs are fitted with the function $a * (-t')^{p/2}$ using theory-predicted values of p_{min} (solid line) and treating p as free parameters (dashed line).

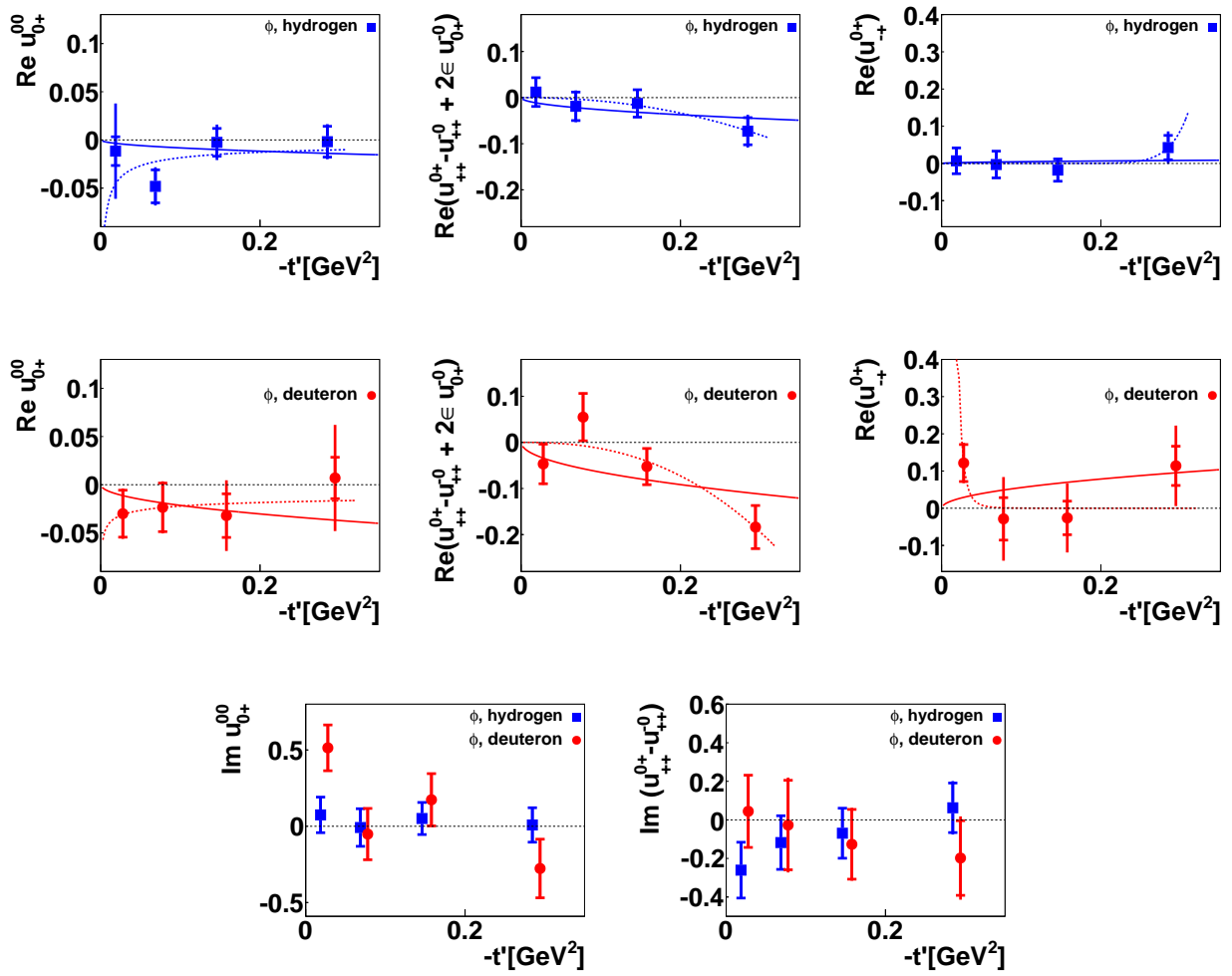


Figure 5.20: As in Figure 5.15, but for t' dependence.

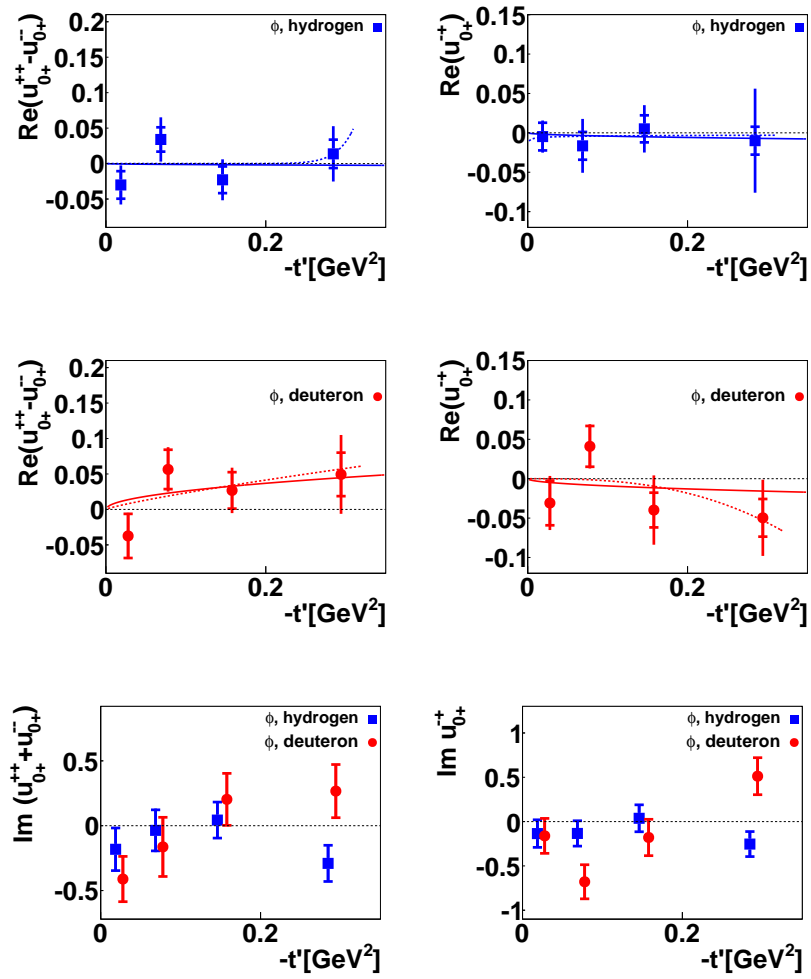


Figure 5.21: As in Figure 5.16, but for t' dependence.

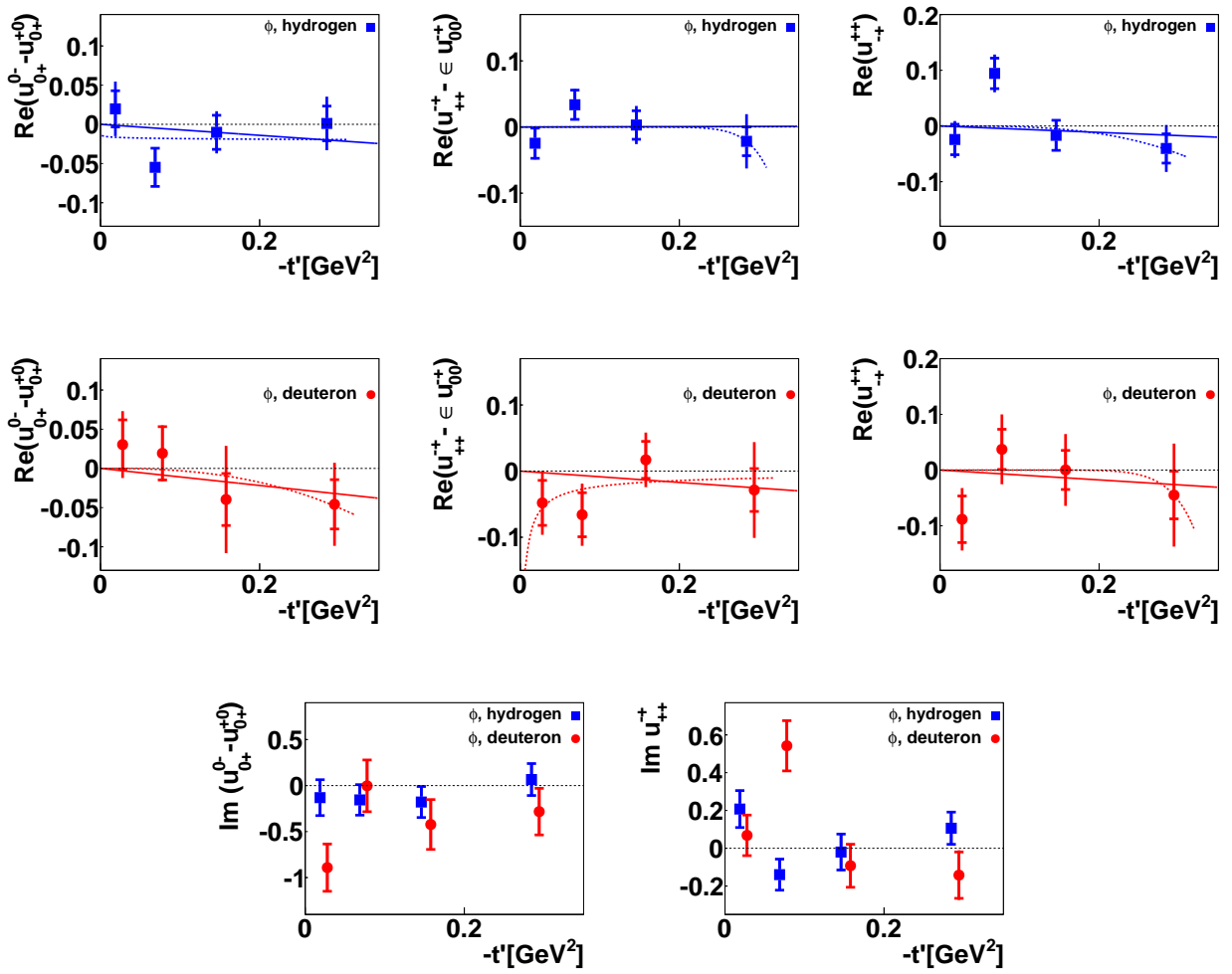


Figure 5.22: As in Figure 5.17, but for t' dependence.

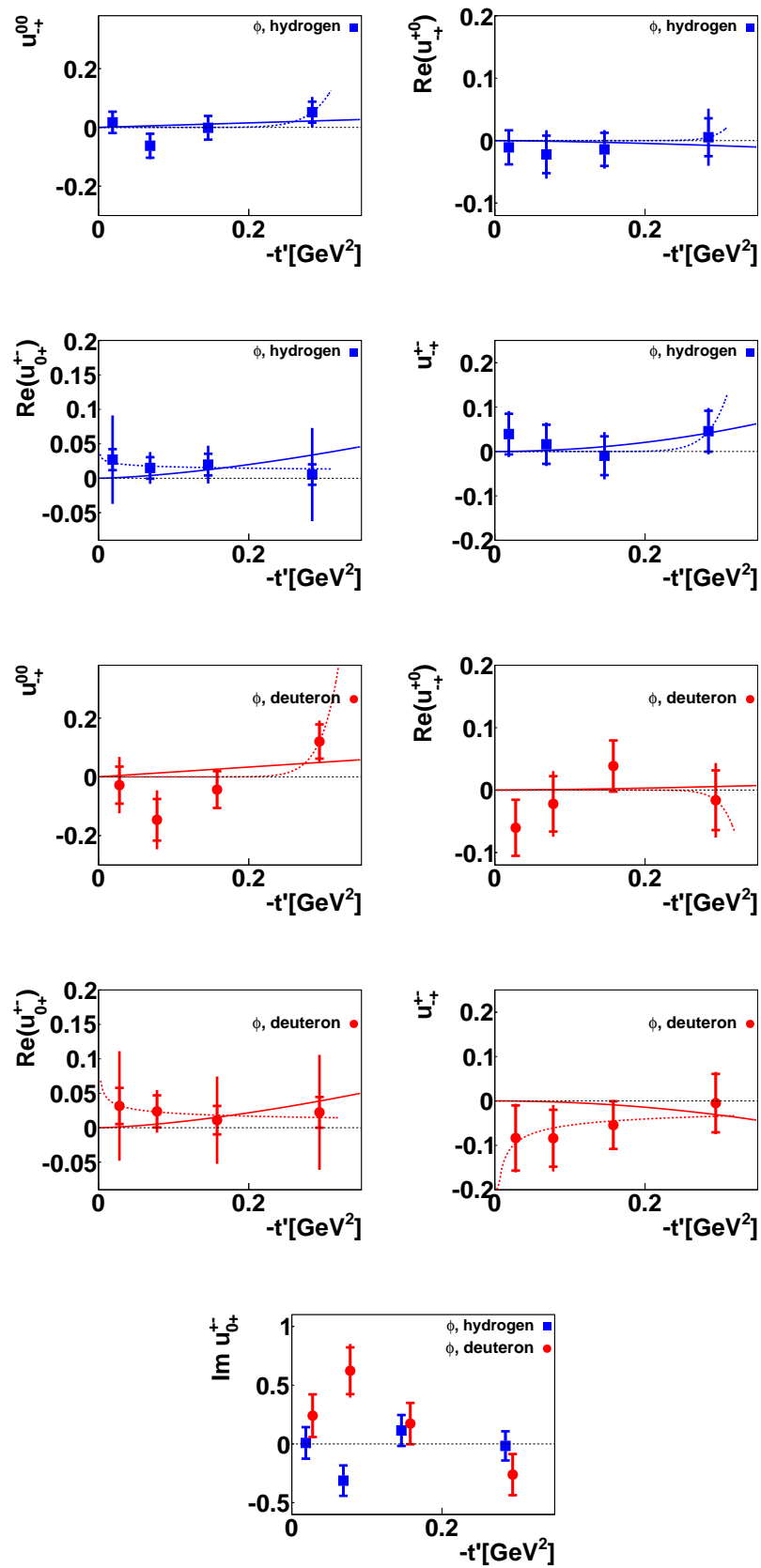


Figure 5.23: As in Figure 5.18, but for t' dependence.

Target		Hydrogen			Deuteron		
SDME	p_{min}	$\frac{\chi^2_{theory}}{n.d.f}$	$p_{fit} \pm err$	$\frac{\chi^2}{n.d.f}$	$\frac{\chi^2_{theory}}{n.d.f}$	$p_{fit} \pm err$	$\frac{\chi^2}{n.d.f}$
$u_{++}^{00} + \epsilon u_{00}^{00}$	0	4.212	-0.007 \pm 0.176	4.211	1.896	0.001 \pm 0.143	1.896
$Re(u_{0+}^{0+} - u_{0+}^{-0})$	0	4.728	-0.182 \pm 0.0916	2.774	0.899	-0.0768 \pm 0.075	0.382
u_{-+}^{+-}	0	1.860	-0.195 \pm 0.197	1.375	2.954	-0.294 \pm 0.125	0.258
Reu_{0+}^{00}	1	2.480	-2.140 \pm 1.886	1.411	0.597	-0.523 \pm 1.613	0.150
$Re(u_{++}^{0+} - u_{++}^{-0} + 2\epsilon u_{0+}^{-0})$	1	0.806	8.663 \pm 11.140	0.188	3.646	4.857 \pm 2.744	1.244
$Re(u_{-+}^{0+})$	1	0.626	55.530 \pm 127.927	0.183	2.241	31.981 \pm 24.209	2.596
$Re(u_{0+}^{++} - u_{0+}^{--})$	1	1.561	61.728 \pm 244.056	1.503	1.817	1.658 \pm 1.645	1.720
$Re(u_{0+}^{-+})$	1	0.141	-0.914 \pm 11.387	0.112	2.268	5.492 \pm 6.598	1.779
$Re(u_{0+}^{0-} - u_{0+}^{+0})$	2	2.365	0.230 \pm 2.385	1.862	0.696	5.136 \pm 9.162	0.523
$Re(u_{++}^{-+} - \epsilon u_{00}^{-+})$	2	1.659	49.701 \pm 157.498	1.520	1.519	34.925 \pm 120.724	1.567
$Re(u_{-+}^{++})$	2	4.660	12.754 \pm 15.504	4.273	1.467	20.609 \pm 130.422	1.419
u_{-+}^{00}	2	1.410	42.416 \pm 161.493	1.049	2.423	30.514 \pm 35.208	1.341
$Re(u_{-+}^{+0})$	3	0.327	65.232 \pm 622.117	0.338	1.417	33.134 \pm 45.738	1.385
$Re(u_{0+}^{+-})$	3	0.322	-0.722 \pm 6.226	0.0297	0.272	-0.648 \pm 3.937	0.011
u_{-+}^{+-}	4	1.570	29.705 \pm 142.589	0.358	1.570	18.018 \pm 21.836	1.677

Table 5.1: Comparison of the theory-predicted slopes of a t' -dependence for unpolarized Markus-Diehl SDMEs with those found via fit. In the first column SDME is given. The theory-predicted slope values (p) are shown in the second column. The $\frac{\chi^2_{th}}{n.d.f}$ values corresponding to these parameter values are presented in the third (sixth) column for hydrogen (deuteron) SDMEs. Slope parameter values obtained via fit are given in the fourth (seventh) column with corresponding $\frac{\chi^2}{n.d.f}$ values in fifth (eighth) column for hydrogen (deuteron).

5.4 UPE quantities

To check the presence of UPE exchange for ϕ meson (see Section 2.14 for the details), the U_1 , U_2 and U_3 quantities were calculated via Formulas 2.78– 2.80 in each kinematic bin. The corresponding results are presented in Figure 5.24. The overall values shown as open symbols are zero within 1σ , which indicates that UPE contribution for the ϕ meson production mechanism is negligible. A non-zero signal of UPE would be evidence for the existence of quark-anti-quark exchange, which is observed for exclusive ρ production ([24], [25], [26]). A negligible contribution of UPE amplitudes to the production of the ϕ meson as indicated by U_1 and U_3 values in some kinematic bins is consistent with the small content of strangeness in the nucleon and also of light $q\bar{q}$ pairs in the ϕ meson.

The values of U_1 , U_2 and U_3 quantities with their statistical and systematic uncertainties are given in Appendix F in Tables F.9 for hydrogen and F.10 for deuteron.

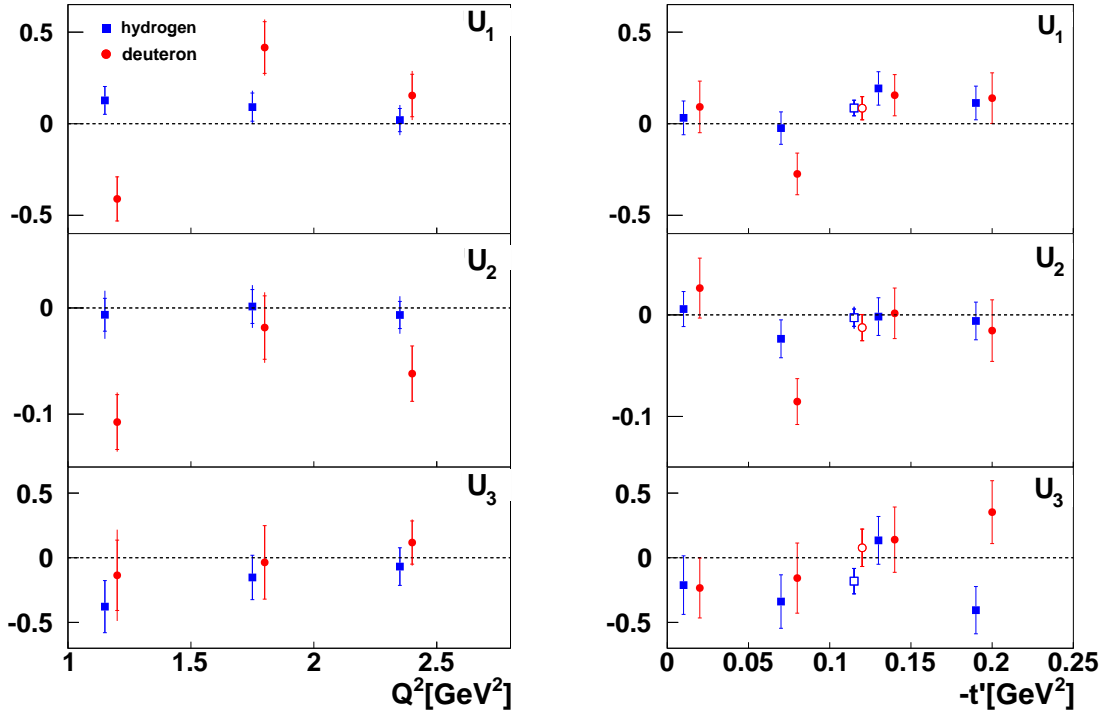


Figure 5.24: Kinematic dependencies of quantities U_1 , U_2 and U_3 for the data set of 1998-2000 and 2006-2007 years are presented. Open symbols denote overall values, blue squares represent hydrogen, red circles represent deuteron. The Q^2 (t') dependence is shown in the left (right) panel. The inner error bars represent the statistical uncertainties, the outer ones indicate the statistical and systematic uncertainties added in quadrature. For the calculation of the uncertainties the correlations between SDMEs are taken into account. The first t' bin is excluded from each Q^2 bin of deuteron data, in t' dependence it is still shown for completeness.

5.5 Cross section ratio

In the left panel of Figure 5.25 the ratio R of longitudinal-to-transverse ϕ meson leptonproduction cross-section is presented as a function of Q^2 . The ratio was calculated using the first SDME r_{00}^{04} according to the equation $R^{04} = \frac{1}{\epsilon} \frac{r_{00}^{04}}{1-r_{00}^{04}}$, which is valid only under the SCHC assumption. The values of R with the statistical and systematic uncertainties can be found in Appendix F in Table F for the various Q^2 bins. Note that the values for hydrogen and deuteron targets are same taking into account uncertainties. In the right panel of Figure 5.25 the comparison with the world data, namely results from experiments H1 [28] and ZEUS [27] is presented. From H1 and ZEUS data one can conclude that at $Q^2 > 2 \text{ GeV}^2$ the longitudinal cross section prevails over the transverse one, which might be the case for deuteron data of this analysis but not for hydrogen one. The reason for the difference is W dependence of the cross section ratio. The average W value in 3rd Q^2 bin which is the closest one to the ZEUS Q^2 range is 4.8 GeV.

The ratio points obtained in this analysis and world data are fitted with a VMD model

Parameter	c_0	c_1	$\chi^2/n.d.f$
ZEUS and H1 (high W)	0.49 ± 0.11	0.92 ± 0.17	0.359
This analysis (low W)	0.39 ± 0.03	0.80 ± 0.14	1.59

Table 5.2: Parameters of the linear fit of the cross section ratio for low- W results (this analysis) and high- W (world data).

suggested function

$$R^{04} = c_0 \left(\frac{Q^2}{M_V^2} \right)^{c_1}, \quad (5.1)$$

where c_0 and c_1 are free parameters and M_V is the ϕ meson mass. The fit parameter values and χ^2 values for the fits are given in Table 5.5. The small $\chi^2/n.d.f$ indicate that the fits are dominated by uncertainties.

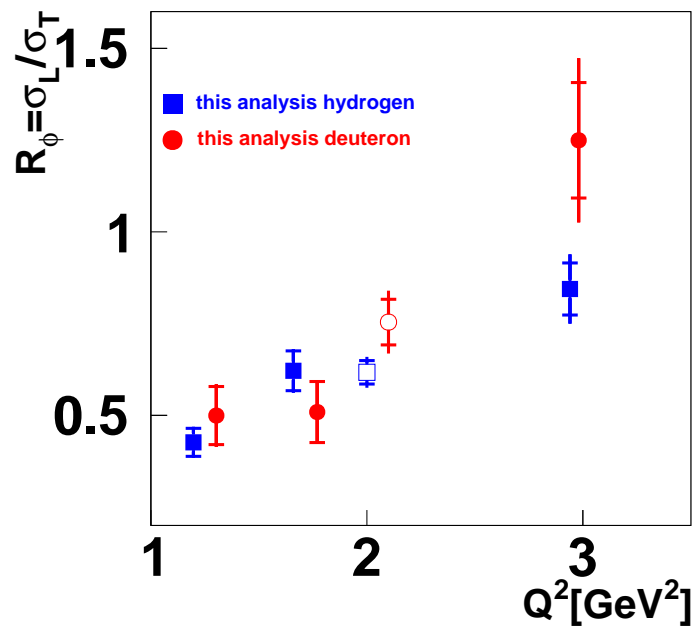


Figure 5.25: Cross section ratio for hydrogen (blue squares) and deuteron (red circles) fitted with a linear function. Black line represents unified fit for hydrogen and deuteron, the fit parameters are shown on the plot. Open symbols denote overall values. The inner error bars represent the statistical uncertainties, the outer ones indicate the statistical and systematic uncertainties added in quadrature. For deuteron data the t' range is $0.04 \text{ GeV} < -t' < 0.4 \text{ GeV}$, for hydrogen one $0. \text{ GeV} < -t' < 0.4 \text{ GeV}$.

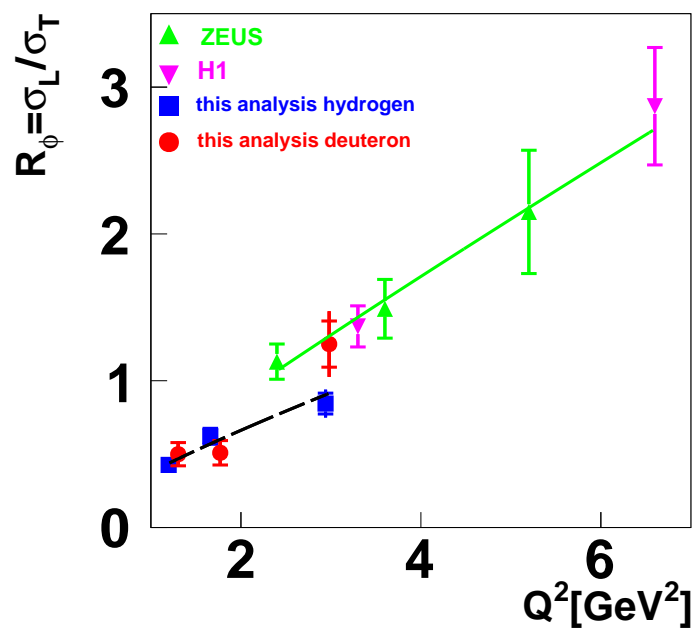


Figure 5.26: Linear fit of the cross section ratio obtained in this analysis (dashed line) in comparison with a linear fit of results from H1 and ZEUS (full line).

Chapter 6

Conclusions

In this thesis the exclusive ϕ meson production from a deep-inelastic scattering of a 27.6 GeV unpolarized lepton beam on an unpolarized hydrogen and an unpolarized or longitudinally polarized deuteron gas targets was studied. The data used in the analysis were recorded at experiment HERMES in in the two time periods from 1998 to 2000 and from 2006 to 2007 years. The results were obtained in the kinematic region of the photon virtuality between $1 \text{ GeV}^2 < Q^2 < 7 \text{ GeV}^2$ and the center-of-mass energy from $W > 2 \text{ GeV}$ in three bins of Q^2 and four bins of t' . Measurements of angular and momentum distributions of the scattered lepton and vector meson decay products, namely two oppositely charged kaons, give an access to the nucleon structure in terms of GPDs and to the production mechanism. The final spin states of the vector meson are described by elements of spin density matrix, which depend on amplitudes for the spin transition processes between the virtual photon and the vector meson.

By performing a maximum likelihood fit, fifteen unpolarized SDMEs and eight beam polarization involving SDMEs were defined in the notations of Wolf-Schilling and Markus Diehl. From the extracted SDMEs in Wolf-Schilling representation the quantities U_1 , U_2 and U_3 which indicate presence of unnatural parity exchange in ϕ meson production mechanism. The quantities are statistically zero for the integrated kinematics, which is in agreement with theory expectations of natural parity exchange dominance for the ϕ meson production. Another important property of the ϕ meson production is s-channel helicity conservation, which can be tested using values of certain SDMEs. No s-channel helicity conservation violation was found for the ϕ meson production.

The longitudinal-to-transverse cross section ratio R was determined as a function of Q^2 . Comparison with the world data indicated W dependence of the ratio.

Appendix A

The relations between the SDME notation of Wolf-Schilling and that of Markus Diehl

The SDMEs in Wolf-Schilling (ρ_{ik}^α , see Sections 2.8, 2.10) and Diehl ($u_{\mu'\mu}^{\nu\nu'}$, see Sections 2.11, 2.12) notations are connected via the next relations:

$$\begin{aligned}
u_{++}^{00} + \epsilon u_{00}^{00} &= r_{00}^{04} & \Im\{u_{0+}^{0+} - u_{0+}^{-0}\} &= \sqrt{2}(\Im r_{10}^7 + \Re r_{10}^8) \\
\Re\{u_{0+}^{0+} - u_{0+}^{-0}\} &= \sqrt{2}(\Im r_{10}^6 - \Re r_{10}^5) & \Im\{u_{0+}^{00}\} &= r_{00}^8/\sqrt{2} \\
u_{++}^{++} + u_{++}^{--} + 2\epsilon u_{00}^{++} &= 1 - r_{00}^{04} & \Im\{u_{++}^{0+} - u_{++}^{-0}\} &= -2\Im r_{10}^3 \\
u_{-+}^{-+} &= r_{1-1}^1 - \Im r_{1-1}^2 & \Im\{u_{0+}^{0-} - u_{0+}^{+0}\} &= \sqrt{2}(\Im r_{10}^7 - \Re r_{10}^8) \\
\Re\{u_{0+}^{00}\} &= -r_{00}^5/\sqrt{2} & \Im\{u_{++}^{-+}\} &= -\Im r_{1-1}^3 \\
\Re\{u_{++}^{0+} - u_{++}^{-0} + 2\epsilon u_{00}^{0+}\} &= 2\Re r_{10}^{04} & \Im(u_{0+}^{++} + u_{0+}^{--}) &= \sqrt{2}r_{11}^8 \\
\Re\{u_{-+}^{0+}\} &= \Re r_{10}^1 - \Im r_{10}^2 & \Im\{u_{0+}^{-+}\} &= (\Im r_{1-1}^7 + \Re r_{1-1}^8)/\sqrt{2} \\
\Re\{u_{0+}^{0-} - u_{0+}^{+0}\} &= \sqrt{2}(\Im r_{10}^6 + \Re r_{10}^5) & \Im\{u_{0+}^{+-}\} &= -(\Im r_{1-1}^7 - \Re r_{1-1}^8)/\sqrt{2} \\
\Re\{u_{++}^{-+} - \epsilon u_{00}^{-+}\} &= r_{1-1}^{04} \\
\Re\{u_{-+}^{++}\} &= r_{11}^1 \\
\Re\{u_{0+}^{++} + u_{0+}^{--}\} &= -\sqrt{2}r_{11}^5 \\
\Re\{u_{0+}^{-+}\} &= -(\Im r_{1-1}^6 - \Re r_{1-1}^5)/\sqrt{2} \\
\Re\{u_{-+}^{00}\} &= r_{00}^1 \\
\Re\{u_{-+}^{+0}\} &= \Re r_{10}^1 + \Im r_{10}^2 \\
\Re\{u_{0+}^{+-}\} &= -(\Im r_{1-1}^6 + \Re r_{1-1}^5)/\sqrt{2} \\
u_{-+}^{+-} &= r_{1-1}^1 + \Im r_{1-1}^2
\end{aligned}$$

Appendix B

The relations between the SDMEs in the Wolf-Schilling notation and amplitudes

Relations between SDMEs in Wolf-Schilling notation (ρ_{ik}^α , see Sections 2.8, 2.10) and helicity amplitudes are presented below. For convenience, the abbreviation $\widetilde{\Sigma} \equiv \frac{1}{2}\sum_{\lambda_N\lambda_N}$ is introduced for the summation over the final nucleon helicity indices and averaging over the initial spin states of the nucleon. If $T_{\lambda_V\lambda_\gamma}$ appears without the symbol $\widetilde{\Sigma}$, all nucleon helicity indices are equal to 1/2.

A: $\gamma_L^* \rightarrow \phi_L$ and $\gamma_T^* \rightarrow \phi_T$

$$\begin{aligned} r_{00}^{04} &= \widetilde{\Sigma} (\epsilon |T_{00}|^2 + |T_{01}|^2 + |U_{01}|^2) / \sigma_{tot}, \\ r_{1-1}^1 &= \frac{1}{2} \widetilde{\Sigma} (|T_{11}|^2 + |T_{1-1}|^2 - |U_{11}|^2 - |U_{1-1}|^2) / \sigma_{tot}, \\ \Im r_{1-1}^2 &= \frac{1}{2} \widetilde{\Sigma} (-|T_{11}|^2 + |T_{1-1}|^2 + |U_{11}|^2 - |U_{1-1}|^2) / \sigma_{tot}, \end{aligned}$$

B: interference of $\gamma_L^* \rightarrow \phi_L$ and $\gamma_T^* \rightarrow \phi_T$

$$\begin{aligned} \Re r_{10}^5 &= \frac{1}{\sqrt{8}} \widetilde{\Sigma} \Re (2T_{10}T_{01}^* + (T_{11} - T_{1-1})T_{00}^*) / \sigma_{tot}, \\ \Im r_{10}^6 &= \frac{1}{\sqrt{8}} \widetilde{\Sigma} \Re (2U_{10}U_{01}^* - (T_{11} + T_{1-1})T_{00}^*) / \sigma_{tot}, \\ \Im r_{10}^7 &= \frac{1}{\sqrt{8}} \widetilde{\Sigma} \Im (2U_{10}U_{01}^* - (T_{11} + T_{1-1})T_{00}^*) / \sigma_{tot}, \\ \Re r_{10}^8 &= \frac{1}{\sqrt{8}} \widetilde{\Sigma} \Im (-2T_{10}T_{01}^* + (T_{11} - T_{1-1})T_{00}^*) / \sigma_{tot}, \end{aligned}$$

C: $\gamma_T^* \rightarrow \phi_L$

$$\begin{aligned} \Re r_{10}^{04} &= \widetilde{\Sigma} \Re (\epsilon T_{10}T_{00}^* + \frac{1}{2}T_{01}(T_{11} - T_{1-1})^* + \frac{1}{2}U_{01}(U_{11} - U_{1-1})^*) / \sigma_{tot}, \\ \Re r_{10}^1 &= \widetilde{\Sigma} \Re (-T_{01}(T_{11} - T_{1-1})^* + U_{01}(U_{11} + U_{1-1})^*) / \sigma_{tot}, \\ \Im r_{10}^2 &= \frac{1}{2} \widetilde{\Sigma} \Re (T_{01}(T_{11} + T_{1-1})^* + U_{01}(U_{11} + U_{1-1})^*) / \sigma_{tot}, \\ r_{00}^5 &= \sqrt{2} \widetilde{\Sigma} \Re (T_{01}T_{00}^*) / \sigma_{tot}, \\ r_{00}^1 &= \sqrt{2} \widetilde{\Sigma} \Re (-|T_{01}|^2 + |U_{01}|^2) / \sigma_{tot}, \\ \Im r_{10}^3 &= -\frac{1}{2} \widetilde{\Sigma} \Im (T_{01}(T_{11} + T_{1-1})^* + U_{01}(U_{11} - U_{1-1})^*) / \sigma_{tot}, \\ r_{00}^8 &= \sqrt{2} \widetilde{\Sigma} \Im (T_{01}T_{00}^*) / \sigma_{tot}, \end{aligned}$$

D: $\gamma_L^* \rightarrow \phi_T$

$$r_{11}^5 = \frac{1}{\sqrt{2}} \widetilde{\sum} \Re (T_{10}(T_{11} - T_{1-1})^* + U_{10}(U_{11} - U_{1-1})^*) / \sigma_{tot},$$

$$r_{1-1}^5 = \frac{1}{\sqrt{2}} \widetilde{\sum} \Re (-T_{10}(T_{11} - T_{1-1})^* + U_{10}(U_{11} - U_{1-1})^*) / \sigma_{tot},$$

$$\Im r_{1-1}^6 = \frac{1}{\sqrt{2}} \widetilde{\sum} \Re (T_{10}(T_{11} + T_{1-1})^* - U_{10}(U_{11} + U_{1-1})^*) / \sigma_{tot},$$

$$\Im r_{1-1}^7 = \frac{1}{\sqrt{2}} \widetilde{\sum} \Im (T_{10}(T_{11} + T_{1-1})^* - U_{10}(U_{11} + U_{1-1})^*) / \sigma_{tot},$$

$$r_{11}^8 = -\frac{1}{\sqrt{2}} \widetilde{\sum} \Im (T_{10}(T_{11} - T_{1-1})^* + U_{10}(U_{11} - U_{1-1})^*) / \sigma_{tot},$$

$$r_{1-1}^8 = \frac{1}{\sqrt{2}} \widetilde{\sum} \Im (T_{10}(T_{11} - T_{1-1})^* - U_{10}(U_{11} - U_{1-1})^*) / \sigma_{tot},$$

E: $\gamma_T^* \rightarrow \phi_{-T}$

$$r_{1-1}^{04} = \widetilde{\sum} \Re (-\epsilon|T_{10}|^2 + \epsilon|U_{10}|^2 + T_{1-1}T_{11}^* - U_{1-1}U_{11}^*) / \sigma_{tot},$$

$$r_{11}^1 = \widetilde{\sum} \Re (T_{1-1}T_{11}^* + U_{1-1}U_{11}^*) / \sigma_{tot},$$

$$\Im r_{1-1}^3 = -\widetilde{\sum} \Im (T_{1-1}T_{11}^* + U_{1-1}U_{11}^*) / \sigma_{tot},$$

Appendix C

Comparison of data to Monte Carlo (PYTHIA and RhoMC generators)

In Figures C.5 -C.7 kinematic distributions for different Q^2 and t' bins of the 1998-2000 and the 2006-2007 years for hydrogen data, PYTHIA and RhoMC for proton target without implemented SDMEs (except from the first one) are presented. In Figures C.1 - C.3 the same kinematic distributions, but for deuteron data are presented. Neither PYTHIA nor RhoMC can produce data for deuteron target, so the MonteCarlo sets used in conjunction with deuteron data were obtained as a mixture of neutron and proton sets. The proportion of the mixture was chosen in such a way that the luminosities of the mixed sets were equal.

All the distributions were normalized to unity.

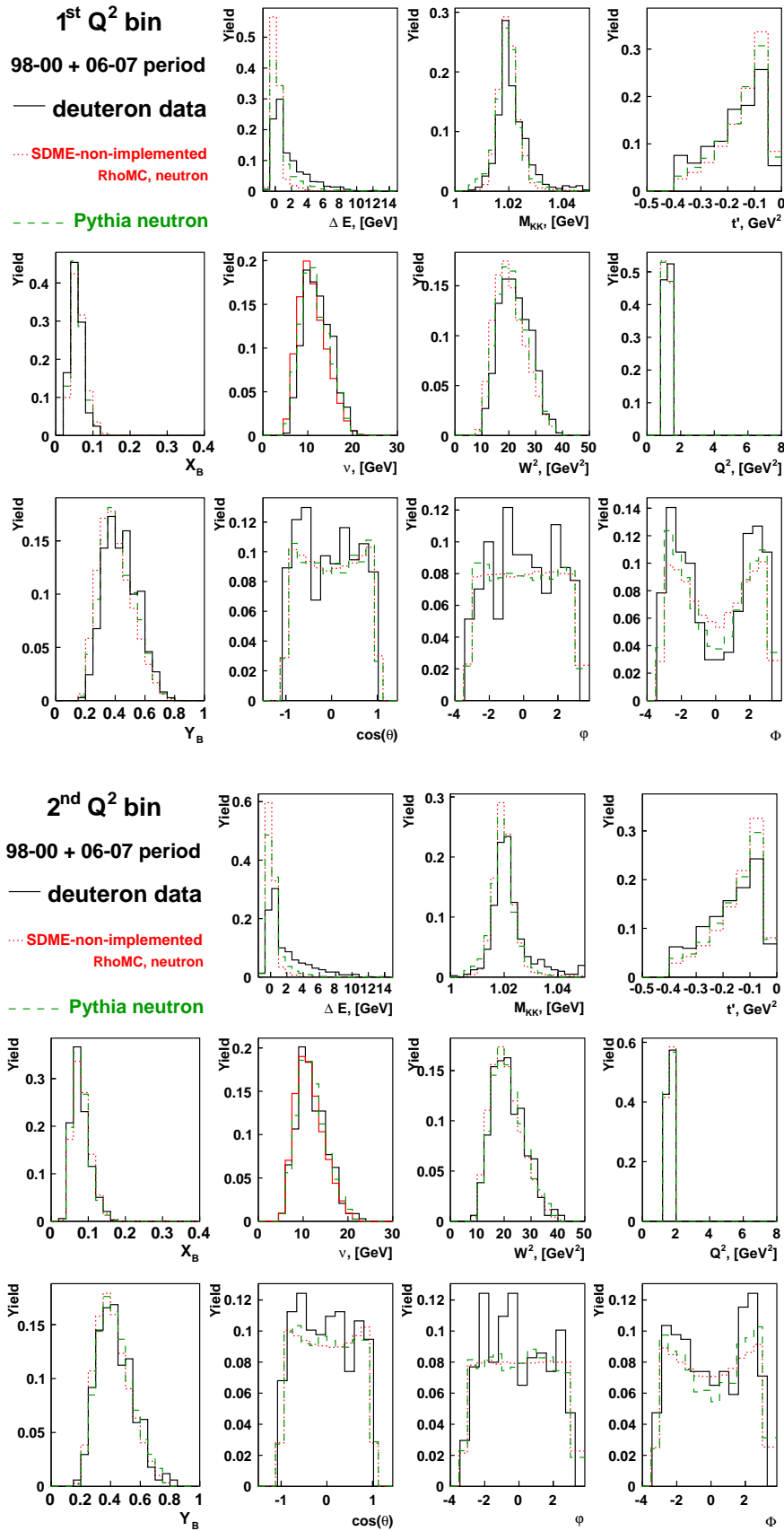
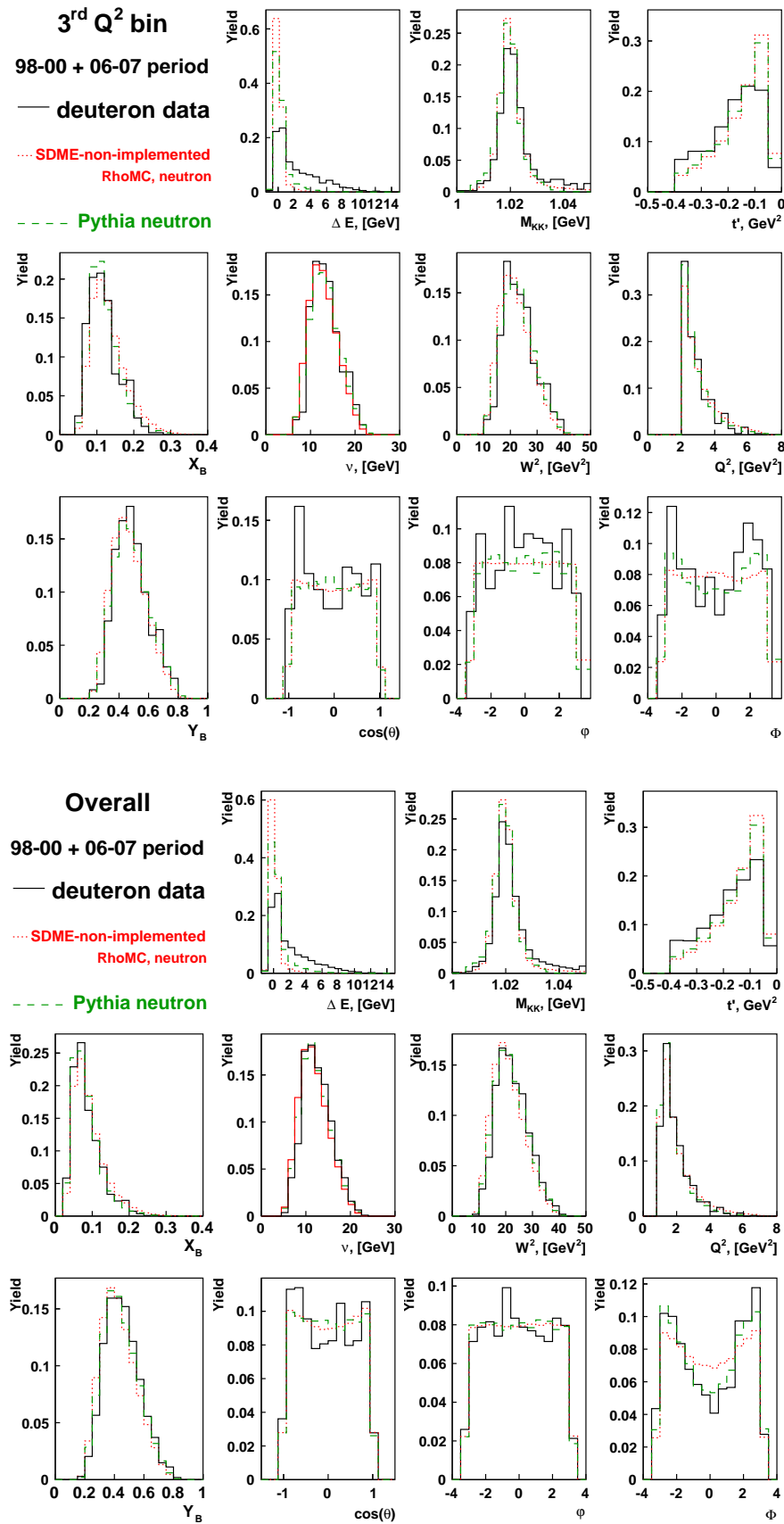


Figure C.1: The comparison of two first Q^2 bins of the full deuteron data set (black line) with Monte Carlo sets, produced by PYTHIA generator (green dashed line) and RhoMC generator (red dotted line) on unpolarized neutron target. PYTHIA and RhoMC does not contain SDMEs (apart from the first one), the angular distributions are affected by HERMES acceptance only. These sets was used for p.d.f normalization.


 Figure C.2: As in Figure C.1, but for the 3rd Q^2 bin and overall kinematics.

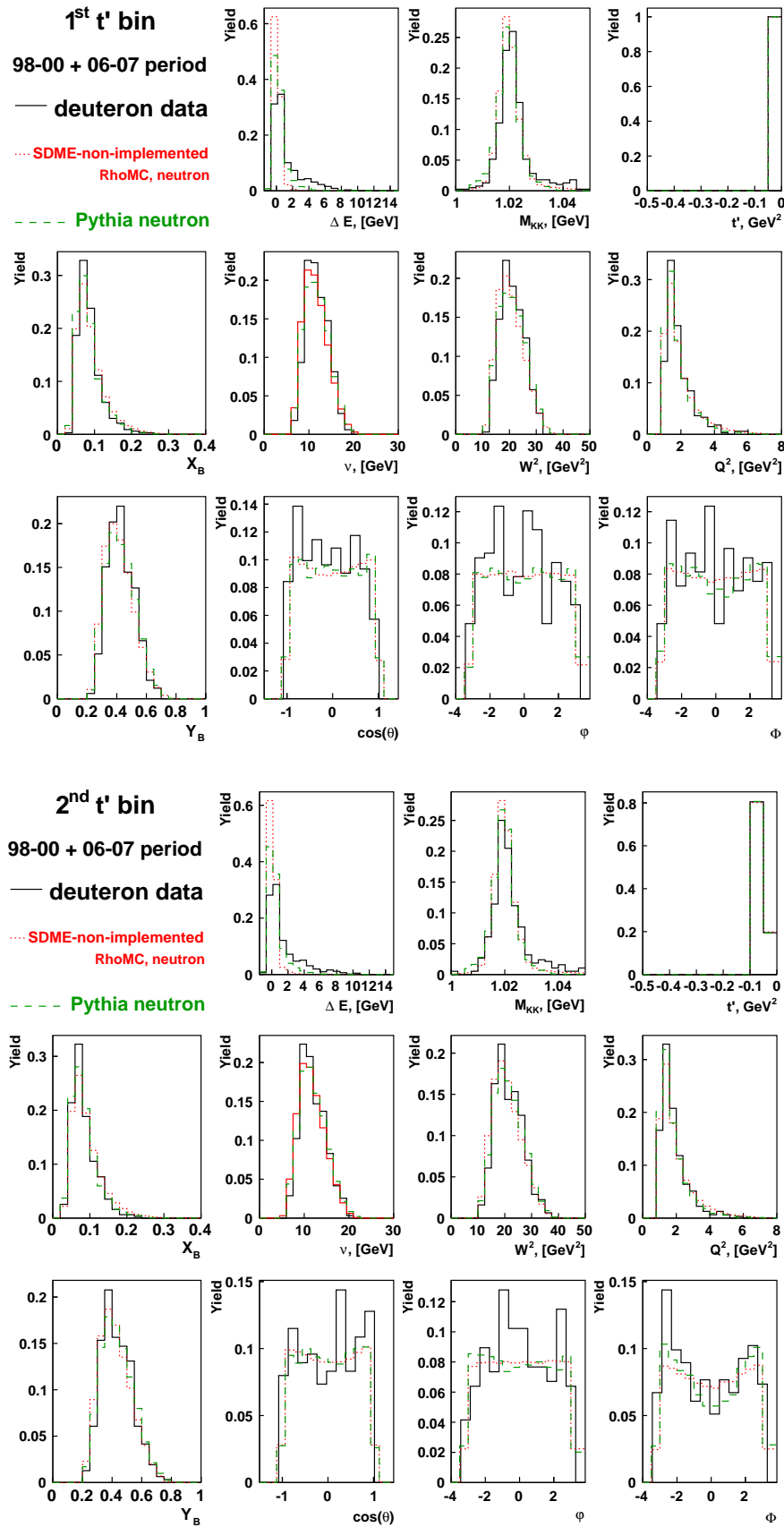
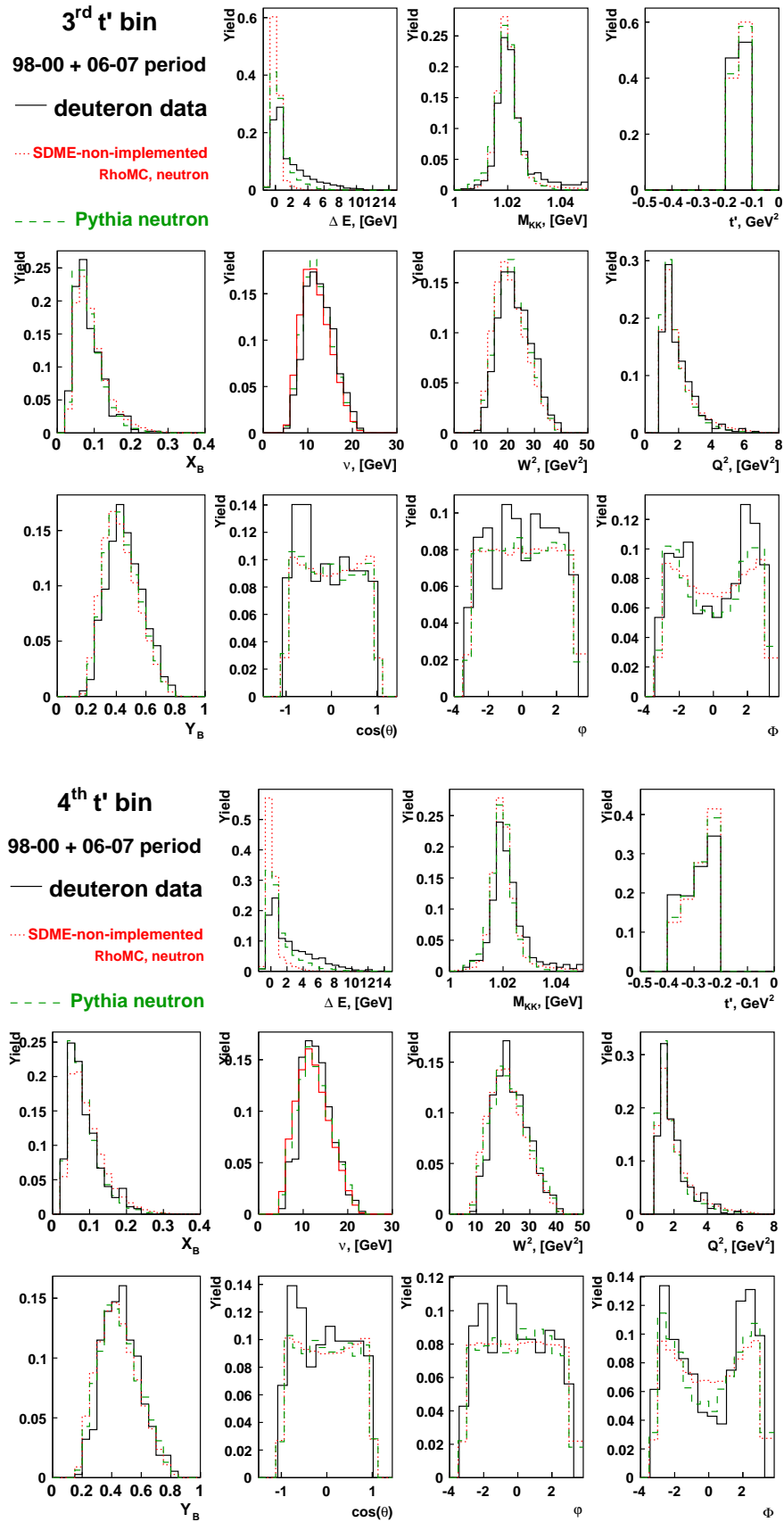


Figure C.3: As in Figure C.1, but for the first two t' bins.


 Figure C.4: As in Figure C.1, but for the 3rd and 4th t' bins.

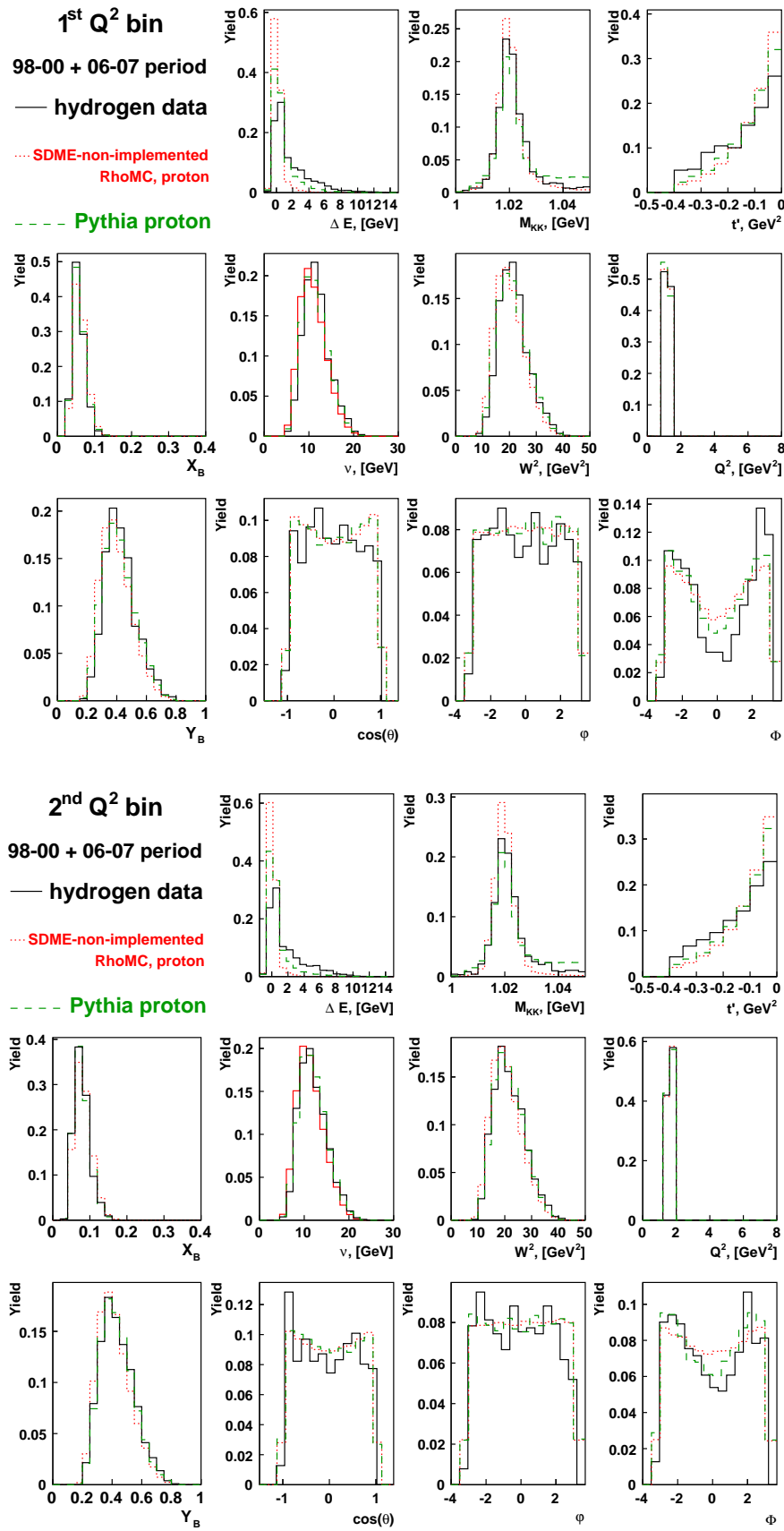


Figure C.5: As in Figure C.1, but for proton data and Monte Carlo sets, generated for hydrogen target.

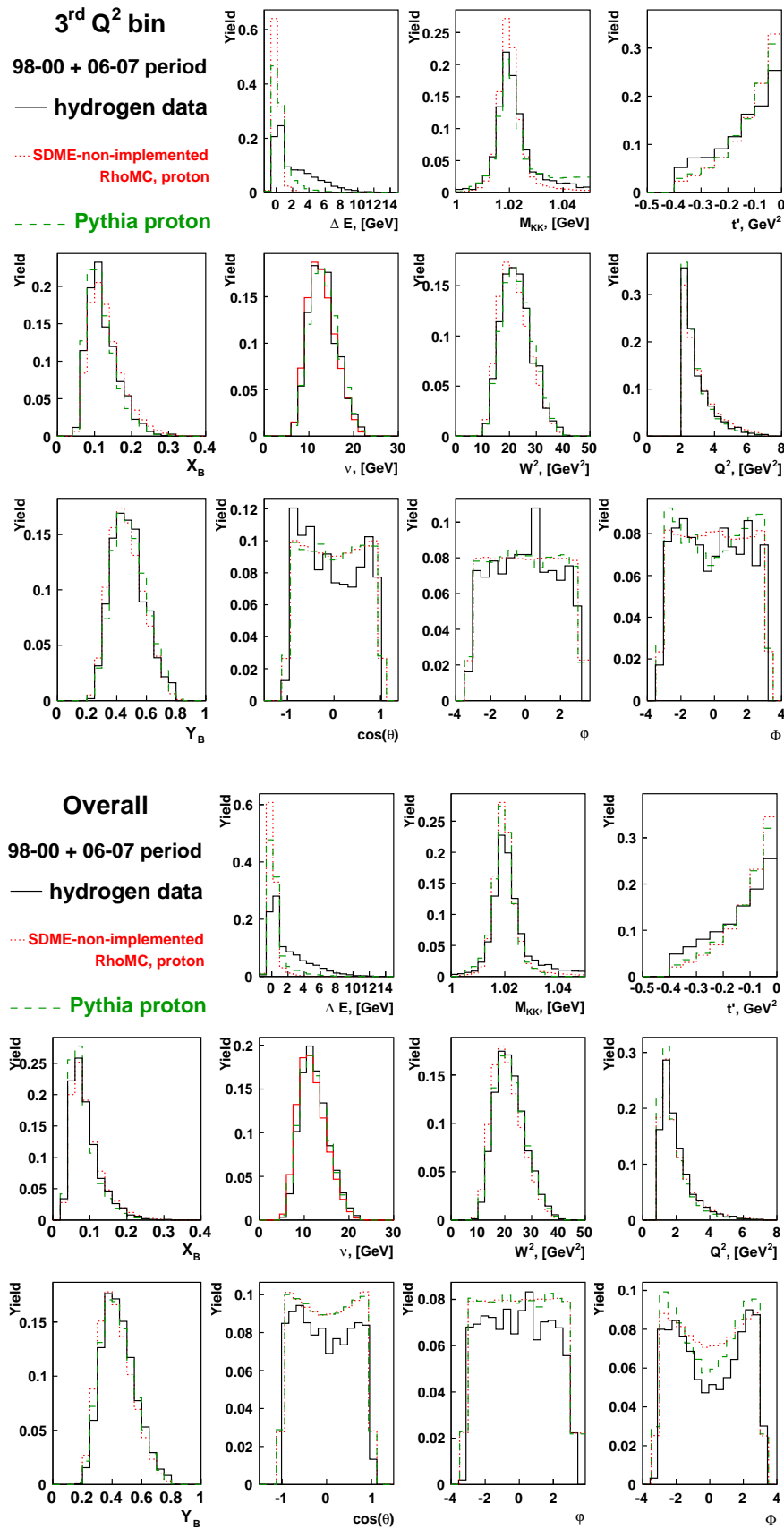


Figure C.6: As in Figure C.2, but for proton data and Monte Carlo sets, generated for hydrogen target.

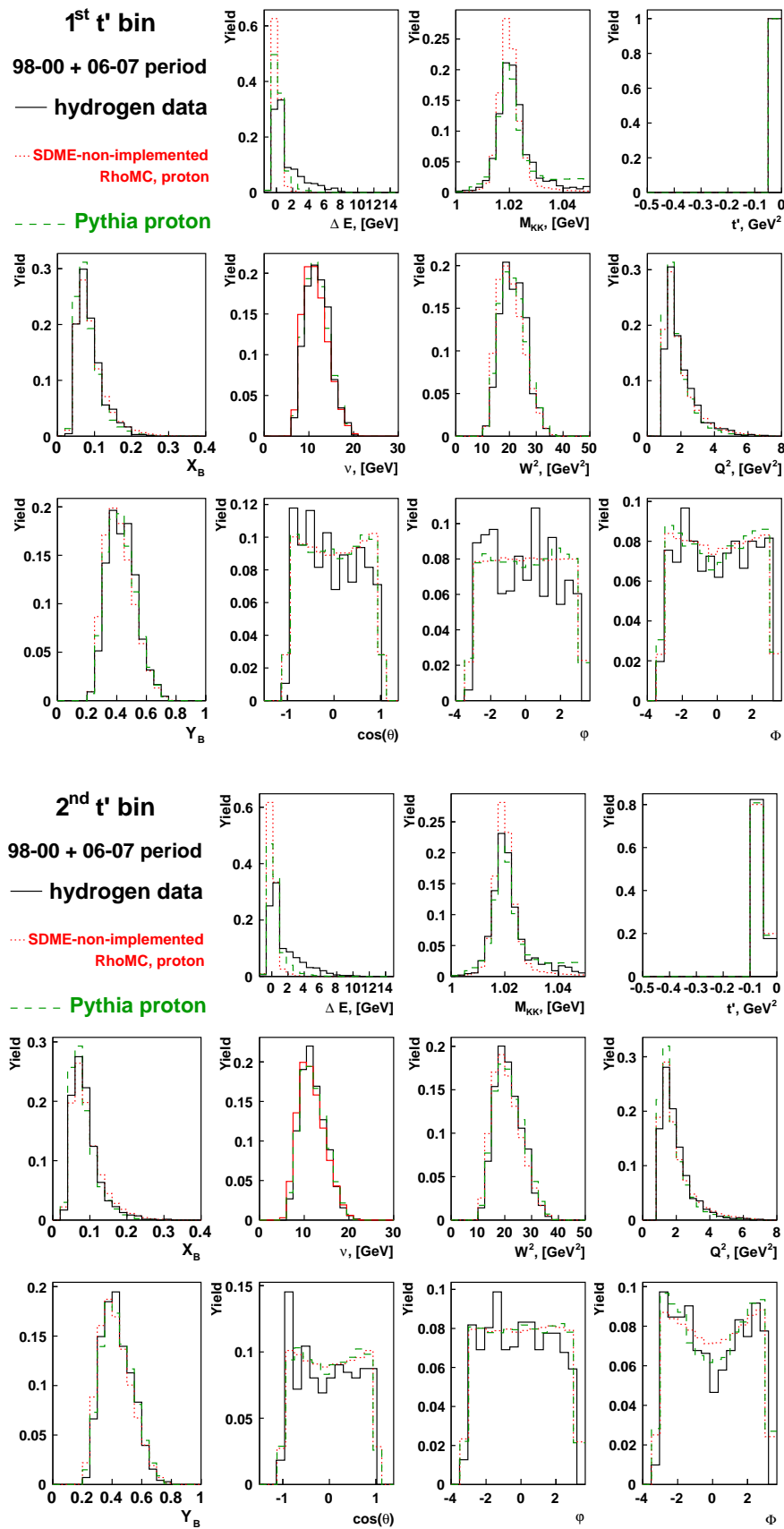


Figure C.7: As in Figure C.3, but for proton data and Monte Carlo sets, generated for hydrogen target.

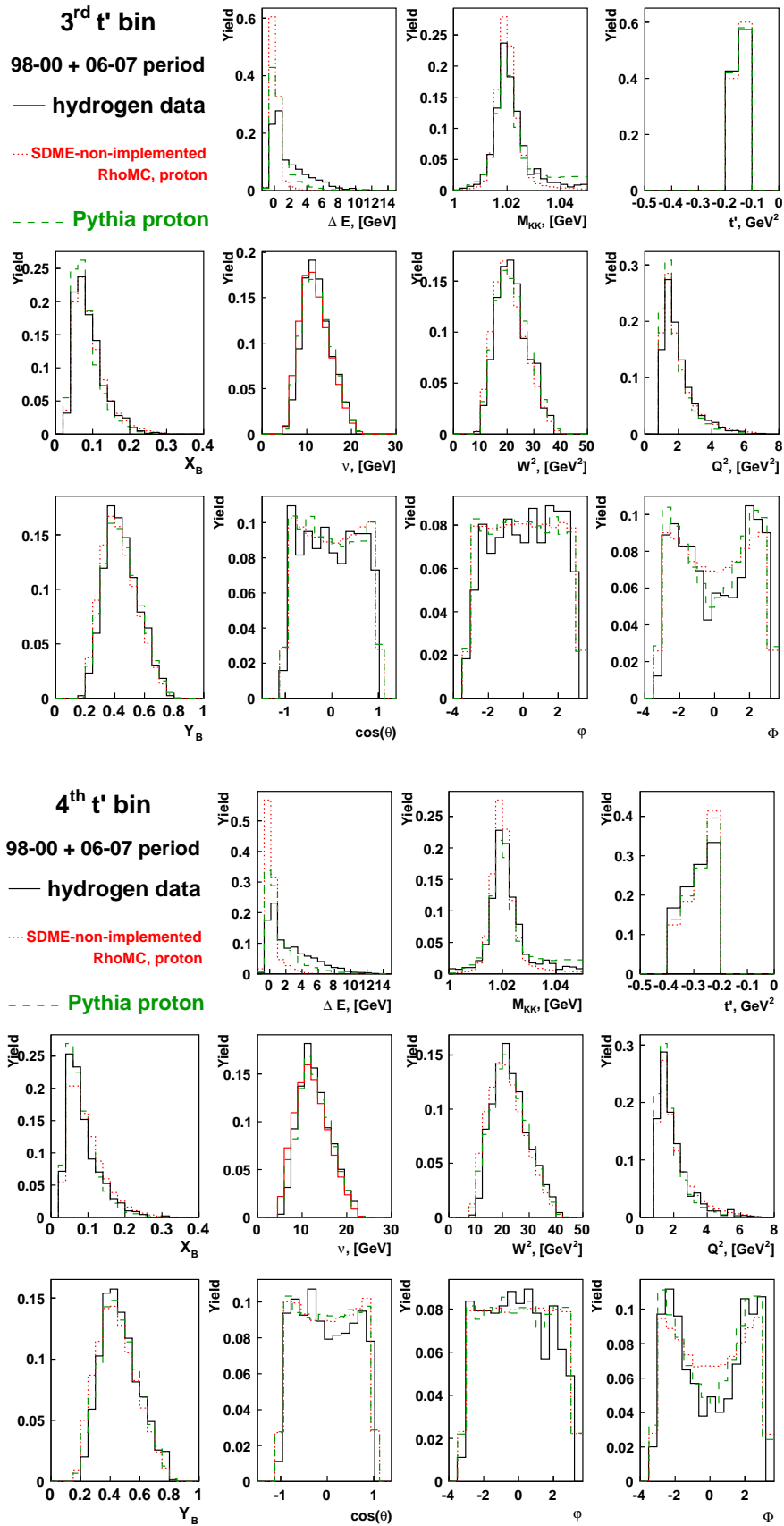


Figure C.8: As in Figure C.4, but for proton data and Monte Carlo sets, generated for hydrogen target.

Appendix D

SDMEs extracted with and without semi-inclusive background subtraction

In Figures D.1 - D.4 Wolf-Schilling SDMEs extracted from 1998-2000, 2006-2007 data set for hydrogen and deuteron targets with and without background subtraction are presented for each Q^2 and t' bin. In Figures D.6 - D.8 are the same results for the SDMEs in Markus Diehl notation.

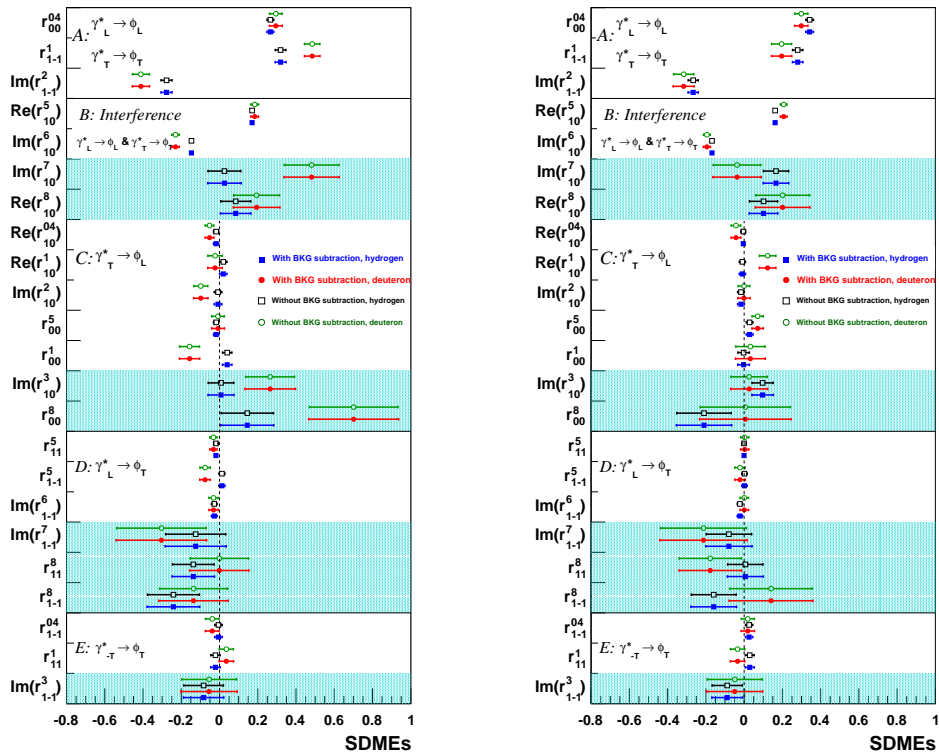


Figure D.1: Wolf-Schilling SDMEs with (solid symbols) and without (open symbols) background subtraction for the 1st (left panel) and the 2nd (right panel) Q^2 bins.

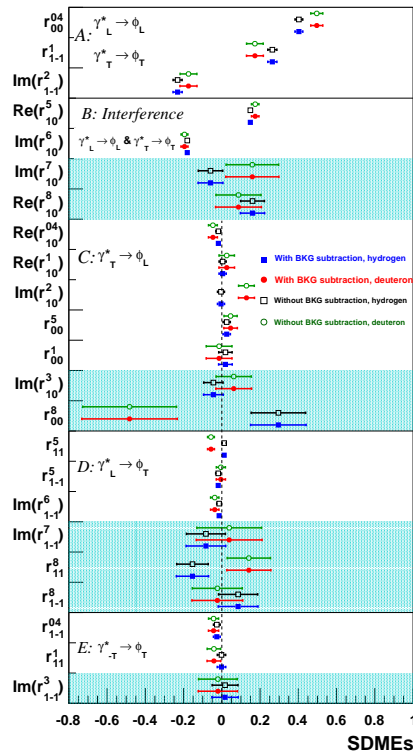


Figure D.2: As in Figure D.1 but for the 3rd Q^2 bin.

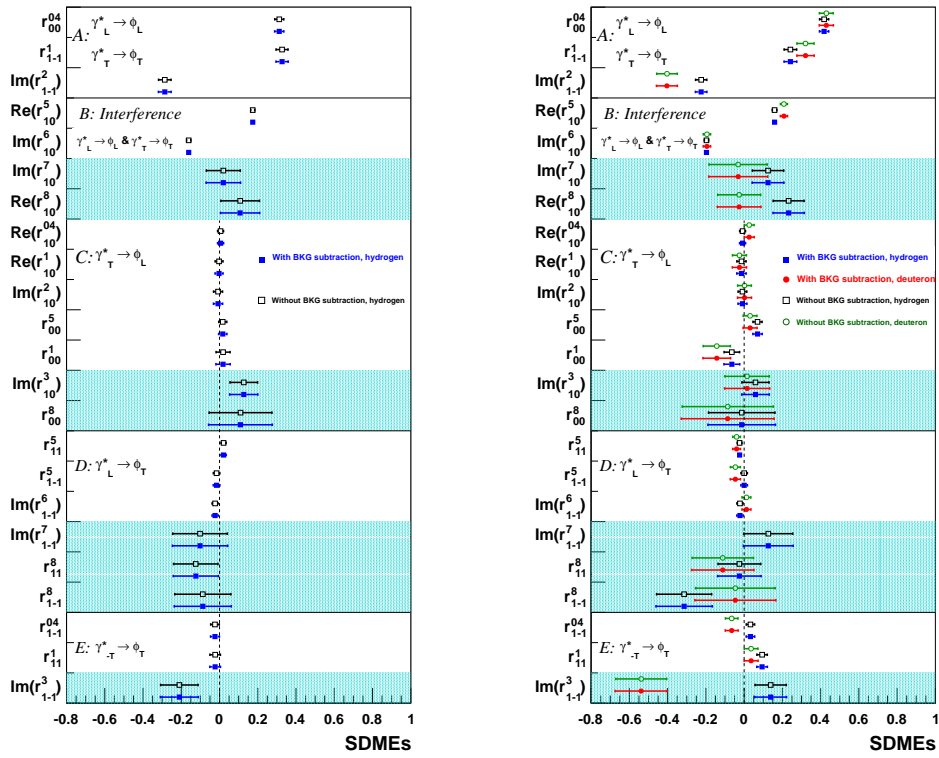


Figure D.3: As in Figure D.1 but for the 1st (left panel) and 2nd (right panel) t' bins.

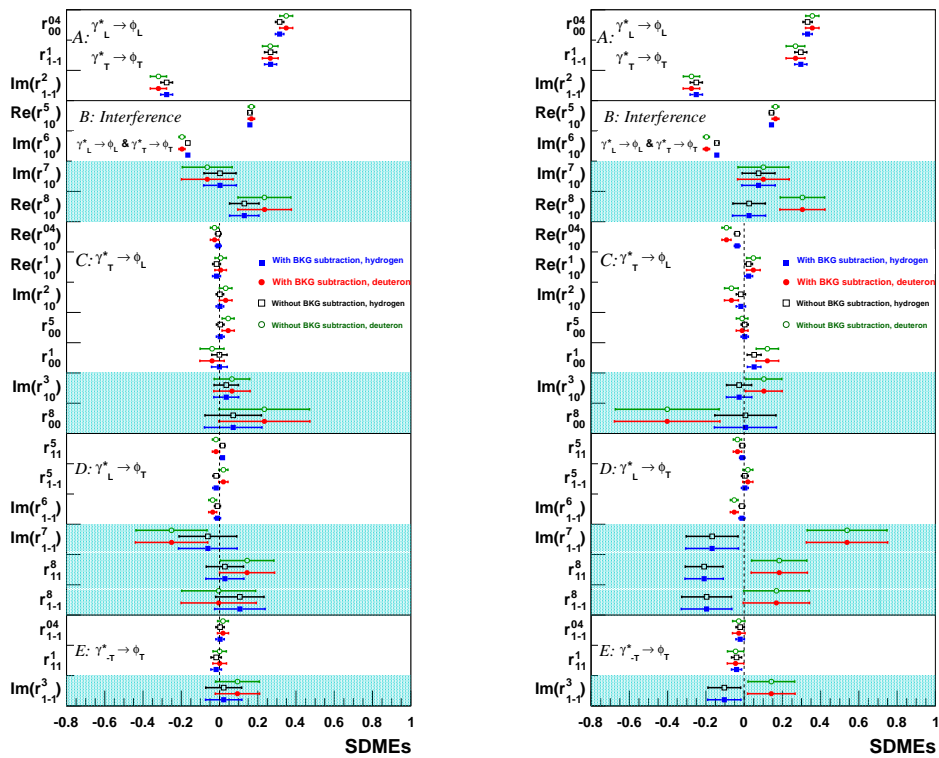


Figure D.4: As in Figure D.1 but for the 3rd (left panel) and 4th (right panel) t' bins.

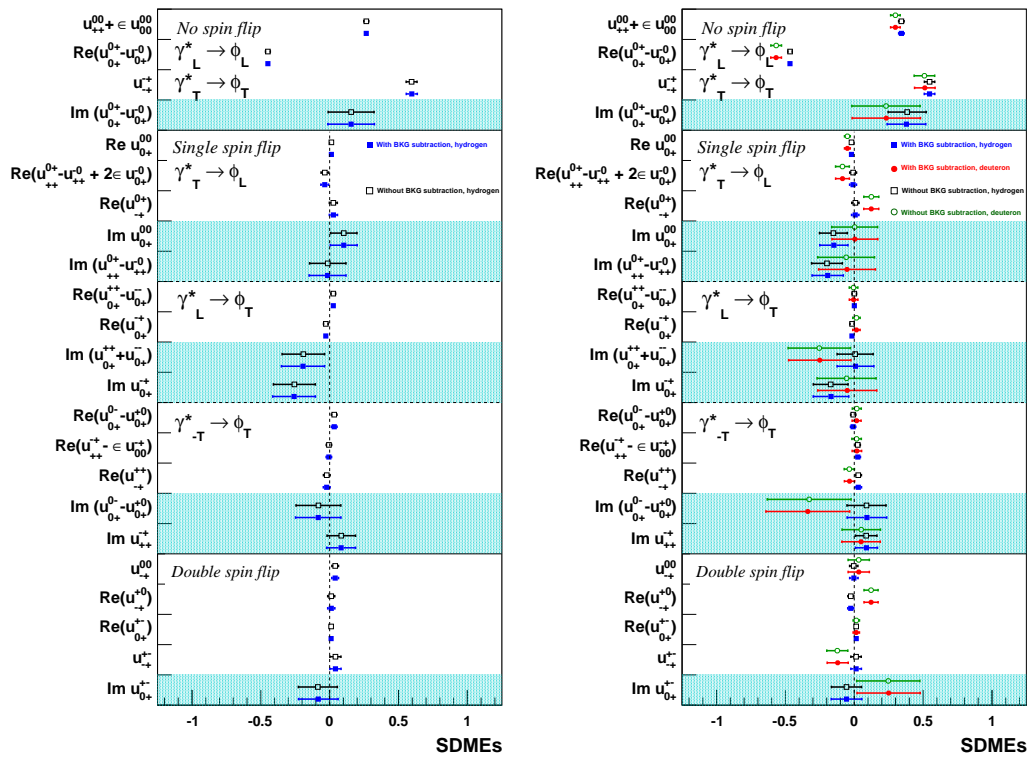


Figure D.5: As in Figure D.1 but for SDMEs in Markus Diehl notation.

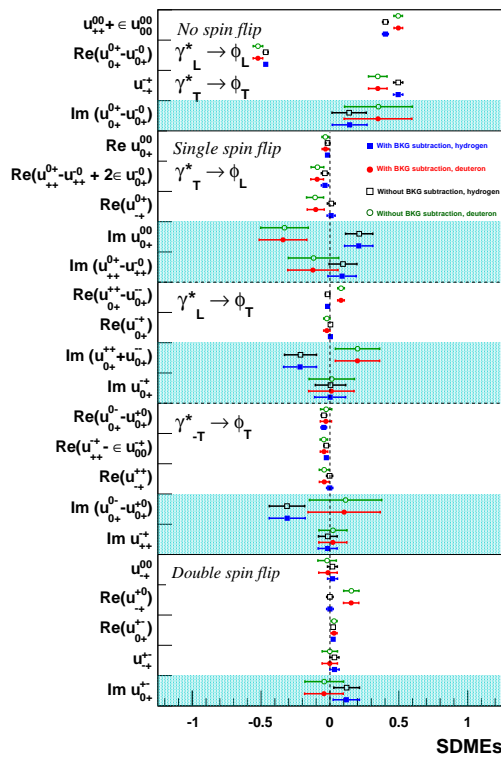


Figure D.6: As in Figure D.2 but for SDMEs in Markus Diehl notation.

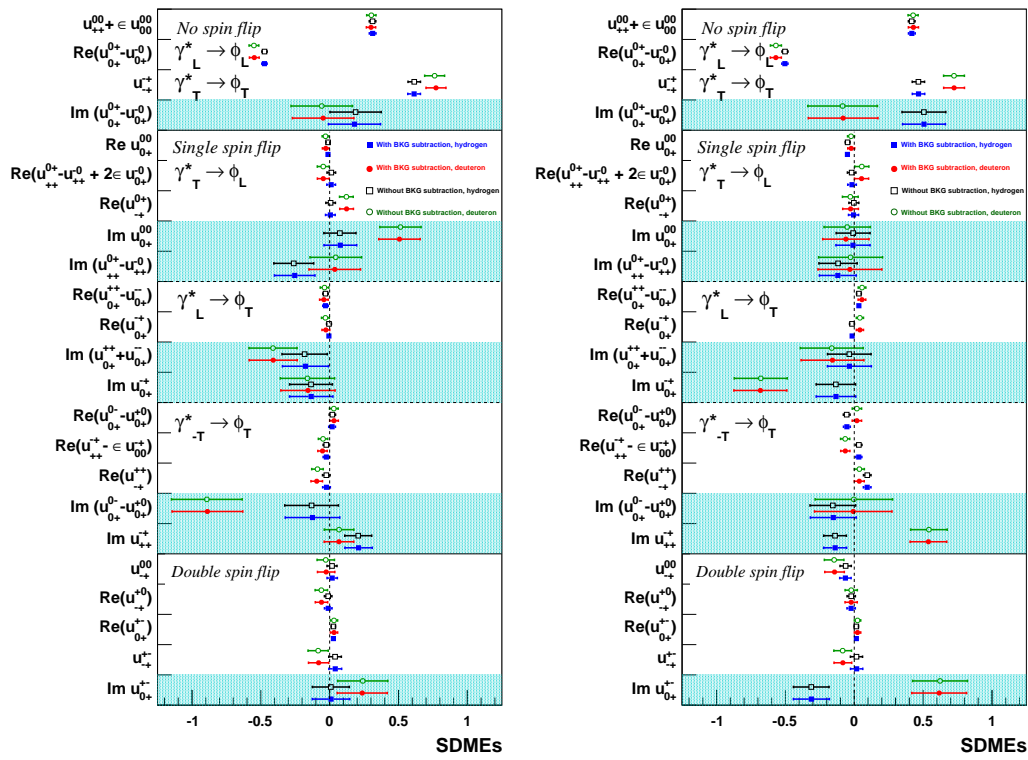


Figure D.7: As in Figure D.3 but for SDMEs in Markus Diehl notation.

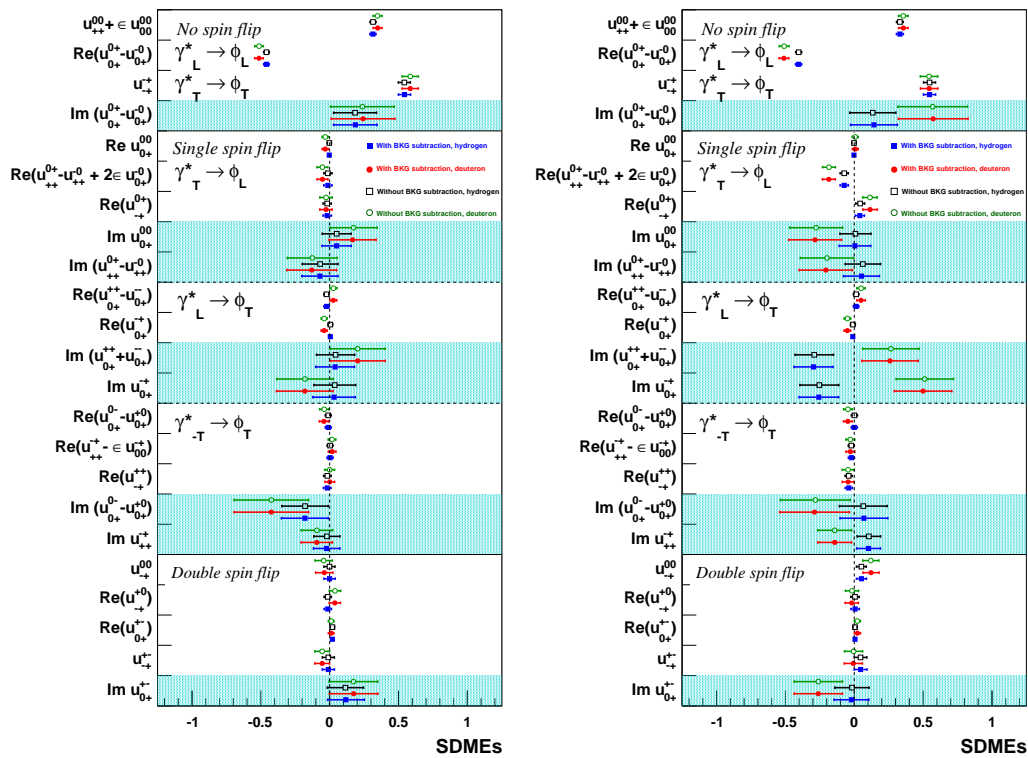


Figure D.8: As in Figure D.4 but for SDMEs in Markus Diehl notation.

Appendix E

SDMEs extracted using for the p. d. f. normalization PYTHIA and RhoMC generated sets.

In Figures E.1 - E.4 Wolf-Schilling SDMEs extracted from 1998-2000, 2006-2007 data set for hydrogen and neutron targets using RhoMC and PYTHIA generated sets for the p. d. f. normalization are presented for each of the Q^2 and t' bin. Figures E.6 - E.6 are the same results for SDMEs in Markus Diehl notation. For th final results extraction PYTHIA-generated sets were used.

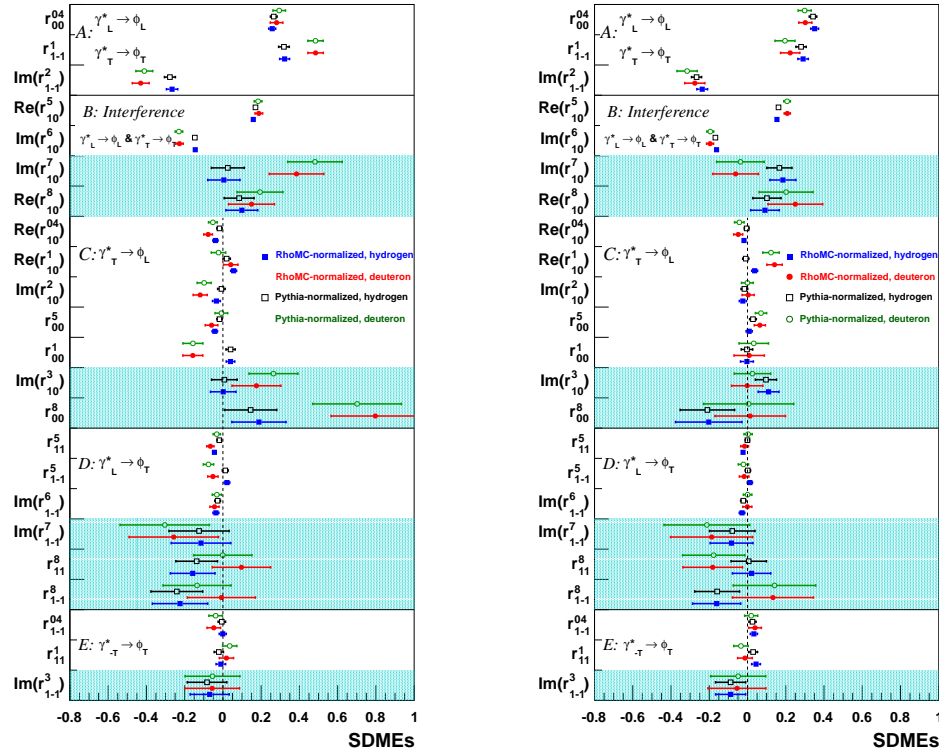


Figure E.1: Wolf-Schilling SDMEs extracted using RhoMC for the p. d. f. normalization (solid symbols) and using PYTHIA (open symbols) for the 1st (left panel) and the 2nd (right panel) Q^2 bins.

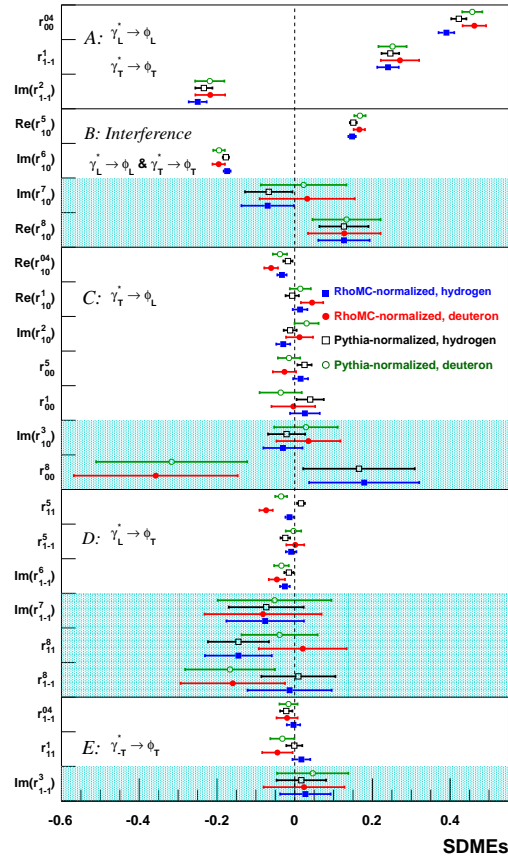


Figure E.2: As in Figure E.1 but for the 3rd Q^2 bin.

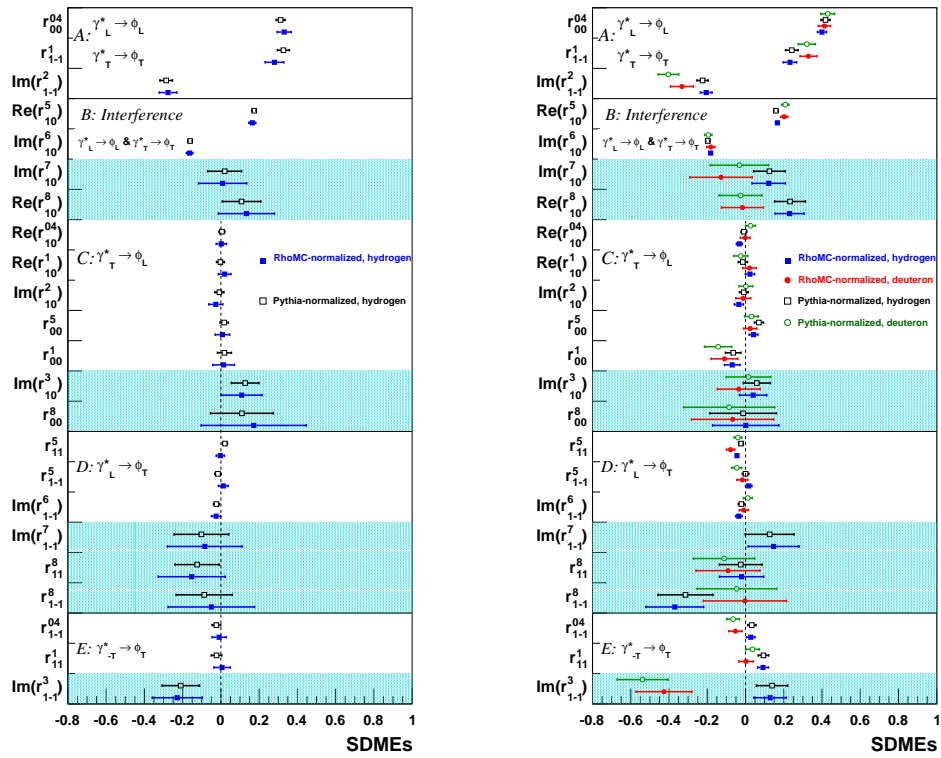


Figure E.3: As in Figure E.1 but for the 1st (left panel) and 2nd (right panel) t' bins.

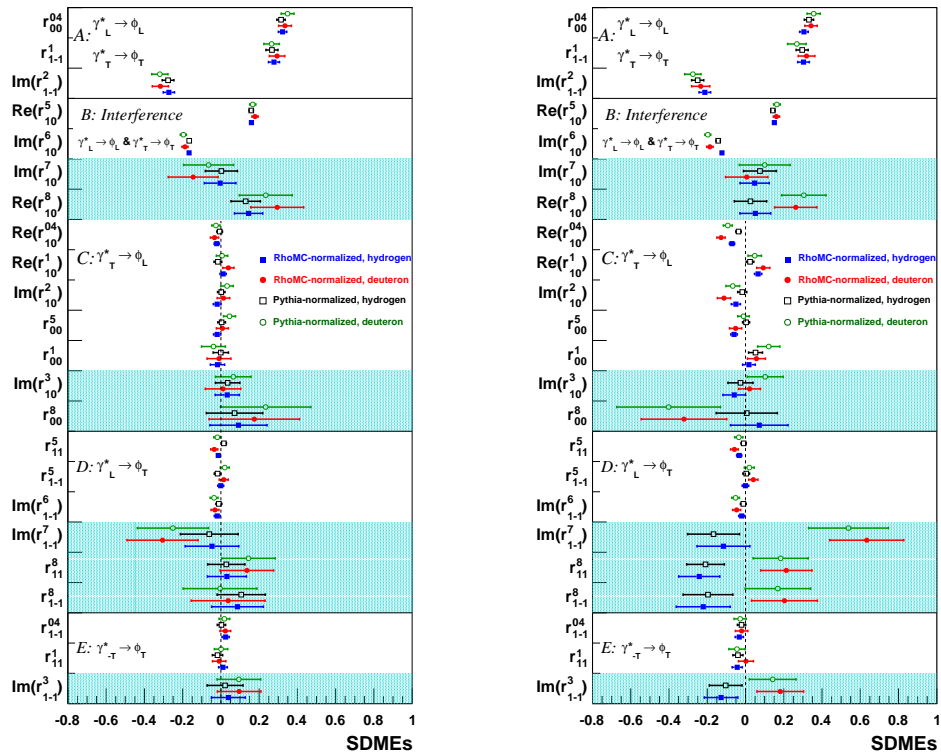


Figure E.4: As in Figure E.1 but for the 3rd (left panel) and 4th (right panel) t' bins.

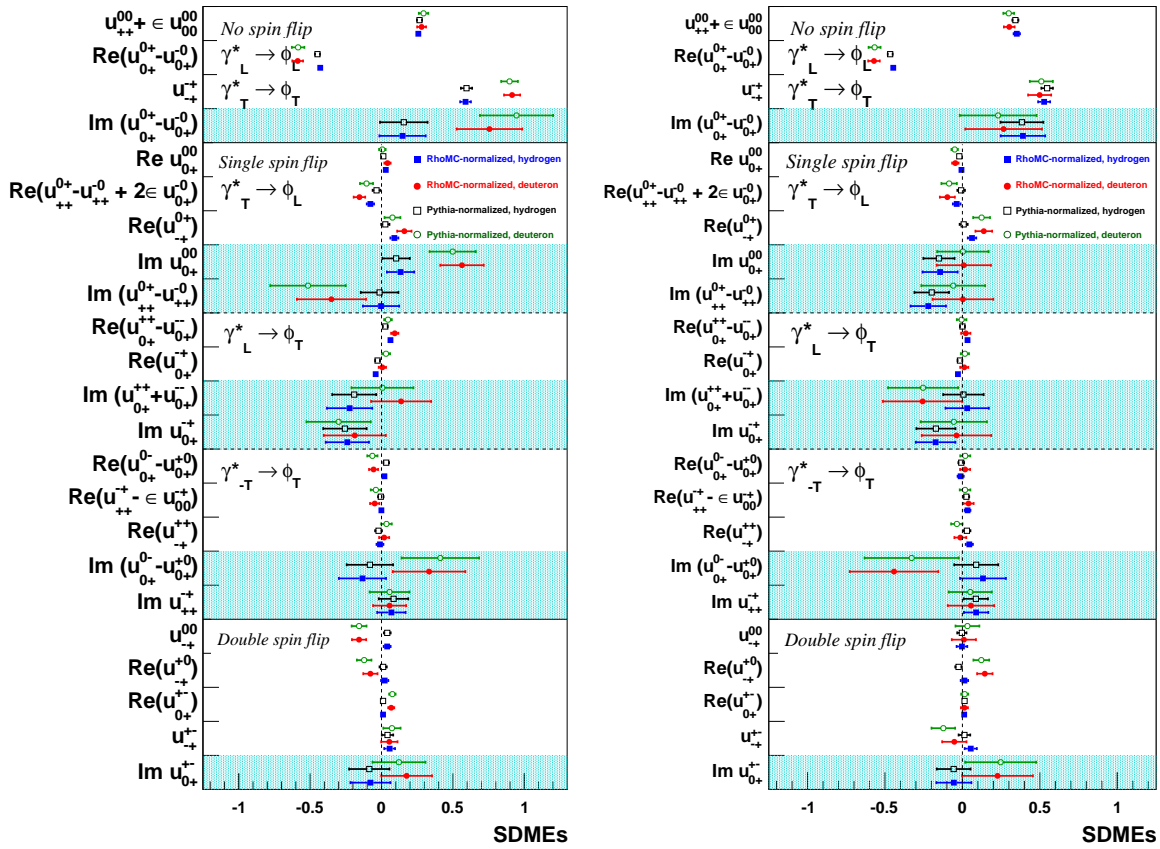


Figure E.5: As in Figure E.1 but for SDMEs in Markus Diehl notation.

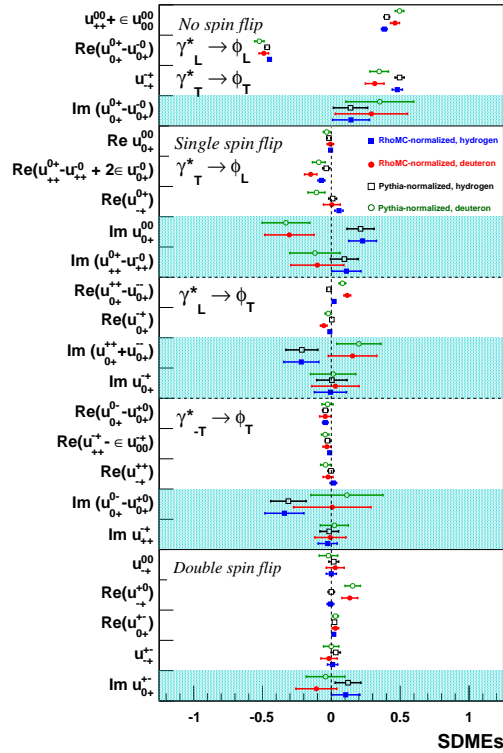


Figure E.6: As in Figure E.2 but for SDMEs in Markus Diehl notation.

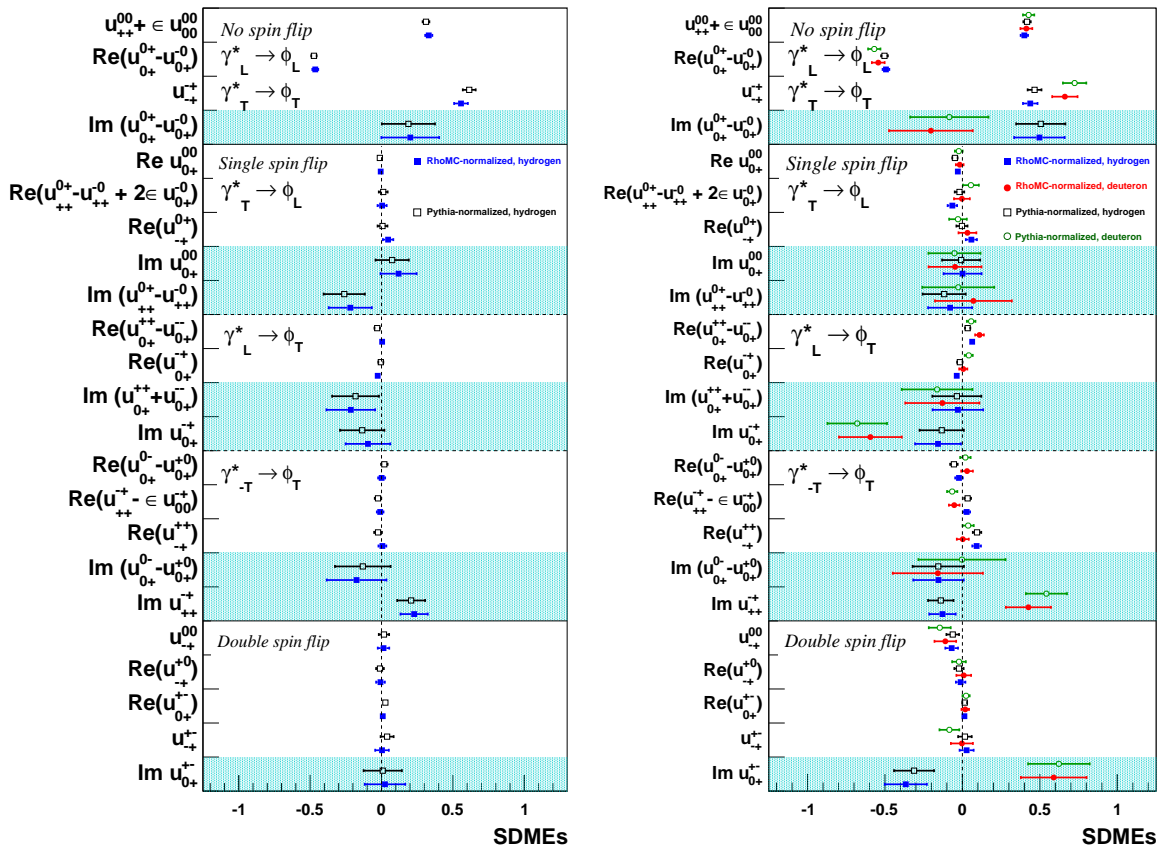


Figure E.7: As in Figure E.3 but for SDMEs in Markus Diehl notation.

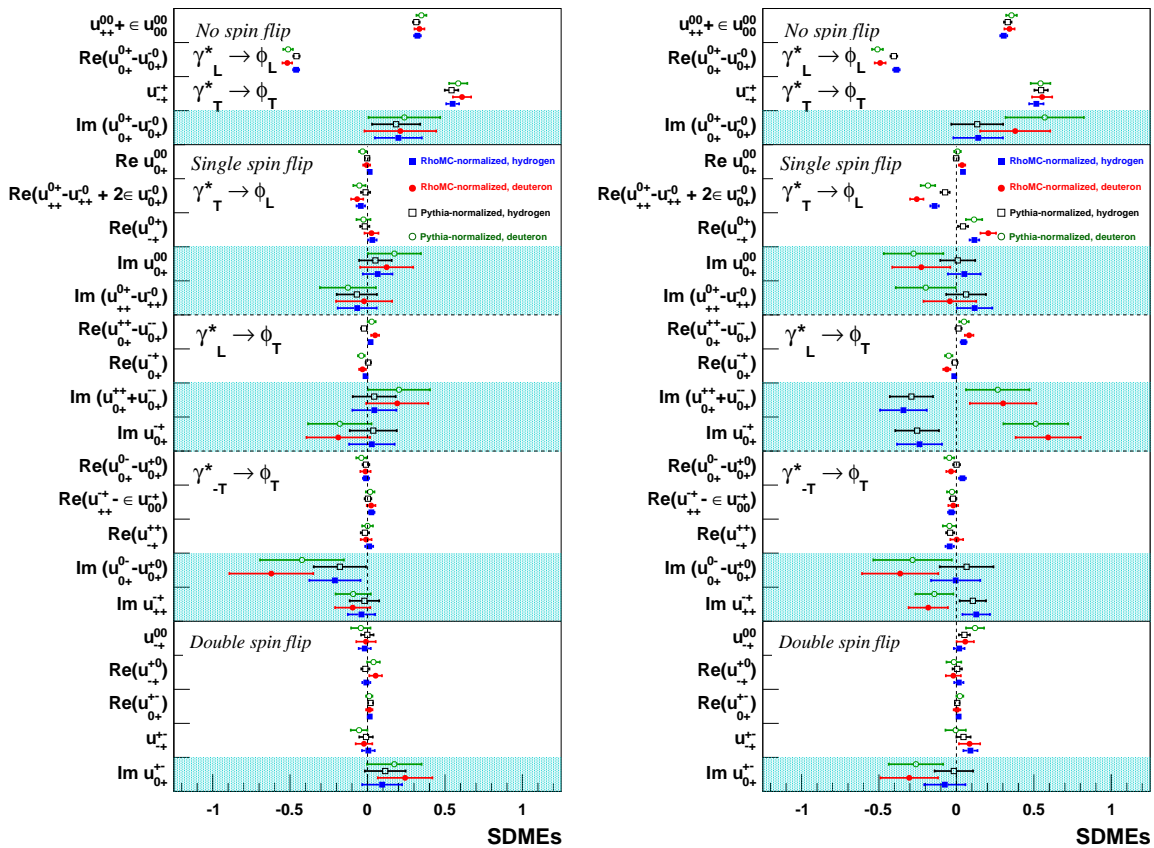


Figure E.8: As in Figure E.4 but for SDMEs in Markus Diehl notation.

Appendix F

Tables of results

In Tables F.1 - F.8 are presented SDMEs in Wolf-Schilling notation for hydrogen and deuteron targets extracted from 3 Q^2 and 4 t' bins and for overall kinematics. Those in Markus Diehl notation are given in Tables F.12 - F.19. The U_1, U_2, U_3 quantities for hydrogen and deuteron targets are shown in Tables F.9 and F.10 correspondingly.

Bin	$1.00 \text{ GeV}^2 < Q^2 < 1.40 \text{ GeV}^2, -0.40 \text{ GeV}^2 < t < 0.00 \text{ GeV}^2$	$H : \text{SDME} \pm \text{stat} \pm \text{sys}$	$D : \text{BG} \pm \text{Par} \pm P$	$1.00 \text{ GeV}^2 < Q^2 < 1.40 \text{ GeV}^2, -0.40 < t < -0.04 \text{ GeV}^2$	$D : \text{SDME} \pm \text{stat} \pm \text{sys}$
Element					
r_{00}^{04}	$0.00003 \pm 0.00799 \pm 0.00410$	$0.26587 \pm 0.01747 \pm 0.00898$	$0.00002 \pm 0.01378 \pm 0.00422$	$0.29443 \pm 0.03292 \pm 0.01441$	
r_{1-1}^1	$0.00016 \pm 0.00356 \pm 0.00250$	$0.31918 \pm 0.02780 \pm 0.00435$	$0.00020 \pm 0.00023 \pm 0.00306$	$0.48437 \pm 0.04019 \pm 0.00308$	
$\Im\text{m}(r_{1-1}^2)$	$0.00012 \pm 0.01128 \pm 0.00277$	$-0.27705 \pm 0.02854 \pm 0.01162$	$0.00015 \pm 0.01873 \pm 0.00323$	$-0.41104 \pm 0.04408 \pm 0.01900$	
$\Re\text{e}(r_{10}^5)$	$0.00002 \pm 0.01141 \pm 0.00425$	$0.17033 \pm 0.00955 \pm 0.01217$	$0.00010 \pm 0.00392 \pm 0.00351$	$0.18392 \pm 0.02004 \pm 0.00527$	
$\Im\text{m}(r_{10}^6)$	$0.00000 \pm 0.00224 \pm 0.00323$	$-0.14678 \pm 0.00914 \pm 0.00393$	$0.00002 \pm 0.00277 \pm 0.00297$	$-0.23003 \pm 0.01971 \pm 0.00406$	
$\Im\text{m}(r_{10}^7)$	$0.00005 \pm 0.02085 \pm 0.00619$	$0.02572 \pm 0.08588 \pm 0.02175$	$0.00001 \pm 0.09649 \pm 0.00738$	$0.48146 \pm 0.14252 \pm 0.09677$	
$\Re\text{e}(r_{10}^8)$	$0.00026 \pm 0.01434 \pm 0.00409$	$0.08476 \pm 0.07824 \pm 0.01492$	$0.00002 \pm 0.04443 \pm 0.00570$	$0.19397 \pm 0.11977 \pm 0.04480$	
$\Re\text{e}(r_{10}^{04})$	$0.00010 \pm 0.02100 \pm 0.00188$	$-0.01791 \pm 0.01363 \pm 0.02109$	$0.00011 \pm 0.02489 \pm 0.00323$	$-0.05241 \pm 0.02275 \pm 0.02510$	
$\Re\text{e}(r_{10}^1)$	$0.00010 \pm 0.03643 \pm 0.00271$	$0.01965 \pm 0.01914 \pm 0.03653$	$0.00005 \pm 0.06405 \pm 0.00436$	$-0.02304 \pm 0.03782 \pm 0.06420$	
$\Im\text{m}(r_{10}^2)$	$0.00008 \pm 0.02615 \pm 0.00269$	$-0.00778 \pm 0.01975 \pm 0.02628$	$0.00017 \pm 0.02078 \pm 0.00317$	$-0.09811 \pm 0.03673 \pm 0.02102$	
r_{00}^5	$0.00006 \pm 0.02459 \pm 0.00801$	$-0.01768 \pm 0.01362 \pm 0.02586$	$0.00004 \pm 0.00053 \pm 0.00498$	$-0.00797 \pm 0.03296 \pm 0.05211$	
r_{00}^1	$0.00003 \pm 0.00059 \pm 0.00355$	$0.04024 \pm 0.02424 \pm 0.00360$	$0.00004 \pm 0.00053 \pm 0.00498$	$-0.15676 \pm 0.05222 \pm 0.00501$	
$\Im\text{m}(r_{10}^3)$	$0.00000 \pm 0.00607 \pm 0.00292$	$0.00772 \pm 0.06678 \pm 0.00674$	$0.00009 \pm 0.08909 \pm 0.00523$	$0.26447 \pm 0.12777 \pm 0.08925$	
r_{00}^8	$0.00014 \pm 0.04333 \pm 0.00647$	$0.14508 \pm 0.13646 \pm 0.04381$	$0.00045 \pm 0.09561 \pm 0.00580$	$0.70165 \pm 0.23155 \pm 0.09578$	
r_{11}^5	$0.00018 \pm 0.02540 \pm 0.00490$	$-0.01891 \pm 0.01186 \pm 0.02587$	$0.00011 \pm 0.03347 \pm 0.00608$	$-0.03206 \pm 0.01893 \pm 0.03402$	
r_{1-1}^5	$0.00013 \pm 0.00886 \pm 0.00283$	$0.01249 \pm 0.01561 \pm 0.00930$	$0.00006 \pm 0.02304 \pm 0.00333$	$-0.07540 \pm 0.02702 \pm 0.02328$	
$\Im\text{m}(r_{1-1}^6)$	$0.00006 \pm 0.00922 \pm 0.00307$	$-0.02733 \pm 0.01480 \pm 0.00972$	$0.00008 \pm 0.01252 \pm 0.00298$	$-0.03150 \pm 0.02399 \pm 0.01287$	
$\Im\text{m}(r_{1-1}^7)$	$0.00007 \pm 0.01016 \pm 0.00526$	$-0.12475 \pm 0.15702 \pm 0.01144$	$0.00034 \pm 0.04693 \pm 0.00637$	$-0.30383 \pm 0.23380 \pm 0.04736$	
r_{11}^8	$0.00003 \pm 0.02072 \pm 0.00319$	$-0.13716 \pm 0.10893 \pm 0.02097$	$0.00006 \pm 0.09763 \pm 0.00526$	$-0.00063 \pm 0.15226 \pm 0.09777$	
r_{1-1}^8	$0.00039 \pm 0.01693 \pm 0.00518$	$-0.24102 \pm 0.13534 \pm 0.01771$	$0.00009 \pm 0.12740 \pm 0.00968$	$-0.13517 \pm 0.17780 \pm 0.12777$	
r_{1-1}^{04}	$0.00001 \pm 0.00470 \pm 0.00293$	$-0.00560 \pm 0.01949 \pm 0.00554$	$0.00008 \pm 0.00971 \pm 0.00332$	$-0.03796 \pm 0.03530 \pm 0.01026$	
r_{11}^1	$0.00007 \pm 0.01053 \pm 0.00300$	$-0.02139 \pm 0.02424 \pm 0.01095$	$0.00004 \pm 0.01725 \pm 0.00373$	$0.03572 \pm 0.03724 \pm 0.01765$	
$\Im\text{m}(r_{1-1}^3)$	$0.00002 \pm 0.01382 \pm 0.00480$	$-0.08304 \pm 0.10327 \pm 0.01463$	$0.00017 \pm 0.00206 \pm 0.00556$	$-0.05440 \pm 0.14336 \pm 0.00594$	

Table F.1: Values and uncertainties of Wolf-Schilling SDMEs extracted from 1998–2000, 2006–2007 combined data set are presented. The kinematic bin is given in the first line, the SDME name is given in the first column. In the second and fourth columns are presented systematic uncertainties for hydrogen and deuterium correspondingly, BG corresponds to the background subtraction, Par to different Monte Carlo input parameters, P to all-in-one study. In the third and fifth columns are presented SDME values with resulting systematic and statistic uncertainties for hydrogen and deuterium correspondingly.

Bin	$1.40 \text{ GeV}^2 < Q^2 < 2.00 \text{ GeV}^2, -0.40 \text{ GeV}^2 < t < 0.00 \text{ GeV}^2$	$H : \text{SDME} \pm \text{stat} \pm \text{sys}$	$D : \text{BG} \pm \text{Par} \pm P$	$D : \text{SDME} \pm \text{stat} \pm \text{sys}$
Element				
r_{00}^{04}	$0.00005 \pm 0.00854 \pm 0.00339$	$0.34252 \pm 0.01965 \pm 0.00919$	$0.00018 \pm 0.00341 \pm 0.00384$	$0.29892 \pm 0.03424 \pm 0.00515$
r_{1-1}^1	$0.00006 \pm 0.01066 \pm 0.00303$	$0.28006 \pm 0.02684 \pm 0.01108$	$0.00017 \pm 0.02732 \pm 0.00374$	$0.19593 \pm 0.05209 \pm 0.02758$
$\Im\text{m}(r_{1-1}^2)$	$0.00010 \pm 0.02959 \pm 0.00312$	$-0.26642 \pm 0.02632 \pm 0.02976$	$0.00055 \pm 0.04041 \pm 0.00562$	$-0.31595 \pm 0.05289 \pm 0.04080$
$\Re\text{e}(r_{10}^5)$	$0.00000 \pm 0.00823 \pm 0.00297$	$0.16208 \pm 0.00860 \pm 0.00875$	$0.00005 \pm 0.00115 \pm 0.00322$	$0.20681 \pm 0.01731 \pm 0.00342$
$\Im\text{m}(r_{10}^6)$	$0.00000 \pm 0.00613 \pm 0.00229$	$-0.16801 \pm 0.00867 \pm 0.00655$	$0.00004 \pm 0.00104 \pm 0.00251$	$-0.19470 \pm 0.01789 \pm 0.00272$
$\Im\text{m}(r_{10}^7)$	$0.00008 \pm 0.01845 \pm 0.00494$	$0.16662 \pm 0.06566 \pm 0.01911$	$0.00031 \pm 0.02496 \pm 0.00646$	$-0.03716 \pm 0.12438 \pm 0.02579$
$\Re\text{e}(r_{10}^8)$	$0.00009 \pm 0.01021 \pm 0.00490$	$0.10157 \pm 0.07364 \pm 0.01133$	$0.00058 \pm 0.04840 \pm 0.00546$	$0.20171 \pm 0.14067 \pm 0.04871$
$\Re\text{e}(r_{10}^{04})$	$0.00004 \pm 0.01398 \pm 0.00362$	$-0.00440 \pm 0.01221 \pm 0.01444$	$0.00005 \pm 0.00584 \pm 0.00298$	$-0.04277 \pm 0.02509 \pm 0.00656$
$\Re\text{e}(r_{10}^1)$	$0.00005 \pm 0.04656 \pm 0.00336$	$-0.00920 \pm 0.01618 \pm 0.04668$	$0.00021 \pm 0.01826 \pm 0.00438$	$0.12292 \pm 0.04304 \pm 0.01878$
$\Im\text{m}(r_{10}^2)$	$0.00001 \pm 0.00816 \pm 0.00327$	$-0.01632 \pm 0.01745 \pm 0.00879$	$0.00003 \pm 0.00406 \pm 0.00258$	$-0.00073 \pm 0.03057 \pm 0.00481$
r_{00}^5	$0.00002 \pm 0.01991 \pm 0.00654$	$0.02859 \pm 0.01744 \pm 0.02096$	$0.00007 \pm 0.00615 \pm 0.00679$	$0.07063 \pm 0.02922 \pm 0.00916$
r_{00}^1	$0.00002 \pm 0.00019 \pm 0.00473$	$-0.00281 \pm 0.02999 \pm 0.00474$	$0.00005 \pm 0.02392 \pm 0.00386$	$0.03270 \pm 0.07688 \pm 0.02423$
$\Im\text{m}(r_{10}^3)$	$0.00011 \pm 0.01361 \pm 0.00292$	$0.09648 \pm 0.05523 \pm 0.01392$	$0.00049 \pm 0.02753 \pm 0.00439$	$0.02591 \pm 0.09494 \pm 0.02788$
r_{00}^8	$0.00011 \pm 0.00710 \pm 0.00442$	$-0.20985 \pm 0.14228 \pm 0.00837$	$0.00045 \pm 0.00814 \pm 0.00604$	$0.00600 \pm 0.23579 \pm 0.01015$
r_{11}^5	$0.00006 \pm 0.02287 \pm 0.00490$	$-0.00042 \pm 0.01119 \pm 0.02339$	$0.00027 \pm 0.01833 \pm 0.00578$	$0.00303 \pm 0.02139 \pm 0.01922$
r_{1-1}^5	$0.00005 \pm 0.01058 \pm 0.00348$	$0.00177 \pm 0.01421 \pm 0.01114$	$0.00008 \pm 0.00380 \pm 0.00335$	$-0.02149 \pm 0.02670 \pm 0.00507$
$\Im\text{m}(r_{1-1}^6)$	$0.00003 \pm 0.00663 \pm 0.00355$	$-0.02196 \pm 0.01398 \pm 0.00752$	$0.00010 \pm 0.00142 \pm 0.00395$	$0.00056 \pm 0.02214 \pm 0.00420$
$\Im\text{m}(r_{1-1}^7)$	$0.00007 \pm 0.00377 \pm 0.00704$	$-0.07973 \pm 0.11871 \pm 0.00798$	$0.00006 \pm 0.02505 \pm 0.00769$	$-0.21258 \pm 0.22422 \pm 0.02621$
r_{11}^8	$0.00012 \pm 0.01498 \pm 0.00394$	$0.00648 \pm 0.09232 \pm 0.01549$	$0.00021 \pm 0.00520 \pm 0.00583$	$-0.17690 \pm 0.16283 \pm 0.00781$
r_{1-1}^8	$0.00009 \pm 0.00245 \pm 0.00629$	$-0.15893 \pm 0.11723 \pm 0.00675$	$0.00034 \pm 0.00788 \pm 0.00578$	$0.14102 \pm 0.21560 \pm 0.00978$
r_{1-1}^{04}	$0.00003 \pm 0.00729 \pm 0.00389$	$0.02598 \pm 0.01865 \pm 0.00826$	$0.00014 \pm 0.02022 \pm 0.00289$	$0.01917 \pm 0.03403 \pm 0.02042$
r_{11}^1	$0.00003 \pm 0.01522 \pm 0.00588$	$0.02931 \pm 0.02305 \pm 0.01632$	$0.00005 \pm 0.02088 \pm 0.00423$	$-0.03422 \pm 0.03759 \pm 0.02130$
$\Im\text{m}(r_{1-1}^3)$	$0.00000 \pm 0.00017 \pm 0.00406$	$-0.08855 \pm 0.07884 \pm 0.00406$	$0.00063 \pm 0.00639 \pm 0.00413$	$-0.04890 \pm 0.14412 \pm 0.00763$

Table F.2: Values and uncertainties of Wolf-Schilling SDMEs extracted from 1998–2000, 2006–2007 combined data set are presented. The kinematic bin is given in the first line, the SDME name is given in the first column. In the second and fourth columns are presented systematic uncertainties for hydrogen and deuterium correspondingly, BG corresponds to the background subtraction, Par to different Monte Carlo input parameters, P to all-in-one study. In the third and fifth columns are presented SDME values with resulting systematic and statistic uncertainties for hydrogen and deuterium correspondingly.

Bin	$2.00 \text{ GeV}^2 < Q^2 < 7.00 \text{ GeV}^2, -0.40 \text{ GeV}^2 < t < 0.00 \text{ GeV}^2$	$H : \text{SDME} \pm \text{stat} \pm \text{sys}$	$2.00 \text{ GeV}^2 < Q^2 < 7.00 \text{ GeV}^2, -0.40 < t < -0.04 \text{ GeV}^2$	$D : \text{SDME} \pm \text{stat} \pm \text{sys}$
Element				
r_{00}^{04}	$0.00000 \pm 0.01817 \pm 0.00372$	$0.40301 \pm 0.02022 \pm 0.01855$	$0.00002 \pm 0.03391 \pm 0.00383$	$0.49650 \pm 0.03147 \pm 0.03412$
r_{1-1}^1	$0.00004 \pm 0.01994 \pm 0.00424$	$0.26413 \pm 0.02369 \pm 0.02038$	$0.00020 \pm 0.02381 \pm 0.00548$	$0.17288 \pm 0.04347 \pm 0.02443$
$\Im\text{m}(r_{1-1}^2)$	$0.00001 \pm 0.00374 \pm 0.00376$	$-0.23127 \pm 0.02351 \pm 0.00530$	$0.00015 \pm 0.00827 \pm 0.00476$	$-0.17430 \pm 0.04379 \pm 0.00954$
$\Re\text{e}(r_{10}^5)$	$0.00002 \pm 0.00578 \pm 0.00349$	$0.14914 \pm 0.00968 \pm 0.00675$	$0.00010 \pm 0.01668 \pm 0.00360$	$0.17451 \pm 0.01954 \pm 0.01706$
$\Im\text{m}(r_{10}^6)$	$0.00001 \pm 0.00651 \pm 0.00260$	$-0.18073 \pm 0.00884 \pm 0.00701$	$0.00002 \pm 0.00637 \pm 0.00271$	$-0.19531 \pm 0.01771 \pm 0.00692$
$\Im\text{m}(r_{10}^7)$	$0.00002 \pm 0.01070 \pm 0.00518$	$-0.05928 \pm 0.06387 \pm 0.01189$	$0.00001 \pm 0.05389 \pm 0.00659$	$0.15952 \pm 0.13734 \pm 0.05429$
$\Re\text{e}(r_{10}^8)$	$0.00003 \pm 0.01047 \pm 0.00385$	$0.16047 \pm 0.06218 \pm 0.01116$	$0.00002 \pm 0.01342 \pm 0.00368$	$0.08703 \pm 0.11786 \pm 0.01392$
$\Re\text{e}(r_{10}^{04})$	$0.00001 \pm 0.01787 \pm 0.00241$	$-0.01809 \pm 0.01275 \pm 0.01803$	$0.00011 \pm 0.02827 \pm 0.00214$	$-0.04665 \pm 0.02295 \pm 0.02835$
$\Re\text{e}(r_{10}^1)$	$0.00003 \pm 0.02040 \pm 0.00363$	$0.00418 \pm 0.01848 \pm 0.02072$	$0.00005 \pm 0.04353 \pm 0.00328$	$0.02557 \pm 0.04020 \pm 0.04365$
$\Im\text{m}(r_{10}^2)$	$0.00007 \pm 0.02657 \pm 0.00277$	$-0.00443 \pm 0.01820 \pm 0.02672$	$0.00017 \pm 0.06347 \pm 0.00220$	$0.12868 \pm 0.04102 \pm 0.06351$
r_{00}^5	$0.00002 \pm 0.01761 \pm 0.00571$	$0.02543 \pm 0.01886 \pm 0.01851$	$0.00004 \pm 0.03604 \pm 0.00611$	$0.04580 \pm 0.03445 \pm 0.03656$
r_{00}^1	$0.00000 \pm 0.01902 \pm 0.00640$	$0.01879 \pm 0.03502 \pm 0.02007$	$0.00004 \pm 0.04265 \pm 0.00628$	$-0.01423 \pm 0.06730 \pm 0.04311$
$\Im\text{m}(r_{10}^3)$	$0.00008 \pm 0.01055 \pm 0.00430$	$-0.04420 \pm 0.05054 \pm 0.01140$	$0.00009 \pm 0.01094 \pm 0.00279$	$0.06199 \pm 0.09205 \pm 0.01129$
r_{00}^8	$0.00019 \pm 0.02586 \pm 0.00790$	$0.29582 \pm 0.14240 \pm 0.02704$	$0.00045 \pm 0.05015 \pm 0.00782$	$-0.48218 \pm 0.24515 \pm 0.05076$
r_{11}^5	$0.00001 \pm 0.02641 \pm 0.00404$	$0.01220 \pm 0.01083 \pm 0.02672$	$0.00011 \pm 0.02514 \pm 0.00540$	$-0.05679 \pm 0.01762 \pm 0.02571$
r_{1-1}^5	$0.00001 \pm 0.01422 \pm 0.00287$	$-0.01883 \pm 0.01326 \pm 0.01451$	$0.00006 \pm 0.02305 \pm 0.00333$	$-0.00507 \pm 0.02364 \pm 0.02329$
$\Im\text{m}(r_{1-1}^6)$	$0.00001 \pm 0.00619 \pm 0.00282$	$-0.01407 \pm 0.01256 \pm 0.00680$	$0.00008 \pm 0.02271 \pm 0.00243$	$-0.03705 \pm 0.02170 \pm 0.02284$
$\Im\text{m}(r_{1-1}^7)$	$0.00006 \pm 0.00488 \pm 0.00901$	$-0.08306 \pm 0.10176 \pm 0.01025$	$0.00034 \pm 0.05951 \pm 0.00636$	$0.03865 \pm 0.16921 \pm 0.05985$
r_{11}^8	$0.00010 \pm 0.00074 \pm 0.00611$	$-0.15341 \pm 0.08244 \pm 0.00616$	$0.00006 \pm 0.03194 \pm 0.00439$	$0.14120 \pm 0.11308 \pm 0.03224$
r_{1-1}^8	$0.00007 \pm 0.01566 \pm 0.00774$	$0.08515 \pm 0.10236 \pm 0.01747$	$0.00009 \pm 0.03209 \pm 0.00576$	$-0.02359 \pm 0.13060 \pm 0.03261$
r_{1-1}^{04}	$0.00001 \pm 0.01397 \pm 0.00328$	$-0.02619 \pm 0.01746 \pm 0.01435$	$0.00008 \pm 0.01072 \pm 0.00280$	$-0.04323 \pm 0.02619 \pm 0.01108$
r_{11}^1	$0.00002 \pm 0.01663 \pm 0.00429$	$-0.00178 \pm 0.02187 \pm 0.01718$	$0.00004 \pm 0.01779 \pm 0.00419$	$-0.04140 \pm 0.03517 \pm 0.01828$
$\Im\text{m}(r_{1-1}^3)$	$0.00006 \pm 0.00944 \pm 0.00438$	$0.01682 \pm 0.06746 \pm 0.01041$	$0.00017 \pm 0.02702 \pm 0.00371$	$-0.02052 \pm 0.10111 \pm 0.02728$

Table F.3: Values and uncertainties of Wolf-Schilling SDMEs extracted from 1998–2000, 2006–2007 combined data set are presented. The kinematic bin is given in the first line, the SDME name is given in the first column. In the second and fourth columns are presented systematic uncertainties for hydrogen and deuterium correspondingly, BG corresponds to the background subtraction, Par to different Monte Carlo input parameters, P to all-in-one study. In the third and fifth columns are presented SDME values with resulting systematic and statistic uncertainties for hydrogen and deuterium correspondingly.

Bin	$1.00 \text{ GeV}^2 < Q^2 < 7.00 \text{ GeV}^2, -0.40 \text{ GeV}^2 < t < -0.20 \text{ GeV}^2$	$1.00 \text{ GeV}^2 < Q^2 < 7.00 \text{ GeV}^2, -0.40 < t < -0.20 \text{ GeV}^2$	$1.00 \text{ GeV}^2 < Q^2 < 7.00 \text{ GeV}^2, -0.40 < t < -0.20 \text{ GeV}^2$
Element	$H : SDME \pm stat \pm sys$	$D : BG \pm Par \pm P$	$D : SDME \pm stat \pm sys$
r_{00}^{04}	$0.00008 \pm 0.02632 \pm 0.00416$	$0.00007 \pm 0.01376 \pm 0.00527$	$0.35646 \pm 0.03443 \pm 0.01474$
r_{1-1}^1	$0.00011 \pm 0.00702 \pm 0.00524$	$0.00022 \pm 0.05059 \pm 0.00369$	$0.26853 \pm 0.04864 \pm 0.05072$
$\Im m(r_{1-1}^2)$	$0.00014 \pm 0.03747 \pm 0.00552$	$0.00031 \pm 0.04100 \pm 0.00502$	$-0.27522 \pm 0.04254 \pm 0.04131$
$\Re (r_{10}^5)$	$0.00002 \pm 0.00766 \pm 0.00347$	$0.00002 \pm 0.00237 \pm 0.00359$	$0.16412 \pm 0.01735 \pm 0.00430$
$\Im m(r_{10}^6)$	$0.00004 \pm 0.01968 \pm 0.00298$	$0.00006 \pm 0.01080 \pm 0.00271$	$-0.19716 \pm 0.01543 \pm 0.01114$
$\Im m(r_{10}^7)$	$0.00021 \pm 0.02773 \pm 0.00718$	$0.00020 \pm 0.09436 \pm 0.00448$	$0.10048 \pm 0.13272 \pm 0.09447$
$\Re (r_{10}^8)$	$0.00020 \pm 0.02543 \pm 0.00565$	$0.00024 \pm 0.04225 \pm 0.00574$	$0.30491 \pm 0.11590 \pm 0.04264$
$\Re (r_{10}^{04})$	$0.00011 \pm 0.03397 \pm 0.00463$	$0.00020 \pm 0.03543 \pm 0.00453$	$-0.09254 \pm 0.02332 \pm 0.03572$
$\Re (r_{10}^1)$	$0.00003 \pm 0.04238 \pm 0.00521$	$0.00008 \pm 0.04464 \pm 0.00506$	$0.04821 \pm 0.03520 \pm 0.04493$
$\Im m(r_{10}^2)$	$0.00007 \pm 0.03320 \pm 0.00445$	$0.00016 \pm 0.04605 \pm 0.00533$	$-0.06660 \pm 0.03567 \pm 0.04636$
r_{00}^5	$0.00006 \pm 0.06286 \pm 0.00979$	$0.00007 \pm 0.04119 \pm 0.00837$	$-0.01045 \pm 0.03023 \pm 0.04203$
r_{00}^1	$0.00006 \pm 0.03438 \pm 0.00550$	$0.00013 \pm 0.06431 \pm 0.00775$	$0.12140 \pm 0.05811 \pm 0.06477$
$\Im m(r_{10}^3)$	$0.00010 \pm 0.03266 \pm 0.00456$	$0.00024 \pm 0.08193 \pm 0.00475$	$0.10306 \pm 0.09391 \pm 0.08206$
r_{00}^8	$0.00009 \pm 0.06549 \pm 0.00846$	$0.00042 \pm 0.08021 \pm 0.00632$	$-0.40193 \pm 0.27114 \pm 0.08046$
r_{11}^5	$0.00015 \pm 0.02325 \pm 0.00797$	$0.00030 \pm 0.02297 \pm 0.00818$	$-0.03504 \pm 0.02145 \pm 0.02439$
r_{1-1}^5	$0.00005 \pm 0.00411 \pm 0.00481$	$0.00017 \pm 0.02142 \pm 0.00450$	$0.01955 \pm 0.02589 \pm 0.02189$
$\Im m(r_{1-1}^6)$	$0.00008 \pm 0.00846 \pm 0.00461$	$0.00012 \pm 0.00555 \pm 0.00470$	$-0.05186 \pm 0.01998 \pm 0.00727$
$\Im m(r_{1-1}^7)$	$0.00032 \pm 0.05186 \pm 0.00670$	$0.00062 \pm 0.09549 \pm 0.01013$	$0.53849 \pm 0.20884 \pm 0.09603$
r_{11}^8	$0.00001 \pm 0.03256 \pm 0.00589$	$0.00025 \pm 0.02975 \pm 0.00582$	$0.18367 \pm 0.14419 \pm 0.03031$
r_{1-1}^8	$0.00014 \pm 0.02483 \pm 0.01015$	$0.00049 \pm 0.03466 \pm 0.00862$	$0.16897 \pm 0.17123 \pm 0.03572$
r_{1-1}^{04}	$0.00004 \pm 0.01173 \pm 0.00379$	$0.00004 \pm 0.00771 \pm 0.00344$	$-0.02800 \pm 0.03204 \pm 0.00844$
r_{11}^1	$0.00002 \pm 0.00371 \pm 0.00671$	$0.00025 \pm 0.04674 \pm 0.00746$	$-0.04457 \pm 0.04234 \pm 0.04734$
$\Im m(r_{1-1}^3)$	$0.00004 \pm 0.02418 \pm 0.00563$	$0.00012 \pm 0.03949 \pm 0.00719$	$0.14221 \pm 0.12205 \pm 0.04014$

Table F.4: Values and uncertainties of Wolf-Schilling SDMEs extracted from 1998–2000, 2006–2007 combined data set are presented. The kinematic bin is given in the first line, the SDME name is given in the first column. In the second and fourth columns are presented systematic uncertainties for hydrogen and deuterium correspondingly, BG corresponds to the background subtraction, Par to different Monte Carlo input parameters, P to all-in-one study. In the third and fifth columns are presented SDME values with resulting systematic and statistic uncertainties for hydrogen and deuterium correspondingly.

Bin	$1.00 \text{ GeV}^2 < Q^2 < 7.00 \text{ GeV}^2, -0.20 < t < -0.10 \text{ GeV}^2$	$1.00 \text{ GeV}^2 < Q^2 < 7.00 \text{ GeV}^2, -0.20 < t < -0.10 \text{ GeV}^2$	$1.00 \text{ GeV}^2 < Q^2 < 7.00 \text{ GeV}^2, -0.20 < t < -0.10 \text{ GeV}^2$
Element	$H : SDME \pm stat \pm sys$	$D : BG \pm Par \pm P$	$D : SDME \pm stat \pm sys$
r_{00}^{04}	$0.00008 \pm 0.00797 \pm 0.00500$	$0.00002 \pm 0.01344 \pm 0.00573$	$0.34865 \pm 0.03356 \pm 0.01461$
r_{1-1}^1	$0.00013 \pm 0.01058 \pm 0.00436$	$0.00023 \pm 0.02843 \pm 0.00502$	$0.26519 \pm 0.04048 \pm 0.02887$
$\Im m(r_{1-1}^2)$	$0.00013 \pm 0.00431 \pm 0.00475$	$0.00027 \pm 0.00282 \pm 0.00557$	$-0.31932 \pm 0.04229 \pm 0.00625$
$\Re (r_{10}^5)$	$0.00001 \pm 0.00093 \pm 0.00414$	$0.00003 \pm 0.01186 \pm 0.00466$	$0.16660 \pm 0.01611 \pm 0.01274$
$\Im m(r_{10}^6)$	$0.00002 \pm 0.00067 \pm 0.00321$	$0.00004 \pm 0.00854 \pm 0.00212$	$-0.19633 \pm 0.01571 \pm 0.00880$
$\Im m(r_{10}^7)$	$0.00015 \pm 0.00627 \pm 0.00765$	$0.00019 \pm 0.08079 \pm 0.00749$	$-0.06425 \pm 0.13042 \pm 0.08114$
$\Re (r_{10}^8)$	$0.00019 \pm 0.01521 \pm 0.00439$	$0.00046 \pm 0.05957 \pm 0.00589$	$0.23493 \pm 0.13829 \pm 0.05986$
$\Re (r_{10}^{04})$	$0.00005 \pm 0.01522 \pm 0.00449$	$0.00008 \pm 0.00743 \pm 0.00436$	$-0.02599 \pm 0.02131 \pm 0.00862$
$\Re (r_{10}^1)$	$0.00005 \pm 0.02732 \pm 0.00656$	$0.00021 \pm 0.03301 \pm 0.00546$	$0.00592 \pm 0.02958 \pm 0.03346$
$\Im m(r_{10}^2)$	$0.00007 \pm 0.02137 \pm 0.00483$	$0.00002 \pm 0.01881 \pm 0.00330$	$0.03218 \pm 0.03268 \pm 0.01909$
r_{00}^5	$0.00006 \pm 0.02329 \pm 0.00813$	$0.00019 \pm 0.03715 \pm 0.00835$	$0.04501 \pm 0.03141 \pm 0.03807$
r_{00}^1	$0.00000 \pm 0.01735 \pm 0.00816$	$0.00009 \pm 0.02922 \pm 0.00828$	$-0.03899 \pm 0.06240 \pm 0.03037$
$\Im m(r_{10}^3)$	$0.00000 \pm 0.00202 \pm 0.00374$	$0.00002 \pm 0.05388 \pm 0.00526$	$0.06495 \pm 0.09276 \pm 0.05414$
r_{00}^8	$0.00000 \pm 0.02063 \pm 0.00887$	$0.00042 \pm 0.05946 \pm 0.00775$	$0.23411 \pm 0.23641 \pm 0.05997$
r_{11}^5	$0.00011 \pm 0.02949 \pm 0.00747$	$0.00015 \pm 0.01594 \pm 0.00788$	$-0.01873 \pm 0.01833 \pm 0.01778$
r_{1-1}^5	$0.00005 \pm 0.01637 \pm 0.00474$	$0.00009 \pm 0.00548 \pm 0.00534$	$0.02026 \pm 0.02365 \pm 0.00766$
$\Im m(r_{1-1}^6)$	$0.00004 \pm 0.00840 \pm 0.00286$	$0.00005 \pm 0.00479 \pm 0.00423$	$-0.03572 \pm 0.02044 \pm 0.00639$
$\Im m(r_{1-1}^7)$	$0.00007 \pm 0.01428 \pm 0.00848$	$0.00024 \pm 0.05409 \pm 0.00957$	$-0.25110 \pm 0.18586 \pm 0.05493$
r_{11}^8	$0.00008 \pm 0.00337 \pm 0.00511$	$0.00036 \pm 0.00843 \pm 0.00724$	$0.14432 \pm 0.13992 \pm 0.01112$
r_{1-1}^8	$0.00007 \pm 0.01957 \pm 0.00772$	$0.00012 \pm 0.04227 \pm 0.00970$	$-0.00445 \pm 0.19305 \pm 0.04337$
r_{1-1}^{04}	$0.00004 \pm 0.02200 \pm 0.00313$	$0.00002 \pm 0.00499 \pm 0.00553$	$0.01814 \pm 0.02811 \pm 0.00745$
r_{11}^1	$0.00002 \pm 0.02831 \pm 0.00465$	$0.00000 \pm 0.00965 \pm 0.00743$	$0.00077 \pm 0.03486 \pm 0.01218$
$\Im m(r_{1-1}^3)$	$0.00003 \pm 0.01734 \pm 0.00564$	$0.00019 \pm 0.00173 \pm 0.00699$	$0.09386 \pm 0.11416 \pm 0.00720$

Table F.5: Values and uncertainties of Wolf-Schilling SDMEs extracted from 1998–2000, 2006–2007 combined data set are presented. The kinematic bin is given in the first line, the SDME name is given in the first column. In the second and fourth columns are presented systematic uncertainties for hydrogen and deuterium correspondingly, BG corresponds to the background subtraction, Par to different Monte Carlo input parameters, P to all-in-one study. In the third and fifth columns are presented SDME values with resulting systematic and statistic uncertainties for hydrogen and deuterium correspondingly.

Bin	$1.00 \text{ GeV}^2 < Q^2 < 7.00 \text{ GeV}^2, -0.10 < t < -0.04 \text{ GeV}^2$	$H : \text{SDME} \pm \text{stat} \pm \text{sys}$	$1.00 \text{ GeV}^2 < Q^2 < 7.00 \text{ GeV}^2, -0.10 < t < -0.04 \text{ GeV}^2$	$D : \text{SDME} \pm \text{stat} \pm \text{sys}$
Element				
r_{00}^{04}	$0.00005 \pm 0.01842 \pm 0.00435$	$0.41824 \pm 0.02381 \pm 0.01892$	$0.00014 \pm 0.01698 \pm 0.00330$	$0.42980 \pm 0.03624 \pm 0.01730$
r_{1-1}^1	$0.00006 \pm 0.00932 \pm 0.00392$	$0.24191 \pm 0.03282 \pm 0.01011$	$0.00025 \pm 0.00827 \pm 0.00542$	$0.32083 \pm 0.04483 \pm 0.00989$
$\Im\text{m}(r_{1-1}^2)$	$0.00010 \pm 0.01921 \pm 0.00496$	$-0.22462 \pm 0.02936 \pm 0.01984$	$0.00054 \pm 0.07098 \pm 0.00469$	$-0.40334 \pm 0.05391 \pm 0.07114$
$\Re(r_{10}^5)$	$0.00000 \pm 0.00748 \pm 0.00421$	$0.15918 \pm 0.01184 \pm 0.00858$	$0.00002 \pm 0.00539 \pm 0.00424$	$0.20810 \pm 0.01836 \pm 0.00685$
$\Im\text{m}(r_{10}^6)$	$0.00000 \pm 0.01471 \pm 0.00446$	$-0.19704 \pm 0.01117 \pm 0.01537$	$0.00000 \pm 0.01311 \pm 0.00413$	$-0.19461 \pm 0.01900 \pm 0.01374$
$\Im\text{m}(r_{10}^7)$	$0.00008 \pm 0.00394 \pm 0.00901$	$0.12499 \pm 0.08209 \pm 0.00984$	$0.00044 \pm 0.09658 \pm 0.00723$	$-0.03148 \pm 0.15199 \pm 0.09685$
$\Re(r_{10}^8)$	$0.00009 \pm 0.00230 \pm 0.00537$	$0.23270 \pm 0.08083 \pm 0.00584$	$0.00024 \pm 0.00988 \pm 0.00441$	$-0.02583 \pm 0.11221 \pm 0.01082$
$\Re(r_{10}^{04})$	$0.00004 \pm 0.02430 \pm 0.00437$	$-0.00816 \pm 0.01536 \pm 0.02469$	$0.00011 \pm 0.02793 \pm 0.00363$	$0.02633 \pm 0.02568 \pm 0.02816$
$\Re(r_{10}^1)$	$0.00005 \pm 0.03716 \pm 0.00515$	$-0.01391 \pm 0.02403 \pm 0.03752$	$0.00016 \pm 0.04501 \pm 0.00468$	$-0.02448 \pm 0.03645 \pm 0.04525$
$\Im\text{m}(r_{10}^2)$	$0.00001 \pm 0.02583 \pm 0.00368$	$-0.00883 \pm 0.02279 \pm 0.02609$	$0.00011 \pm 0.01389 \pm 0.00449$	$0.00196 \pm 0.03592 \pm 0.01460$
r_{00}^5	$0.00002 \pm 0.02804 \pm 0.00847$	$0.07000 \pm 0.02378 \pm 0.02929$	$0.00013 \pm 0.00644 \pm 0.00881$	$0.03096 \pm 0.03584 \pm 0.01091$
r_{00}^1	$0.00002 \pm 0.00508 \pm 0.00654$	$-0.06428 \pm 0.04052 \pm 0.00828$	$0.00001 \pm 0.03273 \pm 0.00527$	$-0.14305 \pm 0.07099 \pm 0.03316$
$\Im\text{m}(r_{10}^3)$	$0.00011 \pm 0.01961 \pm 0.00400$	$0.05935 \pm 0.07094 \pm 0.02002$	$0.00026 \pm 0.05112 \pm 0.00442$	$0.01560 \pm 0.11622 \pm 0.05131$
r_{00}^8	$0.00011 \pm 0.01403 \pm 0.00965$	$-0.01250 \pm 0.17375 \pm 0.01702$	$0.00031 \pm 0.01836 \pm 0.00862$	$-0.08571 \pm 0.23839 \pm 0.02029$
r_{11}^5	$0.00006 \pm 0.02080 \pm 0.00529$	$-0.02376 \pm 0.01209 \pm 0.02146$	$0.00016 \pm 0.03840 \pm 0.00473$	$-0.03962 \pm 0.02014 \pm 0.03869$
r_{1-1}^5	$0.00005 \pm 0.01664 \pm 0.00394$	$0.00020 \pm 0.01679 \pm 0.01710$	$0.00015 \pm 0.02889 \pm 0.00389$	$-0.04574 \pm 0.02615 \pm 0.02915$
$\Im\text{m}(r_{1-1}^6)$	$0.00003 \pm 0.01321 \pm 0.00397$	$-0.02177 \pm 0.01616 \pm 0.01379$	$0.00008 \pm 0.02116 \pm 0.00374$	$0.01208 \pm 0.02308 \pm 0.02149$
$\Im\text{m}(r_{1-1}^7)$	$0.00007 \pm 0.02051 \pm 0.00723$	$0.12644 \pm 0.12786 \pm 0.02175$	$0.00024 \pm 0.08105 \pm 0.00845$	$-0.91795 \pm 0.18046 \pm 0.08149$
r_{11}^8	$0.00012 \pm 0.00438 \pm 0.00432$	$-0.02485 \pm 0.11163 \pm 0.00615$	$0.00010 \pm 0.02011 \pm 0.00563$	$-0.11167 \pm 0.16045 \pm 0.02089$
r_{1-1}^8	$0.00009 \pm 0.05574 \pm 0.00851$	$-0.31393 \pm 0.14387 \pm 0.05638$	$0.00028 \pm 0.04251 \pm 0.00761$	$-0.04572 \pm 0.20810 \pm 0.04319$
r_{1-1}^{04}	$0.00003 \pm 0.00559 \pm 0.00310$	$0.03298 \pm 0.02192 \pm 0.00639$	$0.00005 \pm 0.01221 \pm 0.00395$	$-0.06497 \pm 0.03297 \pm 0.01283$
r_{11}^1	$0.00003 \pm 0.00216 \pm 0.00469$	$0.09390 \pm 0.02726 \pm 0.00517$	$0.00010 \pm 0.03383 \pm 0.00495$	$0.03633 \pm 0.03577 \pm 0.03419$
$\Im\text{m}(r_{1-1}^3)$	$0.00000 \pm 0.00999 \pm 0.00564$	$0.13876 \pm 0.08175 \pm 0.01147$	$0.00063 \pm 0.11186 \pm 0.00596$	$-0.53816 \pm 0.13307 \pm 0.11202$

Table F.6: Values and uncertainties of Wolf-Schilling SDMEs extracted from 1998–2000, 2006–2007 combined data set are presented. The kinematic bin is given in the first line, the SDME name is given in the first column. In the second and fourth columns are presented systematic uncertainties for hydrogen and deuterium correspondingly, BG corresponds to the background subtraction, Par to different Monte Carlo input parameters, P to all-in-one study. In the third and fifth columns are presented SDME values with resulting systematic and statistic uncertainties for hydrogen and deuterium correspondingly.

Bin	$1.00 \text{ GeV}^2 < Q^2 < 7.00 \text{ GeV}^2, -0.04 \text{ GeV}^2 < t < 0.00 \text{ GeV}^2$	$H : \text{SDME} \pm \text{stat} \pm \text{sys}$	$D : \text{BG} \pm \text{Par} \pm P$	$D : \text{SDME} \pm \text{stat} \pm \text{sys}$
Element				
r_{00}^{04}	$0.00011 \pm 0.01849 \pm 0.00450$	$0.31236 \pm 0.02363 \pm 0.01903$	$0.00020 \pm 0.04804 \pm 0.00494$	$0.30055 \pm 0.03158 \pm 0.04829$
r_{1-1}^1	$0.00021 \pm 0.04687 \pm 0.00518$	$0.32693 \pm 0.03137 \pm 0.04715$	$0.00032 \pm 0.00805 \pm 0.00495$	$0.34577 \pm 0.05319 \pm 0.00946$
$\Im\text{m}(r_{1-1}^2)$	$0.00012 \pm 0.00964 \pm 0.00380$	$-0.28619 \pm 0.03276 \pm 0.01037$	$0.00031 \pm 0.07225 \pm 0.00428$	$-0.42588 \pm 0.04688 \pm 0.07238$
$\Re\text{e}(r_{10}^5)$	$0.00002 \pm 0.00943 \pm 0.00456$	$0.17367 \pm 0.01024 \pm 0.01047$	$0.00001 \pm 0.00384 \pm 0.00435$	$0.20463 \pm 0.01440 \pm 0.00580$
$\Im\text{m}(r_{10}^6)$	$0.00002 \pm 0.00253 \pm 0.00248$	$-0.16120 \pm 0.01096 \pm 0.00354$	$0.00007 \pm 0.01403 \pm 0.00230$	$-0.18240 \pm 0.01797 \pm 0.01422$
$\Im\text{m}(r_{10}^7)$	$0.00007 \pm 0.01065 \pm 0.00541$	$0.01993 \pm 0.08871 \pm 0.01194$	$0.00003 \pm 0.02058 \pm 0.00536$	$-0.33041 \pm 0.12436 \pm 0.02127$
$\Re\text{e}(r_{10}^8)$	$0.00056 \pm 0.02544 \pm 0.00565$	$0.10795 \pm 0.10083 \pm 0.02607$	$0.00002 \pm 0.02826 \pm 0.00516$	$0.29730 \pm 0.10981 \pm 0.02872$
$\Re\text{e}(r_{10}^{04})$	$0.00005 \pm 0.00336 \pm 0.00461$	$0.00546 \pm 0.01557 \pm 0.00571$	$0.00003 \pm 0.00723 \pm 0.00393$	$-0.02309 \pm 0.02098 \pm 0.00823$
$\Re\text{e}(r_{10}^1)$	$0.00005 \pm 0.02203 \pm 0.00334$	$-0.00243 \pm 0.02058 \pm 0.02228$	$0.00004 \pm 0.00555 \pm 0.00345$	$0.03181 \pm 0.03256 \pm 0.00653$
$\Im\text{m}(r_{10}^2)$	$0.00006 \pm 0.01900 \pm 0.00468$	$-0.00775 \pm 0.02352 \pm 0.01957$	$0.00001 \pm 0.00855 \pm 0.00459$	$-0.09114 \pm 0.03366 \pm 0.00971$
r_{00}^5	$0.00005 \pm 0.00905 \pm 0.00501$	$0.01699 \pm 0.02108 \pm 0.01034$	$0.00008 \pm 0.01877 \pm 0.00505$	$0.04014 \pm 0.03013 \pm 0.01943$
r_{10}^1	$0.00005 \pm 0.00430 \pm 0.00770$	$0.01853 \pm 0.03664 \pm 0.00882$	$0.00012 \pm 0.03367 \pm 0.00587$	$-0.02547 \pm 0.06229 \pm 0.03417$
$\Im\text{m}(r_{10}^3)$	$0.00009 \pm 0.01807 \pm 0.00477$	$0.12686 \pm 0.07219 \pm 0.01869$	$0.00020 \pm 0.03707 \pm 0.00429$	$-0.01885 \pm 0.09361 \pm 0.03732$
r_{00}^8	$0.00050 \pm 0.06169 \pm 0.00939$	$0.10984 \pm 0.16425 \pm 0.06240$	$0.00037 \pm 0.07421 \pm 0.01152$	$0.71743 \pm 0.20236 \pm 0.07510$
r_{11}^5	$0.00006 \pm 0.02421 \pm 0.00192$	$0.02112 \pm 0.01331 \pm 0.02429$	$0.00017 \pm 0.02448 \pm 0.00208$	$0.02943 \pm 0.02043 \pm 0.02457$
r_{1-1}^5	$0.00007 \pm 0.02806 \pm 0.00201$	$-0.01539 \pm 0.01689 \pm 0.02813$	$0.00017 \pm 0.03580 \pm 0.00234$	$-0.00306 \pm 0.02863 \pm 0.03588$
$\Im\text{m}(r_{1-1}^6)$	$0.00003 \pm 0.00181 \pm 0.00177$	$-0.02319 \pm 0.01579 \pm 0.00253$	$0.00011 \pm 0.01126 \pm 0.00289$	$-0.04202 \pm 0.02358 \pm 0.01163$
$\Im\text{m}(r_{1-1}^7)$	$0.00012 \pm 0.01766 \pm 0.00577$	$-0.10192 \pm 0.14284 \pm 0.01857$	$0.00000 \pm 0.01828 \pm 0.00823$	$-0.27870 \pm 0.18115 \pm 0.02005$
r_{11}^8	$0.00039 \pm 0.02833 \pm 0.00616$	$-0.12428 \pm 0.11614 \pm 0.02899$	$0.00020 \pm 0.02084 \pm 0.00708$	$-0.28953 \pm 0.12083 \pm 0.02201$
r_{1-1}^8	$0.00013 \pm 0.03724 \pm 0.01124$	$-0.08738 \pm 0.14684 \pm 0.03890$	$0.00031 \pm 0.05220 \pm 0.00754$	$0.05572 \pm 0.19413 \pm 0.05275$
r_{1-1}^{04}	$0.00001 \pm 0.01435 \pm 0.00381$	$-0.02378 \pm 0.02263 \pm 0.01485$	$0.00022 \pm 0.02472 \pm 0.00439$	$-0.05164 \pm 0.03360 \pm 0.02511$
r_{11}^1	$0.00006 \pm 0.02890 \pm 0.00421$	$-0.02287 \pm 0.02742 \pm 0.02921$	$0.00026 \pm 0.02814 \pm 0.00434$	$-0.09356 \pm 0.04028 \pm 0.02848$
$\Im\text{m}(r_{1-1}^3)$	$0.00007 \pm 0.01827 \pm 0.00540$	$-0.21009 \pm 0.09792 \pm 0.01906$	$0.00000 \pm 0.01763 \pm 0.00490$	$-0.06762 \pm 0.10515 \pm 0.01830$

Table F.7: Values and uncertainties of Wolf-Schilling SDMEs extracted from 1998–2000, 2006–2007 combined data set are presented. The kinematic bin is given in the first line, the SDME name is given in the first column. In the second and fourth columns are presented systematic uncertainties for hydrogen and deuterium correspondingly, BG corresponds to the background subtraction, Par to different Monte Carlo input parameters, P to all-in-one study. In the third and fifth columns are presented SDME values with resulting systematic and statistic uncertainties for hydrogen and deuterium correspondingly.

Bin	$1.00 \text{ GeV}^2 < Q^2 < 7.00 \text{ GeV}^2, -0.40 < t < 0.00 \text{ GeV}^2$	$H : \text{SDME} \pm \text{stat} \pm \text{sys}$	$D : \text{BG} \pm \text{Par} \pm P$	$D : \text{SDME} \pm \text{stat} \pm \text{sys}$
Element				
r_{00}^{04}	$0.00000 \pm 0.00913 \pm 0.00422$	$0.33817 \pm 0.01159 \pm 0.01006$	$0.00003 \pm 0.03029 \pm 0.00561$	$0.38216 \pm 0.01946 \pm 0.03081$
r_{1-1}^1	$0.00000 \pm 0.00100 \pm 0.00342$	$0.28651 \pm 0.01478 \pm 0.00356$	$0.00006 \pm 0.02352 \pm 0.00738$	$0.27365 \pm 0.02463 \pm 0.02465$
$\Im\text{m}(r_{1-1}^2)$	$0.00000 \pm 0.00589 \pm 0.00418$	$-0.25886 \pm 0.01531 \pm 0.00722$	$0.00010 \pm 0.01728 \pm 0.00584$	$-0.28609 \pm 0.02622 \pm 0.01825$
$\Re\text{e}(r_{10}^5)$	$0.00000 \pm 0.00056 \pm 0.00397$	$0.15789 \pm 0.00522 \pm 0.00401$	$0.00000 \pm 0.00261 \pm 0.00548$	$0.15859 \pm 0.00935 \pm 0.00607$
$\Im\text{m}(r_{10}^6)$	$0.00000 \pm 0.01331 \pm 0.00178$	$-0.16278 \pm 0.00499 \pm 0.01343$	$0.00001 \pm 0.01369 \pm 0.00234$	$-0.17404 \pm 0.00910 \pm 0.01389$
$\Im\text{m}(r_{10}^7)$	$0.00000 \pm 0.00072 \pm 0.00502$	$0.05750 \pm 0.04013 \pm 0.00507$	$0.00003 \pm 0.04302 \pm 0.00836$	$0.06477 \pm 0.07370 \pm 0.04382$
$\Re\text{e}(r_{10}^8)$	$0.00000 \pm 0.00519 \pm 0.00312$	$0.10064 \pm 0.03848 \pm 0.00605$	$0.00005 \pm 0.01258 \pm 0.00537$	$0.14164 \pm 0.06110 \pm 0.01368$
$\Re\text{e}(r_{10}^{04})$	$0.00000 \pm 0.00977 \pm 0.00253$	$-0.01566 \pm 0.00722 \pm 0.01009$	$0.00004 \pm 0.03162 \pm 0.00635$	$-0.03148 \pm 0.01248 \pm 0.03225$
$\Re\text{e}(r_{10}^1)$	$0.00000 \pm 0.02485 \pm 0.00342$	$0.00217 \pm 0.00930 \pm 0.02508$	$0.00005 \pm 0.03214 \pm 0.00582$	$0.02698 \pm 0.01796 \pm 0.03266$
$\Im\text{m}(r_{10}^2)$	$0.00000 \pm 0.01963 \pm 0.00300$	$-0.01350 \pm 0.01029 \pm 0.01986$	$0.00003 \pm 0.02220 \pm 0.00424$	$-0.01705 \pm 0.01934 \pm 0.02260$
r_{00}^5	$0.00000 \pm 0.01125 \pm 0.00798$	$0.01265 \pm 0.00988 \pm 0.01379$	$0.00005 \pm 0.02869 \pm 0.01327$	$0.00509 \pm 0.01851 \pm 0.03161$
r_{10}^1	$0.00000 \pm 0.01881 \pm 0.00419$	$0.01485 \pm 0.01813 \pm 0.01927$	$0.00000 \pm 0.00787 \pm 0.00946$	$-0.00923 \pm 0.03468 \pm 0.01231$
$\Im\text{m}(r_{10}^3)$	$0.00000 \pm 0.00953 \pm 0.00279$	$0.02108 \pm 0.03246 \pm 0.00993$	$0.00001 \pm 0.01573 \pm 0.00354$	$0.06441 \pm 0.05490 \pm 0.01612$
r_{00}^8	$0.00000 \pm 0.02852 \pm 0.00529$	$0.05476 \pm 0.08096 \pm 0.02901$	$0.00000 \pm 0.01040 \pm 0.00634$	$-0.14767 \pm 0.13434 \pm 0.01218$
r_{11}^5	$0.00000 \pm 0.02500 \pm 0.00620$	$-0.00372 \pm 0.00655 \pm 0.02576$	$0.00007 \pm 0.03971 \pm 0.01161$	$-0.01728 \pm 0.01125 \pm 0.04137$
r_{1-1}^5	$0.00000 \pm 0.01843 \pm 0.00348$	$0.00096 \pm 0.00811 \pm 0.01876$	$0.00004 \pm 0.03922 \pm 0.00693$	$0.00475 \pm 0.01340 \pm 0.03983$
$\Im\text{m}(r_{1-1}^6)$	$0.00000 \pm 0.00928 \pm 0.00354$	$-0.02040 \pm 0.00789 \pm 0.00994$	$0.00003 \pm 0.02984 \pm 0.00557$	$-0.01754 \pm 0.01118 \pm 0.03036$
$\Im\text{m}(r_{1-1}^7)$	$0.00000 \pm 0.00571 \pm 0.00423$	$-0.06900 \pm 0.06968 \pm 0.00710$	$0.00002 \pm 0.03697 \pm 0.00757$	$-0.07279 \pm 0.10946 \pm 0.03774$
r_{11}^8	$0.00000 \pm 0.00530 \pm 0.00467$	$-0.08185 \pm 0.05400 \pm 0.00706$	$0.00001 \pm 0.00731 \pm 0.00445$	$0.04228 \pm 0.08186 \pm 0.00855$
r_{1-1}^8	$0.00000 \pm 0.01947 \pm 0.00356$	$-0.09904 \pm 0.06516 \pm 0.01980$	$0.00000 \pm 0.02405 \pm 0.00576$	$0.03456 \pm 0.10642 \pm 0.02473$
r_{1-1}^{04}	$0.00000 \pm 0.01246 \pm 0.00285$	$-0.00075 \pm 0.01066 \pm 0.01279$	$0.00001 \pm 0.01016 \pm 0.00588$	$-0.01560 \pm 0.01741 \pm 0.01174$
r_{11}^1	$0.00000 \pm 0.01161 \pm 0.00505$	$0.00074 \pm 0.01329 \pm 0.01266$	$0.00002 \pm 0.00907 \pm 0.00858$	$-0.02265 \pm 0.02023 \pm 0.01249$
$\Im\text{m}(r_{1-1}^3)$	$0.00000 \pm 0.00265 \pm 0.00270$	$-0.03004 \pm 0.04601 \pm 0.00379$	$0.00003 \pm 0.00330 \pm 0.00537$	$0.01093 \pm 0.06667 \pm 0.00630$

Table F.8: Values and uncertainties of Wolf-Schilling SDMEs extracted from 1998–2000, 2006–2007 combined data set are presented. The kinematic bin is given in the first line, the SDME name is given in the first column. In the second and fourth columns are presented systematic uncertainties for hydrogen and deuterium correspondingly, BG corresponds to the background subtraction, Par to different Monte Carlo input parameters, P to all-in-one study. In the third and fifth columns are presented SDME values with resulting systematic and statistic uncertainties for hydrogen and deuterium correspondingly.

Bin	$U_1 \pm stat \pm syst$	$U_2 \pm stat \pm syst$	$U_3 \pm stat \pm syst$
$1.0 \text{ GeV}^2 < Q^2 < 1.4 \text{ GeV}^2, -0.40 \text{ GeV}^2 < t < 0.00 \text{ GeV}^2$	$0.127 \pm 0.011 \pm 0.076$	$-0.006 \pm 0.017 \pm 0.015$	$-0.378 \pm 0.004 \pm 0.202$
$1.4 \text{ GeV}^2 < Q^2 < 2.0 \text{ GeV}^2, -0.40 \text{ GeV}^2 < t < 0.00 \text{ GeV}^2$	$0.091 \pm 0.046 \pm 0.077$	$0.001 \pm 0.012 \pm 0.016$	$-0.152 \pm 0.013 \pm 0.172$
$2.0 \text{ GeV}^2 < Q^2 < 7.0 \text{ GeV}^2, -0.40 \text{ GeV}^2 < t < 0.00 \text{ GeV}^2$	$0.020 \pm 0.053 \pm 0.063$	$-0.007 \pm 0.012 \pm 0.013$	$-0.068 \pm 0.017 \pm 0.145$
$1.0 \text{ GeV}^2 < Q^2 < 7.0 \text{ GeV}^2, -0.40 \text{ GeV}^2 < t < -0.20 \text{ GeV}^2$	$0.032 \pm 0.046 \pm 0.092$	$0.006 \pm 0.004 \pm 0.017$	$-0.212 \pm 0.010 \pm 0.226$
$1.0 \text{ GeV}^2 < Q^2 < 7.0 \text{ GeV}^2, -0.20 \text{ GeV}^2 < t < -0.10 \text{ GeV}^2$	$-0.024 \pm 0.030 \pm 0.089$	$-0.024 \pm 0.004 \pm 0.019$	$-0.339 \pm 0.051 \pm 0.207$
$1.0 \text{ GeV}^2 < Q^2 < 7.0 \text{ GeV}^2, -0.10 \text{ GeV}^2 < t < -0.04 \text{ GeV}^2$	$0.193 \pm 0.042 \pm 0.091$	$-0.002 \pm 0.013 \pm 0.019$	$0.134 \pm 0.016 \pm 0.185$
$1.0 \text{ GeV}^2 < Q^2 < 7.0 \text{ GeV}^2, -0.04 \text{ GeV}^2 < t < 0.00 \text{ GeV}^2$	$0.113 \pm 0.005 \pm 0.092$	$-0.006 \pm 0.027 \pm 0.019$	$-0.405 \pm 0.058 \pm 0.183$
$1.0 \text{ GeV}^2 < Q^2 < 7.0 \text{ GeV}^2, -0.40 \text{ GeV}^2 < t < 0.00 \text{ GeV}^2$	$0.086 \pm 0.013 \pm 0.042$	$-0.003 \pm 0.007 \pm 0.009$	$-0.181 \pm 0.025 \pm 0.098$

Table F.9: Values, statistical and systematic uncertainties of U_1, U_2, U_3 quantities, used for the test of NPE dominance are presented. The quantities are extracted from 1998–2000, 2006–2007 unified hydrogen data set. The kinematic bin is given in the first column, the quantity name is given in the first line. The values for overall kinematics are shown in the last line.

Bin	$U_1 \pm stat \pm syst$	$U_2 \pm stat \pm syst$	$U_3 \pm stat \pm syst$
$1.0 \text{ GeV}^2 < Q^2 < 1.4 \text{ GeV}^2, -0.40 \text{ GeV}^2 < t < -0.04 \text{ GeV}^2$	$-0.411 \pm 0.028 \pm 0.120$	$-0.107 \pm 0.010 \pm 0.026$	$-0.136 \pm 0.225 \pm 0.272$
$1.4 \text{ GeV}^2 < Q^2 < 2.0 \text{ GeV}^2, -0.40 \text{ GeV}^2 < t < -0.04 \text{ GeV}^2$	$0.416 \pm 0.060 \pm 0.141$	$-0.018 \pm 0.015 \pm 0.030$	$-0.036 \pm 0.013 \pm 0.284$
$2.0 \text{ GeV}^2 < Q^2 < 7.0 \text{ GeV}^2, -0.40 \text{ GeV}^2 < t < -0.04 \text{ GeV}^2$	$0.154 \pm 0.067 \pm 0.116$	$-0.062 \pm 0.002 \pm 0.026$	$0.118 \pm 0.064 \pm 0.167$
$1.0 \text{ GeV}^2 < Q^2 < 7.0 \text{ GeV}^2, -0.40 \text{ GeV}^2 < t < -0.20 \text{ GeV}^2$	$0.092 \pm 0.039 \pm 0.141$	$0.026 \pm 0.011 \pm 0.030$	$-0.234 \pm 0.032 \pm 0.232$
$1.0 \text{ GeV}^2 < Q^2 < 7.0 \text{ GeV}^2, -0.20 \text{ GeV}^2 < t < -0.10 \text{ GeV}^2$	$-0.274 \pm 0.093 \pm 0.114$	$-0.085 \pm 0.010 \pm 0.023$	$-0.157 \pm 0.063 \pm 0.271$
$1.0 \text{ GeV}^2 < Q^2 < 7.0 \text{ GeV}^2, -0.10 \text{ GeV}^2 < t < -0.04 \text{ GeV}^2$	$0.156 \pm 0.015 \pm 0.112$	$0.002 \pm 0.021 \pm 0.025$	$0.140 \pm 0.034 \pm 0.253$
$1.0 \text{ GeV}^2 < Q^2 < 7.0 \text{ GeV}^2, -0.04 \text{ GeV}^2 < t < 0.00 \text{ GeV}^2$	$0.140 \pm 0.166 \pm 0.138$	$-0.015 \pm 0.002 \pm 0.030$	$0.353 \pm 0.064 \pm 0.243$
$1.0 \text{ GeV}^2 < Q^2 < 7.0 \text{ GeV}^2, -0.40 \text{ GeV}^2 < t < -0.04 \text{ GeV}^2$	$0.085 \pm 0.015 \pm 0.063$	$-0.013 \pm 0.001 \pm 0.013$	$0.077 \pm 0.031 \pm 0.145$

Table F.10: Values and uncertainties of U_1, U_2, U_3 quantities, used for the test of NPE dominance are presented. The quantities are extracted from 1998–2000, 2006–2007 combined deuterium data set. The kinematic bin is given in the first column, the quantity name is given in the first line. The values for overall kinematics are shown in the last line.

Q^2 Bin	Hydrogen	Deuterium
$1.0 \text{ GeV}^2 < Q^2 < 1.4 \text{ GeV}^2$	$0.426 \pm 0.038 \pm 0.000$	$0.499 \pm 0.079 \pm 0.001$
$1.4 \text{ GeV}^2 < Q^2 < 2.0 \text{ GeV}^2$	$0.621 \pm 0.054 \pm 0.000$	$0.509 \pm 0.083 \pm 0.000$
$2.0 \text{ GeV}^2 < Q^2 < 7.0 \text{ GeV}^2$	$0.844 \pm 0.071 \pm 0.004$	$1.249 \pm 0.157 \pm 0.025$
$1.0 \text{ GeV}^2 < Q^2 < 7.0 \text{ GeV}^2$	$0.617 \pm 0.032 \pm 0.000$	$0.754 \pm 0.062 \pm 0.008$

Table F.11: Values and uncertainties of the longitudinal-to-transverse cross-section ratio R are presented. Values \pm statistical \pm systematic uncertainties for hydrogen (deuterium) data are given in the second (third) column for Q^2 bins. Results for integrated over all kinematics are shown in the last line.

Bin	$1.00 \text{ GeV}^2 < Q^2 < 1.40 \text{ GeV}^2, -0.40 < t < 0.00 \text{ GeV}^2$	$1.00 \text{ GeV}^2 < Q^2 < 1.40 \text{ GeV}^2, -0.40 < t < -0.04 \text{ GeV}^2$
Element	$H : SDME \pm stat \pm sys$	$D : SDME \pm stat \pm sys$
$u_{++}^{00} + \epsilon u_{00}^{00}$	$0.2661 \pm 0.0179 \pm 0.0092$	$0.0001 \pm 0.0136 \pm 0.0042$
$\Re(u_{0+}^{0+} - u_{0+}^{-0})$	$0.0124 \pm 0.0094 \pm 0.0177$	$0.0005 \pm 0.0360 \pm 0.0031$
u_{-+}^{+-}	$0.0403 \pm 0.0241 \pm 0.0028$	$0.0003 \pm 0.0001 \pm 0.0032$
$\Im(u_{0+}^{0+} - u_{0+}^{-0})$	$-0.4485 \pm 0.0174 \pm 0.0197$	$0.0010 \pm 0.0028 \pm 0.0035$
$\Re u_{0+}^{00}$	$-0.0349 \pm 0.0275 \pm 0.0431$	$0.0005 \pm 0.0496 \pm 0.0030$
$\Re(u_{++}^{0+} - u_{++}^{-0} + 2\epsilon u_{0+}^{-0})$	$0.0267 \pm 0.0289 \pm 0.0636$	$0.0020 \pm 0.0832 \pm 0.0074$
$\Re(u_{-+}^{0+})$	$0.0330 \pm 0.0200 \pm 0.0133$	$0.0011 \pm 0.0082 \pm 0.0057$
$\Im u_{0+}^{00}$	$0.0115 \pm 0.0255 \pm 0.0109$	$0.0002 \pm 0.0436 \pm 0.0032$
$\Im(u_{++}^{0+} - u_{++}^{-0})$	$0.5952 \pm 0.0395 \pm 0.0074$	$0.0008 \pm 0.0178 \pm 0.0044$
$\Re(u_{0+}^{++} - u_{0+}^{--})$	$0.0262 \pm 0.0170 \pm 0.0365$	$0.0004 \pm 0.0474 \pm 0.0032$
$\Re(u_{0+}^{+-})$	$-0.0277 \pm 0.0166 \pm 0.0155$	$0.0001 \pm 0.0256 \pm 0.0091$
$\Im(u_{0+}^{++} + u_{0+}^{--})$	$-0.0051 \pm 0.0195 \pm 0.0055$	$0.0016 \pm 0.0079 \pm 0.0050$
$\Im u_{0+}^{+-}$	$-0.0209 \pm 0.0242 \pm 0.0105$	$0.0008 \pm 0.0163 \pm 0.0052$
$\Re(u_{0+}^{0-} - u_{0+}^{+0})$	$0.0107 \pm 0.0135 \pm 0.0065$	$0.0004 \pm 0.0079 \pm 0.0058$
$\Re(u_{-+}^{+-} - \epsilon u_{00}^{--})$	$0.0420 \pm 0.0401 \pm 0.0157$	$0.0004 \pm 0.0183 \pm 0.0061$
$\Re(u_{-+}^{+-})$	$0.1024 \pm 0.0962 \pm 0.0310$	$0.0029 \pm 0.0652 \pm 0.0033$
$\Im(u_{0+}^{0-} - u_{0+}^{+0})$	$0.1560 \pm 0.1666 \pm 0.0093$	$0.0098 \pm 0.1896 \pm 0.0030$
$\Im u_{-+}^{+-}$	$-0.0136 \pm 0.1320 \pm 0.0118$	$0.0146 \pm 0.1642 \pm 0.0064$
u_{-+}^{00}	$-0.0815 \pm 0.1628 \pm 0.0519$	$0.0056 \pm 0.0788 \pm 0.0053$
$\Re(u_{-+}^{+0})$	$-0.1911 \pm 0.1542 \pm 0.0327$	$0.0081 \pm 0.1309 \pm 0.0097$
$\Re(u_{0+}^{+-})$	$-0.2562 \pm 0.1521 \pm 0.0172$	$0.0108 \pm 0.1134 \pm 0.0033$
u_{-+}^{+-}	$0.0844 \pm 0.1034 \pm 0.0156$	$0.0013 \pm 0.0003 \pm 0.0037$
$\Im u_{0+}^{+-}$	$-0.0856 \pm 0.1414 \pm 0.0100$	$0.0033 \pm 0.0540 \pm 0.0056$
		$0.2942 \pm 0.0332 \pm 0.0142$
		$0.0059 \pm 0.0232 \pm 0.0361$
		$-0.1571 \pm 0.0522 \pm 0.0032$
		$-0.5842 \pm 0.0440 \pm 0.0046$
		$-0.1051 \pm 0.0459 \pm 0.0496$
		$0.0767 \pm 0.0557 \pm 0.0836$
		$-0.0639 \pm 0.0359 \pm 0.0100$
		$-0.1215 \pm 0.0510 \pm 0.0437$
		$0.8966 \pm 0.0586 \pm 0.0183$
		$0.0453 \pm 0.0271 \pm 0.0475$
		$0.0315 \pm 0.0285 \pm 0.0272$
		$-0.0398 \pm 0.0358 \pm 0.0095$
		$0.0347 \pm 0.0373 \pm 0.0171$
		$0.0760 \pm 0.0228 \pm 0.0098$
		$0.0731 \pm 0.0605 \pm 0.0193$
		$0.4984 \pm 0.1621 \pm 0.0654$
		$0.9454 \pm 0.2565 \pm 0.1899$
		$-0.5148 \pm 0.2648 \pm 0.1650$
		$0.4119 \pm 0.2715 \pm 0.0791$
		$0.0065 \pm 0.2170 \pm 0.1315$
		$-0.3005 \pm 0.2256 \pm 0.1140$
		$0.0563 \pm 0.1397 \pm 0.0040$
		$0.1221 \pm 0.1856 \pm 0.0543$

Table F.12: Values and uncertainties of Markus Diehl SDMEs extracted from 1998–2000, 2006–2007 combined data set. The kinematic bin is given in the first line, the SDME name is given in the first column. In the second and fourth columns are presented systematic uncertainties for hydrogen and deuterium correspondingly, BG corresponds to the background subtraction, Par to different Monte Carlo input parameters, P to all-in-one study. In the third and fifth columns are presented SDME values with resulting systematic and statistic uncertainties for hydrogen and deuterium correspondingly.

Bin	$1.40 \text{ GeV}^2 < Q^2 < 2.00 \text{ GeV}^2, -0.40 < t < 0.00 \text{ GeV}^2$	$1.40 \text{ GeV}^2 < Q^2 < 2.00 \text{ GeV}^2, -0.40 < t < -0.04 \text{ GeV}^2$
Element	$H : SDME \pm stat \pm sys$	$D : SDME \pm stat \pm sys$
$u_{++}^{00} + \epsilon u_{00}^{00}$	$0.3421 \pm 0.0197 \pm 0.0096$	$0.0001 \pm 0.0035 \pm 0.0038$
$\Re(u_{0+}^{0+} - u_{0+}^{-0})$	$-0.0201 \pm 0.0127 \pm 0.0143$	$0.0001 \pm 0.0042 \pm 0.0037$
u_{-+}^{-+}	$-0.0036 \pm 0.0300 \pm 0.0033$	$0.0002 \pm 0.0230 \pm 0.0056$
$\Im(u_{0+}^{0+} - u_{0+}^{-0})$	$-0.4663 \pm 0.0158 \pm 0.0201$	$0.0006 \pm 0.0038 \pm 0.0032$
$\Re u_{0+}^{00}$	$-0.0082 \pm 0.0246 \pm 0.0288$	$0.0003 \pm 0.0115 \pm 0.0025$
$\Re(u_{++}^{0+} - u_{++}^{-0} + 2\epsilon u_{0+}^{-0})$	$0.0081 \pm 0.0261 \pm 0.0541$	$0.0004 \pm 0.0141 \pm 0.0065$
$\Re(u_{-+}^{0+})$	$-0.0074 \pm 0.0187 \pm 0.0064$	$0.0013 \pm 0.0011 \pm 0.0055$
$\Im u_{0+}^{00}$	$-0.0249 \pm 0.0214 \pm 0.0380$	$0.0001 \pm 0.0226 \pm 0.0030$
$\Im(u_{++}^{0+} - u_{++}^{-0})$	$0.5470 \pm 0.0375 \pm 0.0198$	$0.0030 \pm 0.0109 \pm 0.0044$
$\Re(u_{0+}^{++} - u_{0+}^{--})$	$0.0002 \pm 0.0160 \pm 0.0329$	$0.0005 \pm 0.0268 \pm 0.0026$
$\Re(u_{0+}^{++})$	$-0.0160 \pm 0.0152 \pm 0.0146$	$0.0004 \pm 0.0042 \pm 0.0068$
$\Im(u_{0+}^{++} + u_{0+}^{--})$	$0.0254 \pm 0.0187 \pm 0.0092$	$0.0021 \pm 0.0225 \pm 0.0039$
$\Im u_{0+}^{++}$	$0.0289 \pm 0.0230 \pm 0.0159$	$0.0016 \pm 0.0224 \pm 0.0044$
$\Re(u_{0+}^{0-} - u_{0+}^{+0})$	$0.0138 \pm 0.0130 \pm 0.0050$	$0.0001 \pm 0.0018 \pm 0.0060$
$\Re(u_{-+}^{++} - \epsilon u_{00}^{--})$	$0.0130 \pm 0.0377 \pm 0.0412$	$0.0029 \pm 0.0710 \pm 0.0058$
$\Re(u_{-+}^{++})$	$-0.1516 \pm 0.1008 \pm 0.0089$	$0.0015 \pm 0.0062 \pm 0.0034$
$\Im(u_{0+}^{0-} - u_{0+}^{+0})$	$0.3842 \pm 0.1382 \pm 0.0091$	$0.0020 \pm 0.0354 \pm 0.0039$
$\Im u_{-+}^{++}$	$-0.1981 \pm 0.1116 \pm 0.0239$	$0.0065 \pm 0.0623 \pm 0.0077$
u_{-+}^{00}	$0.0889 \pm 0.1420 \pm 0.0442$	$0.0096 \pm 0.1139 \pm 0.0058$
$\Re(u_{-+}^{+0})$	$0.0066 \pm 0.1307 \pm 0.0251$	$0.0035 \pm 0.0029 \pm 0.0058$
$\Re(u_{0+}^{+-})$	$-0.1711 \pm 0.1262 \pm 0.0050$	$0.0048 \pm 0.0176 \pm 0.0029$
u_{-+}^{+-}	$0.0866 \pm 0.0783 \pm 0.0064$	$0.0014 \pm 0.0043 \pm 0.0042$
$\Im u_{0+}^{+-}$	$-0.0565 \pm 0.1091 \pm 0.0043$	$0.0029 \pm 0.0201 \pm 0.0041$

Table F.13: Values and uncertainties of Markus Diehl SDMEs extracted from 1998–2000, 2006–2007 combined data set. The kinematic bin is given in the first line, the SDME name is given in the first column. In the second and fourth columns are presented systematic uncertainties for hydrogen and deuterium correspondingly, BG corresponds to the background subtraction, Par to different Monte Carlo input parameters, P to all-in-one study. In the third and fifth columns are presented SDME values with resulting systematic and statistic uncertainties for hydrogen and deuterium correspondingly.

Bin	$2.00 \text{ GeV}^2 < Q^2 < 7.00 \text{ GeV}^2, -0.40 < t < 0.00 \text{ GeV}^2$	$2.00 \text{ GeV}^2 < Q^2 < 7.00 \text{ GeV}^2, -0.40 < t < -0.04 \text{ GeV}^2$
Element	$H : SDME \pm stat \pm sys$	$D : SDME \pm stat \pm sys$
$u_{++}^{00} + \epsilon u_{00}^{00}$	$0.4028 \pm 0.0204 \pm 0.0184$	$0.0013 \pm 0.0327 \pm 0.0038$
$\Re(u_{0+}^{0+} - u_{0+}^{-0})$	$-0.0176 \pm 0.0141 \pm 0.0128$	$0.0012 \pm 0.0268 \pm 0.0055$
u_{-+}^{+-}	$0.0178 \pm 0.0356 \pm 0.0184$	$0.0064 \pm 0.0494 \pm 0.0048$
$\Im(u_{0+}^{0+} - u_{0+}^{-0})$	$-0.4663 \pm 0.0171 \pm 0.0176$	$0.0002 \pm 0.0324 \pm 0.0036$
$\Re u_{0+}^{00}$	$-0.0365 \pm 0.0258 \pm 0.0356$	$0.0021 \pm 0.0588 \pm 0.0027$
$\Re(u_{++}^{0+} - u_{++}^{-0} + 2\epsilon u_{0+}^{-0})$	$0.0098 \pm 0.0286 \pm 0.0462$	$0.0048 \pm 0.1119 \pm 0.0066$
$\Re(u_{-+}^{0+})$	$-0.0435 \pm 0.0201 \pm 0.0041$	$0.0019 \pm 0.0166 \pm 0.0037$
$\Im u_{0+}^{00}$	$-0.0005 \pm 0.0231 \pm 0.0064$	$0.0013 \pm 0.0211 \pm 0.0021$
$\Im(u_{++}^{0+} - u_{++}^{-0})$	$0.4958 \pm 0.0332 \pm 0.0169$	$0.0002 \pm 0.0324 \pm 0.0033$
$\Re(u_{0+}^{++} - u_{0+}^{--})$	$-0.0172 \pm 0.0157 \pm 0.0374$	$0.0003 \pm 0.0353 \pm 0.0022$
$\Re(u_{0+}^{+-})$	$0.0035 \pm 0.0139 \pm 0.0157$	$0.0002 \pm 0.0327 \pm 0.0061$
$\Im(u_{0+}^{++} + u_{0+}^{--})$	$-0.0269 \pm 0.0174 \pm 0.0160$	$0.0013 \pm 0.0121 \pm 0.0063$
$\Im u_{0+}^{+-}$	$-0.0025 \pm 0.0221 \pm 0.0179$	$0.0006 \pm 0.0185 \pm 0.0028$
$\Re(u_{0+}^{0-} - u_{0+}^{+0})$	$0.0231 \pm 0.0120 \pm 0.0096$	$0.0000 \pm 0.0003 \pm 0.0078$
$\Re(u_{-+}^{+-} - \epsilon u_{00}^{--})$	$0.0323 \pm 0.0334 \pm 0.0234$	$0.0005 \pm 0.0160 \pm 0.0054$
$\Re(u_{-+}^{+-})$	$0.2124 \pm 0.0988 \pm 0.0158$	$0.0108 \pm 0.0251 \pm 0.0033$
$\Im(u_{0+}^{0-} - u_{0+}^{+0})$	$0.1392 \pm 0.1242 \pm 0.0059$	$0.0031 \pm 0.0611 \pm 0.0024$
$\Im u_{-+}^{+-}$	$0.0947 \pm 0.1010 \pm 0.0185$	$0.0050 \pm 0.0170 \pm 0.0064$
u_{-+}^{00}	$-0.3120 \pm 0.1285 \pm 0.0294$	$0.0103 \pm 0.1065 \pm 0.0044$
$\Re(u_{-+}^{+0})$	$-0.2139 \pm 0.1161 \pm 0.0093$	$0.0006 \pm 0.0461 \pm 0.0058$
$\Re(u_{0+}^{+-})$	$0.0041 \pm 0.1102 \pm 0.0111$	$0.0027 \pm 0.0170 \pm 0.0028$
u_{-+}^{+-}	$-0.0153 \pm 0.0677 \pm 0.0119$	$0.0013 \pm 0.0286 \pm 0.0042$
$\Im u_{0+}^{+-}$	$0.1212 \pm 0.0932 \pm 0.0175$	$0.0021 \pm 0.0671 \pm 0.0037$

Table F.14: Values and uncertainties of Markus Diehl SDMEs extracted from 1998–2000, 2006–2007 combined data set. The kinematic bin is given in the first line, the SDME name is given in the first column. In the second and fourth columns are presented systematic uncertainties for hydrogen and deuterium correspondingly, BG corresponds to the background subtraction, Par to different Monte Carlo input parameters, P to all-in-one study. In the third and fifth columns are presented SDME values with resulting systematic and statistic uncertainties for hydrogen and deuterium correspondingly.

Bin	$1.00 \text{ GeV}^2 < Q^2 < 7.00 \text{ GeV}^2, -0.40 < t < -0.20 \text{ GeV}^2$	$1.00 \text{ GeV}^2 < Q^2 < 7.00 \text{ GeV}^2, -0.40 < t < -0.20 \text{ GeV}^2$	$1.00 \text{ GeV}^2 < Q^2 < 7.00 \text{ GeV}^2, -0.40 < t < -0.20 \text{ GeV}^2$
Element	$H : BG \pm Par \pm P$	$H : SDME \pm stat \pm sys$	$D : SDME \pm stat \pm sys$
$u_{++}^{00} + \epsilon u_{00}^{00}$	$0.0002 \pm 0.0259 \pm 0.0042$	$0.3314 \pm 0.0244 \pm 0.0263$	$0.3557 \pm 0.0347 \pm 0.0140$
$\Re(u_{0+}^{0+} - u_{0+}^{-0})$	$0.0003 \pm 0.0442 \pm 0.0052$	$-0.0018 \pm 0.0160 \pm 0.0445$	$0.0070 \pm 0.0215 \pm 0.0297$
u_{-+}^{+-}	$0.0006 \pm 0.0337 \pm 0.0055$	$0.0518 \pm 0.0357 \pm 0.0342$	$0.1203 \pm 0.0584 \pm 0.0634$
$\Im(u_{0+}^{0+} - u_{0+}^{-0})$	$0.0006 \pm 0.0165 \pm 0.0035$	$-0.4039 \pm 0.0219 \pm 0.0168$	$-0.5097 \pm 0.0354 \pm 0.0178$
$\Re u_{0+}^{00}$	$0.0001 \pm 0.0681 \pm 0.0030$	$-0.0729 \pm 0.0295 \pm 0.0682$	$-0.1837 \pm 0.0468 \pm 0.0723$
$\Re(u_{++}^{0+} - u_{++}^{-0} + 2\epsilon u_{0+}^{-0})$	$0.0021 \pm 0.0736 \pm 0.0072$	$0.0427 \pm 0.0327 \pm 0.0740$	$0.1139 \pm 0.0527 \pm 0.0917$
$\Re(u_{-+}^{0+})$	$0.0008 \pm 0.0379 \pm 0.0056$	$0.0011 \pm 0.0221 \pm 0.0383$	$-0.0458 \pm 0.0315 \pm 0.0124$
$\Im \epsilon u_{0+}^{00}$	$0.0009 \pm 0.0102 \pm 0.0046$	$0.0054 \pm 0.0303 \pm 0.0113$	$-0.0163 \pm 0.0478 \pm 0.0060$
$\Im(u_{++}^{0+} - u_{++}^{-0})$	$0.0001 \pm 0.0309 \pm 0.0052$	$0.5469 \pm 0.0434 \pm 0.0313$	$0.5431 \pm 0.0634 \pm 0.0114$
$\Re(u_{0+}^{++} - u_{0+}^{--})$	$0.0001 \pm 0.0330 \pm 0.0044$	$0.0137 \pm 0.0200 \pm 0.0333$	$0.0494 \pm 0.0307 \pm 0.0331$
$\Re(u_{0+}^{++})$	$0.0007 \pm 0.0039 \pm 0.0098$	$-0.0100 \pm 0.0177 \pm 0.0106$	$-0.0497 \pm 0.0239 \pm 0.0147$
$\Im(u_{0+}^{++} + u_{0+}^{--})$	$0.0008 \pm 0.0109 \pm 0.0055$	$-0.0216 \pm 0.0218 \pm 0.0122$	$-0.0286 \pm 0.0324 \pm 0.0114$
$\Im \epsilon u_{0+}^{++}$	$0.0007 \pm 0.0029 \pm 0.0046$	$-0.0404 \pm 0.0263 \pm 0.0055$	$-0.0449 \pm 0.0427 \pm 0.0473$
$\Re(u_{0+}^{0-} - u_{0+}^{+0})$	$0.0000 \pm 0.0089 \pm 0.0085$	$0.0054 \pm 0.0148 \pm 0.0123$	$0.0223 \pm 0.0223 \pm 0.0196$
$\Re(u_{-+}^{++} - \epsilon u_{00}^{++})$	$0.0004 \pm 0.0449 \pm 0.0080$	$0.0457 \pm 0.0460 \pm 0.0456$	$-0.0049 \pm 0.0658 \pm 0.0902$
$\Re(u_{-+}^{++})$	$0.0037 \pm 0.0424 \pm 0.0048$	$0.0085 \pm 0.1128 \pm 0.0429$	$-0.2768 \pm 0.1921 \pm 0.0508$
$\Im(u_{0+}^{0-} - u_{0+}^{+0})$	$0.0087 \pm 0.0059 \pm 0.0046$	$0.1345 \pm 0.1672 \pm 0.0115$	$0.5700 \pm 0.2528 \pm 0.1903$
$\Im \epsilon u_{-+}^{++}$	$0.0102 \pm 0.0550 \pm 0.0067$	$0.0627 \pm 0.1285 \pm 0.0563$	$-0.1979 \pm 0.1936 \pm 0.1563$
u_{-+}^{00}	$0.0045 \pm 0.0707 \pm 0.0059$	$0.0656 \pm 0.1735 \pm 0.0711$	$-0.2831 \pm 0.2532 \pm 0.0805$
$\Re(u_{-+}^{+0})$	$0.0053 \pm 0.0515 \pm 0.0101$	$-0.2905 \pm 0.1395 \pm 0.0528$	$0.2667 \pm 0.2050 \pm 0.0364$
$\Re(u_{0+}^{+-})$	$0.0039 \pm 0.0154 \pm 0.0038$	$-0.2536 \pm 0.1411 \pm 0.0163$	$0.5121 \pm 0.2087 \pm 0.0813$
u_{-+}^{+-}	$0.0026 \pm 0.0217 \pm 0.0067$	$0.1061 \pm 0.0852 \pm 0.0228$	$-0.1423 \pm 0.1227 \pm 0.0401$
$\Im \epsilon u_{0+}^{+-}$	$0.0038 \pm 0.0581 \pm 0.0056$	$-0.0166 \pm 0.1241 \pm 0.0585$	$-0.2612 \pm 0.1753 \pm 0.0438$

Table F.15: Values and uncertainties of Markus Diehl SDMEs extracted from 1998–2000, 2006–2007 combined data set. The kinematic bin is given in the first line, the SDME name is given in the first column. In the second and fourth columns are presented systematic uncertainties for hydrogen and deuterium correspondingly, BG corresponds to the background subtraction, Par to different Monte Carlo input parameters, P to all-in-one study. In the third and fifth columns are presented SDME values with resulting systematic and statistic uncertainties for hydrogen and deuterium correspondingly.

Bin	$1.00 \text{ GeV}^2 < Q^2 < 7.00 \text{ GeV}^2, -0.20 < t < -0.10 \text{ GeV}^2$	$1.00 \text{ GeV}^2 < Q^2 < 7.00 \text{ GeV}^2, -0.20 < t < -0.10 \text{ GeV}^2$	$1.00 \text{ GeV}^2 < Q^2 < 7.00 \text{ GeV}^2, -0.20 < t < -0.10 \text{ GeV}^2$
Element	$H : BG \pm Par \pm P$	$H : SDME \pm stat \pm sys$	$D : SDME \pm stat \pm sys$
$u_{++}^{00} + \epsilon u_{00}^{00}$	$0.0007 \pm 0.0074 \pm 0.0050$	$0.3150 \pm 0.0218 \pm 0.0089$	$0.3479 \pm 0.0321 \pm 0.0139$
$\Re(u_{0+}^{0+} - u_{0+}^{-0})$	$0.0002 \pm 0.0163 \pm 0.0044$	$-0.0025 \pm 0.0144 \pm 0.0169$	$-0.0321 \pm 0.0226 \pm 0.0271$
u_{-+}^{-+}	$0.0007 \pm 0.0165 \pm 0.0048$	$-0.0013 \pm 0.0403 \pm 0.0172$	$-0.0434 \pm 0.0627 \pm 0.0343$
$\Im(u_{0+}^{0+} - u_{0+}^{-0})$	$0.0001 \pm 0.0023 \pm 0.0041$	$-0.4587 \pm 0.0206 \pm 0.0047$	$-0.5128 \pm 0.0313 \pm 0.0070$
$\Re u_{0+}^{00}$	$0.0002 \pm 0.0307 \pm 0.0032$	$-0.0127 \pm 0.0297 \pm 0.0309$	$-0.0525 \pm 0.0393 \pm 0.0146$
$\Re(u_{++}^{0+} - u_{++}^{-0} + 2\epsilon u_{0+}^{-0})$	$0.0002 \pm 0.0490 \pm 0.0077$	$-0.0179 \pm 0.0299 \pm 0.0496$	$-0.0261 \pm 0.0451 \pm 0.0522$
$\Re(u_{-+}^{0+})$	$0.0003 \pm 0.0006 \pm 0.0044$	$-0.0102 \pm 0.0217 \pm 0.0044$	$-0.0397 \pm 0.0332 \pm 0.0272$
$\Im u_{0+}^{00}$	$0.0003 \pm 0.0062 \pm 0.0045$	$-0.0140 \pm 0.0265 \pm 0.0076$	$0.0385 \pm 0.0410 \pm 0.0145$
$\Im(u_{++}^{0+} - u_{++}^{-0})$	$0.0012 \pm 0.0072 \pm 0.0066$	$0.5423 \pm 0.0437 \pm 0.0099$	$0.5856 \pm 0.0588 \pm 0.0251$
$\Re(u_{0+}^{++} - u_{0+}^{--})$	$0.0006 \pm 0.0425 \pm 0.0048$	$-0.0229 \pm 0.0188 \pm 0.0427$	$0.0268 \pm 0.0257 \pm 0.0224$
$\Re(u_{0+}^{--})$	$0.0003 \pm 0.0179 \pm 0.0081$	$0.0051 \pm 0.0172 \pm 0.0196$	$-0.0398 \pm 0.0220 \pm 0.0112$
$\Im(u_{0+}^{++} + u_{0+}^{--})$	$0.0002 \pm 0.0218 \pm 0.0082$	$0.0030 \pm 0.0216 \pm 0.0233$	$0.0170 \pm 0.0279 \pm 0.0104$
$\Im u_{0+}^{--}$	$0.0009 \pm 0.0274 \pm 0.0037$	$-0.0168 \pm 0.0270 \pm 0.0277$	$0.0002 \pm 0.0351 \pm 0.0105$
$\Re(u_{0+}^{0-} - u_{0+}^{+0})$	$0.0000 \pm 0.0056 \pm 0.0089$	$0.0198 \pm 0.0157 \pm 0.0105$	$0.0110 \pm 0.0206 \pm 0.0078$
$\Re(u_{++}^{+-} - \epsilon u_{00}^{++})$	$0.0001 \pm 0.0151 \pm 0.0075$	$-0.0096 \pm 0.0437 \pm 0.0168$	$-0.0545 \pm 0.0537 \pm 0.0326$
$\Re(u_{-+}^{++})$	$0.0003 \pm 0.0146 \pm 0.0047$	$0.0509 \pm 0.1052 \pm 0.0154$	$0.1737 \pm 0.1712 \pm 0.0510$
$\Im(u_{0+}^{0-} - u_{0+}^{+0})$	$0.0022 \pm 0.0148 \pm 0.0029$	$0.1845 \pm 0.1556 \pm 0.0153$	$0.2379 \pm 0.2314 \pm 0.0269$
$\Im u_{++}^{+-}$	$0.0014 \pm 0.0027 \pm 0.0085$	$-0.0692 \pm 0.1297 \pm 0.0090$	$-0.1267 \pm 0.1809 \pm 0.1050$
u_{-+}^{00}	$0.0009 \pm 0.0316 \pm 0.0051$	$-0.1787 \pm 0.1686 \pm 0.0320$	$-0.4230 \pm 0.2708 \pm 0.1982$
$\Re(u_{-+}^{+0})$	$0.0037 \pm 0.0009 \pm 0.0077$	$0.0433 \pm 0.1388 \pm 0.0086$	$0.2031 \pm 0.2003 \pm 0.0149$
$\Re(u_{0+}^{+-})$	$0.0052 \pm 0.0091 \pm 0.0031$	$0.0372 \pm 0.1520 \pm 0.0109$	$-0.1793 \pm 0.2052 \pm 0.0112$
u_{-+}^{+-}	$0.0017 \pm 0.0191 \pm 0.0047$	$-0.0201 \pm 0.0951 \pm 0.0197$	$-0.0926 \pm 0.1138 \pm 0.0081$
$\Im u_{0+}^{+-}$	$0.0040 \pm 0.0200 \pm 0.0056$	$0.1143 \pm 0.1317 \pm 0.0212$	$0.1730 \pm 0.1761 \pm 0.0699$

Table F.16: Values and uncertainties of Markus Diehl SDMEs extracted from 1998–2000, 2006–2007 combined data set. The kinematic bin is given in the first line, the SDME name is given in the first column. In the second and fourth columns are presented systematic uncertainties for hydrogen and deuterium correspondingly, BG corresponds to the background subtraction, Par to different Monte Carlo input parameters, P to all-in-one study. In the third and fifth columns are presented SDME values with resulting systematic and statistic uncertainties for hydrogen and deuterium correspondingly.

Bin	$1.00 \text{ GeV}^2 < Q^2 < 7.00 \text{ GeV}^2, -0.10 < t < -0.04 \text{ GeV}^2$	$1.00 \text{ GeV}^2 < Q^2 < 7.00 \text{ GeV}^2, -0.10 < t < -0.04 \text{ GeV}^2$	$1.00 \text{ GeV}^2 < Q^2 < 7.00 \text{ GeV}^2, -0.10 < t < -0.04 \text{ GeV}^2$
Element	$H : BG \pm Par \pm P$	$H : SDME \pm stat \pm sys$	$D : SDME \pm stat \pm sys$
$u_{++}^{00} + \epsilon u_{00}^{00}$	$0.0009 \pm 0.0175 \pm 0.0044$	$0.4173 \pm 0.0240 \pm 0.0181$	$0.4274 \pm 0.0366 \pm 0.0152$
$\Re(u_{0+}^{0+} - u_{0+}^{-0})$	$0.0014 \pm 0.0185 \pm 0.0039$	$-0.0482 \pm 0.0171 \pm 0.0190$	$-0.0235 \pm 0.0252 \pm 0.0083$
u_{-+}^{-+}	$0.0018 \pm 0.0069 \pm 0.0050$	$-0.0625 \pm 0.0409 \pm 0.0087$	$-0.1462 \pm 0.0709 \pm 0.0364$
$\Im(u_{0+}^{0+} - u_{0+}^{-0})$	$0.0007 \pm 0.0095 \pm 0.0042$	$-0.5031 \pm 0.0219 \pm 0.0104$	$-0.5691 \pm 0.0400 \pm 0.0261$
$\Re u_{0+}^{00}$	$0.0027 \pm 0.0460 \pm 0.0045$	$-0.0189 \pm 0.0308 \pm 0.0463$	$0.0548 \pm 0.0514 \pm 0.0582$
$\Re(u_{++}^{0+} - u_{++}^{-0} + 2\epsilon u_{0+}^{-0})$	$0.0023 \pm 0.0608 \pm 0.0090$	$-0.0029 \pm 0.0360 \pm 0.0615$	$-0.0286 \pm 0.0571 \pm 0.0615$
$\Re(u_{-+}^{0+})$	$0.0013 \pm 0.0327 \pm 0.0054$	$-0.0549 \pm 0.0244 \pm 0.0332$	$0.0193 \pm 0.0340 \pm 0.0116$
$\Im \pi u_{0+}^{00}$	$0.0006 \pm 0.0107 \pm 0.0044$	$-0.0221 \pm 0.0301 \pm 0.0115$	$-0.0221 \pm 0.0444 \pm 0.0309$
$\Im(u_{++}^{0+} - u_{++}^{-0})$	$0.0009 \pm 0.0278 \pm 0.0051$	$0.4658 \pm 0.0448 \pm 0.0283$	$0.7244 \pm 0.0755 \pm 0.0631$
$\Re(u_{0+}^{++} - u_{0+}^{--})$	$0.0005 \pm 0.0290 \pm 0.0037$	$0.0340 \pm 0.0172 \pm 0.0293$	$0.0564 \pm 0.0278 \pm 0.0541$
$\Re(u_{0+}^{--})$	$0.0010 \pm 0.0201 \pm 0.0085$	$-0.0165 \pm 0.0176 \pm 0.0219$	$0.0411 \pm 0.0259 \pm 0.0366$
$\Im(u_{0+}^{++} + u_{0+}^{--})$	$0.0007 \pm 0.0063 \pm 0.0065$	$0.0337 \pm 0.0221 \pm 0.0091$	$-0.0660 \pm 0.0333 \pm 0.0143$
$\Im \pi u_{0+}^{--}$	$0.0005 \pm 0.0027 \pm 0.0040$	$0.0944 \pm 0.0274 \pm 0.0048$	$0.0372 \pm 0.0360 \pm 0.0350$
$\Re(u_{0+}^{0-} - u_{0+}^{+0})$	$0.0003 \pm 0.0022 \pm 0.0096$	$0.0150 \pm 0.0156 \pm 0.0099$	$0.0237 \pm 0.0233 \pm 0.0101$
$\Re(u_{++}^{+-} - \epsilon u_{00}^{++})$	$0.0011 \pm 0.0110 \pm 0.0053$	$0.0162 \pm 0.0440 \pm 0.0122$	$-0.0841 \pm 0.0641 \pm 0.0809$
$\Re(u_{-+}^{++})$	$0.0010 \pm 0.0094 \pm 0.0039$	$-0.0082 \pm 0.1232 \pm 0.0102$	$-0.0513 \pm 0.1682 \pm 0.0108$
$\Im(u_{0+}^{0-} - u_{0+}^{+0})$	$0.0006 \pm 0.0087 \pm 0.0040$	$0.5058 \pm 0.1589 \pm 0.0096$	$-0.0845 \pm 0.2529 \pm 0.1193$
$\Im \pi u_{++}^{--}$	$0.0018 \pm 0.0381 \pm 0.0072$	$-0.1177 \pm 0.1390 \pm 0.0388$	$-0.0267 \pm 0.2322 \pm 0.0982$
u_{-+}^{00}	$0.0036 \pm 0.0013 \pm 0.0043$	$-0.1556 \pm 0.1658 \pm 0.0058$	$-0.0029 \pm 0.2812 \pm 0.1558$
$\Re(u_{-+}^{+0})$	$0.0006 \pm 0.0068 \pm 0.0085$	$-0.0359 \pm 0.1582 \pm 0.0109$	$-0.1634 \pm 0.2281 \pm 0.0352$
$\Re(u_{0+}^{+-})$	$0.0010 \pm 0.0240 \pm 0.0031$	$-0.1337 \pm 0.1430 \pm 0.0242$	$-0.6791 \pm 0.1924 \pm 0.0852$
u_{-+}^{+-}	$0.0009 \pm 0.0109 \pm 0.0047$	$-0.1396 \pm 0.0822 \pm 0.0119$	$0.5423 \pm 0.1329 \pm 0.1162$
$\Im \pi u_{0+}^{+-}$	$0.0010 \pm 0.0529 \pm 0.0056$	$-0.3124 \pm 0.1293 \pm 0.0532$	$0.6229 \pm 0.1989 \pm 0.0344$

Table F.17: Values and uncertainties of Markus Diehl SDMEs extracted from 1998–2000, 2006–2007 combined data set. The kinematic bin is given in the first line, the SDME name is given in the first column. In the second and fourth columns are presented systematic uncertainties for hydrogen and deuterium correspondingly, BG corresponds to the background subtraction, Par to different Monte Carlo input parameters, P to all-in-one study. In the third and fifth columns are presented SDME values with resulting systematic and statistic uncertainties for hydrogen and deuterium correspondingly.

Bin	$1.00 \text{ GeV}^2 < Q^2 < 7.00 \text{ GeV}^2, -0.04 < t < 0.00 \text{ GeV}^2$	$1.00 \text{ GeV}^2 < Q^2 < 7.00 \text{ GeV}^2, -0.04 < t < 0.00 \text{ GeV}^2$	$1.00 \text{ GeV}^2 < Q^2 < 7.00 \text{ GeV}^2, -0.04 < t < 0.00 \text{ GeV}^2$
Element	$H : BG \pm Par \pm P$	$H : SDME \pm stat \pm sys$	$D : BG \pm Par \pm P$
$u_{++}^{00} + \epsilon u_{00}^{00}$	$0.0007 \pm 0.0193 \pm 0.0045$	$0.3116 \pm 0.0237 \pm 0.0198$	$0.0024 \pm 0.0458 \pm 0.0049$
$\Re(u_{0+}^{0+} - u_{0+}^{-0})$	$0.0004 \pm 0.0059 \pm 0.0052$	$-0.0116 \pm 0.0149 \pm 0.0079$	$0.0017 \pm 0.0116 \pm 0.0050$
u_{--}^{++}	$0.0014 \pm 0.0032 \pm 0.0038$	$0.0172 \pm 0.0363 \pm 0.0051$	$0.0028 \pm 0.0312 \pm 0.0043$
$\Im(u_{0+}^{0+} - u_{0+}^{-0})$	$0.0004 \pm 0.0093 \pm 0.0046$	$-0.4732 \pm 0.0188 \pm 0.0104$	$0.0027 \pm 0.0118 \pm 0.0043$
$\Re u_{0+}^{00}$	$0.0010 \pm 0.0078 \pm 0.0025$	$0.0120 \pm 0.0312 \pm 0.0082$	$0.0006 \pm 0.0150 \pm 0.0023$
$\Re(u_{++}^{0+} - u_{++}^{-0} + 2\epsilon u_{0+}^{-0})$	$0.0019 \pm 0.0391 \pm 0.0054$	$0.0070 \pm 0.0347 \pm 0.0395$	$0.0015 \pm 0.0126 \pm 0.0054$
$\Re(u_{++}^{0+})$	$0.0020 \pm 0.0189 \pm 0.0057$	$0.0197 \pm 0.0231 \pm 0.0199$	$0.0011 \pm 0.0242 \pm 0.0052$
$\Im u_{0+}^{00}$	$0.0005 \pm 0.0035 \pm 0.0046$	$-0.0108 \pm 0.0273 \pm 0.0058$	$0.0012 \pm 0.0042 \pm 0.0039$
$\Im(u_{++}^{0+} - u_{++}^{-0})$	$0.0009 \pm 0.0577 \pm 0.0033$	$0.6143 \pm 0.0453 \pm 0.0578$	$0.0098 \pm 0.0712 \pm 0.0034$
$\Re(u_{0+}^{++} - u_{0+}^{--})$	$0.0002 \pm 0.0345 \pm 0.0047$	$-0.0301 \pm 0.0194 \pm 0.0349$	$0.0044 \pm 0.0304 \pm 0.0046$
$\Re(u_{0+}^{++} + u_{0+}^{--})$	$0.0007 \pm 0.0219 \pm 0.0050$	$-0.0047 \pm 0.0176 \pm 0.0225$	$0.0035 \pm 0.0300 \pm 0.0051$
$\Im(u_{0+}^{++} + u_{0+}^{--})$	$0.0007 \pm 0.0151 \pm 0.0077$	$-0.0245 \pm 0.0228 \pm 0.0170$	$0.0038 \pm 0.0211 \pm 0.0059$
$\Im u_{0+}^{++}$	$0.0013 \pm 0.0304 \pm 0.0048$	$-0.0243 \pm 0.0274 \pm 0.0308$	$0.0054 \pm 0.0230 \pm 0.0043$
$\Re(u_{0+}^{0-} - u_{0+}^{+0})$	$0.0003 \pm 0.0183 \pm 0.0094$	$0.0270 \pm 0.0152 \pm 0.0205$	$0.0003 \pm 0.0171 \pm 0.0115$
$\Re(u_{++}^{0+} - \epsilon u_{00}^{++})$	$0.0015 \pm 0.0357 \pm 0.0019$	$0.0392 \pm 0.0457 \pm 0.0358$	$0.0034 \pm 0.0677 \pm 0.0021$
$\Re(u_{-+}^{++})$	$0.0031 \pm 0.0449 \pm 0.0020$	$0.0745 \pm 0.1166 \pm 0.0450$	$0.0069 \pm 0.0452 \pm 0.0023$
$\Im(u_{0+}^{0-} - u_{0+}^{+0})$	$0.0080 \pm 0.0130 \pm 0.0018$	$0.1885 \pm 0.1861 \pm 0.0154$	$0.0100 \pm 0.0798 \pm 0.0029$
$\Im u_{++}^{++}$	$0.0070 \pm 0.0421 \pm 0.0058$	$-0.2607 \pm 0.1447 \pm 0.0430$	$0.0073 \pm 0.0671 \pm 0.0082$
u_{-+}^{00}	$0.0066 \pm 0.0434 \pm 0.0062$	$-0.1312 \pm 0.1949 \pm 0.0443$	$0.0041 \pm 0.0064 \pm 0.0071$
$\Re(u_{-+}^{+0})$	$0.0063 \pm 0.0332 \pm 0.0112$	$-0.1819 \pm 0.1643 \pm 0.0356$	$0.0015 \pm 0.0313 \pm 0.0075$
$\Re(u_{0+}^{+-})$	$0.0015 \pm 0.0402 \pm 0.0038$	$-0.1353 \pm 0.1556 \pm 0.0404$	$0.0037 \pm 0.0464 \pm 0.0044$
u_{-+}^{+-}	$0.0025 \pm 0.0208 \pm 0.0042$	$0.2075 \pm 0.0978 \pm 0.0214$	$0.0007 \pm 0.0184 \pm 0.0043$
$\Im u_{0+}^{+-}$	$0.0015 \pm 0.0158 \pm 0.0054$	$0.0087 \pm 0.1342 \pm 0.0167$	$0.0037 \pm 0.0281 \pm 0.0049$
			$D : SDME \pm stat \pm sys$
			$0.3028 \pm 0.0337 \pm 0.0462$
			$-0.0300 \pm 0.0244 \pm 0.0128$
			$-0.0282 \pm 0.0630 \pm 0.0317$
			$-0.5499 \pm 0.0354 \pm 0.0128$
			$-0.0468 \pm 0.0429 \pm 0.0152$
			$0.1215 \pm 0.0497 \pm 0.0138$
			$0.0304 \pm 0.0315 \pm 0.0248$
			$-0.0604 \pm 0.0449 \pm 0.0059$
			$0.7624 \pm 0.0723 \pm 0.0719$
			$-0.0374 \pm 0.0311 \pm 0.0311$
			$-0.0308 \pm 0.0283 \pm 0.0306$
			$-0.0480 \pm 0.0340 \pm 0.0223$
			$-0.0884 \pm 0.0418 \pm 0.0240$
			$0.0316 \pm 0.0262 \pm 0.0206$
			$-0.0836 \pm 0.0734 \pm 0.0678$
			$0.5139 \pm 0.1501 \pm 0.0458$
			$-0.0573 \pm 0.2231 \pm 0.0805$
			$0.0445 \pm 0.1873 \pm 0.0680$
			$-0.8918 \pm 0.2568 \pm 0.0104$
			$-0.4113 \pm 0.1746 \pm 0.0323$
			$-0.1611 \pm 0.1971 \pm 0.0468$
			$0.0683 \pm 0.1074 \pm 0.0189$
			$0.2405 \pm 0.1816 \pm 0.0288$

Table F.18: Values and uncertainties of Markus Diehl SDMEs extracted from 1998–2000, 2006–2007 combined data set. The kinematic bin is given in the first line, the SDME name is given in the first column. In the second and fourth columns are presented systematic uncertainties for hydrogen and deuterium correspondingly, BG corresponds to the background subtraction, Par to different Monte Carlo input parameters, P to all-in-one study. In the third and fifth columns are presented SDME values with resulting systematic and statistic uncertainties for hydrogen and deuterium correspondingly.

Bin	$1.00 \text{ GeV}^2 < Q^2 < 7.00 \text{ GeV}^2, -0.40 < t < 0.00 \text{ GeV}^2$	$1.00 \text{ GeV}^2 < Q^2 < 7.00 \text{ GeV}^2, -0.40 < t < -0.04 \text{ GeV}^2$
Element	$H : SDME \pm stat \pm sys$	$D : SDME \pm stat \pm sys$
$u_{++}^{00} + \epsilon u_{00}^{00}$	$0.3383 \pm 0.0116 \pm 0.0102$	$0.3820 \pm 0.0196 \pm 0.0306$
$\Re(u_{0+}^{0+} - u_{0+}^{-0})$	$-0.0090 \pm 0.0076 \pm 0.0087$	$-0.0038 \pm 0.0135 \pm 0.0218$
u_{-+}^{+-}	$0.0148 \pm 0.0181 \pm 0.0193$	$-0.0096 \pm 0.0348 \pm 0.0101$
$\Im(u_{0+}^{0+} - u_{0+}^{-0})$	$-0.4535 \pm 0.0092 \pm 0.0184$	$-0.4703 \pm 0.0180 \pm 0.0165$
$\Re u_{0+}^{00}$	$-0.0311 \pm 0.0147 \pm 0.0199$	$-0.0625 \pm 0.0252 \pm 0.0637$
$\Re(u_{++}^{0+} - u_{++}^{-0} + 2\epsilon u_{0+}^{-0})$	$0.0155 \pm 0.0152 \pm 0.0449$	$0.0436 \pm 0.0269 \pm 0.0554$
$\Re(u_{-+}^{0+})$	$-0.0071 \pm 0.0111 \pm 0.0200$	$-0.0214 \pm 0.0191 \pm 0.0233$
$\Im u_{0+}^{00}$	$-0.0114 \pm 0.0130 \pm 0.0059$	$0.0107 \pm 0.0259 \pm 0.0112$
$\Im(u_{++}^{0+} - u_{++}^{-0})$	$0.5450 \pm 0.0211 \pm 0.0073$	$0.5597 \pm 0.0361 \pm 0.0085$
$\Re(u_{0+}^{++} - u_{0+}^{--})$	$0.0051 \pm 0.0094 \pm 0.0356$	$0.0243 \pm 0.0156 \pm 0.0565$
$\Re(u_{0+}^{+-})$	$-0.0149 \pm 0.0086 \pm 0.0213$	$-0.0156 \pm 0.0132 \pm 0.0507$
$\Im(u_{0+}^{++} + u_{0+}^{--})$	$-0.0006 \pm 0.0107 \pm 0.0130$	$-0.0160 \pm 0.0175 \pm 0.0142$
$\Im u_{0+}^{+-}$	$0.0009 \pm 0.0133 \pm 0.0117$	$-0.0229 \pm 0.0202 \pm 0.0100$
$\Re(u_{0+}^{0-} - u_{0+}^{+0})$	$0.0138 \pm 0.0074 \pm 0.0084$	$0.0089 \pm 0.0111 \pm 0.0091$
$\Re(u_{++}^{+-} - \epsilon u_{00}^{--})$	$0.0276 \pm 0.0215 \pm 0.0079$	$-0.0126 \pm 0.0354 \pm 0.0425$
$\Re(u_{-+}^{+-})$	$0.0387 \pm 0.0574 \pm 0.0205$	$-0.1022 \pm 0.0951 \pm 0.0089$
$\Im(u_{0+}^{0-} - u_{0+}^{+0})$	$0.2235 \pm 0.0779 \pm 0.0091$	$0.2922 \pm 0.1335 \pm 0.0790$
$\Im u_{-+}^{+-}$	$-0.0416 \pm 0.0653 \pm 0.0190$	$-0.1251 \pm 0.1096 \pm 0.0290$
u_{-+}^{00}	$-0.0608 \pm 0.0798 \pm 0.0081$	$-0.1065 \pm 0.1378 \pm 0.0452$
$\Re(u_{-+}^{+0})$	$-0.1149 \pm 0.0765 \pm 0.0092$	$0.0620 \pm 0.1152 \pm 0.0103$
$\Re(u_{0+}^{+-})$	$-0.1176 \pm 0.0724 \pm 0.0113$	$-0.0238 \pm 0.1133 \pm 0.0406$
u_{-+}^{+-}	$0.0305 \pm 0.0460 \pm 0.0059$	$-0.0105 \pm 0.0669 \pm 0.0091$
$\Im u_{0+}^{+-}$	$-0.0220 \pm 0.0628 \pm 0.0173$	$0.0772 \pm 0.1026 \pm 0.0121$
	$H : BG \pm Par \pm P$	$D : BG \pm Par \pm P$
$u_{++}^{00} + \epsilon u_{00}^{00}$	$0.0001 \pm 0.0092 \pm 0.0042$	$0.0001 \pm 0.0301 \pm 0.0056$
$\Re(u_{0+}^{0+} - u_{0+}^{-0})$	$0.0000 \pm 0.0080 \pm 0.0034$	$0.0002 \pm 0.0205 \pm 0.0074$
u_{-+}^{+-}	$0.0000 \pm 0.0188 \pm 0.0042$	$0.0004 \pm 0.0082 \pm 0.0058$
$\Im(u_{0+}^{0+} - u_{0+}^{-0})$	$0.0000 \pm 0.0180 \pm 0.0040$	$0.0001 \pm 0.0155 \pm 0.0055$
$\Re u_{0+}^{00}$	$0.0002 \pm 0.0198 \pm 0.0018$	$0.0004 \pm 0.0637 \pm 0.0023$
$\Re(u_{++}^{0+} - u_{++}^{-0} + 2\epsilon u_{0+}^{-0})$	$0.0001 \pm 0.0446 \pm 0.0050$	$0.0004 \pm 0.0548 \pm 0.0084$
$\Re(u_{-+}^{0+})$	$0.0001 \pm 0.0198 \pm 0.0031$	$0.0004 \pm 0.0226 \pm 0.0054$
$\Im u_{0+}^{00}$	$0.0001 \pm 0.0053 \pm 0.0025$	$0.0008 \pm 0.0091 \pm 0.0064$
$\Im(u_{++}^{0+} - u_{++}^{-0})$	$0.0004 \pm 0.0065 \pm 0.0034$	$0.0002 \pm 0.0062 \pm 0.0058$
$\Re(u_{0+}^{++} - u_{0+}^{--})$	$0.0001 \pm 0.0355 \pm 0.0030$	$0.0001 \pm 0.0563 \pm 0.0042$
$\Re(u_{0+}^{+-})$	$0.0002 \pm 0.0198 \pm 0.0080$	$0.0001 \pm 0.0490 \pm 0.0133$
$\Im(u_{0+}^{++} + u_{0+}^{--})$	$0.0002 \pm 0.0123 \pm 0.0042$	$0.0004 \pm 0.0106 \pm 0.0095$
$\Im u_{0+}^{+-}$	$0.0002 \pm 0.0114 \pm 0.0028$	$0.0002 \pm 0.0093 \pm 0.0035$
$\Re(u_{0+}^{0-} - u_{0+}^{+0})$	$0.0001 \pm 0.0065 \pm 0.0053$	$0.0002 \pm 0.0065 \pm 0.0063$
$\Re(u_{++}^{+-} - \epsilon u_{00}^{--})$	$0.0001 \pm 0.0049 \pm 0.0062$	$0.0001 \pm 0.0409 \pm 0.0116$
$\Re(u_{-+}^{+-})$	$0.0000 \pm 0.0202 \pm 0.0035$	$0.0022 \pm 0.0051 \pm 0.0069$
$\Im(u_{0+}^{0-} - u_{0+}^{+0})$	$0.0001 \pm 0.0084 \pm 0.0035$	$0.0004 \pm 0.0788 \pm 0.0056$
$\Im u_{-+}^{+-}$	$0.0004 \pm 0.0186 \pm 0.0042$	$0.0038 \pm 0.0278 \pm 0.0076$
u_{-+}^{00}	$0.0004 \pm 0.0067 \pm 0.0047$	$0.0022 \pm 0.0449 \pm 0.0044$
$\Re(u_{-+}^{+0})$	$0.0008 \pm 0.0084 \pm 0.0036$	$0.0023 \pm 0.0082 \pm 0.0058$
$\Re(u_{0+}^{+-})$	$0.0011 \pm 0.0109 \pm 0.0028$	$0.0032 \pm 0.0400 \pm 0.0059$
u_{-+}^{+-}	$0.0005 \pm 0.0031 \pm 0.0050$	$0.0004 \pm 0.0029 \pm 0.0086$
$\Im u_{0+}^{+-}$	$0.0008 \pm 0.0171 \pm 0.0027$	$0.0013 \pm 0.0108 \pm 0.0054$

Table F.19: Values and uncertainties of Markus Diehl SDMEs extracted from 1998–2000, 2006–2007 combined data set. The kinematic bin is given in the first line, the SDME name is given in the first column. In the second and fourth columns are presented systematic uncertainties for hydrogen and deuterium correspondingly, BG corresponds to the background subtraction, Par to different Monte Carlo input parameters, P to all-in-one study. In the third and fifth columns are presented SDME values with resulting systematic and statistic uncertainties for hydrogen and deuterium correspondingly.

Bibliography

- [1] R. Hofstadter and R. W. McAllister, *Electron Scattering from the Proton*, Phys. Rev. 98, 217 - 218 (1955).
- [2] E. Leader and M. Anselmino, *A crisis in the parton model: where, oh where is the proton spin?*, Z. Phys. C41, 239, (1988).
- [3] R. Devenish and A. Cooper-Sarkar, *Deep Inelastic Scattering*, p 263 (Oxford university Press, 2004).
- [4] M. Anselmino, A. Efremov and E. Leader, *The theory and phenomenology of polarized deep inelastic scattering*, Phys. Rept. 261 (1995), [hep-ph/9501369].
- [5] J.D. Bjorken, *Current Algebra at Small Distances*, Proceedings of the International School of Physics "Enrico Fermi", Course XLI (New York:Academic Press, 1968), pp. 55-81.
- [6] T.H. Bauer, R.D. Spital, D.R. Yennie, and F.M. Pipkin, *The hadronic properties of the photon in high-energy interactions*, Rev. Mod. Phys. 50, 261 (1978).
- [7] J. Sakurai, *Vector-meson dominance and high-energy electron-proton inelastic scattering*, Phys. Rev. Lett. 22, 981 (1969).
- [8] M.L. Perl, *High-Energy Hadron Physics*, Wiley-Sons, (1974).
- [9] *Exclusive vector-meson production in muon-proton scattering*, C. del Papa and al., Phys. Rev. D19, 1303, (1979).
- [10] M.R. Adams et al., *Diffraction production of $\rho(770)$ mesons in muon-proton interactions at 490 GeV*, Z. Phys. C74, 237, (1997).
- [11] P.D.B. Collins, *An Introduction to Regge Theory and High Energy Physics*, Cambridge University press (1977).
- [12] J.C. Collins, L. Frankfurt, M. Strikman, *Factorization for hard exclusive electroproduction of mesons in QCD*, Phys. Rev. D 56, 2982 (1997) [hep-ph/9611433].
- [13] K. Goeke, M.V. Polyakov, M. Vanderhaeghen, *Hard Exclusive Reactions and the Structure of Hadrons*, Prog. Part. Nucl. Phys .47, 401 (2001) [hep-ph/0106012].
- [14] A.V. Belitsky, D. Müller, *Nucleon hologram with exclusive lepton production*, Nucl. Phys. A711, 118-126 (2002), [hep-ph/0206306].

- [15] A. Donnachie, P.V. Landshoff, *Phys. Lett. B* 185, 403 (1987).
- [16] S.V. Goloskokov, P. Kroll, *Vector-meson electroproduction at small Bjorken- x and generalized parton distributions*, *Eur. Phys. J. C* 42, 281-301 (2005), [hep-ph/0501242].
- [17] S.V. Goloskokov, P. Kroll, *The role of the quark and gluon GPDs in hard vector-meson electroproduction*, *Eur. Phys. J. C* 53, 367-384 (2008), [arXiv:0708.3569] .
- [18] R. L. Jaffe, *Spin, twist and hadron structure in deep inelastic processes*, Talk given at Ettore Majorana International School of Nucleon Structure, 1st Course: the Spin structure of the Nucleon, Erice, Italy, 3-10 August 1995, [arXiv:hep-ph/9602236].
- [19] K. Schilling, G.Wolf, *How to analyze vector-meson production in inelastic lepton scattering*, *Nucl. Phys. B* 61, 381-413 (1973).
- [20] P. Joos et al., *ρ production by virtual photons*, *Nucl. Phys. B* 113, 53 (1976).
- [21] M. Diehl, *Vector meson production from a polarized nucleon*, *J. High Energy Phys.* 09, 064. (2007), arXiv:0704.1565[hep-ph].
- [22] M. Diehl, ρ^0 , *J. High Energy Phys. B* 545, 505 (1999).
- [23] J. Breitweg et al., ZEUS Coll., *Measurement of the Spin-Density Matrix Elements in Exclusive Electroproduction of ρ^0 mesons at HERA*, *Eur. Phys. J. C*12, 393 (2000).
- [24] S. Chekanov et al., ZEUS Coll., *Measurement of the Spin-Density Matrix Elements in Exclusive Electroproduction of ρ^0 mesons at HERA*, *PMC Physics A* 1,6 (2007).
- [25] C. Adloff et al., H1 Coll., *Elastic electroproduction of ρ mesons at HERA*, *Eur. Phys. J. C*13, 371 (2000).
- [26] A. Airapetian et al, HERMES Coll., *Spin density matrix elements in exclusive ρ^0 electroproduction on 1H and 2H targets at 27.6 GeV beam energy*, *Eur. Phys. J.* 62 659-694 (2009).
- [27] J. Breitweg et al., ZEUS Coll., *Exclusive electroproduction of ϕ meson at HERA*, DESY 05-038, [arXiv:hep-ex/0504010v1].
- [28] C. Adloff et al., H1 Coll., *Diffraction electroproduction of ρ and ϕ mesons at HERA*, *J. High Energy Phys.* 05 032 [arxiv:0910.5831], (2010) .
- [29] J. P. Santoro et al. (CLAS Collaboration), *Electroproduction of $\phi(1020)$ mesons at $1.4\text{GeV}^2 < Q^2 < 3.8\text{GeV}^2$ measured with the CLAS spectrometer*, *Phys. Rev. C* 78, 025210 (2008).
- [30] I. Akushevich, *Radiative effects in processes of diffractive vector meson electroproduction*, *Eur. Phys. J. C*6 (1999), [arXiv:hep-ph/9808309].
- [31] I. Akushevich, P. Kuzhir, *QED radiative corrections to spin-density matrix elements in exclusive vector meson production*, *Phys. Lett. B*474 , 411-415 (2000), [arXiv:hep-ph/9911346].

- [32] A.A. Sokolov and I.M. Ternov, *Synchrotron radiation*, Pergamon Press, New York, 1968; Akademie-Verlag, Berlin, (1968).
- [33] I. Flegel and P. Sodling, *Super microscope HERA: Gazing into the heart of matter*, DESY brochure (2002).
- [34] A. Airapetian et al., *The HERMES polarized hydrogen and deuterium gas target in the HERA electron storage ring*, Nucl. Instr. and Meth. A540, 68 (2005), physics/0408137.
- [35] M. Beckmann, A. Borissov, S. Brauksiepe, F. Burkart, H. Fischer, J. Franz, F.H. Heinsius, K. Königsmann, W. Lorenzon, F.M. Menden, A. Most, S. Rudnitsky, C. Schill, J. Seibert, A. Simon *The Longitudinal Polarimeter at HERA*, Nucl. Instr. and Meth. A479 334, (2002).
- [36] D.P. Barber et al., *The HERA Polarimeter and the First Observation of Electron Spin Polarization at HERA* Nucl. Instr. and Meth. A329, 79 (1993).
- [37] K. Ackerstaff et al., *The HERMES Spectrometer*, Nucl. Instr. and Meth. A417, 230 (1998), [arXiv:hep-ex/9806008].
- [38] M.G. van Beuzekom, E. Garutti, D. Heesben, J.J.M. Steijger and J. Visser, *First experience with the HERMES silicon detector*, Nucl. Instrum.Meth. A461, 247-250 (2001).
- [39] J.T. Brack, J.E. Belz, S. Clark, J. Ely, B. Fox, G.J. Hofman, E.R. Kinney and D.J. Mercer, *The HERMES forward tracking chambers: Construction, operation and aging effects*, Nucl. Instrum. Meth. A469, 47 (2001).
- [40] S. Bernreuther et al., *The HERMES back drift chambers* Nucl. Instrum. Meth. A416, 45 (1998), [hep-ex/9803005].
- [41] N. Akopov et al., *The HERMES dual ring imaging Cherenkov detector*, Nucl. Instrum. Meth. A479, 511-530 (2002), [arXiv:physics/0104033].
- [42] H. Avakian et al., *Performance of the electromagnetic calorimeter of the HERMES experiment*, Nucl. Instrum. Meth. A417, 69 (1998), [arXiv:hep-ex/9810004].
- [43] W. Augustyniak et al., *TMC - vertex reconstruction in the presence of the HERMES transverse magnet.*, HERMES Internal Note 07-008 (2008).
- [44] M. Golembiovskaya, A. Rostomyan, D. Veretennikov, S. Yaschenko, *Spin density matrix elements of exclusive phi meson production extracted from 1998-2007 data.*, HERMES release report, <http://www-hermes.desy.de/reports/0412/PHI-SDME/>, last availability on 26.11.2013.
- [45] T. Sjöstrand, S. Mrenna and P.Z. Skands, *PYTHIA 6.4 Physics and Manual*, JHEP 0605 026, (2006), [hep-ph/0603175].
- [46] https://hermes-wiki.desy.de/MC_Generators Hermes web-page on Monte Carlo generators, last availability on 26.11.2013..
- [47] I. Akushevich, H. Böttcher, and D. Ryckbosch, *Monte Carlo Generator for Radiative Events in DIS on Polarized and Unpolarized Targets*, [arXiv:hep-ph/9906408].

- [48] B. Anderson et al., *Parton Fragmentation and String dynamics*, Phys. Rept. 97, 31 (1983).
- [49] G.A. Schuler and T. Sjöstrand, Phys. Lett. B300, 169, (1993).
- [50] GEANT manual *Detector description and simulation tool*, wwwinfo.cern.ch/asdoc/pdfdir/geant.pdf, (1993)
- [51] <https://hermes-wiki.desy.de/HTC> Hermes web-page on trackings, last availability on 26.11.2013.
- [52] G. Wolf, *Review of High Energy Diffraction in Real and virtual Photon Proton scattering at HERA*, Rept. Prog. Phys. 73:116202, (2010), [arXiv:0907.1217/hep-ex].
- [53] http://www-hermes.desy.de/groups/daqlgrp/OFFLINE_DQ/uDST/index.html#docu HERMES data quality web page, last availability on 26.11.2013.
- [54] Particle Data Group, C. Caso et al., Eur. Phys. J. C3 (1998)
- [55] http://www-hermes.desy.de/groups/daqlgrp/OFFLINE_DQ/uDST/general/docu/DISstats.html#lumiconstant HERMES luminosity page, last availability on 26.11.2013.
- [56] B. Povh and J. Hufner, *Geometric interpretation of hadron-proton total cross section and a determination of hadronic radii*, Phys. Rev. Lett. 58 (1987) 1612.
- [57] S. Manaenkov, private communication.
- [58] C. A. Miller, http://www-hermes.desy.de/groups/mgmtgrp/COLLABMEETINGS/TRANSVERSITY_JUNE06/MaxLike.pdf, Maximum likelihood method, last availability on 26.11.2013.
- [59] <http://www-hermes.desy.de/groups/vmgrp/mayya/14.01.2013/PEPSI/>, last availability on 26.11.2013.
- [60] <http://www-hermes.desy.de/groups/vmgrp/mayya/14.01.2013/PEPSI/MD/>, last availability on 26.11.2013.
- [61] <http://www-hermes.desy.de/reports/0407/SDME-phi/>, last availability on 26.11.2013.